Synthesis of metal-organic frameworks for energetic applications

Boushra Mortada

Université de Haute-Alsace

Université de Strasbourg

Thèse

Présentée pour l'obtention du grade de

Docteur de l'Université de Haute-Alsace

Ecole Doctorale : Physique et Chimie Physique (ED 182)

Discipline : Chimie des Matériaux

Présentée et soutenue publiquement par

Boushra MORTADA

14 Novembre 2019

Synthesis of Metal-Organic Frameworks for Energetic Applications

Synthèse de Matériaux de Type Metal-Organic Frameworks pour l'Energétique

Directrice de thèse : Pr. Claire MARICHAL

Codirecteur de thèse : Dr. Gérald CHAPLAIS

Jury :

Pr. Nathalie AUDEBRAND , Université de Rennes 1 (Rapporteur)

Dr. Renaud DENOYEL, Aix-Marseille Université, CNRS (Rapporteur)

Dr. François-Xavier COUDERT, Chimie Paristech, PSL Université, CNRS (Examinateur)

Dr. Habiba NOUALI, Institut de Sciences des Matériaux de Mulhouse (Membre invitée)

Dr. Joël PATARIN, Directeur de recherche, CNRS (Membre invité)

Acknowledgements

This PhD work was realized at l'Institut de Sciences des Matériaux de Mulhouse (IS2M). Therefore, I would like to thank the directors of the institute and my team "Matériaux à Porosité Controlée (MPC)", Vincent ROUCOULES and Benedict LEBEAU, respectively, for welcoming me at the lab during the past three years.

To my supervisors, Professor Claire MARICHAL and Doctor Gérald CHAPLAIS. Thank you for trusting me and giving me the chance to pursue this PhD. I cannot say that doing a PhD was easy, but, indeed, I learned a lot thanks to your objective comments and suggestions. Thank you for all the time that you have given me and for being highly dedicated to your job. I really appreciate it all.

I would also like to thank Pr. Nathalie AUDEBRAUND and Dr. Renaud DENOYEL for accepting to be reviewers of this thesis manuscript. In addition, I thank Dr François-Xavier COUDERT for accepting to be member of the jury. Special thanks to Dr. Joël PATARIN and Dr. Habiba NOUALI for the great help and all the useful advice that they gave me during my PhD.

I also thank all the permanent members of the team MPC for their help in the laboratory work. Especially Laure MICHELIN and Doctors Ludovic JOSIEN and Didier LE NOUEN for the training and the great help they provided me while using the different techniques in the laboratory. I would also like to thank Dr. Jean-Louis PALLIAUD for the Rietveld refinements and the very interesting scientific discussions. Special thanks to Nathalie CASTELEIN for all the great help she provided during the past three years.
PS: Nathalie and Laure, thank you for all the nice and fun conversations we had ☺

To the nice people I met in Mulhouse, (in alphabetical order) Adrian, Ashling, Assi, Carole, Charles, Dylan, Elyssa, Fatima, Flaurian, Gwandoline, Jocelin, Kassem, Kawthar, Lize, Luis-Felipe, Lydie, Marie, Marion, Mathieu, Melania, Mirna, Natalia, Nghia, Nour, Oumina, Zainab and *Zakaria*. Thank you for adding so much to the past three years.
PS: To those who were great listeners when I needed to speak, a very special thank you ;)

To my dad, the one and only man, and my angel in heaven… Thank you for all the love and trust that you gave me. For all the days you worked so hard to provide us a happy life. You may not be physically with us anymore, but I know that your pure and beautiful soul has never left us and is always around. Thank you for being a great role model. Thank you for all the beautiful memories… I love you ♡

So much love and hugs and kisses from the other world Baba…

To my mother, the super mom, my super hero, my role model and the best gift from God … Who is never tired of being strong and of facing all life's difficulties to protect and support her family. Words will never be enough to thank you for your unconditional love and support, they will never be enough to express how much I love you mama! It would have never been the same without you …May God bless you and keep you healthy and safe and sound.
So much love and hugs and kisses from the other side of the world Mama…
To my amazing sisters Sara and Lama, thank you for coming to this world and making me a big sister. I can never imagine my life without my two babies. I am so proud of you and could not have asked for a better gift from god.
Forever sisters and best friends, forever all the love in the world… (my baby Sarou and baby Lamloumi♡)

To my brother in law, thank you for becoming part of our family. Your kind and, indeed, fun personality brings us so much joy. We all love you so much♡

To my big family, my grandparents, aunts, uncles, and cousins (the youths and the babies), I love you all so much. You truly make our life so much better. Thank you all for loving us, for being supportive, and for sticking by our side during the happy days and, more importantly, during the bad ones. We are so lucky to have you♡

Special thanks to my aunt Hanadi, who has always shown me extraordinary love and support, since I was a little girl. Thank you for being an amazing second mother, whom I can trust and ask for advice about anything, anytime. I love you to the moon and back khalto.

Also special thanks to my Aunt Inaya, the purest heart I have ever known, the cool and fun aunt! Thank you for being not only an amazing aunt, but also a second mother. I love you to the moon and back khalto.

Résumés du Manuscrit en Français

Comme ce manuscrit a été rédigé en anglais, un résumé en français de chaque chapitre a été ajouté.

Résumé du Chapitre 1

Dans le domaine de nouvelles applications énergétiques, Eroshenko a d'abord exploré et puis développé des expériences d'intrusion–extrusion de liquides non-mouillants dans des matériaux poreux lyophobes destinées au stockage et à l'absorption de l'énergie mécanique. L'invention d'Eroshenko repose sur l'existence d'un système hétérogène lyophobe (SHL), constitué d'un solide poreux lyophobe entourée d'un liquide non-mouillant, qui est capable de restituer, d'accumuler ou de dissiper de l'énergie. Selon Soulard *et al*., le phénomène d'intrusion–extrusion peut s'expliquer de la manière suivante : pour introduire un liquide non-mouillant dans un matériau poreux, il convient d'appliquer une pression mécanique, appelée pression d'intrusion (P_{int}). Pendant la phase d'intrusion, l'énergie mécanique est progressivement appliquée sur le SHL. À des pressions très basses (0,003-1 MPa), les particules du solide sont comprimées et le liquide non-mouillant s'infiltre dans la porosité interparticulaire. Sur les diagrammes pression-volume (*P–V*), cette étape se traduit par une variation de volume (augmentation du volume) du liquide non-mouillant. Lorsque la pression appliquée atteint une valeur critique, correspondant à la pression d'intrusion (P_{int}), les molécules du liquide non-mouillant peuvent pénétrer dans la porosité du matériau solide. Dans le cas idéal, cette étape est caractérisée sur les diagrammes *P–V* par une forte augmentation du volume du liquide non-mouillant à une pression constante. Après le remplissage complet de la porosité, théoriquement, aucune variation de volume supplémentaire ne devrait être observée lors de l'application continue de la pression externe. Au niveau microscopique, au cours de l'étape d'intrusion, le liquide massif est transformé en une multitude d'agrégats moléculaires, qui pénètrent dans les pores et développent ainsi une grande interface solide-liquide ($\Delta\Omega > 0$). Par conséquent, une partie de l'énergie mécanique, fournie par la pression externe, est convertie en énergie interfaciale. Du point de vue thermodynamique, l'augmentation du contact à l'interface solide-liquide est associée à une augmentation de l'énergie libre de Gibbs du système ($\Delta G > 0$). Lors de la deuxième étape, l'étape d'extrusion, la pression externe est progressivement relâchée. En fonction de la nature du SHL, trois principaux comportements énergétiques peuvent être observés. Certains systèmes peuvent réagir spontanément ($\Delta G < 0$) et diminuer leur interface solide/liquide ($\Delta\Omega < 0$) en expulsant complètement le liquide des nanopores à l'aide de l'énergie interfaciale stockée. Deux phénomènes réversibles possibles sont courants. Dans le premier cas, l'expulsion du liquide a lieu à une pression d'extrusion (P_{ext}) qui est, idéalement, exactement égale à P_{int}. L'énergie stockée est donc entièrement restaurée, avec un rendement énergétique (défini comme le rapport entre l'énergie restaurée, E_r, et l'énergie stockée, E_s) de 100 %. Le système affiche alors un comportement de parfait ressort (représenté sur les diagrammes *P–V* par le chevauchement des courbes d'intrusion et

d’extrusion). Dans le second cas, l’énergie interfaciale est partiellement dissipée sous forme d’énergie thermique (en raison du frottement de l’interface solide-liquide) pendant l’expulsion complète du liquide hors des pores. Dans ce cas, le rendement énergétique est inférieur à 100 %. Les diagrammes *P–V* révèlent alors une hystérèse nette entre les courbes d’intrusion et d’extrusion puisque $P_{ext} < P_{int}$. Le système est défini comme un amortisseur. A travers ce manuscrit, la distinction entre les comportements ressort et amortisseur est basée sur la valeur du rendement énergétique. Pour des valeurs supérieures ou égales à 80%, il s’agit d’un ressort. Dans le cas contraire, le système est défini comme amortisseur. Pour d’autres systèmes, le liquide est retenu dans les nanopores. Dans ce cas, le phénomène d’intrusion–extrusion est irréversible car l'énergie mécanique fournie est complètement absorbée. Le rendement énergétique est donc nul et le système se comporte comme un pare-choc. Sur les diagrammes *P–V*, le comportement pare-choc est singularisé par l'absence de variation de volume sur la courbe d'extrusion. A partir des diagrammes *P–V*, il est également possible d'estimer le travail ou l'énergie stockée/restituée/absorbée ($E_s/E_r/E_a$, respectivement) par le système.

Dans cette étude bibliographique, les résultats des expériences passées d'intrusion–extrusion menées sur des SHLs, basés sur différents types de matériaux solides poreux et des liquides non-mouillants, sont discutés. Les zéosils (zéolithes purement siliciques) ainsi que les Metal-Organic Frameworks (MOFs) ou polymères de coordination sont parmi les matériaux les plus étudiés dans le domaine énergétique, même si les performances énergétiques des matériaux à base de silice mésoporeuse ont également été explorées. A ce titre, notre équipe a été la première à initier les expériences d'intrusion–extrusion sous haute pression en utilisant les zéosils en 2001 et, plus tard, les MOFs en 2013. Par la suite, d’autres équipes se sont intéressées à cette thématique prometteuse.

Concernant ce dernier type de matériaux poreux, les résultats publiés dans la littérature se sont plus spécifiquement focalisés sur la sous-classe des Zeolitic Imidazolate Frameworks (appelés ZIFs). Ces hybrides organiques-inorganiques sont caractérisés par une haute cristallinité, et surtout, par des volumes microporeux plus élevés que ceux des zéosils. Les systèmes correspondants possèdent ainsi comparativement des volumes intrusés plus élevés et, par conséquent, des énergies stockées/absorbées supérieures même si les pressions d’intrusion sont souvent plus faibles. Ces travaux soulignent également les influences de la composition chimique, de la topologie et de la morphologie du MOF/ZIF sur le comportement énergétique du SHL. Alors que la nature du cation de charpente n'a pas d'effet apparent, il a été montré que la présence de groupes fonctionnels polaires ou de substituants volumineux sur le ligand imidazolate empêche l'intrusion d'eau. De plus, la présence de défauts structuraux (associés à une taille de particule plus petite) induit une diminution de la pression d'intrusion. Quelques résultats antérieurs tendent à montrer que la

pression d'intrusion est augmentée par l'utilisation des solutions aqueuses d'électrolytes en tant que liquides non-mouillants et avec des concentrations croissantes. Cette tendance est plus marquée pour des solutions aqueuses de LiCl par rapport à celles de NaCl et KCl. Il a également été prouvé que les mélanges eau-alcool, à base d'alcools de grand diamètre moléculaire, amélioraient la pression d'intrusion, mais dans une moindre mesure que les solutions aqueuses d'électrolytes. Notons également que dans ce présent travail, de l'eau ainsi que des solutions aqueuses de KCl à 4 M et de LiCl à 20 M sont employées comme liquides non-mouillants. En effet, les concentrations des deux solutions aqueuses d'électrolytes correspondent à leur solubilité maximale à température ambiante. Cela implique la présence de moins de molécules d'eau pouvant interagir avec les défauts des matériaux ZIF et pouvant, ainsi, favoriser un phénomène irréversible lors des expériences d'intrusion–extrusion. De telles solutions aqueuses d'électrolytes hautement concentrées sont susceptibles d'être intrusées dans des matériaux hydrophiles, qui, *a priori*, ne présenteraient pas de phénomène d'intrusion avec l'eau comme liquide non-mouillant. En outre, il a été démontré qu'en augmentant la concentration de la solution aqueuse de LiCl, le comportement énergétique de certains SHLs à base de zéosil peut être modifié avec l'évolution du système pare-choc à système amortisseur.

Cette étude bibliographique met également en lumière que l'exploration des comportements énergétiques de systèmes basés sur des matériaux de type ZIF avec des topologies qui n'ont pas encore été étudiées, telles que LTA ou MER, pourrait conduire à des résultats prometteurs. Il serait également intéressant d'aller plus loin dans la compréhension des effets d'autres paramètres sur les comportements énergétiques des SHLs à base de ZIFs. Parmi ces paramètres, la fonctionnalisation du ligand imidazolate ainsi que les ouvertures de pores (délimités avec des cycles à 10 et 12 chaînons) et ainsi la topologie peuvent être citées.

Résumé du Chapitre 2

Ce chapitre est dédié à la description des techniques expérimentales utilisées pour caractériser les échantillons avant et après les expériences d'intrusion−extrusion.

Les techniques utilisées sont la diffraction de rayons X (DRX), la microscopie électronique à balayage (MEB), l'analyse thermogravimétrique (ATG) et la manométrie d'adsorption-désorption de diazote. Un porosimètre à mercure a été utilisé pour forcer l'eau et les solutions aqueuses d'électrolytes dans les pores des matériaux de type MOF et pour étudier le comportement énergétique des systèmes "MOF-liquide non mouillant". Dans certains cas, la composition du matériau a été déterminée en utilisant la résonance magnétique nucléaire en phase liquide (RMN ^{1}H). De plus, pour vérifier la présence des cations de lithium dans la porosité du MOF après des expériences d'intrusion−extrusion d'une solution aqueuse de LiCl 20 M, des analyses ICP (inductively-coupled plasma) ont été réalisées. La porosimétrie au mercure a aussi été utilisée ponctuellement dans le but de confirmer l'absence d'un effet de la pression seule sur la structure. Toutes les techniques sont détaillées dans ce chapitre mais seule une brève explication de celles les plus utilisées est mentionnée dans ce résumé.

La DRX est une technique puissante et non destructive utilisée pour déterminer la structure d'un matériau cristallin. Elle permet l'identification des phases, ce qui est possible en se référant aux bases de données disponibles. Dans ce travail, les diffractogrammes de RX des échantillons de MOF avant et après intrusion ont été essentiellement enregistrés en mode transmission sur un diffractomètre STOE STADI-P équipé d'un monochromateur courbé primaire en germanium (111) et d'un détecteur linéaire sensible à la position (6 ° en 2θ) en utilisant le rayonnement $CuK\alpha_1$ (λ = 1,5406 Å). Dans le cas où seule une petite quantité de poudre était disponible pour l'analyse DRX, l'échantillon a été étalé sur une plaque de verre et les diffractogrammes ont été enregistrés sur un diffractomètre X'Pert Pro fonctionnant avec un rayonnement $CuK\alpha$ (λ = 1,5418 Å) équipé d'un détecteur de bandes multiples en temps réel X'Celerator (longueur active = 2.122 ° 2θ).

La microscopie électronique à balayage est une technique permettant de déterminer la morphologie (taille et forme) des particules d'un échantillon. La préparation des échantillons implique le montage de l'échantillon sur un support recouvert d'un ruban de carbone puis les matériaux sont recouverts d'une fine couche d'or (15 nm) afin de minimiser leur charge de surface. Dans ce travail, le revêtement a été effectué en utilisant la méthode de pulvérisation cathodique par magnétron.

Enfin, un microscope Philips XL 30 FEG a été utilisé. Le faisceau d'électrons utilisé avait une tension de 7 kV et les images ont été obtenues à un grossissement compris entre 20000-50000.

Lors de l'analyse thermogravimétrique (ATG), l'évolution de la masse de l'échantillon (généralement affichée en pourcentage massique) est enregistrée en fonction du temps, ou plus communément en fonction de la température. Dans ce travail, la stabilité thermique des matériaux MOF étudiés a été déterminée en se référant à la température à laquelle commence la dégradation de la charpente organique. En effet, l'ATG est efficace pour indiquer la présence/l'absence de molécules de solvant (eau et solvants organiques), en plus de molécules n'ayant pas réagi qui peuvent être piégées dans la porosité du matériau inactivé/partiellement activé suite à sa synthèse ou dans le matériau MOF après intrusion. Par conséquent, la composition de la charpente peut être déterminée/confirmée partiellement ou totalement en se référant à la courbe TG. Dans ce travail, les analyses TG ont été réalisés sur un appareil TG Mettler Toledo STARe, sous un flux d'air reconstitué, avec une vitesse de chauffage de 2 °C min^{-1} de 30 à 900 °C. Le logiciel STARe a été utilisé pour effectuer les expériences et, plus tard, pour exploiter les données obtenues.

L'étude des propriétés texturales des matériaux poreux de type MOF, c'est-à-dire la surface spécifique et le volume microporeux, a été réalisée à l'aide de mesures d'adsorption-désorption d'azote. Les matériaux MOF après intrusion ont également été analysés et les résultats obtenus ont été comparés à ceux des matériaux initiaux afin d'étudier la stabilité de la structure sous l'effet de la haute pression et/ou du liquide non-mouillant lors des expériences d'intrusion−extrusion. Les isothermes ont été réalisées à 77 K à l'aide d'un appareil Micromeritics ASAP 2420. Avant les mesures d'adsorption, les échantillons ont été dégazés à des températures élevées sous vide secondaire. Le volume microporeux a été déterminé selon la méthode du *t*-plot.

Dans ce travail, des expériences d'intrusion–extrusion d'eau et de solutions aqueuses, de KCl à 4 M et de LiCl à 20 M, ont été effectuées dans des échantillons de type MOF/ZIF, préalablement activés, à l'aide d'un porosimètre à mercure Micromeritics (modèle Autopore IV) équipé du logiciel Autopore IV 9500 VI.06. Ces expériences ont été réalisées à température ambiante, généralement sur trois cycles d'intrusion−extrusion et jusqu'à une pression maximale de 350 MPa. Dans certains cas, des études complémentaires ont été faites à plus basse pression ou avec un seul cycle d'intrusion−extrusion. Le dispositif expérimental comprend un système « matériau poreux−liquide non mouillant », appelé système hétérogène lyophobe (SHL), incorporé dans un cylindre en polypropylène de 2 mL scellé avec un piston mobile, formant ainsi la cellule d'intrusion–extrusion. Cette cellule est à son tour introduite dans un pénétromètre en verre rempli de mercure. L'augmentation de la pression appliquée pendant les expériences d'intrusion–extrusion contraint le mercure à diffuser hors du tube capillaire du pénétromètre, ce qui exerce une pression sur le piston

mobile de la cellule et, par conséquent, provoque l'intrusion forcée des molécules du liquide non-mouillant dans les pores du matériau étudié. L’évolution de la quantité de mercure à l'intérieur du capillaire en verre est suivie par les variations de la capacitance (électrique) du condenseur constitué par le mercure et la couche métallique déposée sur la surface externe du capillaire. La capacitance mesurée est proportionnelle à la variation de volume de mercure pouvant ainsi indiquer un phénomène de compressibilité et/ou d’intrusion. À partir des diagrammes pression–volume, les performances énergétiques peuvent être évaluées, notamment les pressions et les volumes d'intrusion et d'extrusion permettent de déduire l’énergie stockée/absorbée et le comportement (ressort, amortisseur ou pare-chocs).

Résumé du Chapitre 3

Dans ce chapitre, les effets de la nature du liquide non-mouillant (eau ou solutions aqueuses d'électrolytes) et du substituant porté par le ligand imidazolate sur le comportement énergétique des systèmes constitués à partir de dérivés de ZIF-8 sont étudiés. Dans ce but, trois matériaux ont été choisis : ZIF-8 (dénommé ZIF-8_CH_3 dans ce chapitre et également commercialisé sous le nom de Basolite® Z1200) et deux de ses dérivés halogénés récemment publiés dans la littérature, ZIF-8_Cl et ZIF-8_Br. Ces matériaux sont construits à partir de cations Zn^{2+} pontés par des ligands imidazolates qui sont substitués en position 2 par un groupe/atome méthyle (CH_3), chlore (Cl) ou brome (Br), respectivement pour ZIF-8_CH_3, ZIF-8_Cl et ZIF-8_Br. De façon notable, ZIF-8_CH_3 et ZIF-8_Cl se singularisent par la flexibilité de leur charpente, due au basculement des ligands imidazolates sous différents stimuli. Ce phénomène peut être mis en évidence par le profil des isothermes d'adsorption d'azote des deux matériaux de type ZIF, où une nette adsorption est observée à une pression relative autour de 0,005. Le matériau ZIF-8_Br présente, quant à lui, une isotherme d'adsorption d'azote de type Ia habituelle, sans aucune marque de flexibilité structurale. L'encombrement stérique du substituant Br est probablement la cause de la rigidité de la structure du solide ZIF-8_Br. De plus, les trois dérivés de ZIF-8 se caractérisent à la fois par un caractère hydrophobe élevé (évalués par manométrie d'adsorption d'eau) et une porosité élevée comme le soulignent les volumes microporeux de 0,66, 0,57 et 0,35 $cm^3\ g^{-1}$ pour respectivement ZIF-8_CH_3, ZIF-8_Cl et ZIF-8_Br. Ces caractéristiques font de ces matériaux de bons candidats pour les expériences d'intrusion−extrusion.

L'Article 1, publié en 2018 dans le Journal of Physical Chemistry C et inséré dans ce chapitre, décrit les expériences d'intrusion−extrusion effectuées sur ZIF-8_CH_3, ZIF-8_Cl et ZIF-8_Br, en utilisant de l'eau et des solutions aqueuses de KCl à 4 M et de LiCl à 20 M comme liquides non-mouillants. Les expériences ont été réalisées jusqu'à une pression maximale de 80 ou 350 MPa et sur trois cycles d'intrusion−extrusion. Sur la base des résultats expérimentaux, il est confirmé que la pression d'intrusion augmente quand des espèces électrolytiques sont présentes dans le liquide non-mouillant. Ces travaux mettent également en évidence que la nature du substituant présent sur le ligand imidazolate peut influencer les performances énergétiques des systèmes correspondants par l'établissement d'interactions hôte-invité spécifiques entre le ligand et la solution aqueuse d'électrolyte. Le substituant peut également affecter la flexibilité/rigidité du matériau ZIF, ce qui conduit par conséquent à des pressions d'intrusion plus élevées/plus basses, comme le démontrent les systèmes basés sur les trois dérivés de ZIF-8 de topologie SOD. Enfin, cette étude montre que

plus le substituant est volumineux (c'est-à-dire plus le volume microporeux est petit), plus le volume intrusé est petit. Il est également important de souligner les valeurs exceptionnelles des énergies stockée (77 J g^{-1}) et absorbée (104 J g^{-1}) obtenues respectivement pour les systèmes « ZIF-8_Cl− » de type ressort et « ZIF-8_CH_3–solution aqueuse LiCl 20 M » de type pare-choc. Jusqu'à présent, le système "ZIF-8_Cl−solution aqueuse LiCl 20 M" enregistre, en effet, la plus grande valeur d'énergie stockée enregistrée pour un ressort moléculaire lors d'expériences d’intrusion−extrusion.

Résumé du Chapitre 4

Ce chapitre est dédié à l'étude de l'influence du substituant présent sur le ligand imidazolate sur les performances énergétiques de systèmes élaborés à partir de matériaux de type ZIF et de topologie RHO. Quatre matériaux ont été sélectionnés : ZIF-71, MAF-6, ZIF-25 et ZIF-71_Br_2. Après leurs synthèses et caractérisations, ces matériaux ont été ensuite utilisés dans des expériences d'intrusion−extrusion d'eau et d'une solution aqueuse de LiCl à 20 M afin de caractériser les performances énergétiques de leurs systèmes respectifs. Ce chapitre est composé de deux parties.

La première partie se focalise sur les matériaux ZIF-71 et MAF-6. Grâce à son grand volume microporeux et à son caractère hydrophobe, MAF-6, dont la synthèse a été publiée pour la première fois en 2016, est un bon candidat pour les expériences d'intrusion−extrusion d'eau et de solutions aqueuses. Concernant ZIF-71, ses performances énergétiques avaient été restreintes, par le passé, à l'eau comme liquide non-mouillant. Dans cette étude, une solution aqueuse de LiCl à 20 M a également été utilisée. Ces expériences d'intrusion−extrusion ont d'abord été réalisées jusqu'à une pression maximale supérieure de l'ordre de 300 à 350 MPa. Toutefois, afin de mieux comprendre l'effet de la pression appliquée sur la structure des matériaux étudiés, des expériences complémentaires ont été effectuées à des pressions inférieures. Quel que soit le matériau, une seule variation de volume, irréversible, est observée sur les diagrammes pression−volume ($P-V$) lors du premier cycle. Dans tous les cas, les échantillons après intrusion ont été caractérisés principalement par diffraction de rayons X et par manométrie d'adsorption d'azote. Les résultats montrent que les matériaux ZIF-71 et MAF-6 subissent, sous pression, une transformation vers des phases non-poreuses mais cristallines (respectivement, ZIF-72 de topologie lcs et une phase inconnue nommée phase X). Il a été montré que cette transformation structurale, lors des expériences d'intrusion−extrusion, se produit sous l'effet combiné de la pression et du liquide non-mouillant (solution aqueuse de LiCl à 20 M pour ZIF-71, et eau ainsi qu'une solution aqueuse de LiCl à 20 M pour MAF-6). La transformation de phase est associée à une intrusion partielle des molécules du liquide non-mouillant dans la porosité, où elles semblent rester piégées même après le relâchement de la pression mécanique appliquée. Les résultats indiquent que la phase X ne correspond à aucun des polymorphes connus de MAF-6 mais suggèrent qu'il s'agit d'un pseudo-polymorphe de MAF-6 formé par un processus d'hydrolyse-condensation. Enfin, la pression d'intrusion augmente lorsque le liquide non-mouillant incorpore un électrolyte.

La deuxième partie de ce chapitre concerne l'optimisation des paramètres de synthèses de ZIF-25 et ZIF-71_Br_2 en vue de tester leurs performances énergétiques par des expériences

d'intrusion−extrusion. Ce travail souligne la difficulté rencontrée dans la reproductibilité des synthèses des matériaux de type MOF. Par exemple, le protocole de synthèse de ZIF-25 décrit par Yaghi et ses collaborateurs n'a pas pu être reproduit. Plusieurs paramètres de composition et de procédé ont dû être modifiés afin d'obtenir le matériau désiré. A l'issue de nombreux essais, un échantillon pur de ZIF-25 a été synthétisé en quantité suffisante (107 mg) avec un rendement de 36 %, en utilisant de l'acide acétique comme modulateur. Il est bien cristallisé et possède des propriétés texturales comparables à celles rapportées dans la littérature (volume microporeux et surface spécifique BET de l'ordre de 0,55 $cm^3\ g^{-1}$ et 964 $m^2\ g^{-1}$, respectivement). De façon notable, la structure du matériau ZIF-25 a été résolue pour la première fois, avec un groupe d'espace en *Pm*-3*m*, grâce à un affinement Rietveld à partir d'un diffractogramme de poudre. L'échantillon optimisé de ZIF-25 a ensuite été utilisé dans des expériences d'intrusion−extrusion d'eau à haute pression. La pression d'intrusion d'eau est plus faible dans le cas de ZIF-25 par rapport à ZIF-71 (58 MPa par rapport à 71 MPa, respectivement). Cette différence ne peut pas être expliquée par une plus grande flexibilité de ZIF-25 comme le montre une étude comparative basée sur la manométrie d'adsorption d'azote. Les deux systèmes se comportent comme de parfaits amortisseurs.

Concernant le matériau ZIF-71_Br_2, dont la synthèse n'a jamais été rapportée dans la littérature, quels que soient les différents essais de synthèse effectués en modifiant plusieurs paramètres de synthèse, un mélange de phases, contenant la phase attendue de topologie RHO et une autre phase inconnue appelée phase Y, est toujours obtenu. De plus, même pour des conditions de synthèse prometteuses, la synthèse n'est pas reproductible.

En conclusion, les systèmes « ZIF-25– » et « ZIF-71–eau » de topologie RHO présentent des comportements énergétiques similaires (amortisseur), avec des quantités d'énergie stockée comprises entre 26 et 30 $J\ g^{-1}$. Ces résultats indiquent que la nature du substituant (atomes de Cl ou groupes CH_3) sur le ligand imidazolate ne semble pas avoir d'influence majeure sur le comportement énergétique de ces systèmes lorsque l'eau est utilisée comme liquide non-mouillant.

Résumé du Chapitre 5

Le but des travaux exploratoires discutés dans ce chapitre vise à obtenir des valeurs d'énergie stockée/absorbée plus élevées en utilisant des matériaux de type MOF à haute porosité et d'évaluer les influences de la composition chimique et de la topologie de ces matériaux sur leurs comportements et performances énergétiques lors des expériences d'intrusion−extrusion à haute pression.

De par leur grande porosité et leur nouveauté relative, quatre autres ZIFs et deux MOFs à base de ligands de type carboxylates, i. e. NOF-1 (SOD), ZIF-76 (LTA), AFI-Zn$(im)_2$, CAN-Zn$(im)_2$, MOF-919(Sc/Cu) et MIL-101(Cr) étaient considérés comme des candidats prometteurs dans le cadre de ces travaux. Ainsi, leurs synthèses et leurs caractérisations ont été entreprises afin d'explorer leurs comportements énergétiques à travers des expériences d'intrusion−extrusion en utilisant de l'eau et/ou une solution aqueuse de LiCl à 20 M comme liquides non mouillants. Malheureusement, pour MOF-919(Sc/Cu), la synthèse s'est révélée non reproductible. En ce qui concerne NOF-1, des problèmes ont été rencontrés lors de l'étape d'activation par immersion dans du méthanol, à l'issue de laquelle la structure du matériau a perdu sa cristallinité. L'étape d'activation s'est également avérée sensible dans le cas des matériaux de type ZIF de topologies AFI et CAN. En effet, elle a généré une amorphisation partielle des structures avec des propriétés texturales évaluées en deçà de celles attendues, comme indiquées par les analyses par diffraction de rayons X et manométrie d'adsorption-désorption d'azote. De plus, les résultats expérimentaux, montrent que les matériaux de type ZIF de topologies AFI et CAN sont instables dans l'eau, avec un effet plus marqué pour ce dernier. Par conséquent, en raison des difficultés rencontrées dans la reproductibilité des protocoles de synthèse des produits brut de synthèse ou bien lors de l'activation, de la faible stabilité des matériaux dans l'eau, ainsi que du manque de temps nécessaire pour optimiser les paramètres de synthèse et d'activation, les matériaux NOF-1, MOF-919(Sc/Cu) et les ZIFs de topologies AFI et CAN n'ont pas pu être utilisés dans des expériences d'intrusion−extrusion sous haute pression.

Toutefois, les solides ZIF-76 et MIL-101(Cr) ont été reproduits avec succès (synthétisés plusieurs fois et complètement activés). Néanmoins, d'une part, en raison du caractère hydrophile de MIL-101(Cr), et d'autre part à cause de la faible stabilité de ZIF-76 dans l'eau, les expériences d'intrusion−extrusion d'eau n'ont pas été réalisées sur ces deux matériaux. En revanche, il est apparu intéressant d'étudier leur comportement énergétique en utilisant une solution aqueuse de LiCl à 20 M. Les diagrammes pression-volume de MIL-101(Cr) ne montrent aucune étape d'intrusion, ce qui

peut être attribué à son caractère hydrophile et probablement expliqué par l'adsorption de molécules d'eau à basse pression (réhydratation) au contact de la solution aqueuse de LiCl à 20 M, empêchant ainsi l'intrusion du liquide non mouillant à des pressions élevées. Cependant, les résultats indiquent que ce matériau est stable sous des pressions atteignant 350 MPa et au contact de la solution aqueuse d'électrolyte. Ainsi, MIL-101(Cr) demeure un bon candidat pour un emploi dans une stratégie de modification post-synthèse visant à atténuer son caractère hydrophile par le greffage d'agents chimiques hydrophobes. Quant au ZIF-76, les diagrammes pression-volume du système « ZIF-76–solution aqueuse de LiCl à 20 M » présentent une variation de volume lors de l'intrusion au cours du premier cycle. Des études complémentaires d'intrusion−extrusion, à de plus basses pressions (par exemple, 80 MPa) que celles menées à 350 MPa initialement, sont nécessaires pour mieux comprendre les performances énergétiques de ce système.

Enfin, comme pour le Chapitre 4, ce chapitre souligne aussi la difficulté liée à la synthèse des matériaux de type MOF. En effet, les synthèses publiées ne sont pas toujours facilement reproductibles. L'étape d'activation peut également être délicate. De plus, la stabilité des matériaux MOF dans l'eau ou dans des milieux aqueux, ce qui est crucial pour les expériences d'intrusion−extrusion, est difficile à prédire.

Table of Contents

Introduction

With the accumulating negative environmental impacts associated with the use of fossil fuels and concerns about petroleum supplies, has come the growing need for clean and renewable energy resources. Biofuels (ethanol) and hydrogen gas are among the most remarkable examples of alternative energy solutions that have been developed, while solar cells and lithium batteries, in addition to being clean and renewable energy resources, provide the possibility to store and restore the unused energy.[1-4]

Nowadays, energy storage, defined as the process of storing a certain type of energy that can be recovered at a later time and usefully re-applied in a given operation, has become an urgent demand for the world on its way to a sustainable future.[5-6] Whereas electrical, thermal, and chemical energy storage technologies are considered to be highly efficient and well developed, available mechanical energy storage processes (pumped hydro, compressed air, and flywheel) still present variable limitations in terms of the geographical location, high price, low energy density, etc.[5-6] Therefore, novel methods of mechanical energy storage, with the ability to overcome the above limitations are highly desirable. Moreover, systems that are capable of partially dissipating or absorbing mechanical energy in a clean and cheap way, while providing higher efficiency compared to the conventional methods, are also desired.[7]

In the 1990's, Eroshenko *et al.* suggested that the storage/dissipation of mechanical energy can be achieved by coupling a porous solid with a non-wetting liquid, thereby forming a lyophobic heterogeneous system (LHS). The feasibility of this concept was widely proven by using zeosils (hydrophobic pure silica zeolites) as lyophobic porous matrices and water as the non-wetting liquid.[8] Under the effect of an applied mechanical energy, the non-wetting liquid is transformed into numerous molecular clusters, which are intruded into the pores of the solid, thus, developing a large solid-liquid interface. During this process, the mechanical energy is converted into interfacial energy. When the pressure is released during the extrusion step, three energetic behaviors can be observed: bumper (supplied mechanical energy is absorbed), shock-absorber (partial dissipation of the supplied mechanical energy), and spring (80-100 % of the supplied mechanical energy is restored). Applying the process suggested by Eroshenko, several heterogeneous systems, based on zeosils as the lyophobic solid matrices, have been investigated in high-pressure intrusion−extrusion experiments until now. The non-wetting liquids used being, mainly, water or aqueous electrolyte solutions of different

concentrations. Even though interesting results have been obtained, however, the reported values of stored/absorbed energies still remain low for the employment of the zeosil-based LHSs in industrial applications.

Increasing the porosity of the solid matrix and/or interfacial tension of the non-wetting liquid, have been proven to increase the values of the intruded volume and/or intrusion pressure, respectively. Consequently, the amount of stored/absorbed energy is also enhanced.

Among porous materials, MOFs (Metal-Organic Frameworks), also known as porous coordination polymers, are hybrid materials with a mixed organic-inorganic matrix. MOFs can be defined as porous crystalline solids in which the metal components are connected through organic linkers to form bi- or three-dimensional and eventually porous structures. The great diversity of linkers (carboxylic esters or acids, phosphonic acids, sulfonic acids, or nitrogen-rich compounds) and metal cations makes it possible to obtain an immense variety of hybrid materials. MOFs are, first and foremost, characterized by their outstanding textural properties, with specific surfaces and pore volumes far superior to those of zeolites, thus, making them interesting candidates for high pressure intrusion−extrusion experiments. Moreover, MOFs also offer great modularity as the pore dimensionality, the pore and pore aperture size, as well as the hydrophilic/hydrophobic character can be modulated by the appropriate choice of the linker. Among the different classes of MOFs, that of ZIFs (Zeolitic Imidazolate Frameworks) establishes the link, from a topological aspect, between hybrid porous materials and zeolites. Indeed, ZIFs consist of assemblies of tetrahedral units, which, in turn, are composed of a divalent cation (M^{2+}: Zn^{2+}, Co^{2+}… localized at the center of the tetrahedron) that is linked to four nitrogen atoms from four (benz)imidazolates (L^-, localized at the vertices of the tetrahedron). The tetrahedra are, thus, connected to each other through the (benz)imidazolate linkers. The $M^{2+}L^-_{4/2}$ units are similar to the $SiO_{4/2}$ units found in zeolites, with the M-L-M angle (in ZIFs) being close to the Si-O-Si angle (in zeolites). As a result, ZIF structures of zeolitic topologies are often obtained. The figurative substitution of transition metals and, more specifically, organic units for Si or Al atoms and oxygen atoms, respectively, leads to expanded pore structures, which explains the higher pore size and pore volume exhibited by some ZIFs compared to those of zeolites of an analogous topology. This is mainly the reason why ZIFs were used for the first time in high-pressure intrusion−extrusion experiments in 2013.[9]

In this work, we intend to find perfect heterogeneous systems formed of MOFs; as lyophobic porous materials, and non-wetting liquids that are capable of storing/absorbing large amounts of energy and can be used as springs, shock-absorbers, or bumpers for practical applications.

However, in order to develop the perfect system for the target application, a better understanding of the effect of various parameters (related to both porous material and the non-wetting liquid) on the energetic behaviors of LHSs during intrusion−extrusion experiments, is crucial. To this end, our work involves the synthesis and characterization of MOF/ZIF materials (some of which are new) of high microporous volumes, followed by the study of their energetic performances in high-pressure intrusion−extrusion experiments. Different combinations of highly porous MOFs/ZIFs and non-wetting liquids are explored, where water and the LiCl 20 M aqueous electrolyte solution are mainly used as non-wetting liquids. Indeed, water is among the most extensively employed non-wetting liquids, due to its molecular diameter that allows it to access even the very small micropores, in addition to its availability, low price, and the fact that it is nontoxic. Furthermore, the use of aqueous electrolyte solutions was proven to increase the intrusion pressure and, consequently, the stored/absorbed energy. The post-intruded MOF/ZIF materials are also fully characterized in order to investigate the influence of the high pressure and non-wetting liquid associated with intrusion−extrusion experiments on their structure.

In this thesis manuscript, Chapter 1 involves a bibliographic study, wherein we shed light on several characteristics of MOF/ZIF materials that are essential for applications in intrusion−extrusion experiments. Among these characteristics are the high porous volume, in addition to the hydrophobicity and water stability. The two latter parameters are essential in the cases where water is used as the non-wetting liquid, nevertheless, are less important if a highly concentrated aqueous electrolyte solution (for example, LiCl 20 M aqueous solution) is employed instead.

In Chapter 2, all the techniques, that are required to characterize the parent and post-intruded MOF materials, are developed, including, mainly: X-ray diffraction (XRD), thermogravimetric analysis (TGA), N_2 adsorption-desorption, scanning electron microscopy (SEM), and proton nuclear magnetic resonance (^{1}H NMR) spectroscopy.

Prior to this work, only two topologies have been successfully studied in high-pressure intrusion−extrusion experiments; the SOD and RHO topologies, involving the ZIF-8 and ZIF-71 materials, respectively, where both ZIFs are characterized by high porosity and a strong hydrophobic character. In Chapter 3, based on new results, we complete the existing work on intrusion−extrusion experiments performed on ZIF-8, by investigating the influence of the substituent present on the imidazolate linker and the nature of the non-wetting liquid on the energetic performances of different LHSs based on SOD-type ZIF materials.

Chapter 4 is devoted to the synthesis and characterization, as well as the study of the energetic performances of systems based on RHO-type ZIFs. The first part of this chapter develops the results obtained from intrusion−extrusion experiments realized on ZIF-71 and the highly porous MAF-6. In the second part, we aim at exploring the influence of the substitution on the imidazolate linker (Cl for ZIF-71, Br for ZIF-71_Br_2 and CH_3 for ZIF-25) on the energetic performances of the ZIF-based LHSs.

Chapter 5 is devoted to prospective studies of new MOFs/ZIFs that may be considered promising for energetic applications. Among these materials are the cage-type ZIF-76 and NOF-1 materials of LTA and SOD topologies, respectively. Furthermore, two new hydrophobic, and highly porous MOF materials of a 1D channel pore system and large 12-membered ring pore apertures have been recently reported in the literature, i. e. CAN- and AFI-$Zn(im)_2$, where im stands for imidazolate. As Cu_2(tebpz) (with tebpz = 3,3′,5,5′-tetraethyl-4,4′-bipyrazolate) is the only channel-type MOF that has been studied until now in intrusion−extrusion experiments, investigating the energetic performances of the AFI- and CAN-type ZIF materials would, indeed, provide new information on the effect of the pore dimensionality on the energetic performances of MOF-based LHSs. Another target of this work is to post-synthetically modify highly porous, however, hydrophilic MOF materials, such as MIL-101(Cr) and MOF-919(Sc/Cu), so as to study their energetic performances in water and aqueous electrolyte solutions intrusion−extrusion experiments.

Finally, a general conclusion summarizes the major results and advances of this PhD work and sheds light on the perspectives in the areas of MOF synthesis and intrusion−extrusion experiments.

1. Mofijur, M.; Rasul, M. G.; Hyde, J.; Azad, A. K.; Mamat, R.; Bhuiya, M. M. K., Role of Biofuel and their Binary (Diesel–Biodiesel) and Ternary (Ethanol–Biodiesel–Diesel) Blends on Internal Combustion Engines Emission Reduction. *Renewable and Sustainable Energy Rev.* **2016,** *53*, 265-278.

2. Dadashzadeh, M.; Ahmad, A.; Khan, F., Dispersion Modelling and Analysis of Hydrogen Fuel Gas Released in an Enclosed Area: A CFD-Based Approach. *Fuel* **2016,** *184*, 192-201.

3. Tarascon, J. M.; Armand, M., Issues and Challenges Facing Rechargeable Lithium Batteries. *Nature* **2001,** *414*, 359-367.

4. Lewis, N. S., Toward Cost-Effective Solar Energy Use. *Science* **2007,** *315*, 798-801.

5. Grosu, Y.; Li, M.; Peng, Y.-L.; Luo, D.; Li, D.; Faik, A.; Nedelec, J.-M.; Grolier, J.-P., A Highly Stable Nonhysteretic {Cu2(tebpz) MOF+water} Molecular Spring. *ChemPhysChem* **2016,** *17*, 3359-3364.

6. Berrada, A.; Loudiyi, K., Operation, Sizing, and Economic Evaluation of Storage for Solar and Wind Power Plants. *Renewable and Sustainable Energy Rev.* **2016,** *59*, 1117-1129.

7. Eroshenko, V., Interfacial Energy in the Lyophobic Systems and Thermomolecular Energetics: Challange to All Physico-Chemists. **2014**, 212-229.

8. Eroshenko, V.; Regis, R.-C.; Soulard, M.; Patarin, J., Energetics: A New Field of Applications for Hydrophobic Zeolites. *J. Am. Chem. Soc.* **2001,** *123*, 8129-8130.

9. Ortiz, G.; Nouali, H.; Marichal, C.; Chaplais, G.; Patarin, J., Energetic Performances of the Metal–Organic Framework ZIF-8 Obtained Using High Pressure Water Intrusion–Extrusion Experiments. *Phys. Chem. Chem. Phys.* **2013,** *15*, 4888-4891.

Chapter 1: Bibliographic Studies

In this chapter, a review of intrusion−extrusion experiments in porous materials is presented. First, the basic principle of these experiments is explained in details. Later, we discuss the different types of lyophobic porous materials that have been employed in intrusion−extrusion experiments up to our date. We mainly develop the results obtained for zeosils and, more recently, MOF materials. Moreover, we shed light on how various parameters related to the topology, pore dimensionality (1D or 3D), nature of the cation and the organic linker, and crystal shape and size can influence the energetic behaviors of the lyophobic heterogeneous systems during intrusion−extrusion experiments. The effect of the nature of the non-wetting liquid; aqueous electrolyte solutions and other liquids (alcohol-water mixtures), on the energetic performances of the studied systems is also investigated.

I. Basic Principle of Energy Storage in Lyophobic Heterogeneous Systems

In the field of new energetic applications, intrusion−extrusion experiments of non-wetting liquids in lyophobic porous materials for mechanical energy storage and absorption have been first explored and widely developed by Eroshenko.[1-2] Eroshenko's invention is illustrated by a heterogeneous structure that is capable of restoring, accumulating or dissipating energy that can be used in thermodynamic systems or devices in a clean and renewable way. The device consists of a porous capillary solid matrix, which is characterized by open capillary porosity and a liquid surrounding it, therefore, forming what is known as a lyophobic heterogeneous system (LHS). The latter component of the device exhibits high surface tension at its interface with the solid and is selected to define a solid/liquid separation surface whose area varies isothermally and reversibly as a function of an external pressure applied on the system. In other words, according to Soulard *et al.*,[3] the phenomenon can be explained as follows: In order to spread a drop of a non-wetting liquid on the surface of a solid, a certain pressure must be applied (Scheme 1a). Similarly, to introduce a non-wetting liquid into a porous material, a hydraulic pressure, referred to as the intrusion pressure (P_{int}), should be applied (Scheme 1b) that is determined by the Laplace-Washburn relation[4] (Equation 1).

$$P_{int} = 2\,\gamma_L\,|\cos\theta| / r \qquad \text{(Equation 1)}$$

With: P_{int}, the intrusion pressure (Pa)

γ_L, the liquid-vapor surface tension (N m^{-1})

r, the radius of the pores (m)

θ, the contact angle between the liquid and the solid (θ > 90° for a non-wetting liquid)

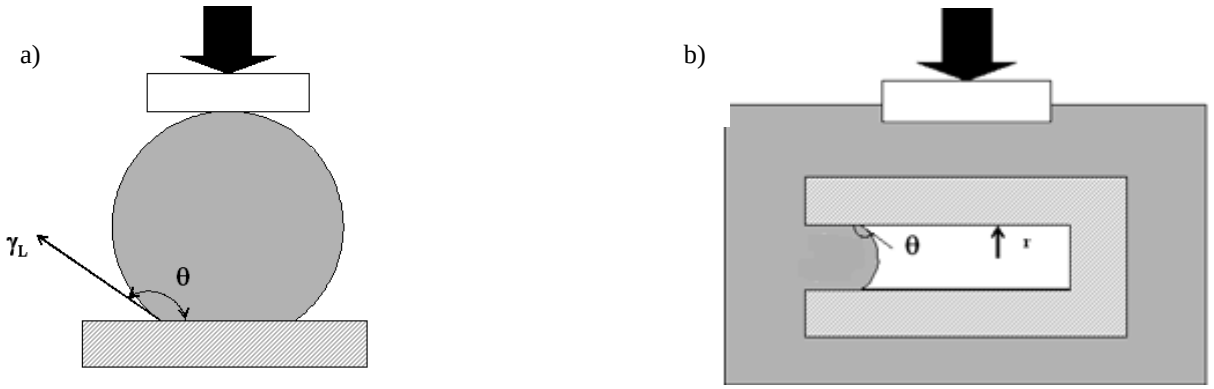

Scheme 1. Applying force to (a) spread a drop of a non-wetting liquid on the surface of a lyophobic solid and (b) intrude a non-wetting liquid into the porosity of a lyophobic solid matrix.5

During the intrusion phase of an intrusion−extrusion experiment, mechanical energy is progressively applied on the LHS. At very low pressures (0.003-1 MPa), the solid particles are compressed and the non-wetting liquid is intruded (diffused) in the interparticular porosity. On the pressure−volume (*P*−*V*) diagram (Figure 1), this step is reflected by a small volume variation (an increase in the volume) of the non-wetting liquid (step A). The applied pressure continues to increase until it reaches a critical value, corresponding to the intrusion pressure (P_{int}), at which the non-wetting liquid molecules are forced into the porosity of the solid material. In the case of an ideal *P*−*V* diagram, this step is characterized by a steep increase in the volume of the non-wetting liquid at a constant pressure (step B). Nevertheless, on an experimentally obtained *P*−*V* diagram, this increase rarely occurs at a constant pressure and the intrusion step exhibits a small slope. After complete filling of the porosity, theoretically, no further volume variation should be observed on the *P*−*V* diagram with the continuous application of external pressure (step C). However, experimentally obtained *P*−*V* diagrams clearly reveal a slight increase in the volume of the non-wetting liquid that is attributed to a further compression of the "porous material−non-wetting liquid" system at elevated pressures (see experimentally obtained *P*−*V* diagrams in Chapters 3 and 4).

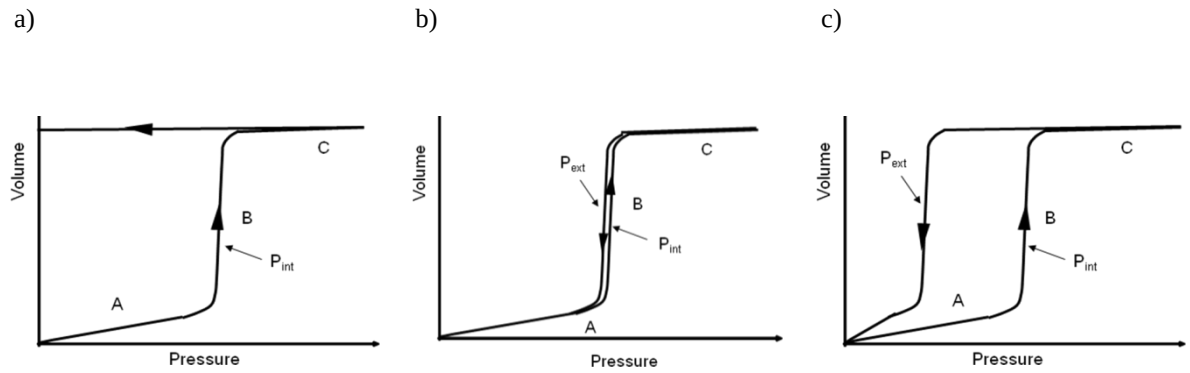

Figure 1. Schematic P−V diagrams demonstrating (a) bumper (b) spring and (c) shock absorber behaviors of LHSs.

At the microscopic scale, during the intrusion step, the massive liquid is transformed into a multitude of molecular clusters, which are intruded into the pores and, thus, develop a large solid-liquid interface ($\Delta\Omega > 0$). Therefore, part of the mechanical energy spent by the pressure forces is converted into interfacial energy. Indeed, the forced increase in the interfacial surface area requires both mechanical work and heat and is, thus, accompanied with an endothermic effect. However, the extensive solid-liquid interface friction that is created as the liquid is transported along the nanopores, leads to the irreversible dissipation of the excessive part of the applied mechanical energy in the form of thermal energy, which contributes to an exothermic effect.[3-4, 6] Consequently, the intrusion step can be viewed as both an endothermic and exothermic process. From a thermodynamic point of view, the increased contact at the solid-liquid interface is associated with an increase in the Gibb's free energy of the system ($\Delta G > 0$). The variation in Gibb's free energy can be expressed as mentioned in the literature and, thus, according to Equation 2[1]:

$$\Delta G = - \gamma_L \cos\theta \, \Delta\Omega \qquad \text{(Equation 2)}$$

With: ΔG, the variation in Gibb's free energy

γ_L, the liquid-vapor interfacial tension

θ, the contact angle between the liquid and the solid ($\theta > 90°$ for a non-wetting liquid)

$\Delta\Omega$, the solid-liquid interface

In the second step, the pressure is progressively decreased, and depending on the nature of the LHS (including both the porous material and the non-wetting liquid), three main energetic behaviors can be observed. For instance, some systems can spontaneously react ($\Delta G < 0$) and decrease their solid/liquid interface ($\Delta\Omega < 0$) by completely expelling the liquid out of the nanopores using the stored interfacial energy. Two possible reversible phenomena are common here: In the first case, expulsion of the liquid occurs at an extrusion pressure (P_{ext}) that is, ideally, exactly equal to P_{int} (Figure 1b). The stored energy is, thus, entirely restored, with an energy yield, defined as the ratio

of the restored to the stored energies, of 100% and the system displays perfect spring behavior that is indicated from the overlap of the intrusion and extrusion curves on the $P-V$ diagram (Figure 1b). In the second phenomenon, the interfacial energy is partially dissipated as thermal energy (due to the solid-liquid interface friction), as the liquid is completely extruded out of the pores, which contributes to an exothermic effect similar to the one observed in the intrusion step. In this case, the energy yield is less than 100% and the $P-V$ diagram reveals that extrusion occurs at $P_{ext} < P_{int}$, which results in a clear hysteresis between the intrusion and extrusion curves (Figure 1c). The system, therefore, is defined as a shock-absorber.[3, 6] Nevertheless, in some heterogeneous systems, the liquid is retained in the nanopores. In this case, the phenomenon is irreversible, as the system only absorbs the supplied mechanical energy and is not capable of restoring it. Herein, the total amount of energy absorbed is equal to the sum of the energy converted into interfacial energy and the energy dissipated during the intrusion step.[6] The energy yield is, thus, equal to zero and the system is said to behave as a bumper. On the pressure−volume ($P-V$) diagram, bumper behavior is indicated from the absence of a volume variation step on the extrusion curve (Figure 1a). From the $P-V$ diagrams, it is possible as well to estimate the work or the energy stored/restored/absorbed ($E_s/E_r/E_a$, respectively) by the system (Equation 3).

$$E = \int_{V_0}^{V_f} P.dV \qquad \text{(Equation 3)}$$

With: $E = E_s$ and $P = P_{int}$ (spring and shock-absorber behaviors)

Or $E = E_a$ and $P = P_{int}$ (bumper behavior)

Or $E = E_r$ and $P = P_{ext}$ (spring and shock-absorber behaviors)

V_0: volume at the beginning of the volume variation step

V_f: volume at the end of the volume variation step

A simplified version of Equation 3 also exists and is often used to calculate the stored/restored/absorbed energy of the LHS (Equation 4):

$$E = P*V \qquad \text{(Equation 4)}$$

With: $E = E_s$, $P = P_{int}$ and $V = V_{int}$ (spring and shock-absorber behaviors)

Or $E = E_a$, $P = P_{int}$ and $V = V_{int}$ (bumper behavior)

Or $E = E_r$, $P = P_{ext}$ and $V = V_{ext}$ (spring and shock-absorber behaviors)

Note that in Equations 3 and 4, the pressure (P_{int}/P_{ext}) is expressed in MPa, the volume (V_{int}/V_{ext}) in mL g^{-1}, and the energy (E_a/ E_s/E_r) in J g^{-1}.

The energy yield is calculated according to Equation 5:

$$\text{Energy yield} = (E_r / E_s) *100 \qquad \text{(Equation 5)}$$

Therefore, the energetic performances of a LHSs that will be discussed throughout this manuscript include the systems' behaviors (spring, bumper or shock-absorber) and the associated parameters (P_{int}, P_{ext}, V_{int}, V_{ext}) leading to the absorption/storage/restoring of energy (E_s, E_r, E_a), in addition to the corresponding energy yield when relevant. It is worthy to note that the description and exploitation of the intrusion−extrusion experiments will be developed in the experimental part of this manuscript (Chapter 2).

The following sections involve a review of the energetic performances of LHSs that have been explored in intrusion−extrusion experiments up to our date, excluding the results that were obtained during this PhD work. The results obtained for zeosils, mesoporous solids, and, more recently, MOF materials are developed. Moreover, special attention is devoted to the influence of some previously studied parameters (topology, pore volume and dimensionality, pore aperture) on the energetic performances of the investigated LHSs.

II. **Zeosils for Energetic Applications**

Zeolites constitute a unique class of solid inorganic materials that are known for being highly crystalline and porous, in which their porosity is a consequence of ordered micropores of molecular dimensions in the range of 0.25-1 nm.[7] These materials consist of hard, crystalline silica- (SiO_2) based frameworks. At some places in the framework, Al^{3+} ions may replace the Si^{4+} ions, resulting in negatively-charged aluminosilicate frameworks. However, the presence of loosely-held cations (Ca^{2+}, K^+, Mg^{2+}, and H^+, etc), also commonly called non-framework or charge-compensating cations, within the zeolitic cavities maintains the electroneutrality of the zeolite. Zeolites are also highly stable materials that are capable of maintaining their structure and properties even under harsh conditions of high acidity, temperature, and humidity. Characterized by these unique properties, zeolites have been marked commercially successful and employed in different fields, especially in adsorption-separation, ion exchange, and catalysis processes.[8-11]

In 2001, our group applied the process suggested by Eroshenko to strongly hydrophobic pure-silica zeolites (so-called zeosils) for the first time, using water as the non-wetting liquid.[12-13] It is important to note that water is well suited as the mobile phase in such experiments for the following reasons: it is liquid at room temperature, non-toxic, accessible, inexpensive, and has a high surface tension (72.7 mN m^{-1} at room temperature) that is often desired in intrusion−extrusion experiments (Equation 1). Moreover, water molecules possess a small diameter of around 2.7 Å that enables them to access very small micropores.[12]

After the first investigation of zeosils in intrusion−extrusion experiments in 2001, the energetic performances of numerous "zeosil–non-wetting liquid" systems have been explored. The most studied solid was the pure-silica Silicalite-1, of MFI topology and 3D channel system. The

"Silicalite-1–water" system displayed molecular spring behavior with an intrusion pressure around 96 MPa and a stored energy of 10 J g^{-1}.[14] Water intrusion−extrusion experiments were also performed on hydrophobic pure-silica chabazite zeolite (Si-CHA) of cage system. Results showed that the "Si-CHA–water" system displays spring behavior in the second and third cycles (compared to bumper behavior in the first cycle).[15-16] Spring behavior was also observed for the pure-silica AFI (SSZ-24), MTW (ZSM-12), and TON-type (ZSM-22) zeolites, where the amount of stored energy ranges between 6-14 J g^{-1}.[17] In another study, the $P-V$ diagrams of the "RUB-41–water" system (RUB-41 of RRO topology) revealed shock-absorber behavior at a very low intrusion pressure (P_{int} = 1.5 MPa), which was indicated from the hysteresis ($P_{int} > P_{ext}$) between the intrusion and extrusion curves (P_{ext} = 0.5 MPa). On the other hand, the pure-silica sodalite material, so-called S-SOD, showed no water intrusion during three water intrusion−extrusion cycles, which is attributed to the material's high degree of hydrophobicity and small pore openings, or to the high value of capillary pressure that probably exceeds the value tolerated by the instrument (i.e. 413 MPa).[18]

It appears that different parameters related to the nature of the solid matrix and non-wetting liquid constituents of the heterogeneous system can have an effect on the latter's energetic performance. Table 1 represents the characteristics of the zeosils discussed in this section and the results obtained from intrusion–extrusion experiments performed on the corresponding "zeosil–water" systems. These zeosils were selected so as to illustrate the main parameters that affect the energetic behaviors of the corresponding "zeosil–water" systems during intrusion–extrusion experiments.

Table 1. Structural and energetic characteristics of some "zeosil–water" systems.

Zeosil Sample (pure-silica zeolite)	Zeolite topology	Pore structure	$V_{micropore}$ ($cm^3\ g^{-1}$)	Pore opening (Å) (number of membered-ring O atoms)	P_{int} (MPa)	P_{ext} (MPa)	V_{int} ($mL\ g^{-1}$)	E_{stored} ($J\ g^{-1}$)	$E_{restored}$ ($J\ g^{-1}$)	Energy yield (%)	Energetic behavior literature	Energetic behavior new definition	Reference
SSZ-24	AFI	1D channels	0.05	7.3 (12 MR)	58	55	0.102	5.80	5.60	97	S	S	[14]
ZSM-12	MTW	1D channels	0.015	5.6-6.0 (12 MR)	132	126	0.114	15.00	14.40	96	S	S	[14]
S-MTT	MTT	1D channels	0.03	4.5-5.2 (10 MR)	176	174	0.03	5.28	5.22	99	S	S	[19]
ZSM-22	TON	1D channels	0.02	4.6-5.7 (10 MR)	186	172	0.075	14.00	12.70	92	S	S	[14]
RUB-41	RRO	2D channels	0.18	2.7-5.0 (8 MR) 4.0-6.5 (10 MR)	1.3	0.5	0.15	0.34	0.18	53	SA	SA	[18]
Silicalite-1	MFI	3D channels	0.17	5.1-5.6 (10 MR)	96	91	0.110	10.60	10.00	94	S	S	[14]
S-SOD	SOD	cages	-	-	-	-	-	-	-	-	-	-	[18]
Si-CHA	CHA	cages	0.30	3.8 (8 MR)	42^a 37^b	31	0.157^a 0.148^b	6.60^a 5.50^b	4.60	70^a 84^b	B^a S^b	B^a S^b	[14-16]
S-STF	STF	cages	0.11	5.4-5.7 (10 MR)	51^a 38^b	37	0.04^a 0.03^b	2.04^a 1.14^b	1.11	54^a 97^b	B-SA^a S^b	B-SA^a S^b	[19]
SSZ-23(F)	STT	cages	0.20	2.4-3.5 (7 MR) 3.7-5.3 (9 MR)	40^a 36^b 36^c	33^a 32^b 32^c	0.135^a 0.114^b 0.100^c	7.00^a 5.70^b 5.20^c	5.60^a 4.70^b 4.40^c	80^a 82^b 85^c	S	S	[14, 20]
SSZ-23(OH)	STT	cages	0.22	2.4-3.5 (7 MR) 3.7-5.3 (9 MR)	34^a 31^b 30^c	31^a 29^b 29^c	0.137^a 0.118^b 0.111^c	7.00^a 6.60^b 6.10^c	5.80^a 5.70^b 5.00^c	83^a 86^b 82^c	S	S	[14, 20]
Si-CHA	CHA	cages	0.30	3.8 (8 MR)	37	31	0.148	5.50	4.60	84	S	S	[14]
Pure-silica LTA	LTA	cages	0.25	4.1 (8 MR)	20	-	0.17	3.40	-	-	-	-	[21]

Intrusion (Pint) and extrusion (Pext) pressures, intruded (Vint) and extruded (Vext) volumes, stored (Es) and restored (Er) energies. a, b, and c refer to the first, second, and third intrusion-extrusion cycles, respectively.

For example, in the case of channel-type zeosils, it has been shown that the intrusion pressure and stored energy increase with the decrease in the pore diameter (the intrusion pressures for the 1D channel AFI, MTW, and TON-type zeosils are around 60, 130, and 190 MPa for pore diameters of 7.3, 5.6 to 6.0, and 4.6 to 5.7 Å, respectively).[14] In the case of cage-type zeosils, however, it is the cage size (even though the cage size is not noted in Table 1) that influences the intrusion pressure and no direct relationship was found between the intrusion pressure and the size of the window opening.[14] Nevertheless, the pore opening must be sufficiently large in order to enable the intrusion of the non-wetting liquid molecules. For instance, the SOD-type zeosil, which displays no water intrusion, and whose textural properties have not been reported (probably due to its inaccessible porosity even through the largest 6-membered ring pore opening), tends to illustrate the importance of this parameter. Moreover, the values obtained from water intrusion−extrusion experiments performed on MTT, TON and STF-type zeosils, all three of 10-membered ring pore apertures and similar pore diameters, prove that 1D channel-type zeosils (MTT and TON) exhibit higher intrusion pressures of water than do cage-type (STF) zeosils.[19] On another note, the presence of structure defects has been proven to decrease the intrusion pressure in both channel and cage-type zeosils. During the forced intrusion of water, the breaking of a siloxane bond (Si-O-Si) can occur, which results in the formation of two neighboring silanols (Si-OH). A silanol can act as a defect by trapping intruded water molecules through hydrogen bonding. Therefore, the reversibility of the process is limited during extrusion, which also leads to lower intrusion pressures and intruded volumes (V_{int}) in the next intrusion steps.[14-15, 19] For instance, the energetic behaviors of two STT-type zeosils, SSZ-23(F) and SSZ-23(OH), were shown to be influenced by the presence of defects. Although the zeosil synthesized in the fluoride medium (SSZ-23(F)) presents less silanol defects, the intrusion pressures and volumes are decreased after each water intrusion−extrusion cycle for both samples due to the hydrogen bonding between water molecules and the silanol groups.[20, 22] Other typical examples showing the influence of defects in high-pressure intrusion−extrusion experiments are the "Si-CHA–water" and "pure-silica-LTA–water" systems.[15, 21] In the former case, in the first cycle, the extruded volume (V_{ext}) is lower than V_{int}, which leads to a lower intruded volume in the next cycle.[15] As for the "pure-silica-LTA−water" system, decreasing the pressure does not lead to the expulsion of water molecules, and the system, thus, behaves as a bumper.[21] In both cases, the irreversible phenomena are attributed to the defect sites that are created during the first water intrusion step.

In conclusion, numerous "zeosil–water" heterogeneous systems have been investigated in high-pressure intrusion−extrusion experiments until now. The results obtained from the different studies make it possible to understand some of the general parameters that can influence the intrusion pressures and energetic behaviors of zeosil-based LHSs. The studied systems display variable

energetic behaviors, ranging from bumpers to shock-absorbers and springs, which are dependent on the nature of the zeosil. For instance, **channel-type zeosils show higher intrusion pressures than do cage-type zeosils, when both exhibit the same number of membered-ring pore apertures and similar pore diameters. In the case of channel-type zeosils, the intrusion pressure increases with the decrease in the pore diameter (i.e. the pore opening of the largest ring)**. **However, for cage-type zeosils, the intrusion pressure is no longer correlated to the size of the window opening and increases with the decrease in the cage size**. **Finally, the presence of structural defects such as silanol groups in the zeosil material affects the reversibility of the intrusion−extrusion phenomenon**. Another factor that can affect the energetic performances of zeosil-based LHSs, that is the nature of the non-wetting liquid (aqueous electrolyte solutions and alcohol-water mixtures), will be discussed in Sections V and VI.

Therefore, all the results published in the literature indicate that the energetic performances of the "zeosil−water" systems rely on various structural parameters, whose roles are interdependent. The highest stored energy value registered until now for a "zeosil−water" system is 14-15 J g^{-1} and is obtained with the ZSM-12 and ZSM-22 materials of MTW and TON topologies, respectively, and both of 1D-channel pore structures (Table 1). Even though these stored energy values are considered relatively high compared to those attained by the various other studied "zeosil−water" systems, however, they are still considered insufficient for real industrial applications (minimum estimated value of stored energy required is approximately = 80 J g^{-1}). It is also important to note that for both systems, the intrusion pressure is high (132-186 MPa), which can limit their practical applications. For instance, the intrusion pressure value required for vehicle bumpers is in the 30-60 MPa range.[23] Furthermore, the intruded volume is low (0.114 and 0.075 mL g^{-1} for the ZSM-12 and ZSM-22 materials, respectively) which, indeed, represents another limitation to the implication of zeosils in LHSs, as it contributes to relatively low stored/absorbed energy values.

According to Equation 3 (and the related Equation 4), there are two ways by which the amount of energy stored/absorbed by LHSs can be possibly increased. This is either by increasing the intruded volume through increasingthe porous volume of host materials or by increasing the intrusion pressure.

As mentioned above, even though promising results have been obtained with LHSs that are based on zeosils and water, however, the relatively low microporous volume displayed by zeolites limits the intruded volume and, consequently, the amount of energy that can be stored/absorbed by the "zeolite–water" system. Therefore, in a first approach towards increasing the amount of stored/absorbed energy, materials that are characterized by a degree of porosity that exceeds that of zeosils are desired (we note that the second approach towards increasing the stored/absorbed energy, which is dependent of the nature on the non-wetting liquid, will be discussed in Sections V

and VI). Some examples include grafted mesoporous materials. The "grafted mesoporous silica–water" systems generally exhibit shock-absorber behavior with a pronounced hysteresis, which is beneficial for energy dissipation applications. However, a lower amount of stored energy (in the order of 10 J g^{-1}) was registered for these systems compared to those based on zeosils and water, which is attributed to the larger pore diameter of the grafted mesoporous silica materials, leading to lower intrusion pressures (10-50 MPa).[24-27] Spring or better shock-absorber behavior associated with a very low intrusion pressure (< 5 MPa) was also observed for the periodic mesoporous organosilica materials when studied in water intrusion−extrusion experiments.[26] Furthermore, experiments were performed on zeosils to create additional micro-, meso-, and macropores using porogen (carbon black) or templating agents (surfactants), respectively.[28] Obtained results reveal that the formation of few additional micropores leads to only a slight increase in the amount of stored energy, whereas, the presence of meso- and macropores does not have any real contribution.

Furthermore, Metal-Organic Frameworks (MOFs) have emerged as an important class of crystalline hybrid organic-inorganic solid materials. MOFs are characterized by their exceptional textural properties such as specific surface area and microporous volume, where the latter may reach 1 to 2 cm^3 g^{-1}, whereas in zeolites a microporous volume in the range of only 0.3 cm^3 g^{-1} is considered among the most extremely high values.[29-30] In this regard, MOFs are considered highly promising for energetic applications. Moreover, their pore size and hydrophilic/hydrophobic character can be modulated by the appropriate choice of the organic precursor(s). The next section will be devoted to the definition of MOF materials and their different synthetic routes. Light will be also shed on several MOFs that are potentially interesting for energetic applications.

III. Metal-Organic Frameworks (MOFs)

A. Definition, Synthesis, and Properties

MOFs are made up of a metal component, which can be a single cation (0D), a 0D arrangement of several bridged metal cations (usually defined as cluster), a metal chain (1D), a metal layer (2D) or even a 3D metal architecture, coordinated to organic molecules (linkers). They are known for being highly crystalline and porous materials forming one- or three-dimensional pore structures.[31-33] The wide variety of available metal and organic precursors leads to a large number of combinations, which can be studied for potential applications in various fields, including gas storage, gas separation, catalysis, sensing, drug delivery, and bactericidal applications.[34-37]

MOFs are formed by the self-assembly of metal cations with polytopic organic sources, in a two-step process that involves a nucleation step followed by crystal growth. Their synthesis usually

takes place in a solvent, either at room-temperature or using conventional heating syntheses methods (up to a maximum temperature of approximately 250 °C). However, alternative synthesis routes also exist, where the required energy input is introduced through microwave heating, electrochemistry, or ultrasonic waves.[38] In addition, solvent-free syntheses of MOFs have also been established in the aim of reducing the use of harmful solvents, which, in turn, constitute an important environmental challenge.[39] These include mechanosynthesis, in addition to ambient- and high-pressure synthesis.[38-40]

Controlling both, process parameters (pressure, temperature, heating source, and reaction duration) and compositional parameters (nature of metal and organic precursors, their ratio, their concentrations in the reaction mixture, the solvent(s), and pH), in addition to the use of structure-directing agents (SDAs), additives (polymers, molecular-blocking agents, capping agents, and modulators), reverse microemulsions, and temperature programming, can help control the nature (composition and morphology) of the final MOF product. This is important because the morphology (related to the size and shape of physical objects) of the obtained MOF material is strongly related to its consequent application.[38, 41-42] For example, in biosensing and drug delivery applications, nanosized MOF crystals are highly desired, where the key for their synthesis is mainly in the nucleation step. In this case, temperature programming allows increasing the temperature rapidly in the beginning, so that nucleation occurs at a high rate, resulting in very small nuclei. Later in the process, the temperature is decreased during crystal growth, which consequently leads to the formation of nanocrystals.[38] Moreover, MOFs can be prepared in the form of thin films or membranes and as MOF composites. The thin films or membranes can be fabricated from nano-sized MOF crystals and grow on the surface of a support (organic or inorganic). They can be synthesized following the direct-growth, layer-by-layer, secondary/seeded-growth, or chemical solution deposition methods, and are promising candidates for catalytic coatings and chemical sensors.[38, 43] MOF composites, on the other hand, which consist of a continuous phase (organic/inorganic matrix) and a dispersed phase (MOF crystals) are of interest in catalysis, as the catalytic activity of the dispersed phase combined with the superior stability of the continuous phase allows for an easy recovery of the catalyst.[38]

Aside from the morphology, the chemical properties of a MOF material can also either limit or enhance its performance in a specific application. For example, water-stability is highly desired in MOFs applied to water treatment, antibacterial applications, and in some cases, to catalysis.[44-46] Indeed, water-stability of the MOF materials employed in intrusion−extrusion experiments is also a crucial parameter, especially when these experiments are performed using water or in a dilute aqueous electrolyte solution as non-wetting liquids. This property of MOFs is usually characteristic of the metal cluster. For instance, the strong chemical bonding and higher coordination number in

the secondary building units (SBU) of the Zr(IV)-based UiO-66 and UiO-67 MOFs and of the Cr(III)-based MIL-101(Cr), make these materials water-stable (water-stability: MIL-101(Cr) > UiO-66(Zr) > UiO-67(Zr)).[47-48] The hydrophilic/hydrophobic character of MOFs is also important for their final applications.[49-50] This property, however, depends on the nature of both the metal and organic components of the material. Indeed, the presence of coordinating water molecules at the metal site and/or free non-coordinating polar functional groups in polytopic linkers can lead to further adsorption of water molecules through hydrogen bonding, which eventually contributes to the formation of hydrophilic MOF pore and crystal surfaces. Structural defects can also contribute to the hydrophilic character of MOFs. For example, the ideal UiO-66(Zr) unit cell shows a particular hydrophobic behavior. In the defect unit cell, however, the coordination of additional water molecules to the zirconium center at the sites where linker molecules are missing increases the hydrophilic character of the MOF material.[51-52] It is important to note that there is no generally accepted definition for hydrophobicity in porous materials, but the pressure at which the pores fill with water is a convenient metric.[49, 52]

In addition to the high crystallinity and porosity (microporous volume as high as 1-2 $cm^3\ g^{-1}$),[29] and to the wide variety of combinations of metal and organic precursors, another advantage of MOFs is the possibility to post-synthetically modify them at the metal center or linker positions, *via* coordinative interactions or covalent bonds, respectively. Post-synthetic modification (PSM) of MOFs can be defined as the chemical alteration of these materials after their synthesis, which allows obtaining sophisticated materials for variable applications due to the economic and convenient synthetic processes, in addition to the available variety of functionalized organic groups.[53] For instance, unsaturated metal centers can provide modification sites for the functionalization of MOFs. An example is the MIL-101(Cr) material, where the open Cr(III) metal sites could be successfully functionalized with a number of organic multifunctional amines such as ethylene diamine (ED), diethylenetriamine (DETA), and 3-amino- propyltrialkoxysilane (APS). It was proposed that only one amine group from each additive is involved in coordination to the metal center, whereas, the other amine group(s) can serve as an immobilized base catalyst. The resulting modified products, ED-MIL-101, DETA-MIL-101, and APS-MIL-101 were, therefore, evaluated for their catalytic properties in the Knoevenagel condensation of benzaldehyde and ethyl cyanoacetate.[53] Furthermore, as previously mentioned, PSM also enables altering the organic functionality of the MOF material that can, in certain cases, eventually modify the latter's moisture-stability and physical properties. For instance, the moisture-sensitive and hydrophilic IRMOF-3, made up from ZnO_4 units and 2-aminobenzene-1,4-dicarboxylate, can be modified into a highly moisture-resistant and hydrophobic material by the post-synthetic transformation of the amino group into an amide group.[54] Moreover, the PSM approach offers potential advantages to

functionalizing MOFs, which can be appreciated for the following reasons: (1) it is possible to include a more diverse range of functional groups, in the absence of the restrictions imposed by MOF synthetic conditions, (2) modified products are easily isolated and purified, as the chemical derivatization is performed directly on the crystalline solids, (3) a given MOF structure can be modified with different reagents, thus, generating a large number of isomorphic materials (topologically identical, however, with different compositions).[53]

Thus, post-synthetic modification of MOF materials can be envisaged in order to obtain hydrophobic MOFs from initially hydrophilic materials, which can be tested in intrusion−extrusion experiments using water and/or low-concentration aqueous electrolyte solutions as non-wetting liquids.

Among the different classes of MOFs, Zeolitic Imidazolate Frameworks (ZIFs) establish the link, from a topological point of view, between zeolites and hybrid porous materials. The next section is dedicated to the description of ZIF materials.

B. Zeolitic Imidazolate Frameworks: a Sub-Class of MOFs

Zeolitic imidazolate frameworks are made from divalent metal ions (e. g., Zn^{2+}, Co^{2+}, Cd^{2+}, Fe^{2+}, Cu^{2+}) and bridging ditopic imidazolate anions or imidazolate derivatives.[55-56] Each metal cation is tetrahedrally linked, through nitrogen atoms, to four imidazolate derivatives, thus, forming extended 3D structures. The word “zeolitic” in ZIFs can be ascribed to the fact that the M-L-M angle (with M = divalent metal cation and L = imidazolate anion or its derivatives) is similar to the Si-O-Si angle (145°) in zeolites. Until now, a large number of crystalline ZIFs have been synthesized, where many of these materials share common topologies with zeolites (RHO, SOD, MER, GIS, etc.). Indeed, the introduction of transition metals (instead of Si or Al atoms) and more specifically organic units (instead of oxygen atoms) into the backbones of these zeolites leads to expanded pore structures, which explains the higher pore size and pore volume exhibited by some ZIFs as compared to those of zeolites of same topology. Furthermore, similar to MOFs, ZIFs are highly crystalline materials. However, compared to other MOF materials, ZIFs display higher chemical and thermal stabilities.[57] This can be attributed to the strong nature of the M-N bond. For instance, both ZIF-8 and ZIF-11 maintain their full crystallinity when suspended in boiling organic solvents (benzene and methanol) for 7 days.[58] The ZIF-8 structure was also shown to remain intact after suspending in boiling water for 7 days and in 0.1 and 8 M aqueous NaOH solution at 100°C for 24 h.[58] All these properties of ZIFs, which combine the advantages of both MOFs and zeolites, have made them attractive candidates for applications in the fields of catalysis, gas storage, gas separation, drug delivery, and, recently, in the energy storage and dissipation fields.[59-62] By associating the superior chemical and thermal stabilities of ZIFs compared to other MOF materials

and their higher microporous volumes compared to zeolites, promising results can be expected from the implication of ZIFs in LHSs during intrusion−extrusion experiments, especially in terms of the amount of stored/absorbed energy. Table 2 shows a list of the structural properties of ZIF materials possessing zeolite topologies, in addition to a number of ZIFs possessing topologies that do not exist in zeolites. In Table 2, we highlight the ZIF materials that were previously studied in intrusion−extrusion experiments (in light green), the ones that have been further investigated in this work (in green), those that have been newly studied (in cyan), and those that are considered potential candidates for intrusion−extrusion experiments (in deep sky-blue, light grey, and grey). MAF-32 and ZIF-14 are highlighted in yellow in order to emphasize on the fact that they are polymorphs of MAF-6. Similarly, highlighted in yellow is ZIF-72, a polymorph of ZIF-71. It is worthy to note that the d_a and d_p values reported in Table 2 provide only a first estimation of the size of the pore apertures and pore diameters of the ZIF materials, respectively. Indeed, it is important to note that these values can vary in the case of the materials, defined as flexible ZIFs, for which a swing of the linkers can intervene under the effect of an external stimuli.

Table 2. Name, composition, CCDC code, topology, and the number of member-rings corresponding to the largest pore aperture (da) and the pore diameter (dp)of porous ZIF materials.

Sample	Composition	CCDC code	RCSR topology	Zeolite topology	Number of imidazolate anions delimiting the largest window	d_a (Å)	d_p (Å)
ZIF-8[57]	$Zn(mim)_2$	VELVOY	sod	SOD	6	3.4 - 6.7	11.6
ZIF-67[57]	$Co(mim)_2$	GITTOT	sod	SOD	6	3.4	11.6
CdIF-1[63]	$Cd(mim)_2$	GUPBUP	sod	SOD	6	6.2	14.2
$Zn(dcim)_2$-SALE[64]	$Zn(dcim)_2$	-[a]	sod	SOD	6	-[a]	3.2
ZIF-7[57]	$Zn(bim)_2$	VELVIS	sod	SOD	6	2.9	4.31
ZIF-90[57]	$Zn(ica)_2$	WOJGEI	sod	SOD	6	3.5	11.2
ZIF-8_Cl[65]	$Zn(cim\text{-}2)_2$	YITKIY	sod	SOD	6	-[a]	-[a]
ZIF-8_Br[65]	$Zn(bim\text{-}2)_2$	YITKEU	sod	SOD	6	-[a]	-[a]
NOF-1[66]	$Zn(nim)_2$	CIMFUB	sod	SOD	6	-[a]	4.97
ZIF-65[57]	$Co(nim)_2$	GITTIN	sod	SOD	6	3.4	10.4
ZIF-71[57]	$Zn(dcim)_2$	GITVIP	rho	RHO	8	4.2-4.8	16.5-16.8
ZIF-72[57]	$Zn(dcim)_2$	GIZJUV	lcs	-[a]	6	1.9	1.9
ZIF-25[67]	$Zn(dmim)_2$	-[a]	rho	RHO	8	-[a]	-[a]
ZIF-71_Br_2	$Zn(dbim)_2$	-[a]	rho	RHO	8	-[a]	-[a]
ZIF-11[57]	$Zn(bim)_2$	VEJZOA	rho	RHO	8	3	14.6
MAF-6[68]	$Zn(eim)_2$	MECWOH	rho	RHO	8	7.6	18.1
MAF-32[68]	$Zn(eim)_2$	EHETER	qtz	-[a]	8	-[a]	-[a]
ZIF-14[57]	$Zn(eim)_2$	MECWIB	ana	ANA	8	2.2	2.2
ZIF-76[69]	Zn(im)(cbim)	GITWEM	lta	LTA	8	5.4	12.2
ZIF-22[57]	$Zn(abzd\text{-}5)_2$	MIHHIV	lta	LTA	8	2.9	14.8
ZIF-60[57]	$Zn_2(im)_3(mim)$	GITSUY	mer	MER	8	7.2	9.4
ZIF-10[57]	$Zn(im)_2$	VEJZIU	mer	MER	8	8.2	12.2
AFI-$Zn(im)_2$[70]	$Zn(im)_2$	IMIDZB13	afi	AFI	12	15.6	15.6
CAN-$Zn(im)_2$[70]	$Zn(im)_2$	PAJRUQ	can	CAN	12	13.2	13.2
ZIF-70[57]	$Zn(im)_{1.13}(nim)_{0.87}$	GITVEL	gme	GME	12	13.1	15.9
ZIF-80[57]	Zn(dcim)(nim)	YOZBUL	gme	GME	12	9.8	13.2
ZIF-82[57]	Zn(cnim)(nim)	YOZCEW	gme	GME	12	8.1	12.3
ZIF-95[57]	$Zn(cbim)_2$	NOFQAB	poz	-[a]	12	3.7	24

_a indicates that the zeolite topology are not applicable or that the CCDC code, pore aperture, and pore size are not reported. da is the diameter of the largest sphere that will pass through the pore. dp is the diameter of the largest sphere that will fit into the cages without contacting the framework atoms. Pore metrics measurements exclude guests when present. The ZIF materials highlighted in light green are those studied in intrusion−extrusion experiments exclusively prior to this work. ZIF materials highlighted in green and in cyan are those studied in intrusion−extrusion experiments in this thesis work. The ZIF materials highlighted in deep sky-blue are considered potentially interesting candidates for intrusion−extrusion experiments and will be discussed in Chapters 4 and 5. Presumed hydrophobic and hydrophilic ZIFs that are also considered potentially interesting candidates for intrusion−extrusion experiments but are not

discussed further in the next chapters of this manuscript are highlighted in light grey and grey, respectively. Some ZIFs are highlighted in yellow in order to emphasize that they are polymorphs of other ZIFs mentioned in the table.

Due to its high hydrophobicity [65, 68] and water stability,[58] in addition to its high porosity,[71] ZIF-8 is among the most intensively studied MOF materials in intrusion−extrusion experiments, using water and other types of non-wetting liquids.[60, 72-73]

It is also worthy to note that some ZIFs mentioned in Table 2 exhibit a presumed hydrophobic character (absence of polar hydrophilic functional groups on the imidazolate linker), in addition to large pore diameters and, thus, can be interesting candidates for intrusion−extrusion experiments. Examples include ZIF-10 and -60 of MER topology and ZIF-95 of poz topology. Indeed, to the best of our knowledge, the energetic behaviors of these materials have not yet been explored in intrusion−extrusion experiments, whereby they are expected to display relatively low intrusion pressures and high intruded volumes (due to their relatively large pore apertures and pore diameters, respectively), which is required for some practical applications. ZIF-22 of LTA topology can also be interesting in terms of the large pore diameter. Nevertheless, high intrusion pressure values are expected with this material during intrusion−extrusion experiments, as it displays relatively small pore apertures. Finally, despite their relatively large pore diameters, ZIF-70, -80, and -82 of GME topology, and NOF-1 as well as ZIF-65 of SOD topology are expected to be hydrophilic. This can be attributed to the presence of the nitro group on the imidazolate linker. Indeed, this prevents their application to water intrusion−extrusion experiments. However, their energetic performances can be investigated using highly concentrated aqueous electrolyte solutions as non-wetting liquids (Section V. A.). Nevertheless, before proceeding to intrusion−extrusion experiments, further studies must be carried out on these materials in the aim of investigating, mainly, the reproducibility of their syntheses, in addition to their stability in water and/or the aqueous electrolyte solution(s) to-be employed in the intrusion−extrusion experiments.

The following section particularly sheds light on water intrusion−extrusion experiments that have been reported in the literature using ZIFs and MOFs as the lyophobic porous component of the studied LHSs. In Sections V and VI, the systems involving ZIF-type materials and non-wetting liquids other than water will be commented.

IV. Energetic Applications of Metal-Organic- and Zeolitic Imidazolate Frameworks

There are two ways by which MOFs can be used for energetic applications. For instance, flexible carboxylate-based MOFs can be employed in the so-called compression−decompression experiments, where a reversible structural transformation can lead to shock-absorber or spring behaviors, whereas bumper behavior is accompanied with an irreversible structural transformation.

On the other hand, the second way of exploring the energetic performances of MOFs is through the intrusion−extrusion of non-wetting liquids into their porosity. Both compression−decompression and water intrusion−extrusion phenomena will be further described in the two next sub-sections.

A. "Breathing" Metal-Organic Frameworks for Energetic Applications

The study of phase transitions in flexible MOFs under high isostatic pressures for energetic applications has been carried out using fluids that are unable to penetrate the pores due to either wettability or size reasons. A typical example is the MIL-53(Cr) MOF material that is known for undergoing a "breathing" phenomenon during room temperature CO_2 adsorption.[74] This phenomenon consists of two successive crystal-to-crystal transformations from the initially large pore (lp) state, obtained after evacuating the pores, to the narrow pore (np) state at low CO_2 pressures, and then back to the lp state at higher CO_2 pressures. Another well-known example is the MIL-53(Al), which also undergoes similar lp-np and then np-lp breathing transitions during xenon adsorption experiments carried out at 195, 220, 273, and 292 K.[75] It seems that the internal adsorption stress responsible for inducing structural transitions is equivalent to the external hydrostatic pressure required to trigger the lp to np transition in the empty-pore material during compression-decompression experiments.[76] Such experiments were first conducted by Beurroies *et al*. and demonstrated phase transitions in MIL-53(Cr) based on mercury porosimetry experiments.[77] The "MIL-53(Cr)–mercury" system displayed shock-absorber behavior during a reversible structural transition, with an amount of stored energy of 12 J g^{-1} that is comparable to that obtained for the best "zeosil–water" systems, for example, the "MTW–" and "ZSM-12–water" systems displaying an amount of stored energy of 15 J g^{-1}.[14, 17, 77] This approach was then successfully extended to other flexible carboxylate-based MOFs, where the "MIL-53(Al)–mercury" system showed bumper behavior during compression−decompression experiments accompanied with irreversible phase transitions.[78] On the other hand, the reversible phenomena observed for the "MIL-47(V^{IV})–" and "MIL-53(Al)-FA–mercury" systems (where MIL-53(Al)-FA is aluminum fumarate, also known as Basolite® A520), and also for both "MIL-53(Al)-FA–" and "MIL-53(Al)–silicon-oil" systems led to shock-absorber behavior.[23, 79-80] Remarkably, the "MIL-53(Al)-FA−mercury" system registers a very high value of stored energy ≈ 60 J g^{-1} that is, however, obtained by virtue of the relatively high transition pressure value, which is in the order of 260 MPa.[79] Table 3 represents the energetic performances of flexible MOF materials determined *via* compression−decompression experiments carried out using mercury or silicon oil as non-wetting liquids.

Note that the term "intrusion−extrusion" is inappropriate in this case, as even though the experiments are carried out under high pressures, the non-wetting liquid does not enter the pores of the flexible solid porous material when undergoing phase transitions. Therefore, the term "compression−decompression" is more relevant here.

Table 3. Phase transition pressure ($P_{transition}$), volume variation corresponding to the lp-np transition (V_{lp-np}), stored (E_s) and absorbed (E_a) energies of flexible MOF materials studied in mercury (Hg) and silicon oil compression−decompression experiments.

"MOF−non-wetting liquid" system	**$P_{transition}$ (MPa)**	**V_{lp-np} (mL g^{-1})**	**E_s or E_a (J g^{-1})**	**Energetic behavior**	**Reference**
MIL-53(Cr)−Hg	55	0.25	12.0	SA	[77]
MIL-53(Al)−Hg	15	0.24	3.6*	B	[23]
MIL-53(Al)−silicon oil	33	0.22[c] 0.16[d]	7.8[a] 7.0[b]	B[a] SA[b]	[23]
MIL-47(V)−Hg	85	0.39	33.0	SA	[80]
MIL-53(Al)-FA−Hg	240	0.25	60.0	SA	[79]
MIL-53(Al)-FA−silicon oil	167[a] 115[b]	0.25[a] 0.20[b]	41.7[a] 23.0*[b]	B[a] SA[b]	[79]

(*) Indicates that the stored and absorbed energy values are calculated from the product of the transition pressure and the volume variation corresponding to the lp-np transition. a and b refer to the values obtained from the first and second compression cycles, respectively. The energetic behaviors of the systems are based on those indicated in the corresponding literature, where SA and B correspond to shock-absorber and bumper behaviors, respectively.

B. Water Intrusion−Extrusion in Metal-organic Frameworks

The energetic performances of ZIF materials based on water intrusion–extrusion experiments were first investigated by our group in 2013.[60] This work was part of the approach toward increasing the amount of stored/absorbed energy in LHSs by increasing the volume of intruded water molecules, which, as already mentioned in Section III, can be accomplished by using lyophobic solid materials with a degree of porosity that exceeds that of zeosils. The first ZIF material studied in such experiments was ZIF-8.

1. ZIF-8

ZIF-8 [$Zn(mim)_2$, with mim = 2-methylimidazolate], which possesses a SOD framework topology (cubic symmetry, space group *I*-43*m* with $a \approx 17.0$ Å), displays sod cages of ≈ 12.0 Å in diameter with 4- and 6- membered ring pore apertures. The 6-membered ring pore opening of the sod cage in

ZIF-8 has an initial formal diameter of 3.4 Å. However, this value can be almost doubled to reach approximately 6.4 Å during the diffusion of *p*-xylene molecules (of kinetic diameter ≈ 6.7 Å) through its pore apertures.[81] This phenomenon can be attributed to the swinging of the mim linkers under pressure. Nevertheless, the swung conformation of ZIF-8 is energetically unfavorable and the linkers, thus, relax back to their initial orientation after the *p*-xylene molecules have passed through the pore opening. Other remarkable characteristics of ZIF-8 include its high microporous volume (around 0.66 cm^3 g^{-1})[71,82] and stability in aqueous media, even if framework degradation was observed under extreme conditions.[58, 83-87] For instance, hydrothermal stability tests were carried out by Liu *et al*., by suspending ZIF-8 in water at 80°C for 24 h, using different ZIF mass concentrations.[85] The obtained results show that at a high mass concentration of around 6% (ZIF / (ZIF + water) mass ratio = 0.06), the ZIF-8 structure remains intact. Nevertheless, with decreasing concentration, a gradual decomposition of the ZIF-8 structure is clearly observed, which leads to a complete transformation into ZnO at a ZIF mass concentration of 0.06%.[85] Later in 2015, Zhang *et al*. studied the water-stability of ZIF-8 crystals, by suspending the material in water at room temperature and using a ZIF / water mass ratio of 0.006.[87] The obtained results prove that ZIF-8 crystals undergo a degradation process upon contact with water, which is due to a hydrolysis mechanism that results in the release of Zn^{2+} ions and protonated Hmim molecules.[87] The presence of Hmim molecules initially in the mother solution, however, protects the material from being attacked by water molecules and, consequently, from being hydrolyzed.[87] Sheng *et al*. investigated the effect of the nature of the zinc source (zinc nitrate, acetate, chloride, or sulfate) on the hydrothermal stability of ZIF-8 nanocrystals.[83] The stability tests were carried out by suspending ZIF-8 nanocrystals in water at 80°C, with a ZIF / (ZIF + water) mass percentage equal to 3%.[83] Experimental results show that after being suspended in water for 7 days, the ZIF-8 nanocrystals maintain their structure, regardless of the zinc source from which they were synthesized. Nevertheless, by extending the stability test duration to 10 days, all the ZIF-8 samples, except for that synthesized from zinc acetate, are degraded and become completely amorphous, whereas zinc-acetate-based ZIF-8 retains 45% of its crystallinity. These results indicate that using zinc acetate as a metal source leads to ZIF-8 materials of much higher hydrothermal stability compared to those derived from zinc nitrate.[83] Finally, in a very recent study, Zhang *et al*. highlighted the transformation of ZIF-8 into a new phase, a nonporous pseudo-polymorph, *via* a hydrolysis-condensation mechanism, when ZIF-8 is suspended in water under a low ZIF / (ZIF + water) mass ratio for 24 h at room temperature.[88] Nevertheless, according to Park *et al.*, the crystalline structure of ZIF-8 is stable after suspending in water for 7 days at room temperature or at 50°C, and even in boiling water, thus, indicating the material's high hydrothermal stability.[58] Indeed, these results indicate that ZIF-8 is stable in aqueous medium, however, to a certain limit, which is mainly

dependent on the ZIF mass concentration. In other words, the lower the ZIF / (ZIF+ water) mass ratio, the higher is the probability of the ZIF-8 structure undergoing degradation through hydrolysis. It is also important to note that during the intrusion−extrusion experiments carried out in this work, a ZIF / (ZIF + water) mass ratio of ≈ 0.09 (9%) is employed. This value, being much higher than the ZIF mass concentration at which hydrolysis is observed in ZIF-8, neglects the possibility of structure degradation during intrusion−extrusion experiments performed on this material. Moreover, the contact time with water during intrusion−extrusion experiments does not exceed 24 h.

Furthermore, in an aqueous solution, a hypothesis suggests that dissolved anions can replace the imidazolate (mim) linker by forming amorphous zinc complexes. In this context, Wang *et al*. studied the effect of the presence of anions in the aqueous solution on the stability of ZIF-8.[86] The stability tests were performed by suspending the ZIF-8 crystals for 48 h and at room temperature in a 50 mM aqueous solution containing a sodium salt, with a low ZIF / (ZIF + aqueous solution) mass ratio of 0.006%.[86] The effect of different sodium salts, and particularly that of counter-anion, was studied (as the presence of sodium cations was shown to have no effect on the structure of ZIF-8). The obtained results reveal that the ZIF-8 structure is maintained in the presence of Cl^-, SO_4^{2-}, NO^{3-}, PO_4^{3-}, and CO_4^{2-} anions, whereas with HPO_4^{2-} and HCO_4^-, ZIF-8 transforms into a nonporous, yet crystalline, material.[86] Nonetheless, the ZIF-8 structure was shown to be maintained after suspending in 0.1 and 8 M aqueous NaOH solution at 100°C for 24 h (ZIF / aqueous solution mass ratio is unspecified for these tests).[58] The use of saturated LiCl (20 M) and KCl (4 M) aqueous solutions during intrusion−extrusion experiments in ZIF-8 will be discussed in Chapter 3 of this thesis manuscript. However, it is important to note that framework degradation was not observed for any of the "ZIF-8−aqueous electrolyte solution" systems, even at pressures as high as 350 MPa.

Furthermore, some vapor-phase water adsorption experiments realized by Küsgens *et al*. and Cousin Saint Remi *et al.* have also evidenced the hydrophobic character of ZIF-8, which may be likely due to the methyl group borne by the imidazolate linker.[65, 68] All these characteristics, that is, the high porous volume, relatively high water stability, and hydrophobic nature, which are highly desired in the lyophobic solid matrix employed in high-pressure water intrusion−extrusion experiments, have made ZIF-8 a very interesting MOF-type candidate for the investigation of its energetic performances.[60, 82]

Another important feature of ZIF-8 is that its unit cell may expand or contract under hydrostatic pressure depending on the solvent molecules used as the Pressure-Transmitting Medium (PTM). To this end, several studies have been carried out using water, methanol, ethanol, and silicon oil as PTM.[89-90] Moggach *et al.* demonstrated the capability of ZIF-8 of undergoing a reversible structural transition caused by the swinging effect of the imidazolate linkers when the pressure applied by methanol as the hydrostatic medium reaches a certain value.[90] A similar swing effect of the

imidazolate linkers under pressure can be highly advantageous in intrusion−extrusion experiments, as it is expected to allow the accommodation of a relatively larger amount of non-wetting liquid molecules. Figure 2 demonstrates the *P*−*V* diagrams of the "ZIF-8–water" system obtained from the very first water intrusion−extrusion experiment carried out on ZIF-8.[60] The first intrusion curve (in black) of the *P*−*V* diagrams exhibits three parts corresponding to three distinct steps that take place while mechanical energy is progressively applied on the LHS. A logarithmic scale is used for the pressure axis in order to emphasize the phenomenon in the low-pressure range (Figure 2a). In the first step, at pressures between 0.003 and 0.13 MPa, the small volume variation corresponds to the compression of the non-intruded ZIF particles (Part 1, Figure 2a). In the second step, at pressures between 0.13 and 1 MPa, the volume gain corresponds to the intrusion of water in the interparticular porosity (Part 2, Figure 2a). The third step, which occurs at around 27 MPa (P_{int}), is assigned to the intrusion of water molecules into the ZIF pores (Figure 2b). The slight volume gain observed between 40 and 80 MPa, that is, after complete filling of the micropores, can be explained by the weak compression of the "ZIF-8–water" system. When the pressure is gradually released, the extrusion of water molecules occurs at around 22 MPa (P_{ext}). The intrusion−extrusion process is completely reversible, with a small hysteresis between the intrusion and extrusion curves indicating, thus, according to the literature, fairly good shock-absorber behavior of this system.[60] Nevertheless, by referring to our new definition of shock-absorber/spring behavior that is provided in Chapter 2 (experimental part), the "ZIF-8–water" system is better described as a spring. Moreover, the intrusion−extrusion phenomenon is reproducible over three cycles and the stability of the ZIF-8 structure is maintained as confirmed by XRD, SEM, TGA, and N_2 sorption analyses. We note that the amount of energy stored by the "ZIF-8–water" system is equal to 13 J g^{-1}. Compared to the "Chabazite–", "DD3R–", and "SSZ-23–water" systems, where the corresponding zeosils, similar to ZIF-8, exhibit a cage-pore system and pore apertures of diameter (2.4-4.4 Å) in the same range as ZIF-8 (3.4 Å for nominal cage aperture size), the "ZIF-8–water" system is capable of storing almost twice the amount of energy (13 J g^{-1} for the "ZIF-8–water" system, compared to 6 and 7 J g^{-1} for the "Chabazite–", "DD3R–", and "SSZ-23–water" systems, respectively).[14, 16, 60] Thus, these results illustrate that increasing the microporous volume may enhance the amount of stored/absorbed energy in LHSs during intrusion−extrusion experiments.

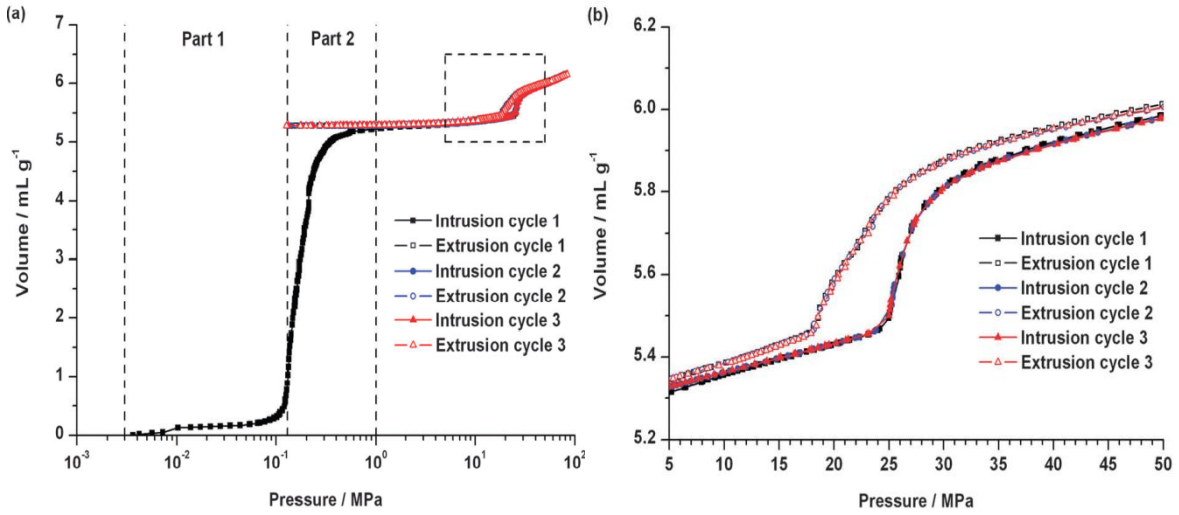

Figure 2. P-V diagrams obtained from water intrusion-extrusion in ZIF-8 with (a) a logarithmic scale for the pressure values and (b) enlargement of the pressure area from 5 to 50 MPa.60

Later, in 2014, Coudert and coworkers investigated, using molecular simulations, the water adsorption properties of ZIF-8 at 300 K.[91] The obtained results highlighted again the hydrophobic character of this material, as the water adsorption isotherm reveals no water adsorption in the gas phase. Nevertheless, when the pressure exceeds the water saturation pressure (3.8 kPa at 300 K), the isotherm reveals a steep step, indicating water adsorption in the liquid phase, with an adsorbed water quantity of 29.1 mmol g^{-1}. Indeed, these results are in agreement with those experimentally obtained from water intrusion−extrusion experiments, where 27.9 mmol g^{-1} of water are estimated to be intruded into the porosity.[60] ZIF-8 displays a type V water sorption isotherm, with a large hysteresis loop, showing the desorption of water at 15 MPa, which is close to the experimentally obtained value of extrusion pressure during water intrusion−extrusion experiments (around 20 MPa).[60, 91] Therefore, the molecular simulation results are compatible with those revealed from experimental water intrusion−extrusion experiments in ZIF-8.

In another experimental study realized in 2015 on ZIF-8, Grosu *et al*. investigated the energetic characteristics of the "ZIF-8–water" system in wide temperature and pressure ranges by means of high-pressure calorimetry.[92] It is important to note that, even though rarely studied, the thermal effects on LHSs during compression−decompression or intrusion−extrusion experiments are essential for practical applications and for the understanding of their working mechanisms. The high pressure intrusion−extrusion experiments were performed in the 275-360 K temperature range. Based on the obtained results, the "ZIF-8–water" system is said to display stable spring behavior at temperatures ranging between 275 and 350 K. Furthermore, in this temperature range, the intrusion pressure is almost independent of the temperature and in the order of 25 MPa. Intrusion−extrusion experiments performed at higher temperatures, however, reveal an irreversible decrease in the intrusion and extrusion volumes of water. According to the authors, this is due to the simultaneous

effect of temperature and pressure during intrusion−extrusion experiments, which leads to an irreversible structural transition of ZIF-8 from the cubic to the orthorhombic symmetry.

Michelin-Jamois *et al*. also carried out water intrusion−extrusion experiments in ZIF-8 at temperatures higher than room temperature.[93] The obtained results reveal that at 343 K, the "ZIF-8−water" system exhibits intrusion and extrusion pressures in the order of 25.2 and 20.9 MPa, respectively, with the intruded volume ≈ 0.5 mL g^{-1}. The $P-V$ diagram reveals a reversible intrusion−extrusion phenomenon, with a small hysteresis between the intrusion and extrusion curves. These results are close to the ones obtained from the experimental work published by Ortiz *et al*. in terms of the values of the intrusion and extrusion pressures and are also in agreement with the results obtained by Grosu *et al*., indicating the reversibility of the phenomenon at such a temperature.[60, 92] However, the intruded volume is higher in this case,[93] which contradicts with the data published by Grosu *et al*. concerning the negative dependence of the intruded/extruded volume on the temperature.[92] Furthermore, according to Sun *et al*., the water intrusion−extrusion phenomenon in ZIF-8 is reproducible over 40 consecutive cycles, with the corresponding $P-V$ curves being almost overlapping.[94]

On another note, another study performed by our team in 2015 on the energetic performances of the "ZIF-8–water" system shed light on the influence of particle morphology (particles size and shape).[82] Previous investigation of the effect of the crystal size (nanometer/micrometer) on the energetic behavior of zeosils during intrusion−extrusion experiments was first realized in 2014 on the "pure-silica MFI–water" system by Humplik *et al.*[95] Nonetheless, the study indicates no real influence of the studied parameter. However, the relative decrease in the energetic performances in the case of the nanosized crystals is attributed to the presence of non-crystalline silica regions and, thus, to a decreased porosity available for water intrusion. Besides, in order to evaluate the impact of the morphological parameters on the energetic performance of the "ZIF-8–water" system, various ZIF-8 samples revealing variable crystal sizes and shapes were prepared according to different protocols. The ZIF samples were synthesized as nanometer-sized spheres, nanometer-sized rhombic dodecahedra, nanometer-sized cubes, micrometer-sized rhombic dodecahedra, and micrometer-sized cubes with truncated edges. The water intrusion−extrusion experiments show that higher intrusion pressures are encountered as the crystal size of ZIF-8 increases from nano- to micrometers. This is explained by the presence of a larger number of defects in the nanosized ZIF-8 particles compared to the microsized analogues, even if the different samples exhibit similar accessibility towards nitrogen (displaying similar microporous volumes of around 0.66 cm^3 g^{-1}). These framework defects tend to inhibit the extrusion of water molecules at low pressures, as pointed out for MFI-type zeolites as well. Moreover, the crystal shape of the ZIF materials was also demonstrated to affect the materials' energetic performances. The experimentally obtained results

reveal that in each group of size (nanometer and micrometer), the sample with the rhombic dodecahedron shape exhibits lower starting and final intrusion pressures than those of cubic and cubic with truncated-edges shaped ZIF-8 crystals. This is ascribed to the fact that rhombic-dodecahedron-shaped crystals present only {110} facets, with the 4- and 6-membered rings delimiting the cage aperture being exposed in a similar manner, whereas, crystals of cubic and cubic with truncated edges shapes display only or mainly {100} facets, with only the 4-membered rings of the cage aperture being directly exposed. By assuming that water intrusion occurs preferentially through 6-membered rings and more difficultly, or most probably not at all, through 4-membered rings, higher intrusion pressures are, thus, required so as to provoke the intrusion of water molecules into the pores of the cubic and cubic with truncated edges. Regarding the intermediate values obtained for the nanometer-sized spheres, they are explained by the random distribution of the {110} and {100} facets on the surface of the crystallites. Therefore, for both nano- and micro-sized crystals, the intrusion/extrusion pressures are higher for the cubic shaped crystals. Nevertheless, the size and shape of the crystals do not seem to have an impact on the energetic behavior, as all systems were classified as shock-absorbers. Here also, given our new definition of shock-absorber/spring behavior that is provided in Chapter 2 (experimental part), all "ZIF-8–water" systems are better described as springs.

2. Other ZIFs

ZIF-8 is undoubtedly the most extensively studied material in water intrusion-extrusion experiments. Nevertheless, different other ZIFs have also been investigated in water intrusion−extrusion experiments and the effects of the physicochemical (related to the water stability, hydrophilicity/hydrophobicity, natures of linkers and cations), structural (pore size and geometry), topological (SOD and RHO), and morphological (crystal size and shape) parameters on their energetic behavior have been explored.

Indeed, it has been shown that ZIFs that lack water-stability are unsuitable for water intrusion−extrusion experiments. A typical example is the CdIF-1 material, the SOD-type Cd-based analogue of ZIF-8.[64] Moreover, ZIFs of hydrophilic character, usually related to the hydrophilic nature of the organic linker, are ineffective in water intrusion−extrusion experiments.[64] An example is the case of ZIF-90 based on imidazole-2-carboxyaldehyde (Hica), in which no water intrusion is observed after three intrusion−extrusion cycles. This phenomenon is ascribed to the presence of the aldehyde group that interacts with water molecules at low pressures, while limiting their accommodation at higher pressures in the process.[64] The interaction between water molecules and the aldehyde groups (polar functional groups) through hydrogen bonding can also inhibit water from being expelled from the porosity during extrusion, which results in lower intrusion volumes in

the following cycles and, hence, in a decreased reproducibility of the phenomenon. In addition to the functionalization of the organic linker, the presence of bulky substituents can also influence the intrusion step. Typical examples include both ZIF-7 (of SOD topology) and ZIF-11 (of RHO topology), where regardless of the topology of the ZIF material, the 4,5-disubstitution with a benzyl group on the imidazolate ring causes steric hindrance that prevents the intrusion of water molecules.[64]

To continue to assess the effect of the topology of the ZIF material on the energetic performance of the LHS during water intrusion−extrusion (in addition to the case of ZIF-7/ZIF-11 pair), the energetic behaviors of two polymorphic ZIF materials (constructed from Zn^{2+} cations and 4,5-dichloroimidazolate but having different topologies) were compared. These are $Zn(dcim)_2$-SALE and ZIF-71 of SOD and RHO topologies, respectively. Obtained results show that intrusion could only occur in ZIF-71 (RHO). This is attributed to the fact that SOD-type $Zn(dcim)_2$-SALE displaying 4- and 6-membered facets and constituting of 4,5-disubstitued organic linkers are not capable of allowing the diffusion of water molecules into their pores. However, in the case of ZIF-71 (RHO) the 8-membered facets (in addition to the 4- and 6-membered facets) encountered in the RHO topology are large enough to allow the intrusion of water molecules into the ZIF pores even if constructed of 4,5-disubstituted linkers.[64, 96] For the "ZIF-71−water" system, perfect shock-absorber behavior was observed, with an energy yield of 42% and an amount of stored energy of 26 J g^{-1},[64] which is two times higher than the value registered for the "ZIF-8−water" system (13 J g^{-1}). Indeed, this can be attributed to the intrusion pressure that is higher for ZIF-71 (71 MPa) than for ZIF-8 (27 MPa). **A comparison between the "ZIF-8−" and "ZIF-71−water" systems is difficult, as both materials are formed of different imidazolate derivatives and exhibit different topologies. However, it seems that those ZIF materials do not follow the trends observed for "zeosil−water" systems. Indeed, in the case of zeosils of cage structures, the intrusion pressure is independent of the size of the pore aperture and increases with the decrease in the cage size.[14] Nevertheless, if the ZIF-8 flexibility is taken into account, its pore aperture becomes ≈ 6.7 Å, which is greater than that of ZIF-71 (Table 2) and, thus, a cage aperture-size-dependent phenomenon may be addressed.**

The nature of the metal cation was proven to have a negligible effect on the performance of ZIF materials during water intrusion−extrusion experiments.[64] For instance, isomorphic ZIF-8 and ZIF-67 (possessing both SOD topology and formed from the same organic linker (mim) but different metal cations (Zn^{2+} for ZIF-8 and Co^{2+} for ZIF-67)) show similar shock-absorber behaviors with stored energies in the order of magnitude of 11-13 J g^{-1}, and intrusion pressures of 27 and 25 MPa, respectively.[64] We note that according to our new definition of shock-absorber/spring behavior that

is provided in Chapter 2 (experimental part), both the "ZIF-8–" and "ZIF-67−water" systems are better described as springs.

In another study, the MOF material Cu_2(tebpz) was explored in high pressure water intrusion−extrusion experiments.[97] This MOF material, which is made up of Cu(I) cations and bridging bipyrazolate linkers, possesses 1D channels lined with ethyl groups, which provide an overall hydrophobic character. Cu_2(tebpz) is also characterized by high thermal (stable up to 450 °C) and chemical stabilities that make it a good candidate for the investigation of its energetic performances. The novelty of this work is related to the pore structure of the MOF material, as MOFs with 1D channels had not been studied in intrusion−extrusion experiments before. The "Cu_2(tebpz)–water" system displays spring behavior that is highly reversible and reproducible over 10 cycles. According to the authors, this was the first reported LHS based on MOFs presenting a negligible hysteresis. Compared to other LHSs based on zeolites that exhibit a small hysteresis, the "Cu_2(tebpz)–water" system displays a comparable but lower energy capacity of about 4.3 J g^{-1}, which, however, is not attributed to the lower intrusion volume (0.12 cm^3 g^{-1}) but rather to the lower intrusion/extrusion pressure (35 MPa), which may be considered advantageous, as lower intrusion pressures are more suitable for practical applications.[97]

Based on this work, it would have been interesting to study the effect of the pore structure (cage or channel pore system) on the intrusion pressure and/or energetic behavior of the LHSs during water intrusion−extrusion experiments, by comparing the energetic performance of the "Cu_2(tebpz)−water" system to that of another "ZIF−water" system of a cage pore structure. Nevertheless, Cu_2(tebpz) has three types of pore apertures, of 3- and 6-membered rings, with the largest pore aperture having a diameter of 11.6 Å.[98] Therefore, owing to the strong structural differences between Cu_2(tebpz) and the other ZIFs studied in water intrusion−extrusion experiments (denoted in Table 4), a comparison of the energetic results does not seem to be relevant.

3. Summary

In conclusion, various MOF/ZIF materials have been explored in water intrusion−extrusion experiments prior to this PhD work. Their textural and structural characteristics (0.207 cm^3 g^{-1} < $V_{micropore}$< 0.680 cm^3 g^{-1} and 2.9 Å < pore opening < 11.6 Å) and energetic performances (spring or shock-absorber behavior and stored energy < 25.5 J g^{-1}) are reported in Table 4. The higher porosity of MOFs/ZIFs compared to zeosils leads to enhanced amounts of stored/absorbed energies. Experimental results reveal the influence of the MOF/ZIF's chemical composition, topology, and morphology on the energetic behavior of the LHS during intrusion−extrusion experiments. Whereas the nature of the cation has no apparent effect, the presence of polar functional groups or bulky substituents on the imidazolate linker is proven to prevent water intrusion. Moreover, the presence

of structural defects (associated with smaller particle size) is also linked to lower intrusion pressures and irreversible intrusion−extrusion phenomena.

Table 4. Structural properties of MOFs and energetic characteristics of the corresponding "MOF–water" systems.

MOF sample	Composition	Zeolite topology	Pore structure	$V_{micropore}$ ($cm^3\ g^{-1}$)	Pore opening (Å) (number of membered - ring)	P_{int} (MPa)	P_{ext} (MPa)	V_{int} ($mL\ g^{-1}$)	E_{stored} ($J\ g^{-1}$)	$E_{restored}$ ($J\ g^{-1}$)	Energy yield (%)	Energetic behavior literature	Energetic behavior new definition	Ref.
ZIF-8	$Zn(mim)_2$	SOD	cages	0.66	3.4 (6 MR)	27	24	0.40	10.8	9.8	91	SA	S	[64]
ZIF-67	$Co(mim)_2$	SOD	cages	0.68	3.4 (6MR)	24	19	0.53	12.7	10.3	81	SA	S	[64]
CdIF-1	$Cd(mim)_2$	SOD	cages	0.86	6.2 (6 MR)	Phase transformation in contact with water								[64]
Zn(dcim)$_2$-SALE	$Zn(dcim)_2$	SOD	cages	0.23	3.2 (6 MR)	No observed intrusion-extrusion phenomenon in the range 0-350 MPa								[64]
ZIF-7	$Zn(bim)_2$	SOD	cages	0.21	2.9 (6 MR)	No observed intrusion-extrusion phenomenon in the range 0-350 MPa								[64]
ZIF-90	$Zn(ica)_2$	SOD	cages	0.48 0.58	3.5 (6 MR)	No observed intrusion-extrusion phenomenon in the 0-300 MPa pressure range								[64]
ZIF-71	$Zn(dcim)_2$	RHO	cages	0.39	4.2 (8 MR)	71	30	0.36	25.5	10.8	42	SA	SA	[64]
ZIF-11	$Zn(bim)_2$	RHO	cages	0.46 0.58	3.0 (8 MR)	No observed intrusion-extrusion phenomenon in the 0-300 MPa pressure range								[64]
Cu_2(tebpz)	Cu_2(tebpz)		1D channels	0.37	5.9 6.7 11.6	35.7	35.4	0.12	4.3	4.3	99	S	S	[97]

For the Cu2(tebpz) material, the diameters of the pore openings are estimated from DFT pore size distribution performed after exploitation of N2 sorption experiments. For the other ZIF materials, this value is estimated based on structure analyses. Intrusion (Pint) and extrusion (Pext) pressures, intrusion volume (Vint), stored (Estored) and restored

(Erestored) energies of MOF materials studied. S, SA, and B correspond to spring, shock-absorber, and bumper behaviors, respectively.

Indeed, exploring the energetic behaviors of ZIF materials of topologies that have not been previously investigated can be interesting (LTA, MER). It would be also interesting to go further with studying the effects of other parameters on the energetic behaviors of the ZIF-based LHSs during intrusion−extrusion experiments. Among these parameters can be the susbstitution on the imidazolate linker in addition to extremely large pore apertures (10- and 12-membered ring pore apertures).

V. Intrusion-Extrusion Experiments Using Aqueous Electrolyte Solutions

The second approach toward enhancing the amount of stored/absorbed energy, as mentioned previously, involves increasing the intrusion pressure. As experimentally proven, this could be accomplished by replacing water with aqueous electrolyte solutions. Furthermore, experimental work has also proven the enhancement of the intrusion pressure with the increased concentration of the aqueous electrolyte solution.[6, 73, 95, 99] In fact, different hypotheses have been suggested to explain the increase in intrusion and extrusion pressures and, consequently, the stored/absorbed energy associated with the use of aqueous electrolyte solutions as non-wetting liquids. In the next sub-sections, we will discuss these hypotheses and support them with examples given in the literature.

A. Zeosil-Based Systems

Indeed, by referring to the Laplace-Washburn relation (Equation 1), higher intrusion pressures are expected with an increased value of the liquid-vapor interfacial tension. As **aqueous electrolyte solutions are characterized by higher liquid-vapor interfacial tensions compared to water**, this can be a first explanation of the increased intrusion pressure.[73, 96] Another explanation is the **electrostatic repulsion**, **which contributes to a higher transport resistant force**. These two hypotheses were used to explain the increase in intrusion pressures accompanied with the use of aqueous electrolyte solutions during intrusion-extrusion experiments performed on zeolite Y and ZSM-5.[6, 95]

In another study, the influence of the addition of electrolytes on the intrusion pressure of the non-wetting liquid in Silicalite-1 was studied and the results were compared to those obtained from water intrusion−extrusion experiments.[100] The selected media were $LiCl{\cdot}3H_2O$, $MgCl_2{\cdot}21H_2O$, and $NaCl{\cdot}11H_2O$. Regardless of its nature, the addition of salt into the system strongly enhances its energetic performance, with the intrusion and extrusion pressures being strongly higher than those

observed in the case of the "Silicalite-1–water" system.[14] All the systems behave as springs with a small hysteresis, where the phenomenon is reversible and reproducible over several cycles. However, the stored energy is the highest in the case of the "Silicalite-1–$LiCl \cdot 3H_2O$" system. According to the authors, this is due to the **small radius of the lithium cation compared to sodium and magnesium cations, and to the higher solubility of LiCl in water compared to $MgCl_2$ and NaCl.**[99-100] In a complementary study, the effect of the concentration of the LiCl aqueous solution on the energetic performance of the "Silicalite-1–LiCl aqueous solution" system was investigated.[101] Both intrusion and extrusion pressures and, consequently, the stored and restored energies increase with increasing LiCl concentrations, with the highest values obtained when using the LiCl 20 M aqueous solution (saturated solution at room temperature). Indeed, the stored energy is tripled in the case of the "Silicalite-1–LiCl 20 M" system (31 J g^{-1}) compared to the "Silicalite-1–water" system (11 J g^{-1}).[14, 101]

In addition to increasing the intrusion pressure, the addition of electrolytes to the non-wetting liquid may also lead to a change in the energetic behavior of the LHS. Based on the work carried out by Ryzhikov *et al*., the "*BEA zeosil–LiCl aqueous solution" system shifts from bumper to shock-absorber behavior upon increasing the concentration of the LiCl solution from 10 to 15 M.[102] A similar phenomenon was also observed for the CHA-type zeosil, where the mixed bumper/shock-absorber behavior observed with water is transformed into pure shock-absorber behavior upon using LiCl as a non-wetting liquid.[15, 103] The bumper behavior is attributed to the formation of silanol defects, through hydration, in the presence of water. With aqueous electrolyte solutions (especially those of high concentrations), however, the zeosil is protected from hydration, due to the presence of less water molecules. In addition to this, it was shown that **even in the case of weakly hydrophilic zeolites, which exhibit no intrusion step with water, intrusion can occur in the presence of aqueous electrolyte solutions**.[104]

In spite of all the studies carried out on "porous materials–aqueous electrolyte solution" systems, the main debate remained over the nature of the intruded species. Is it only water, only salt ions, a mixture of both water and salt ions? To answer to this question, Arletti *et al*. investigated the energetic behavior of the pure-silica FER-type zeolite (Si-FER) based on intrusion-extrusion experiments, using $MgCl_2 \cdot 21H_2O$ solution as the non-wetting liquid.[105] For the first time, intrusion-extrusion experiments were coupled to in situ synchrotron X-ray powder diffraction analysis, where the data were collected over a wide pressure range (from ambient pressure to 1.47 GPa).[105] Obtained results reveal that the intrusion occurs at a relatively high pressure of 195 MPa, with the phenomenon being completely reversible and the "Si-FER–$MgCl_2$ aqueous solution" system displaying spring behavior. Rietveld refinement of the data collected at 280 MPa, a pressure close to the intrusion value, reveal that the composition of the intruded species is $MgCl_2 \cdot 10H_2O$. This

indicates that both water molecules and ions of the aqueous electrolyte solution are intruded in the zeolite pores. However, the lower solvation degree of the intruded ions ($MgCl_2 \cdot 10H_2O$) compared to the initial solution ($MgCl_2 \cdot 21H_2O$) indicates a partial desolvation of magnesium and chloride ions.[105] This can be explained by the fact that in aqueous electrolyte media, water molecules tend to form solvation shells around the constituent salt ions, through ion-dipole interactions. These interactions that depend on the size of the ion, in addition to its charge, polarizability, and concentration in the medium, involve interaction energies of hundreds of kJ mol^{-1}. Therefore, in the presence of electrolytes, **another explanation for the increase in the applied pressure during intrusion may be the additional force needed to break these solvation bonds**.[82, 99, 105]

It is also important to note that the "Si-DDR–LiCl 20 M" system studied by Ronchi *et al.* reveals shock-absorber behavior with an intrusion pressure of 357 MPa, which in turn contributes to a very high amount of stored mechanical energy (≈ 93 J g^{-1}).[106] Interestingly, these values of intrusion pressure and stored energy are the highest registered until now in the history of intrusion−extrusion experiments. However, unfortunately, such elevated values of intrusion pressures are considered a limitation for the employment of the corresponding LHSs in practical applications.[107]

B. ZIF-Based Systems

The effect of additive electrolytes in high-pressure intrusion−extrusion experiments was also studied for ZIF materials.[73, 93, 96, 108] Table 5 summarizes the energetic characteristics reported for different studied "ZIF-8−" and "ZIF-71−aqueous solution" systems.

Table 5. Energetic characteristics of some "MOF–electrolyte aqueous solution" systems.

"ZIF–aqueous electrolyte solution" system	P_{int} (MPa)	P_{ext} (MPa)	V_{int} (mL g^{-1})	E_s or E_a (J g^{-1})	Energy yield (%)	Energetic behavior	Energetic behavior new definition	Reference
ZIF-8–KCl 1 M	26.6	22.3	0.50	13.3	84	SA	S	73
ZIF-8–KCl 2.5 M	31	27.5	0.50	15.5	88	SA	S	73
ZIF-8–KCl 4 M	39	34.7	0.50	19.5	89	SA	S	73
ZIF-8–LiCl 1 M	30	25.6	0.50	15.0	85	SA	S	73
ZIF-8–LiCl 2.5 M	40^a 37.2^b	30.3	0.50^c 0.45^d	20^a 16.7^b	68^a 81^b	B^a SA^b	B^a $S^{b,}$	73
ZIF-8–LiCl 4 M	52.1^a 44.8^b	33.7	0.50^c 0.35^d	26^a 15.7^b	45^a 75^b	B^a SA^b	B^a SA^b	73
ZIF-8–NaCl 1 M	31.2	28.2	0.50	15.6	90	SA	S	73
ZIF-8–NaCl 2.5 M	39	34.7	0.49	19.11	87	SA	S	73
ZIF-8–NaCl 4 M	52	44	0.50^c 0.45^d	26^a 23.4^b	76^a 85^b	B^a SA^b	B^a S^b	73
ZIF-71–KCl 1 M	74^a 65^b 61^c	32	0.36^c 0.24^d 0.20^e	26.6^c 15.6^b 12.2^c	29^a 41^b 51^c	B^a $SA^{b,c}$	B^a $SA^{b,c}$	96
ZIF-71–KCl 4 M	96^a 62^b	36	0.36^c 0.05^d	34.6^a 3.1^b	5^a 58^b	B	B	96

a, b, and c refer to the values obtained from the first, second and third intrusion/extrusion cycles, respectively. SA, S, and B correspond to shock-absorber, spring, and bumper behaviors, respectively.

Similar to what was observed for zeosils, Ortiz *et al.*,[73] and later Michelin-Jamois *et al.*,[93] highlighted the increase in intrusion and extrusion pressures and stored energies with increasing ion concentrations in LHSs using mainly ZIF-8 as the porous material. The former team studied the influence of the cation size and salt concentration on the energetic performance of ZIF-8 using three types of salts, namely LiCl, KCl, and NaCl of three different concentrations each (1, 2.5, and 4

M).[73] For all aqueous electrolyte solutions, **the intrusion pressure and, thus, the stored energy increase with the increase in the salt concentration**. The "ZIF-8–aqueous electrolyte solution" systems show shock-absorber (spring behavior based on our new definition) behavior that is reproducible over several cycles for intrusion−extrusion experiments carried out using both water and low-concentration (1 and 2.5 M) aqueous electrolyte solutions. However, at high salt concentrations (4 M), depending on their nature, the cations can interact differently with the imidazolate linker, which eventually leads to variable energetic behaviors. Herein, considering the highest salt concentration (4 M) and the first intrusion−extrusion cycle, the "ZIF-8–KCl 4 M aqueous solution" system shows shock-absorber (spring based on our new definition) behavior that is maintained over several cycles, whereas, in the case of "ZIF-8–LiCl 4 M aqueous solution" and "ZIF-8–NaCl 4 M aqueous solution" systems, the liquid is not completely expelled in the extrusion step of the first cycle, which leads to lower intruded volumes in the second intrusion cycle. This is explained by **the interaction of sodium and, especially, lithium cations with the imidazolate linker, which is stronger than the interaction encountered with potassium cations.** Furthermore, also for the highest salt concentration (4 M), it can also be noted that the intrusion pressure decreases, even if slightly, with the increase in the ionic radius, r_i, of the constituent cation of the salt (P_{int} (LiCl) = 52.1 MPa, P_{int} (NaCl) = 52.0 MPa, P_{int} (KCl) = 47.2 MPa for $r_i(Li^+)$ = 0.76 Å, $r_i(Na^+)$ = 1.02 Å, $r_i(K^+)$ = 1.38 Å). In other words, **higher intrusion pressures can be obtained for the cations of smaller ionic radius and higher hydrodynamic diameter, as the two parameters evolve in opposite sense**.[109-110]

However, in a later study carried out on the effect of electrolytes, Michelin-Jamois *et al.* suggested **a fourth hypothesis that contributes the higher pressure values to the osmotic pressure**, that is, the additional pressure required to partially or totally filtrate the solution through the pores, such that only water is intruded.[93] They demonstrated that in the case of complete filtration, the osmotic pressure can be written following the van 't Hoff law:

$$\prod = icRT \qquad \text{(Equation 4)}$$

With: $\prod$, osmotic pressure (in Pa)

i, coefficient corresponding to the number of ions in a salt (for instance i = 2 for NaCl which will dissociate into one Na^+ and one Cl^-)

c, molarity

R, perfect gas constant

T, temperature (in K)

The authors studied the energetic behaviors of various "ZIF-8−aqueous solution" systems, in addition to the "ZIF-8−water" system for comparison. The intrusion−extrusion experiments were carried out at variable temperatures (303-343 K), using different concentrations of NaCl, NaI, and

$CaCl_2$, in addition to 1 M LiCl and NaBr aqueous solutions and LiI and CsCl aqueous solutions of 0.75 M and 0.86 M in concentration.[93] The van 't Hoff law, however, is only valid till a limit concentration in the case of $CaCl_2$, above which the intrusion and extrusion pressures seem to increase more quickly with concentration than what is predicted by the law. However, based on this study, only iodide ions are capable of entering the pores. According to the authors, this can be explained by the very specific affinity of iodide ions to hydrophobic surfaces.[93]

Interestingly, the work published by Arletti *et al.*, which was performed after the study of Michelin-Jamois *et al.*, disclaim the osmotic pressure hypothesis suggested by the latter team, as Arletti *et al.* proved the presence of both water molecules and $MgCl_2$ constituent ions in the intruded solution, with the concentration of the confined liquid increasing compared to that of the bulk solution.[105]

Moreover, in a very recent study, Fraux *et al*. investigated, using molecular dynamic simulations, the properties of the LiCl aqueous solution when confined in the ZIF-8 nanopores during intrusion−extrusion experiments.[111] Their results demonstrate that Li^+, Cl^- and water molecules enter the porosity but only Cl anions undergo a desolvation mechanism during intrusion into the ZIF-8 pores. Furthermore, the ion solvation shells are restricted to specific preferential locations in the porosity, which is due to interactions with the imidazolate linker.[111] The authors also note that the relatively small kinetic radius of lithium ions (2.1 Å) allows them to fit in smaller spaces.[111] However, chloride ions and water molecules are more polarizable than lithium, and interact more strongly with the aromatic linkers, which favors a highly organized arrangement.[111]

Ortiz *et al.* also studied the energetic behavior of ZIF-71 using KCl 1 and 4 M (saturated) aqueous electrolyte solutions.[96] At low KCl concentration (1 M), the LHS behaves as a shock-absorber, which is similar to the energetic behavior encountered with the "ZIF-71−water" system.[96] With the saturated KCl aqueous solution, however, the LHS displays bumper behavior and the ZIF-71 framework collapses. We note that with ZIF-8, regardless of the concentration of the KCl solution, the system behaves as a shock-absorber (spring according to our definition). This probably indicates that KCl is more corrosive to the ZIF-71 framework than to ZIF-8 and highlights the influence of the nature of the linker, which may be more important than that of the topology.

In conclusion, compared to the cases where water is used as a non-wetting liquid, an increase in the intrusion pressure associated with the use of aqueous electrolyte solutions as non-wetting liquids in intrusion−extrusion experiments has always been observed and highlighted in the case of both MOF- and zeosil-based LHSs. Several explanations for this trend have been proposed. They mainly include the higher liquid-vapor interfacial tensions of aqueous electrolyte solutions compared to water and the electrostatic repulsion between ions, which contributes to a higher transport resistant force. Furthermore, the increase in the applied pressure during intrusion may be the additional force needed to break the solvation bonds that are initially formed around the ions of the non-wetting

liquid in the bulk solution. Moreover, for all aqueous electrolyte solutions, the intrusion pressure increases with the increase in the salt concentration. However, for different aqueous electrolyte solutions of the same concentration, higher intrusion pressures can be obtained for the cations of smaller ionic radius and higher hydrodynamic diameter. In addition, using aqueous electrolyte solutions as non-wetting liquids may also lead to a change in the energetic behavior of the LHS. Finally, even in the cases of weakly hydrophilic porous materials, which exhibit no intrusion step with water, intrusion may occur in the presence of aqueous electrolyte solutions. It must also be taken into account that a very high intrusion pressure value is undesired for practical applications of the LHSs. For instance, the intrusion pressure value required for vehicle bumpers is in the 30-60 MPa range.[23] In this regard, the choice of the combination of the non-wetting liquid and lyophobic porous material should be finely established so that the value of intrusion pressure obtained remains in the order of magnitude that is suitable for the corresponding application, while enabling the storage/absorption of a large amount of energy.

VI. Intrusion−Extrusion Experiments Using Other Non-Wetting Liquids

In addition to water and aqueous electrolyte solutions, other non-wetting liquids have also been used during intrusion−extrusion experiments in ZIF-8. For instance, Sun *et al.* employed different alcohol-water solution mixtures in order to follow up on the variations in the intrusion pressure and the size of the pore apertures of ZIF-8 when subjected to moderate pressures (in the order of several to tens of MPa) during intrusion−extrusion experiments carried out over 40 consecutive cycles.[94] In their work, the authors used mixtures of water and ethylene glycol (C_2), glycerol (C_3), erythritol (C_4), and xylitol (C_5) (mainly at 10 wt% in alcohol) and compare the data obtained from the corresponding alcohol-water intrusion−extrusion experiments to those obtained using only water as a non-wetting liquid. Their results show that in the case of "pure" water, a slight decrease in the intrusion pressure from 25 to 24 MPa is detected and can be linked to a slight loss of reproducibility of the mechanism, due to the reversible swing of the imidazolate linkers and the consequent gate opening mechanism in ZIF-8. However, in the case of the C_3-C_5 alcohol-water mixtures (involving glycerol, erythritol, xylitol and water), in the first cycle, the intrusion pressure increases compared to the case of water. This can be explained by the higher energy required so that the water molecules can dissociate themselves from the alcohol-water clusters (by breaking down the hydrogen bonds between them) and enter the ZIF-8 pores.[94] Consequently, the C_3-C_5 alcohol molecules serve as intrusion inhibitors in the first cycle (leading to an increase in the intrusion pressure).

Nevertheless, under the effect of consecutive multicycle loading, a decrease in intrusion pressure is observed, however, only with the glycerol-water mixture. Similar to the case of "pure" water, this phenomenon is ascribed to the presence of water molecules confined in the porosity, which leads to the famous gate opening mechanism and expansion of the ZIF-8 pore apertures. Therefore, the glycerol molecules act as intrusion promoters upon consecutive multicycle loading.[94] As for the case of the erythritol-, and xylitol-water mixtures, the large size of the alcohol molecules inhibits their intrusion into the porosity even after gate opening and the intrusion pressure does not decrease after several intrusion−extrusion cycles. Finally, due to its smaller molecular size, ethylene glycol can be accommodated inside the ZIF-8 pores without deforming the pore apertures and, thus, only acts as an intrusion promoter, facilitating the intrusion of water molecules into the ZIF-8 pores at lower intrusion pressures.[94] In the case of "pure" water and the glycerol-water solution mixture, the post-intruded ZIF-8 samples were left to rest during 24 hours before carrying out a second set of 40 intrusion−extrusion cycles. The obtained results reveal that the gate opening mechanism in ZIF-8 is reversible and the size of the pore aperture decreases (intrusion pressure increases) back in the first cycle, whereas multicycle loading again leads to framework distortion (intrusion pressure decreases). Finally, increasing the displacement rate from 5 to 50 mm min^{-1} (100 times increase), leads to almost identical $P-V$ curves for the "ZIF-8−10 wt% glycerol (C3)-water" system. According to the authors, this can be explained by the fact that the gate opening mechanism in ZIF-8 occurs gradually upon low-rate liquid intrusion (5 mm min^{-1}) and requires a continuous application of pressure.[94]

It is important to note that, during intrusion−extrusion experiments in ZIF-8, even though compared to the "pure" water case, the glycerol-, xylitol- and erythritol-water mixtures lead to higher intrusion pressures in the first cycle and during multicycle loading,[94] respectively, nonetheless, the attained elevated intrusion pressure values are lower compared to those registered using KCl, LiCl, and NaCl aqueous solutions of concentrations ranging between 1-4 M.[73] Furthermore, the intrusion−extrusion curves are superimposable even after 40 consecutive intrusion−extrusion cycles using alcohol-water mixtures,[94] whereas using LiCl and NaCl 4 M aqueous solutions, partial bumper behavior is observed in the first cycle.[73] This bumper behavior is linked to the presence of non-wetting liquid molecules in the porosity at reduced pressure, which is due to their relatively high binding energies to the imidazolate linker, or in other words, to the strong host-guest interactions.[73] Thus, alcohol-water mixtures can serve as alternatives to aqueous electrolyte solutions, when the aim is to increase the intrusion pressure. Moreover, the host-guest interactions can be diminished when using alcohols of molecular size that does not allow them to enter the porosity.

Therefore, similar to aqueous electrolyte solutions, alcohol-water mixtures can lead to increased intrusion pressures during intrusion−extrusion experiments. The key, however, is to employ alcohols of a molecular size that is much larger than that of the pore opening of the porous solid material, in order to sustain the intrusion-inhibition effect. On the other hand, the pore aperture should not expand upon multicycle loading (due to a gate opening phenomenon), so as not to induce the decrease of the intrusion pressure. In other words, the porous solid component of the LHS must display high rigidity. Finally, varying the nature of the non-wetting liquid allows tuning the energetic behavior of the LHS.

VII. **Conclusions**

In this bibliographic study, we discussed intrusion−extrusion experiments that have been performed on LHSs that are based on variable types of solid porous materials and non-wetting liquids. Zeosils and MOFs are among the most extensively studied materials in the energetic field, even though the energetic performances of mesoporous silica materials have also been investigated. The obtained results reveal that MOFs, characterized by higher microporous volumes compared to zeosils provide higher intruded volumes during intrusion−extrusion experiments. Moreover, in all cases, the intrusion pressure is increased with the use of aqueous electrolyte solutions as non-wetting liquids and with increasing concentrations of these solutions, where LiCl aqueous solution leads to higher intrusion pressure values compared to NaCl and KCl. Alcohol-water mixtures, based on alcohols of large molecular diameters, are also proven to enhance the intrusion pressure, however, to a lower extent compared to aqueous electrolyte solutions. We note that in this work we use water, KCl 4 M and LiCl 20 M aqueous solutions as non-wetting liquids. Indeed, the concentrations of both aqueous electrolyte solutions correspond to their maximum solubility at room temperature. This implies the presence of less water molecules that could interact with defects in the ZIF materials, if any are present, and which can favor an irreversible phenomenon during intrusion−extrusion experiments. Such highly concentrated aqueous solutions may also be intruded even in hydrophilic materials, which, ideally, would not display an intrusion step when water is used as the non-wetting liquid. Furthermore, it was shown that upon increasing the concentration of the LiCl aqueous solution, the energetic behavior of some zeosil-based LHSs can be modified from bumper to shock-absorber.[102]

This bibliographic study also shows that exploring the energetic behaviors of ZIF materials of topologies that have not been previously investigated, such as LTA and MER, can lead to promising results. It would be also interesting to go further with studying the effects of other parameters on the energetic behaviors of the ZIF-based LHSs during intrusion−extrusion experiments. Among these

parameters can be the susbstitution on the imidazolate linker, in addition to extremely large pore apertures (10- and 12-membered ring pore apertures).

References

1. Eroshenko, V. Heterogeneous Energy Accumulation or Dissipation Structure, Methods for Using Such Structure and Associated Apparatus. June 13, 1996.

2. Eroshenko, V. A., Unusual Properties of One Complex Thermodynamic System. *Dopov. Akad. Nauk Ukr. RSR, Ser. A: Fiz.-Tekh. Mat. Nauki* **1990,** *10*, 77-80.

3. Soulard, M.; Patarin, J.; Eroshenko, V.; Regis, R., Molecular Spring or Bumper: A New Application for Hydrophobic Zeolitic Materials. *Stud. Surf. Sci. Catal.* **2004,** *154B*, 1830-1837.

4. Eroshenko, V. A.; Grosu, Y. G., Thermomechanical and thermophysical properties of repulsive clathrates. *J. Appl. Mech. Tech. Phys.* **2013,** *54*, 798-808.

5. Soulard, M.; Patarin, J., Mechanics: Nanoporous Solids as Molecular Springs, Shock Absorbers and Bumpers. In *Nanomaterials and Nanochemistry, Part V: Applications of Naqnomaterials*, Lahami, M.; C.Bréchignac; Houdy, P., Eds. Springer, Berlin: 2007; pp 684-693.

6. Zhao, J.; Culligan, P. J.; Germaine, J. T.; Chen, X., Experimental Study on Energy Dissipation of Electrolytes in Nanopores. *Langmuir* **2009,** *25*, 12687-12696.

7. Perez-Ramirez, J.; Christensen, C. H.; Egeblad, K.; Christensen, C. H.; Groen, J. C., Hierarchical Zeolites: Enhanced Utilisation of Microporous Crystals in Catalysis by Advances in Materials Design. *Chem. Soc. Rev.* **2008,** *37*, 2530-2542.

8. Mofarahi, M.; Gholipour, F., Gas Adsorption Separation of CO_2/CH_4 System Using Zeolite 5A. *Microporous Mesoporous Mater.* **2014,** *200*, 1-10.

9. El Hanache, L.; Lebeau, B.; Nouali, H.; Toufaily, J.; Hamieh, T.; Daou, T. J., Performance of Surfactant-Modified *BEA-Type Zeolite Nanosponges for the Removal of Nitrate in Contaminated Water: Effect of the External Surface. *J. Hazard. Mater.* **2019,** *364*, 206-217.

10. Weckhuysen, B. M.; Yu, J., Recent Advances in Zeolite Chemistry and Catalysis. *Chem. Soc. Rev.* **2015,** *44*, 7022-7024.

11. El Hanache, L.; Sundermann, L.; Lebeau, B.; Toufaily, J.; Hamieh, T.; Daou, T. J., Surfactant-Modified MFI-Type Nanozeolites: Super-Adsorbents for Nitrate Removal from Contaminated Water. *Microporous and Mesoporous Mater.* **2019,** *283*, 1-13.

12. Eroshenko, V.; Regis, R.-C.; Soulard, M.; Patarin, J., Energetics: A New Field of Applications for Hydrophobic Zeolites. *J. Am. Chem. Soc.* **2001,** *123*, 8129-8130.

13. Eroshenko, V.; Regis, R.-C.; Soulard, M.; Patarin, J., The Heterogeneous Systems "Water-Hydrophobic Zeolites": New Molecular Springs. *C. R. Phys.* **2002,** *3*, 111-119.

14. Tzanis, L.; Trzpit, M.; Soulard, M.; Patarin, J., Energetic Performances of Channel and Cage-Type Zeosils. *J. Phys. Chem. C* **2012,** *116*, 20389-20395.

15. Trzpit, M.; Rigolet, S.; Paillaud, J.-L.; Marichal, C.; Soulard, M.; Patarin, J., Pure Silica Chabazite Molecular Spring: A Structural Study on Water Intrusion-Extrusion Processes. *J. Phys. Chem. B* **2008,** *112*, 7257-7266.

16. Trzpit, M.; Soulard, M.; Patarin, J., The Pure Silica Chabazite: a High Volume Molecular Spring at Low Pressure for Energy Storage. *Chem. Lett.* **2007,** *36*, 980-981.

17. Tzanis, L.; Trzpit, M.; Soulard, M.; Patarin, J., High Pressure Water Intrusion Investigation of Pure Silica 1D Channel AFI, MTW and TON-Type Zeolites. *Microporous Mesoporous Mater.* **2011,** *146*, 119-126.

18. Saada, M. A.; Soulard, M.; Marler, B.; Gies, H.; Patarin, J., High-Pressure Water Intrusion Investigation of Pure Silica RUB-41 and S-SOD Zeolite Materials. *J. Phys. Chem. C* **2011,** *115*, 425-430.

19. Ryzhikov, A.; Khay, I.; Nouali, H.; Daou, T. J.; Patarin, J., Energetic Performances of Pure Silica STF and MTT-Type Zeolites Under High Pressure Water Intrusion. *RSC Adv.* **2014,** *4*, 37655-37661.

20. Tzanis, L.; Trzpit, M.; Soulard, M.; Patarin, J., Energetic Performances of STT-Type Zeosil: Influence of the Nature of the Mineralizing Agent Used for the Synthesis. *J. Phys. Chem. C* **2012,** *116*, 4802-4808.

21. Ryzhikov, A.; Ronchi, L.; Nouali, H.; Daou, T. J.; Paillaud, J.-L.; Patarin, J., High-Pressure Intrusion-Extrusion of Water and Electrolyte Solutions in Pure-Silica LTA Zeolite. *J. Phys. Chem. C* **2015,** *119*, 28319-28325.

22. Ievtushenko, O. V.; Eroshenko, V. A.; Grosu, Y. G.; Nedelec, J.-M.; Grolier, J.-P. E., Evolution of the Energetic Characteristics of {Silicalite-1 + Water} Repulsive Clathrates in a Wide Temperature Range. *Phys. Chem. Chem. Phys.* **2013,** *15*, 4451-4457.

23. Rodriguez, J.; Beurroies, I.; Loiseau, T.; Denoyel, R.; Llewellyn, P. L., The Direct Heat Measurement of Mechanical Energy Storage Metal-Organic Frameworks. *Angew. Chem., Int. Ed.* **2015,** *54*, 4626-4630.

24. Gokulakrishnan, N.; Parmentier, J.; Trzpit, M.; Vonna, L.; Paillaud, J. L.; Soulard, M., Intrusion/Extrusion of Water into Organic Grafted SBA-15 Silica Materials for Energy Storage. *J. Nanosci. Nanotechnol.* **2013,** *13*, 2847-2852.

25. Guillemot, L.; Galarneau, A.; Vigier, G.; Abensur, T.; Charlaix, E., New Device to Measure Dynamic Intrusion/Extrusion Cycles of Lyophobic Heterogeneous Systems. *Rev. Sci. Instrum.* **2012,** *83*, 105105/1-105105/7.

26. Ryzhikov, A.; Daou, T. J.; Nouali, H.; Patarin, J.; Ouwehand, J.; Clerick, S.; De Canck, E.; Van Der Voort, P.; Martens, J. A., Periodic Mesoporous Organosilicas as Porous Matrix for Heterogeneous Lyophobic Systems. *Microporous Mesoporous Mater.* **2018,** *260*, 166-171.

27. Pillot, M.; Lebeau, B.; Nouali, H.; Daou, T. J.; Patarin, J.; Ryzhikov, A., High Pressure Intrusion of Water and LiCl Aqueous Solutions in Hydrophobic KIT-6 Mesoporous Silica: Influence of the Grafted Group Nature. *Microporous Mesoporous Mater.* **2019,** *280*, 248-255.

28. Trzpit, M.; Soulard, M.; Patarin, J., Water Intrusion in Mesoporous Silicalite-1: An Increase of the Stored Energy. *Microporous Mesoporous Mater.* **2008,** *117*, 627-634.

29. Yaghi, O. M.; O'Keeffe, M.; Ockwig, N. W.; Chae, H. K.; Eddaoudi, M.; Kim, J., Reticular Synthesis and the Design of New Materials. *Nature* **2003,** *423*, 705-714.

30. Awala, H.; Gilson, J.-P.; Retoux, R.; Boullay, P.; Goupil, J.-M.; Valtchev, V.; Mintova, S., Template-Free Nanosized Faujasite-Type Zeolites. *Nat. Mater.* **2015,** *14*, 447-451.

31. Furukawa, H.; Cordova, K. E.; O'Keeffe, M.; Yaghi, O. M., The Chemistry and Applications of Metal-Organic Frameworks. *Science* **2013,** *341*, 974.

32. Kong, X.; Deng, H.; Yan, F.; Kim, J.; Swisher, J. A.; Smit, B.; Yaghi, O. M.; Reimer, J. A., Mapping of Functional Groups in Metal-Organic Frameworks. *Science* **2013,** *341*, 882-885.

33. Furukawa, H.; Ko, N.; Go, Y. B.; Aratani, N.; Choi, S. B.; Choi, E.; Yazaydin, A. O.; Snurr, R. Q.; O'Keeffe, M.; Kim, J.; Yaghi, O. M., Ultrahigh Porosity in Metal-Organic Frameworks. *Science* **2010,** *329*, 424-428.

34. Moussa, Z.; Hmadeh, M.; Abiad, M. G.; Dib, O. H.; Patra, D., Encapsulation of Curcumin in Cyclodextrin-Metal Organic Frameworks: Dissociation of Loaded CD-MOFs Enhances Stability of Curcumin. *Food Chem.* **2016,** *212*, 485-494.

35. Dhakshinamoorthy, A.; Opanasenko, M.; Cejka, J.; Garcia, H., Metal Organic Frameworks as Heterogeneous Catalysts for the Production of Fine Chemicals. *Catal. Sci. Technol.* **2013,** *3*, 2509-2540.

36. Cadiau, A.; Adil, K.; Bhatt, P. M.; Belmabkhout, Y.; Eddaoudi, M., A Metal-Organic Framework-Based Splitter for Separating Propylene from Propane. *Science* **2016,** *353*, 137-140.

37. Mortada, B.; Matar, T. A.; Sakaya, A.; Atallah, H.; Kara Ali, Z.; Karam, P.; Hmadeh, M., Postmetalated Zirconium Metal Organic Frameworks as a Highly Potent Bactericide. *Inorg. Chem.* **2017,** *56*, 4740-4745.

38. Stock, N.; Biswas, S., Synthesis of Metal-Organic Frameworks (MOFs): Routes to Various MOF Topologies, Morphologies, and Composites. *Chem. Rev.* **2012,** *112*, 933-969.

39. Paseta, L.; Potier, G.; Sorribas, S.; Coronas, J., Solventless Synthesis of MOFs at High Pressure. *ACS Sustainable Chem. Eng.* **2016,** *4*, 3780-3785.

40. Leng, K.; Sun, Y.; Li, X.; Sun, S.; Xu, W., Rapid Synthesis of Metal-Organic Frameworks MIL-101(Cr) Without the Addition of Solvent and Hydrofluoric Acid. *Cryst. Growth Des.* **2016,** *16*, 1168-1171.

41. Choi, E.-Y.; Park, K.; Yang, C.-M.; Kim, H.; Son, J.-H.; Lee, S. W.; Lee, Y. H.; Min, D.; Kwon, Y.-U., Benzene-Templated Hydrothermal Synthesis of Metal-Organic Frameworks with Selective Sorption Properties. *Chem. - Eur. J.* **2004,** *10*, 5535-5540.

42. Ferey, G., Hybrid Porous Solids: Past, Present, Future. *Chem. Soc. Rev.* **2008,** *37*, 191-214.

43. Shekhah, O.; Liu, J.; Fischer, R. A.; Woell, C., MOF Thin Films: Existing and Future Applications. *Chem. Soc. Rev.* **2011,** *40*, 1081-1106.

44. Lan, X.; Zhang, H.; Bai, P.; Guo, X., Metal Organic Frameworks for Adsorptive Removal of Hydrochloride from Dilute Aqueous Solution. *Microporous Mesoporous Mater.* **2016,** *231*, 40-46.

45. Rueff, J.-M.; Perez, O.; Caignaert, V.; Hix, G.; Berchel, M.; Quentel, F.; Jaffrès, P.-A., Silver-Based Hybrid Materials from meta- or para-Phosphonobenzoic Acid: Influence of the Topology on Silver Release in Water. *Inorg. Chem.* **2015,** *54*, 2152-2159.

46. Fateeva, A.; Chater, P. A.; Ireland, C. P.; Tahir, A. A.; Khimyak, Y. Z.; Wiper, P. V.; Darwent, J. R.; Rosseinsky, M. J., A Water-Stable Porphyrin-Based Metal-Organic Framework Active for Visible-Light Photocatalysis. *Angew. Chem., Int. Ed.* **2012,** *51*, 7440-7444.

47. Jeazet, B. H.; Koschine, T.; Staudt, C.; Raetzke, K.; Janiak, C., Correlation of Gas Permeability in a Metal-Organic Framework MIL-101(Cr)–Polysulfone Mixed-Matrix Membrane with Free Volume Measurements by Positron Annihilation Lifetime Spectroscopy (PALS). *Membranes* **2013,** *3*.

48. Hafizovic Cavka, J.; Jakobsen, S.; Olsbye, U.; Guillou, N.; Lamberti, C.; Bordiga, S.; Lillerud, K. P., A New Zirconium Inorganic Building Brick Forming Metal Organic Frameworks with Exceptional Stability. *J. Am. Chem. Soc.* **2008,** *130*, 13850-13851.

49. Ghosh, P.; Kim, K. C.; Snurr, R. Q., Modeling Water and Ammonia Adsorption in Hydrophobic Metal-Organic Frameworks: Single Components and Mixtures. *J. Phys. Chem. C* **2014,** *118*, 1102-1110.

50. Wade, C. R.; Corrales-Sanchez, T.; Narayan, T. C.; Dinca, M., Postsynthetic Tuning of Hydrophilicity in Pyrazolate MOFs to Modulate Water Adsorption Properties. *Energy Environ. Sci.* **2013,** *6*, 2172-2177.

51. Trickett, C. A.; Gagnon, K. J.; Lee, S.; Gandara, F.; Buergi, H.-B.; Yaghi, O. M., Definitive Molecular Level Characterization of Defects in UiO-66 Crystals. *Angew. Chem., Int. Ed.* **2015,** *54*, 11162-11167.

52. Ghosh, P.; Colon, Y. J.; Snurr, R. Q., Water Adsorption in UiO-66: the Importance of Defects. *Chem. Commun.* **2014,** *50*, 11329-11331.

53. Wang, Z.; Cohen, S. M., Postsynthetic Modification of Metal-Organic Frameworks. *Chem. Soc. Rev.* **2009,** *38*, 1315-1329.

54. Nguyen, J. G.; Cohen, S. M., Moisture-Resistant and Superhydrophobic Metal-Organic Frameworks Obtained via Postsynthetic Modification. *J. Am. Chem. Soc.* **2010,** *132*, 4560-4561.

55. Banerjee, R.; Furukawa, H.; Britt, D.; Knobler, C.; O'Keeffe, M.; Yaghi, O. M., Control of Pore Size and Functionality in Isoreticular Zeolitic Imidazolate Frameworks and Their Carbon Dioxide Selective Capture Properties. *J. Am. Chem. Soc.* **2009,** *131*, 3875-3877.

56. Li, Y.; Zhou, K.; He, M.; Yao, J., Synthesis of ZIF-8 and ZIF-67 Using Mixed-Base and Their Dye Adsorption. *Microporous Mesoporous Mater.* **2016,** *234*, 287-292.

57. Phan, A.; Doonan, C. J.; Uribe-Romo, F. J.; Knobler, C. B.; O'Keeffe, M.; Yaghi, O. M., Synthesis, Structure, and Carbon Dioxide Capture Properties of Zeolitic Imidazolate Frameworks. *Acc. Chem. Res.* **2010,** *43*, 58-67.

58. Park, K. S.; Ni, Z.; Cote, A. P.; Choi, J. Y.; Huang, R.; Uribe-Romo, F. J.; Chae, H. K.; O'Keeffe, M.; Yaghi, O. M., Exceptional Chemical and Thermal Stability of Zeolitic Imidazolate Frameworks. *Proc. Natl. Acad. Sci. U. S. A.* **2006,** *103*, 10186-10191.

59. Murillo, B.; Zornoza, B.; de la Iglesia, O.; Tellez, C.; Coronas, J., Chemocatalysis of Sugars to Produce Lactic Acid Derivatives on Zeolitic Imidazolate Frameworks. *J. Catal.* **2016,** *334*, 60-67.

60. Ortiz, G.; Nouali, H.; Marichal, C.; Chaplais, G.; Patarin, J., Energetic Performances of the Metal–Organic Framework ZIF-8 Obtained Using High Pressure Water Intrusion–Extrusion Experiments. *Phys. Chem. Chem. Phys.* **2013,** *15*, 4888-4891.

61. Liu, B.; Smit, B., Molecular Simulation Studies of Separation of CO2/N2, CO2/CH4, and CH4/N2 by ZIFs. *J. Phys. Chem. C* **2010,** *114*, 8515-8522.

62. Timon, V.; Senent, M. L.; Hochlaf, M., Structural Single and Multiple Molecular Adsorption of CO_2 and H_2O in Zeolitic Imidazolate Framework (ZIF) Crystals. *Microporous Mesoporous Mater.* **2015,** *218*, 33-41.

63. Tian, Y.-Q.; Yao, S.-Y.; Gu, D.; Cui, K.-H.; Guo, D.-W.; Zhang, G.; Chen, Z.-X.; Zhao, D.-Y., Cadmium Imidazolate Frameworks with Polymorphism, High Thermal Stability, and a Large Surface Area. *Chem. - Eur. J.* **2010,** *16*, 1137-1141.

64. Khay, I.; Chaplais, G.; Nouali, H.; Ortiz, G.; Marichal, C.; Patarin, J., Assessment of the Energetic Performances of Various ZIFs with SOD or RHO Topology using High Pressure Water Intrusion-Extrusion Experiments. *Dalton Trans.* **2016,** *45*, 4392-4400.

65. Kuesgens, P.; Rose, M.; Senkovska, I.; Froede, H.; Henschel, A.; Siegle, S.; Kaskel, S., Characterization of Metal-Organic Frameworks by Water Adsorption. *Microporous Mesoporous Mater.* **2009,** *120*, 325-330.

66. Ban, Y.; Li, Y.; Peng, Y.; Jin, H.; Jiao, W.; Liu, X.; Yang, W., Metal-Substituted Zeolitic Imidazolate Framework ZIF-108: Gas-Sorption and Membrane-Separation Properties. *Chem. - Eur. J.* **2014,** *20*, 11402-11409.

67. Gao, M.; Wang, J.; Rong, Z.; Shi, Q.; Dong, J., A Combined Experimental-Computational Investigation on Water Adsorption in Various ZIFs with the SOD and RHO Topologies. *RSC Adv.* **2018,** *8*, 39627-39634.

68. Cousin Saint Remi, J.; Remy, T.; Van Hunskerken, V.; van de Perre, S.; Duerinck, T.; Maes, M.; De Vos, D.; Gobechiya, E.; Kirschhock, C. E. A.; Baron, G. V.; Denayer, J. F. M., Biobutanol Separation with the Metal-Organic Framework ZIF-8. *ChemSusChem* **2011,** *4*, 1074-1077.

69. Banerjee, R.; Phan, A.; Wang, B.; Knobler, C.; Furukawa, H.; O'Keeffe, M.; Yaghi, O. M., High-Throughput Synthesis of Zeolitic Imidazolate Frameworks and Application to CO_2 Capture. *Science* **2008,** *319*, 939-943.

70. Shi, Q.; Xu, W.-J.; Huang, R.-K.; Zhang, W.-X.; Li, Y.; Wang, P.; Shi, F.-N.; Li, L.; Li, J.; Dong, J., Zeolite CAN and AFI-Type Zeolitic Imidazolate Frameworks with Large 12-Membered Ring Pore Openings Synthesized Using Bulky Amides as Structure-Directing Agents. *J. Am. Chem. Soc.* **2016,** *138*, 16232-16235.

71. Perez-Pellitero, J.; Amrouche, H.; Siperstein, F. R.; Pirngruber, G.; Nieto-Draghi, C.; Chaplais, G.; Simon-Masseron, A.; Bazer-Bachi, D.; Peralta, D.; Bats, N., Adsorption of CO_2, CH_4, and N_2 on Zeolitic Imidazolate Frameworks: Experiments and Simulations. *Chem. - Eur. J.* **2010,** *16*, 1560-1571.

72. Fraux, G.; Boutin, A.; Fuchs, A. H.; Coudert, F.-X., Structure, Dynamics and Thermodynamics of Intruded Electrolytes in ZIF-8. *J. Phys. Chem. C* **2019**, Ahead of Print.

73. Ortiz, G.; Nouali, H.; Marichal, C.; Chaplais, G.; Patarin, J., Versatile Energetic Behavior of ZIF-8 upon High Pressure Intrusion-Extrusion of Aqueous Electrolyte Solutions. *J. Phys. Chem. C* **2014,** *118*, 7321-7328.

74. Serre, C.; Bourrelly, S.; Vimont, A.; Ramsahye, N. A.; Maurin, G.; Llewellyn, P. L.; Daturi, M.; Filinchuk, Y.; Leynaud, O.; Barnes, P.; Ferey, G., An Explanation for the Very Large Breathing Effect of a Metal-Organic Framework during CO_2 Adsorption. *Adv. Mater.* **2007,** *19*, 2246-2251.

75. Boutin, A.; Springuel-Huet, M.-A.; Nossov, A.; Gedeon, A.; Loiseau, T.; Volkringer, C.; Ferey, G.; Coudert, F.-X.; Fuchs, A. H., Breathing Transitions in MIL-53(Al) Metal-Organic Framework Upon Xenon Adsorption. *Angew. Chem., Int. Ed.* **2009,** *48*, 8314-8317, S8314/1-S8314/8.

76. Neimark, A. V.; Coudert, F.-X.; Triguero, C.; Boutin, A.; Fuchs, A. H.; Beurroies, I.; Denoyel, R., Structural Transitions in MIL-53 (Cr): View from Outside and Inside. *Langmuir* **2011,** *27*, 4734-4741.

77. Beurroies, I.; Boulhout, M.; Llewellyn, P. L.; Kuchta, B.; Ferey, G.; Serre, C.; Denoyel, R., Using Pressure to Provoke the Structural Transition of Metal-Organic Frameworks. *Angew. Chem., Int. Ed.* **2010,** *49*, 7526-7529.

78. Yot, P. G.; Boudene, Z.; Macia, J.; Granier, D.; Vanduyfhuys, L.; Verstraelen, T.; Van Speybroeck, V.; Devic, T.; Serre, C.; Ferey, G.; Stock, N.; Maurin, G., Metal-Organic Frameworks as Potential Shock Absorbers: the Case of the Highly Flexible MIL-53(Al). *Chem. Commun.* **2014,** *50*, 9462-9464.

79. Yot, P. G.; Vanduyfhuys, L.; Alvarez, E.; Rodriguez, J.; Itie, J.-P.; Fabry, P.; Guillou, N.; Devic, T.; Beurroies, I.; Llewellyn, P. L.; Van Speybroeck, V.; Serre, C.; Maurin, G., Mechanical Energy Storage Performance of an Aluminum Fumarate Metal-Organic Framework. *Chem. Sci.* **2016,** *7*, 446-450.

80. Yot, P. G.; Ma, Q.; Haines, J.; Yang, Q.; Ghoufi, A.; Devic, T.; Serre, C.; Dmitriev, V.; Ferey, G.; Zhong, C.; Maurin, G., Large Breathing of the MOF MIL-47(VIV) Under Mechanical Pressure: a Joint Experimental-Modelling Exploration. *Chem. Sci.* **2012,** *3*, 1100-1104.

81. Peralta, D.; Chaplais, G.; Paillaud, J.-L.; Simon-Masseron, A.; Barthelet, K.; Pirngruber, G. D., The Separation of Xylene Isomers by ZIF-8: A Demonstration of the Extraordinary Flexibility of the ZIF-8 Framework. *Microporous Mesoporous Mater.* **2013,** *173*, 1-5.

82. Khay, I.; Chaplais, G.; Nouali, H.; Marichal, C.; Patarin, J., Water Intrusion-Extrusion Experiments in ZIF-8: Impacts of the Shape and Particle Size on the Energetic Performances. *RSC Adv.* **2015,** *5*, 31514-31518.

83. Sheng, L.; Yang, F.; Wang, C.; Yu, J.; Zhang, L.; Pan, Y., Comparison of the Hydrothermal Stability of ZIF-8 Nanocrystals and Polycrystalline Membranes Derived from Zinc Salt Variations. *Mater. Lett.* **2017,** *197*, 184-187.

84. Zhang, H.; Zhao, M.; Yang, Y.; Lin, Y. S., Hydrolysis and Condensation of ZIF-8 in Water. *Microporous Mesoporous Mater.* **2019,** *288*, 109568.

85. Liu, X.; Li, Y.; Ban, Y.; Peng, Y.; Jin, H.; Bux, H.; Xu, L.; Caro, J.; Yang, W., Improvement of Hydrothermal Stability of Zeolitic Imidazolate Frameworks. *Chem. Commun.* **2013,** *49*, 9140-9142.

86. Wang, H.; Jian, M.; Qi, Z.; Li, Y.; Liu, R.; Qu, J.; Zhang, X., Specific Anion Effects on the Stability of Zeolitic Imidazolate Framework-8 in Aqueous Solution. *Microporous Mesoporous Mater.* **2018,** *259*, 171-177.

87. Zhang, H.; Liu, D.; Yao, Y.; Zhang, B.; Lin, Y. S., Stability of ZIF-8 Membranes and Crystalline Powders in Water at Room Temperature. *J. Membr. Sci.* **2015,** *485*, 103-111.

88. Zhang, H.; Zhao, M.; Yang, Y.; Lin, Y. S., Hydrolysis and Condensation of ZIF-8 in Water. *Microporous Mesoporous Mater.* **2019**.

89. Im, J.; Yim, N.; Kim, J.; Vogt, T.; Lee, Y., High-Pressure Chemistry of a Zeolitic Imidazolate Framework Compound in the Presence of Different Fluids. *J. Am. Chem. Soc.* **2016,** *138*, 11477-11480.

90. Moggach, S. A.; Bennett, T. D.; Cheetham, A. K., The Effect of Pressure on ZIF-8: Increasing Pore Size with Pressure and the Formation of a High-Pressure Phase at 1.47 GPa. *Angew. Chem., Int. Ed.* **2009,** *48*, 7087-7089.

91. Ortiz, A. U.; Freitas, A. P.; Boutin, A.; Fuchs, A. H.; Coudert, F.-X., What Makes Zeolitic Imidazolate Frameworks Hydrophobic or Hydrophilic? The Impact of Geometry and Functionalization on Water Adsorption. *Phys. Chem. Chem. Phys.* **2014,** *16*, 9940-9949.

92. Grosu, Y.; Renaudin, G.; Eroshenko, V.; Nedelec, J. M.; Grolier, J. P. E., Synergetic Effect of Temperature and Pressure on Energetic and Structural Characteristics of {ZIF-8 + Water} Molecular Spring. *Nanoscale* **2015,** *7*, 8803-8810.

93. Michelin-Jamois, M.; Picard, C.; Vigier, G.; Charlaix, E., Giant Osmotic Pressure in the Forced Wetting of Hydrophobic Nanopores. *Phys. Rev. Lett.* **2015,** *115*, 036101/1-036101/4.

94. Sun, Y.; Li, Y.; Tan, J.-C., Framework Flexibility of ZIF-8 Under Liquid Intrusion: Discovering Time-Dependent Mechanical Response and Structural Relaxation. *Phys. Chem. Chem. Phys.* **2018,** *20*, 10108-10113.

95. Humplik, T.; Raj, R.; Maroo, S. C.; Laoui, T.; Wang, E. N., Framework Water Capacity and Infiltration Pressure of MFI Zeolites. *Microporous Mesoporous Mater.* **2014,** *190*, 84-91.

96. Ortiz, G.; Nouali, H.; Marichal, C.; Chaplais, G.; Patarin, J., Energetic Performances of "ZIF-71-Aqueous Solution" Systems: A Perfect Shock-Absorber with Water. *J. Phys. Chem. C* **2014,** *118*, 21316-21322.

97. Grosu, Y.; Li, M.; Peng, Y.-L.; Luo, D.; Li, D.; Faik, A.; Nedelec, J.-M.; Grolier, J.-P., A Highly Stable Nonhysteretic {Cu2(tebpz) MOF+water} Molecular Spring. *ChemPhysChem* **2016,** *17*, 3359-3364.

98. Wang, J.-H.; Li, M.; Li, D., An Exceptionally Stable and Water-Resistant Metal-Organic Framework with Hydrophobic Nanospaces for Extracting Aromatic Pollutants from Water. *Chem. - Eur. J.* **2014,** *20*, 12004-12008.

99. Soulard, M.; Patarin, J. Procédé pour le Stockage d'Energie Haute Pression par Solvatation. WO2012164218A1, 2012.

100. Tzanis, L.; Nouali, H.; Daou, T. J.; Soulard, M.; Patarin, J., Influence of the Aqueous Medium on the Energetic Performances of Silicalite-1. *Mater. Lett.* **2014,** *115*, 229-232.

101. Khay, I.; Daou, T. J.; Nouali, H.; Ryzhikov, A.; Rigolet, S.; Patarin, J., High Pressure Intrusion-Extrusion of LiCl Aqueous Solutions in Silicalite-1 Zeolite: Influence on Energetic Performances. *J. Phys. Chem. C* **2014,** *118*, 3935-3941.

102. Ryzhikov, A.; Khay, I.; Nouali, H.; Daou, T. J.; Patarin, J., Drastic Change of the Intrusion-Extrusion Behavior of Electrolyte Solutions in Pure Silica *BEA-Type Zeolite. *Phys. Chem. Chem. Phys.* **2014,** *16*, 17893-17899.

103. Ronchi, L.; Ryzhikov, A.; Nouali, H.; Daou, T. J.; Patarin, J., Influence of LiCl Aqueous Solution Concentration on the Energetic Performances of Pure Silica Chabazite. *New J. Chem.* **2017,** *41*, 2586-2592.

104. Ryzhikov, A.; Khay, I.; Nouali, H.; Daou, T. J.; Patarin, J., High Pressure Intrusion-Extrusion of Electrolyte Solutions in Aluminosilicate FAU and *BEA-Type Zeolites. *Microporous Mesoporous Mater.* **2016,** *221*, 1-7.

105. Arletti, R.; Ronchi, L.; Quartieri, S.; Vezzalini, G.; Ryzhikov, A.; Nouali, H.; Daou, T. J.; Patarin, J., Intrusion-Extrusion Experiments of $MgCl_2$ Aqueous Solution in Pure Silica Ferrierite:

Evidence of the Nature of Intruded Liquid by in Situ High Pressure Synchrotron X-ray Powder Diffraction. *Microporous Mesoporous Mater.* **2016,** *235*, 253-260.

106. Ronchi, L.; Ryzhikov, A.; Nouali, H.; Daou, T. J.; Patarin, J., Energetic Performances of Pure-Silica DDR Zeolite by High-Pressure Intrusion-Extrusion of Electrolyte Aqueous Solutions: A Shock-Absorber with Huge Absorbed Energy. *J. Phys. Chem. C* **2018,** *122*, 2726-2733.

107. Eroshenko, V., Interfacial Energy in the Lyophobic Systems and Thermomolecular Energetics: Challange to All Physico-Chemists. **2014**, 212-229.

108. Michelin-Jamois, M.; Picard, C.; Charlaix, E.; Vigier, G., Osmotic Pressure Effects upon Intrusion of Liquid Electrolytes Inside Hydrophobic MOFs. *arXiv.org, e-Print Arch., Phys.* **2014**, 1-4, arXiv:1404.5318v1 [physics.chem-ph].

109. Calleja, G.; Botas, J. A.; Martos, C.; Orcajo, G.; Villajos, J. A., Effect of Ion-Exchange Modification on Hydrogen and Carbon Dioxide Adsorption Behaviour of RhoZMOF Material. *Adsorpt. Sci. Technol.* **2012,** *30*, 793-806.

110. Liu, L.; Chen, X.; Lu, W.; Han, A.; Qiao, Y., Infiltration of Electrolytes in Molecular-Sized Nanopores. *Phys. Rev. Lett.* **2009,** *102*, 184501-184504.

111. Fraux, G.; Boutin, A.; Fuchs, A. H.; Coudert, F.-X., Structure, Dynamics, and Thermodynamics of Intruded Electrolytes in ZIF-8. *J. Phys. Chem. C* **2019,** *123*, 15589-15598.

Chapter 2: Experimental Part

In order to determine their structural, textural and physicochemical (morphology, chemical composition, etc…) properties, the MOF materials were fully characterized following their synthesis. Herein, we describe the basic principle and specific conditions of the main characterization techniques employed in this work, i.e. X-ray diffraction (XRD), thermogravimetric analyses (TGA), nitrogen adsorption-desorption measurements, and scanning electron microscopy (SEM). Furthermore, the energetic behaviors of the MOF materials were studied using high pressure intrusion–extrusion experiments. In the aim of studying the influence of the high pressure and/or the nature of non-wetting liquid associated with intrusion–extrusion experiments on their structure and physicochemical properties, similar to their corresponding parent materials, the post-intruded MOF materials were also characterized using the same techniques mentioned above (XRD, TGA, nitrogen adsorption-desorption measurements, and SEM). In some cases, liquid state proton nuclear magnetic resonance (^{1}H NMR) spectroscopy was used to determine the composition of the MOF materials. Moreover, inductively coupled plasma optical emission spectroscopy (ICP-OES) was employed in some of the cases where LiCl 20 M aqueous electrolyte solution was used as a non-wetting liquid, in order to verify the presence of Li^+ cations in the porosity after intrusion–extrusion experiments. Associated with TGA, ICP was also used to determine the chemical composition of the post-intruded ZIF materials. Finally, mercury porosimetry experiments were only employed when needed, in the aim of determining the separate effect of pressure on the structure of the MOF material.

I. Structural Analysis: X-Ray Diffraction (XRD)

Crystals consist of orderly repeated structural motifs, which may consist of atoms, molecules or ions. The crystal structure can be described by the unit cell, which is the smallest repeated imaginary unit in the crystal from which the entire crystal structure can be constructed by using only translations.[1] Crystals can be also viewed as consisting of imaginary planes of atoms, molecules or ions separated by a characteristic interplanar distance d. In 1912, Max von Laue and coworkers discovered that crystalline substances can diffract X-rays of wavelengths similar to the spacing between planes in a certain set of planes in a crystal lattice.[2] Since then, the process of diffraction of X-rays from planes in crystalline materials has been widely developed and nowadays, X-ray diffraction is one of the most common characterization techniques applied, for example, to the fields of material's chemistry, pharmaceuticals, forensic science, and geological applications.[2]

XRD is a powerful and nondestructive technique used to determine the structure of a crystalline material i.e. the unit cell parameters, space group, number and positions of the atoms in the unit cell.[2-3] It also allows the identification of phases, which is enabled by referring to the available databases. In addition to this, XRD provides information on parameters such as the average crystal size and crystal defects.[2] In XRD analysis, a monochromatic beam of X-rays interacts with a crystalline sample to produce constructive interference when the conditions satisfy Bragg's law (Equation 1), i. e. when the path length difference (equal to 2 d sin θ) is in the same order of magnitude as the wavelength (λ) of the incident beam of X-rays.[2]

$$2\,d\sin\theta = n\lambda \qquad \text{(Equation 1)}$$

With: n, an integer

λ, wavelength of the beam of X-rays

d, interpalanar spacing for a particular set of planes

θ, diffraction angle.

XRD analysis of a powder crystalline compound yields a diffractogram (an XRD pattern) with diffraction peaks, whose positions are characteristic of the set of planes diffracting the incident radiation, whereas their intensities are related to the nature and distribution of the atoms within the lattice.[2]

An X-ray diffractometer consists of three basic elements: an X-ray tube, a sample holder, and an X-ray detector. X-rays are generated in a cathode ray tube by heating a filament, thus, producing electrons that are accelerated toward a target material (Cu, Cr, Mo, Fe). If the energy of the electrons hitting the target material is large enough, then they will cause the ejection of the material's inner shell electrons. Outer shell electrons then move to fill in for the ejected electrons, with the excess of energy being emitted in the form of characteristic X-ray spectra.[2] These spectra consist of several components that depend on the type of electron transition that took place in the target material, with the most common being the K_α and K_β radiations.[2] The produced spectra are then filtered (using foils or crystal monochrometers) to produce monochromatic X-ray radiation needed for diffraction. The resulting X-rays are directed toward the sample and when Bragg's law is satisfied, constructive interference occurs and a peak in intensity appears. Finally, the detector records and processes the X-ray signal and converts it to a count rate.[2]

In this work, the powder XRD (PXRD) patterns of the parent and post-intruded MOF samples were essentially recorded in the transmission mode on a STOE STADI-P diffractometer equipped with a curved germanium (111) primary monochromator, and a linear position-sensitive detector (6° in 2θ) using CuKα_1 radiation (λ = 1.5406 Å). Measurements were usually achieved for 2θ angle values in the 3-50° or in the 5-50° (in the case of SOD-type ZIF materials) ranges, with a step of 0.04° in 2θ.

In the case where only a small amount of powder was available for XRD analysis, the sample was spread on a glass or a zero-background silicon plate (to minimize the amorphous signals generated by the glass sample holder) and the XRD patterns were recorded on a X'Pert Pro diffractometer operating with $CuK\alpha_{1,2}$ radiation (λ = 1.5418 Å) equipped with an X'Celerator real-time multiple strip detector (active length = 2.122° 2θ). In this case also, measurements were generally achieved for 2θ angle values in the 3-50° or in the 5-50° (for SOD-type ZIF materials) ranges, with a step of 0.0167° in 2θ.

In order to verify that the targeted structure is obtained after synthesis and to determine the phase purity of both the parent and post-intruded samples, when the MOF material is of known structure, the powdered MOF sample was analyzed with XRD and the obtained pattern was compared to that simulated from the corresponding single crystal structure. The unit cell parameters were then directly refined using the DICVOL04 algorithm of the WinXPOW software (STOE Powder Diffraction Software Package WinXPOW, version 2.20; STOE & Cie GmbH: Darmstadt, 2006) and were later compared to the unit cell parameters obtained for the corresponding single crystal structure.[4] On the other hand, in the case of a MOF material of an unknown structure, the XRD pattern obtained for the corresponding powdered sample was first indexed and then refined (using the same approach previously described), in order to determine the unit cell parameters whenever possible.[4] In parallel, investigations were conducted using the ICDD (International Center for Diffraction Data) database as well as a laboratory-specific database, including the crystallographic data of potential candidates collected from the COD (Crystallography Open Database), CCDC (Cambridge Crystallographic Data Centre) databases or directly from the published data.

II. Determination of the Morphology: Scanning Electron Microscopy (SEM)

Scanning Electron Microscopy is a technique that allows determining the morphology (size and shape) of the particles of a sample.[5] During this process, the electrons from an incident beam lose some of their energy while repeatedly colliding with the electrons of the constituent atoms of the target specimen (inelastic scattering).[5] As a result of these collisions, outer-shell electrons of the specimen constituent atoms are ejected and emitted from the specimen's surface. These are called secondary electrons, which are later accelerated and converted by the detector into an electric signal that is amplified. Consequently, an image of the specimen is obtained by displaying the intensity of the detected secondary electrons on a computer screen as a series of bright spots synchronized with the scan of the electron probe.

Sample preparation involves mounting the sample on a holder covered with a carbon tape i.e. a double-sided conductive adhesive that allows mounting the sample without the use of a liquid or a

colloidal adhesive. Since MOFs are non-conductive specimens, they do not allow the dissipation of beam electrons, which results in charging. Therefore, in the second step of the sample preparation process, the ZIF-type materials are coated with a thin layer of gold (15 nm) in order to minimize their surface charge. Coating also reduces the heating effects and, most importantly, enhances the electron emissions provided by the electrically conductive layer at the sample surface. In this work, coating was done using the magnetron sputtering method. Finally, a Philips XL 30 FEG microscope was used to scan the samples and produce the images. The beam of electrons used was of a voltage of 7 kV and the images were obtained at a magnification in the order of 20000-50000.

III. Chemical Composition

A. Determination of Chemical Composition and Thermal Stability: Thermogravimetric Analyses (TGA)

This technique allows measuring the changes in the mass of a sample that can occur while the latter is subjected to controlled increasing temperature.[6] TGA is carried out in a controlled gaseous atmosphere that can be either static (gas at reduced pressure) or dynamic (inert or reactive gas). The mass of the sample employed is usually in the 1-100 mg range and the sensitivity of the technique is limited by that of the balance, which may be as high as 0.1 µg. During TGA, the studied sample undergoes changes that are mainly accompanied with one or several mass losses. Examples of mass loss processes include: degradation and/or decomposition, vaporization (of bulk liquids or liquids adsorbed by the solid surface or in the porosity), sublimation, desorption of gases, etc. The result of a TG measurement is a TG curve that represents the evolution of the mass of the sample (usually displayed in mass percentage) as a function of time, or more commonly, as a function of temperature.

In this work, the thermal stability of the studied MOF materials was determined by referring to the temperature at which the degradation of the organic network begins. Indeed, TGA is efficient in indicating the presence/absence of solvent molecules (water and organic solvents), in addition to unreacted linker molecules that can be entrapped in the porosity of an inactivated/partially activated material following its synthesis, or in the post-intruded MOF material. Usually, below 200 °C, any observed mass loss is mainly attributed to the loss of physisorbed water and/or occluded molecules, whereas the degradation of the framework linkers occurs at temperatures higher than 200 °C. Consequently, the framework composition can be partially or fully determined/confirmed by referring to the TG curve, through the estimation of the amount of organic matter (that is part of the framework and that entrapped in the porosity) and, in some cases, water present in the studied material and by comparing the obtained values to the calculated/expected ones. Furthermore,

complementary analysis such as ^{1}H NMR spectroscopy can be also coupled to TGA, in the aim of determining/confirming the framework composition. The experimental mass loss corresponding to the degradation of the organic framework, P_3, is expressed in percentage and is calculated according to Equation 2.

$$P_3 = (P_2\text{-}P_1) / (100+P_1) * 100 \qquad \text{(Equation 2)}$$

With: P_1, mass loss (in %) calculated between room temperature and usually 200 °C and corresponding to the release of physisorbed or accommodated species

P_2, mass loss (in %) calculated between room temperature and usually 800 °C and corresponding to the release of physisorbed or accommodated species in addition to the framework degradation

P_3, mass loss (in %) usually calculated between 200 and 800 °C and allowing the determination of the framework composition.

P_i, mass loss (in %) defined by $P_i = (m_0\text{-}m_i)/m_0 *100$ where m_0 and m_i stand for the sample mass (in mg) at room temperature and at the end of a supposed phenomenon (e. g. release of solvent molecules, organic framework decomposition…), respectively

Generally, there is a fine correlation between the mass loss attributed to the degradation of the organic network and the composition of the MOF material. It should be noted, however, that exceptions have been encountered during this thesis work, as in the case of ZIF-8_Br, ZIF-8_Cl, ZIF-71, and ZIF-71_Br_2, where the assumed formation of gaseous $ZnBr_2$ and $ZnCl_2$ leads to experimental mass losses that are higher than those expected.[7-8] Consequently, the reliability of the technique is affected. Finally, the nature of the residues obtained during TGA can also reveal some information concerning the composition of the framework.

In this work, TGA were carried out on a TG Mettler Toledo STARe apparatus, under reconstituted air flow (20.5% O_2, 0.5 ppm of H_2O, and N_2), with a heating rate of 2 °C min^{-1} from 30 to 900 °C. 8-20 mg of the sample were employed in the analysis, which were placed in alumina crucibles. The STARe software was used to perform the experiments and, later, to exploit the data obtained.

B. Proton Nuclear Magnetic Resonance (^{1}H NMR) Spectroscopy

NMR spectroscopy involves the resonant absorption of radiofrequency radiation by a set of nuclei with a spin I ($I \neq 0$) exposed to an external magnetic field. The result is an NMR spectrum revealing a resonance signal for every nucleus characteristic of a surrounding electronic environment in the studied set of nuclei. Therefore, the positions of the resonance signals give information on the local environment of the corresponding nuclei in the sample,[9] whereas their intensities allow quantifying the species.

Herein, the identification and quantification (proportion) of occluded organic species and linker molecules is achieved for some MOF materials (e. g. ZIF-25, ZIF-71_Br_2, and ZIF-76) using liquid-state ^1H (I = 1/2) NMR spectroscopy. This technique is commonly applied for composition determination as the ^1H isotope is highly abundant and present in commonly used solvents and linkers. Moreover, the liquid-state analysis is fast and the sample preparation is easy, with only a small amount of sample required (less than 5 mg). Indeed, deuterated solvents are used in NMR spectroscopy analysis so as to prevent interference from the protons of the solvents.

In this work, the samples were prepared as follows. In a glass bottle, around 3 mg of the MOF material were digested (solubilized) in 1 mL of DCl (35 wt. % in D_2O) by sonication. The solution was then diluted by adding 1 mL of D_2O and sonicated again. 1 mL of the solution was transferred into the NMR tube for analysis. ^1H NMR spectra were recorded on a Bruker Avance II 400 MHz spectrometer.

C. Inductively Coupled Plasma Optical Emission Spectroscopy (ICP-OES)

This technique is used to detect certain elements that are suspected to be present in a sample, often as traces. It involves the presence of inductively coupled plasma, i.e. an ionization source that is capable of fully decomposing the sample into its constituent elements and transforming them into ions.[10] The inductively coupled plasma (ICP) is typically composed of argon gas and an induction coil that provides the energy needed to form the plasma.

In the case of ICP-OES, the plasma excites the atoms and ions that travel through it. When an atom or ion is excited, the electrons jump to higher energy levels. Upon relaxation, the electrons return back to their initial energy level (ground state), while emitting the excess of energy in the form of photons. The emitted photons possess wavelengths that are characteristic of the corresponding element. Some elements can have multiple electron excitations and relaxations and, thus, possess more than one characteristic wavelength.[10]

In this work, ICP-OES analysis was carried out in the aim of detecting the presence of Li^+ ions in the porosity of certain ZIF materials (ZIF-8, ZIF-71, and MAF-6) after intrusion–extrusion experiments with a LiCl 20 M aqueous solution. The analysis was carried out at the Centre Commun de Mesures-Université du Littoral Côte d'Opale, using a Thermo Model 6300DUO spectrometer. Sample preparation involved digesting around 50 mg of the post-intruded ZIF powder in a few milliliters (2-5 mL) of a strong acid (hydrofluoric or nitric acids). The obtained solution was diluted 10 times with ultrapure water and then filtered. The wavelength of the corresponding spectrometric lines that were used for the Li analysis was 670.784 nm.

In order to determine the chemical composition of the material obtained after LiCl 20 M aqueous solution intrusion–extrusion experiments, ICP analysis results are combined with those obtained from TGA. Indeed, ICP gives information on the amount of Li^+ ions present in the porosity (if any), whereas TGA indicates the mass of the entrapped water molecules. The chemical composition of a post-intruded ZIF-type material, expressed as $Zn(linker)_2 \cdot xLiCl \cdot yH_2O$, is calculated by referring to Equations 3 and 4.

$$P_{ATG} = ((m_{Li} + m_{Cl} + m_{ZIF}) / (m_{Li} + m_{Cl} + m_{ZIF} + m_{H2O})) * 100 \quad \text{(Equation 3)}$$

$$P_{ICP} = m_{Li} / (m_{Li} + m_{Cl} + m_{ZIF} + m_{H2O}) * 100 \quad \text{(Equation 4)}$$

With: P_{ATG}, mass percentage of the post-intruded sample remaining after the loss of water molecules entrapped in the porosity and obtained from TGA

P_{ICP}, the mass percentage of Li^+ ions detected in the porosity of the post-intruded ZIF material and obtained from ICP analysis

m_{Li}, m_{Cl}, m_{H2O}, and m_{ZIF} the masses of Li^+ ions, Cl^- ions, water, and the ZIF material, respectively.

By referring to Equations 3 and 4 and by dividing P_{ATG} by P_{ICP}:

$$P_{ATG} / P_{ICP} = (m_{Li} + m_{Cl} + m_{ZIF}) / m_{Li} \quad \text{(Equation 5)}$$

By developing and factorizing by m_{Li}, Equation 5 gives:

$$(P_{ATG} - P_{ICP}) * m_{Li} = P_{ICP} * m_{Cl} + P_{ICP} * m_{ZIF} \quad \text{(Equation 6)}$$

n_{Li}, n_{Cl}, n_{H2O} and n_{ZIF} correspond to the molar quantities of Li^+ ions, Cl^- ions, water, and the ZIF material, respectively, and the corresponding molar masses are M_{Li} (6.941 g mol^{-1}) M_{Cl} (35.453 g mol^{-1}), M_{H2O} (18.015 g mol^{-1}) and M_{ZIF}.

Since $n_{Cl} = n_{Li}$ then: $m_{Cl} = m_{Li} * (M_{Cl} / M_{Li})$.

By substituting m_{Cl} into Equation 6 and by expressing m_{Li} as a function of m_{ZIF}:

$$m_{Li} / m_{ZIF} = P_{ICP} / (P_{ATG} - P_{ICP} * (1 + M_{Cl} / M_{Li})) \quad \text{(Equation 7)}$$

Given that m_{Li} / m_{ZIF} equal also to $(n_{Li} * M_{Li}) / (n_{ZIF} * M_{ZIF})$ then from Equation 7:

$$\mathbf{x = n_{Li} / n_{ZIF} = P_{ICP} / (P_{ATG} - P_{ICP} * (1 + M_{Cl} / M_{Li})) * (M_{ZIF} / M_{Li})} \quad \text{(Equation 8)}$$

For determining y, which is equal to n_{H2O} / n_{ZIF}, from for example Equation 4, it can be demonstrated after conversion of the different masses into products of molar quantities by molar masses that:

$$\mathbf{y = ((x * (100 * M_{Li} - P_{ICP} * (M_{Li} + M_{Cl}))) - P_{ICP} * M_{ZIF}) / (P_{ICP} * M_{H2O})} \quad \text{(Equation 9)}$$

IV. **Textural Properties: N_2 Adsorption-Desorption Measurements at 77 K**

The study of the textural properties of the porous MOF materials, that is, the specific surface area and microporous volume was carried out using N_2 adsorption-desorption measurements. Briefly, in N_2 sorption measurements, molecular nitrogen (the adsorbate) is brought in contact with the solid material (the adsorbent), which results in a physisorption phenomenon (weak adsorbent-adsorbate interactions).[11] At an adsorption temperature below the critical temperature of the adsorbate, the sorption isotherm represents the variation of the gas uptake (volume of gas adsorbed per 1 gram of the adsorbent, expressed in $cm^3\ g^{-1}$ under Standard Temperature and Pressure (STP) conditions) as a function of the relative pressure of this gas (p/p^0), where p is the equilibrium pressure of the gas and p^0 is the saturation pressure at the adsorption temperature.

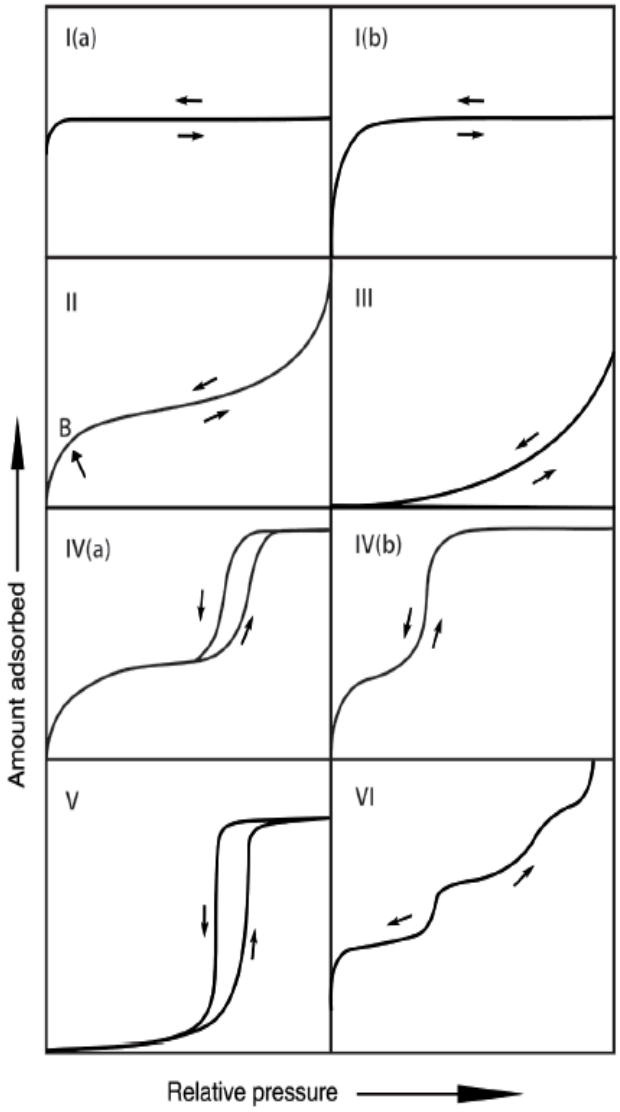

Figure 1. Classification of physisorption isotherms.[11]

The shape of the adsorption-desorption isotherm is characteristic of the studied adsorbent-adsorbate system. According to the IUPAC recommendations, there are six types of physisorption isotherms (Figure 1).[11]

Type I isotherms are characteristic of microporous materials (pore diameter < 2 nm). The isotherm is concave to the p/p^0 axis and the amount adsorbed approaches a limiting value that corresponds to saturation of the adsorbent. There are two sub-types of the Type I isotherm. Type Ia is characteristic of adsorbents having narrow micropores (< 1 nm in diameter), whereas, Type Ib is given by microporous materials having pore size distributions over a broader range (wider micropores and narrow mesopores).

Type II isotherms describe adsorption on macroporous (pore diameter 50-100 nm) or nonporous materials. The inflection point (denoted as B in Figure 1) is an indication of the conversion from the monolayer coverage (the small plateau) to the multilayer adsorption mode (continuous increase in the thickness of the layer with increasing p/p^0 values).

Similar to the Type II, Type III isotherms are also characteristic of macroporous or nonporous adsorbents. However, in this case the adsorbate-adsorbate interactions are much stronger than the adsorbent-adsorbate interactions, and the adsorbed molecules are clustered around the most favorable sites on the surface of the solid. Unlike Type II isotherms, Type III isotherms exhibit no inflection point, and, thus, no identifiable monolayer formation.

Generally, a mesoporous adsorbent (pore diameter 2-50 nm) displays a Type IV isotherm. This type is a variation of the Type II isotherm in the low p/p^0 range, but with a finite number of multilayers corresponding to the complete filling of the pores (indicated by a final saturation plateau at high p/p^0). In the multilayer range, pore condensation occurs. We note that pore condensation is the phenomenon whereby the gas condenses into a liquid-like phase at a pressure p less than the saturation pressure p^0 of the bulk liquid. This phenomenon occurs inside the pores, and is due to the strong adsorbate-adsorbate interactions in the confined pore space. There are two sub-types of the Type IV isotherm. For the Type IVa, capillary condensation is accompanied with a hysteresis (for nitrogen and argon adsorption at 77 and 87 K, respectively, in cylindrical pores wider than 4 nm), whereas, Type IVb isotherms are completely reversible and superimposable (that is characteristic of mesoporous adsorbents having pores of smaller width).

In the low relative pressure range, the shape of the Type V isotherm is very similar to that of Type III, which can be attributed to the weak adsorbent-adsorbate interactions. Molecular clustering, followed by pore filling occur at higher relative pressure values.

Finally, the reversible stepwise Type VI isotherm reveals a step-by-step multilayer adsorption on a highly uniform nonporous adsorbent.

In this work, the textural properties (BET surface area and microporous volume) of the parent (non-intruded) MOF materials were determined from N_2 adsorption-desorption measurements. Later, the post-intruded MOF materials were also analyzed and the obtained results were compared to those of the corresponding parent material in order to investigate the framework stability under the effect of high pressure and/or the non-wetting liquid during intrusion–extrusion experiments. In most of the cases, type I isotherms were obtained.

Herein, all the nitrogen adsorption-desorption isotherms were performed at 77 K using a Micromeritics ASAP 2420 apparatus. Prior to the adsorption measurements, the samples were degassed at elevated temperatures under secondary vacuum. We note that in this work, the temperatures used to degas the MOF materials range between 125 and 250 °C and are dependent of the MOF type and more especially of their thermal stability and the nature of guest molecules to-be desorbed. Table 1 shows a list of the different MOF materials analyzed with N_2 sorption measurements in this work, in addition to the corresponding topology and degassing temperature used. We also note that in all cases, the degassing duration is 12 hours.

Table 1. Degassing conditions prior to nitrogen sorption measurements at 77 K for MOF samples before and after intrusion-extrusion experiments.

MOF sample	**Zeolite Topology**	**Degassing temperature (°C)**	**Degassing time (h)**
ZIF-8	SOD	200	12
ZIF-8_Cl	SOD	200	12
ZIF-8_Br	SOD	200	12
MAF-6	RHO	150	12
ZIF-71	RHO	150	12
ZIF-25	RHO	150	12
ZIF-71_Br_2	RHO	150	12
ZIF-76	LTA	250	12
AFI-Zn$(im)_2$	AFI	125	12
CAN-Zn$(im)_2$	CAN	125	12
MIL-101(Cr)	MTN	200	12

The degassing step is necessary to activate the pores by desorbing gases and evaporating volatile molecules that may be entrapped, thus, making the pores accessible for the adsorption of N_2 molecules. The software MicroActive was used to perform the N_2 sorption measurements and to treat the obtained adsorption-desorption isotherms. The specific surface area (S_{BET}) was calculated according to the criteria given in the literature, which are described below, and by using the Brunauer-Emmett-Teller (BET) method (Equation 10).[12-13] The first step in determining the BET surface area is transforming the adsorption isotherm into a linear BET plot by drawing $1/V[(p^0/p)$ -

1] versus p/p^0. The constant C is first calculated from the slope of the obtained straight line, whereas, the specific monolayer capacity V_m is calculated from the y-intercept.

$$\frac{1}{V\,(p^0/p\text{-}1)} = \frac{1}{V_m C} + \frac{C\text{-}1}{V_m C}\,(p/p^0) \qquad \text{(Equation 10)}$$

In the case of nonporous, mesoporous, and macroporous adsorbents (displaying perfect Type II or Type IVa isotherms), the range of linearity in the BET plot is usually within the 0.05-0.35 p/p^0 range. This partial pressure range is chosen assuming that monolayer formation occurs within it, and works well for materials that do not contain micropores.[11,12] For the majority of MOF materials (exhibiting only micropores), however, the smaller micropores are completely filled with N_2 at pressures below the standard BET range. In addition, several partial pressure ranges on the BET plot may yield a linear region, which can be confusing and may also lead to subjective values of the monolayer capacity and, consequently, of the BET surface area.[12] In order to avoid this uncertainty, three major criteria should be respected: (1) according to Rouquerol *et al.*,[14] $V(p^0\text{-}p)$ should be traced versus p/p^0, and the relative pressure range selected should correspond to a continuous increase of $V(p^0\text{-}p)$, (2) the value of the C parameter must be positive (a negative intercept on the y-axis of the BET plot indicates that one is outside the appropriate p/p^0 range), (3) the BET plot in the selected p/p^0 range should exhibit a high correlation coefficient (> 0.9999).

The microporous volume (V_μ) was determined according to the *t*-plot method.[14] This method allows drawing a *t*-plot relating the adsorbed quantity of the adsorbate ($cm^3\ g^{-1}$) to the thickness of the adsorbate layer (Å) at different p/p^0 values. The point of intersection of the *t*-plot with the y-axis (y-intercept) permits the determination of the uptake corresponding to the formation of a monolayer and, thus, V_μ. The thickness of the layer is obtained from the continuous adsorption of N_2 on a reference nonporous solid of same chemical nature as the studied porous adsorbent at different p/p^0 values. However, since in many cases it is difficult to find a reference, the Harkins-Jura equation can be applied to the determination of the thickness values t (Equation 11).[15]

$$t = [13.99 / (0.034 - \log(p/p^0))]^{1/2} \qquad \text{(Equation 11)}$$

V. Stability under Pressure: Mercury Porosimetry

Mercury is a non-wetting liquid that cannot spontaneously penetrate pores by capillary action and, thus, must be forced into the pores by the application of an external pressure.[16] Mercury porosimetry analysis corresponds to the progressive intrusion of mercury into a porous structure under controlled pressure. The obtained volume versus pressure data allows the determination of the

cumulative pore volume and the pore size distributions by referring to the Laplace-Washburn equation (Equation 12).[17]

$$P_c = 2\,\gamma\,|\cos\theta\,|/\,r \qquad \text{(Equation 12)}$$

With: Pc, capillary pressure

γ, liquid-vapor surface tension (485 mN/m for mercury)

r, radius of the pores

θ, contact angle between the liquid and the solid (θ =130° for mercury)

However, only macroporous materials or those of high mesoporous volumes can be investigated using mercury porosimetry, as mercury cannot penetrate inside micropores or small mesopores.[16] Nevertheless, mercury porosimetry experiments have been applied to the study of the energetic performance of flexible MIL-53-type microporous materials by provoking structural transitions in them *via*, what we use to call, compression-decompression phenomena (Chapter 1, sub-section IV. A.).[18]

It is important to note that in this work, we only carried out once a mercury porosimetry experiment on the ZIF-71 material. This experiment was performed in the aim of proving the absence of a separate effect of pressure on the phase transformation phenomenon evidenced for ZIF-71 during the LiCl 20 M intrusion–extrusion experiments.

The mercury porosimetry experiment was carried out using a Micromeritics mercury porosimeter (Model Autopore IV, in the 0.2 to 400 MPa pressure range).

VI. **Intrusion–Extrusion Experiments**

In the field of energetic applications, the intrusion–extrusion of non-wetting liquids (such as water or aqueous electrolyte solutions) into lyophobic porous materials has been widely investigated by our team.[19,20] In this work, we carried out the intrusion–extrusion of water, KCl 4 M, and LiCl 20 M aqueous solutions in activated MOF/ZIF samples using a Micromeritics mercury porosimeter (Model Autopore IV). The intrusion–extrusion experiments were run using the Autopore IV 9500 VI.06 software. The intrusion–extrusion experiments were realized at room temperature, usually over three intrusion–extrusion cycles and up to a pressure of 350 MPa. In some cases (i.e. for the "MAF-6−water", "MAF-6−" and "ZIF-71−LiCl 20 M aqueous solution" systems), complementary experiments were performed, which involved only one intrusion–extrusion cycle up to maximum pressures of 25, 47, 70, 90, 185, and 215 MPa. The experimental setup involves a "porous material–non-wetting liquid" system, referred to as a Lyophobic Heterogeneous System (LHS), incorporated within a 2 mL polypropylene cylinder that is sealed with a mobile piston, therefore, forming the intrusion–extrusion cell. This cell, in turn, is introduced into a glass penetrometer, which is filled

with mercury. The increasing applied pressure during intrusion–extrusion experiments forces mercury out of the capillary tube of the penetrometer, which, in turn pushes the mobile piston of the cell and, consequently, provokes the forced intrusion of the non-wetting liquid molecules into the pores of the studied material. As the amount of mercury decreases inside the capillary, so does the capacitance. The decrease in capacitance is, thus, proportional to the volume of mercury leaving the capillary at each pressure value.

As previously developed in Chapter 1 section I, during intrusion–extrusion experiments, three different energetic behaviors may be observed: bumper, spring, or shock-absorber (Figure 2). The energetic behavior of the LHS depends on the nature of both of its components: the porous solid material and non-wetting liquid.

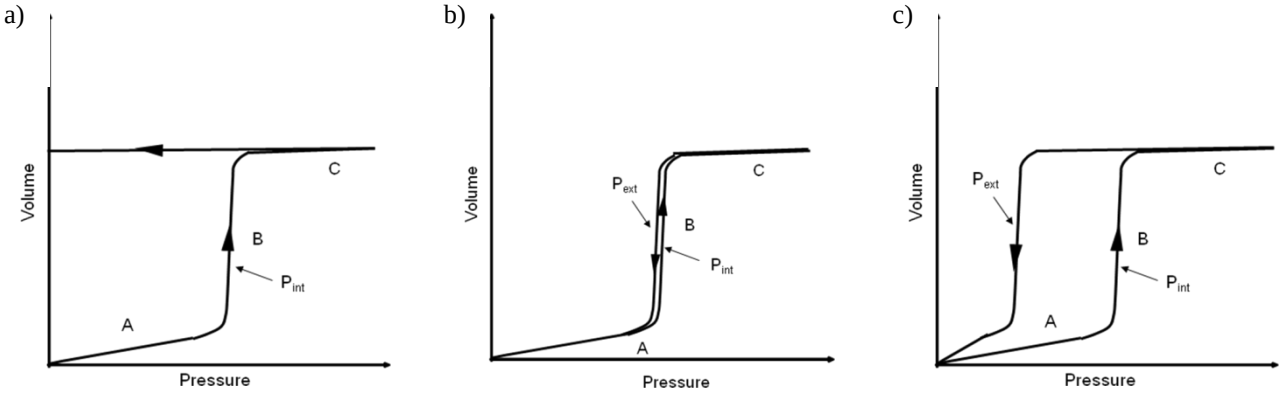

Figure 2. Schematic P–V diagrams demonstrating (a) bumper, (b) spring and (c) shock-absorber behaviors of LHSs.

From the P–V diagrams shown in Figure 2, several experimental parameters can be extracted such as the pressure at which the liquid enters the pores, namely the intrusion pressure (P_{int}), the pressure at which the liquid is expelled from the pores, namely the extrusion pressure (P_{ext}), the corresponding intruded volume (V_{int}) and the extruded volume (V_{ext}). For a better accuracy, we define $V_{int} = V_{inte} - V_{intb}$ and $V_{ext} = V_{extb} - V_{exte}$, where V_{intb} and V_{inte} refer to the volume values at the beginning and end of the intrusion step, respectively. Similarly, V_{extb} and V_{exte} correspond to the volume values at the beginning and end of the extrusion step, respectively. The values P_{int} and P_{ext} correspond to the pressure at half total volume variation. The pressure is expressed in MPa, and the volume variation in milliliter per gram (mL g^{-1}) of the activated MOF/ZIF material. From those experimental parameters it is possible to calculate the energy E that can be, depending on the behavior, the stored, restored, or absorbed energy (E_s, E_r, or E_a, respectively), expressed in J g^{-1}, according to Equation 13.

$$E = \int_{V_0}^{V_f} P.dV \qquad \text{(Equation 13)}$$

With: $E = E_s$ and $P = P_{int}$ (spring and shock-absorber behaviors)

Or $E = E_a$ and $P = P_{int}$ (bumper behavior)

Or $E = E_r$ and $P = P_{ext}$ (spring and shock-absorber behaviors)

V_0, volume at the beginning of the volume variation step

V_f, volume at the end of the volume variation step

A simplified method that we have been using allows calculating the energy value from the product of pressure and volume (Equation 14).

$$E = P*V \qquad \text{(Equation 14)}$$

With: E = Es, P = Pint and V = Vint

Or E = Ea, P = Pint and V = Vint

Or E = Er, P = Pext and V = Vext

Finally, the energetic yield (in %) is calculated from the ratio of E_s to E_r multiplied by 100 (Equation 15).

$$\text{Energetic yield} = E_r/E_s*100 \qquad \text{(Equation 15)}$$

Considering the experimental *P–V* diagrams reported in this work, it is worth noting that the 0-5 MPa pressure range is not shown on the pressure-axis, since the corresponding volume variation is only due to the compression of the "ZIF–non-wetting liquid" system and to the filling of the interparticular porosity.[20]

As previously mentioned, it is the nature of both components of the LHS and how strongly/weakly they interact with each other that determines the resulting energetic behavior of the system. For instance, if the intruded liquid is retained in the pores at reduced pressures, the phenomenon is defined as irreversible, as the system only absorbs the supplied mechanical energy ($E = E_a$, expressed according to Equations 13 and/or 14) and is not capable of restoring it. On the pressure-volume (*P–V*) diagrams, **bumper** behavior is indicated by the absence of volume variation on the extrusion curve (Figure 2a).

We note that in some cases, the solid porous material may undergo an irreversible phase transition phenomenon during the intrusion step (accompanied with a partial or no intrusion of the non-wetting liquid into the porosity), which is usually attributed to the combined effect of the high pressure and non-wetting liquid. In such cases, the LHS is also defined as a bumper, as most of/all the applied mechanical energy is absorbed by the system during the irreversible phase transformation.

On the other hand, some systems can spontaneously react ($\Delta G < 0$) and decrease their solid/liquid interface ($\Delta\Omega < 0$) by completely expelling the liquid out of the pores. In this case, two possible phenomena are common. In the first phenomenon, extrusion of the non-wetting liquid occurs at an

extrusion pressure (P_{ext}) exactly equal to or close to the intrusion pressure (P_{int}). The stored energy is, thus, entirely, or almost entirely, restored, with an energy yield of 100 %, or slightly lower, and the system displays **spring** behavior that is indicated on the *P–V* diagrams from the overlap of the intrusion and extrusion curves or the formation of a small hysteresis (Figure 2b). In the second phenomenon, however, the mechanical energy stored in the form of interfacial energy is partially dissipated during the extrusion of the non-wetting liquid from the pores and, thus, the energy yield is significantly lower than 100 %. In this case, the P–V diagrams reveal that extrusion occurs at P_{ext} significantly lower than P_{int}, which results in the formation of a large hysteresis between the intrusion and extrusion curves (Figure 2c). The system, therefore, is defined as a **shock-absorber**.

Finally, we note that in the presence of a small hysteresis on the *P–V* diagrams, to avoid confusion, herein, the energetic behavior of the studied LHS is classified as shock-absorber or spring based on a complete extrusion of the non-wetting liquid from the porosity with an energy yield lower or equal to/higher than 80%, respectively.

References

1. Atkins, P. W., *Physical Chemistry*. Sixth edition ed.; Oxford University Press: Oxford, 2001.

2. Bunaciu, A. A.; Udristioiu, E. G.; Aboul-Enein, H. Y., X-Ray Diffraction: Instrumentation and Applications. *Crit. Rev. Anal. Chem.* **2015,** *45*, 289-299.

3. Cullity, B. D., *Elements of X-Ray Diffraction*. Addison-Wesley Pub. Co.: United States of America, 1956.

4. Boultif, A.; Louer, D., Powder Pattern Indexing with the Dichotomy Method. *J. Appl. Crystallogr.* **2004,** *37*, 724-731.

5. UI-Hamid, A., *A Beginners' Guide to Scanning Electron Microscopy* First edition ed.; Springer International Publishing: Switzerland, 2018.

6. Vyazovkin, S. Thermogravimetric Analysis 2012.

7. Mortada, B.; Chaplais, G.; Veremeienko, V.; Nouali, H.; Marichal, C.; Patarin, J., Energetic Performances of ZIF-8 Derivatives: Impact of the Substitution (Me, Cl, or Br) on Imidazolate Linker. *J. Phys. Chem. C* **2018,** *122*, 3846-3855.

8. Schweinefuss, M. E.; Springer, S.; Baburin, I. A.; Hikov, T.; Huber, K.; Leoni, S.; Wiebcke, M., Zeolitic Imidazolate Framework-71 Nanocrystals and a Novel SOD-Type Polymorph: Solution Mediated Phase Transformations, Phase Selection Via Coordination Modulation and a Density Functional Theory Derived Energy Landscape. *Dalton Trans.* **2014,** *43*, 3528-3536.

9. Lambert, J. B.; Mazzola, E. P.; Ridge, C., *Nuclear Magnetic Resonance Spectroscopy an Introduction to Principles, Applications, and Experimental Methods*. Second edition ed.; Wiley-Blackwell: United States of America, 2019.

10. Boss, C. B.; Fredeen, K. J., *Concepts, Instrumentation and Techniques in Inductively Coupled Plasma Optical Emission Spectrometry*. Second edition ed.; Perkin Elmer: United States of America, 1999.

11. Matthias, T.; Kaneko, A.; Neimark, A. V.; Olivier, J. P.; Rodriguez-Reinoso, F.; Rouquerol, J.; S.W. Sing, K., Physisorption of Gases, with Special Reference to the Evaluation of Surface area and Pore Size Distribution (IUPAC Technical Report). *Pure. Appl. Chem.* **2015,** *87*, 1051-1069.

12. Walton, K. S.; Snurr, R. Q., Applicability of the BET Method for Determining Surface Areas of Microporous Metal−Organic Frameworks. *J. Am. Chem. Soc.* **2007,** *129*, 8552-8556.

13. Rouquerol, J.; Llewellyn, P.; Rouquerol, F., Is the BET Equation Applicable to Microporous Adsorbents? *Stud. Surf. Sci. Catal.* **2007,** *160*, 49-56.

14. Rouquerol, J.; Rouquerol, F.; Llewellyn, P.; Maurin, G.; Sing, K. S. W., *Adsorption by Powders and Porous Solids: Principles, Methodology and Applications*. Second edition ed.; Elsevier Science: 2013.

15. Aligizaki, K., *Pore Structure of Cement-Based Materials: Testing Interpretation and Requirements*. First edition ed.; Spon: 2003.

16. Giesche, H., Mercury Porosimetry: A General (Practical) Overview. *Part. Part. Syst. Charact.* **2006,** *23*, 9-19.

17. Eroshenko, V. A.; Grosu, Y. G., Thermomechanical and thermophysical properties of repulsive clathrates. *J. Appl. Mech. Tech. Phys.* **2013,** *54*, 798-808.

18. Beurroies, I.; Boulhout, M.; Llewellyn, P. L.; Kuchta, B.; Ferey, G.; Serre, C.; Denoyel, R., Using Pressure to Provoke the Structural Transition of Metal-Organic Frameworks. *Angew. Chem., Int. Ed.* **2010,** *49*, 7526-7529.

19. Eroshenko, V.; Regis, R.-C.; Soulard, M.; Patarin, J., Energetics: A New Field of Applications for Hydrophobic Zeolites. *J. Am. Chem. Soc.* **2001,** *123*, 8129-8130.

20. Ortiz, G.; Nouali, H.; Marichal, C.; Chaplais, G.; Patarin, J., Energetic Performances of the Metal–Organic Framework ZIF-8 Obtained Using High Pressure Water Intrusion–Extrusion Experiments. *Phys. Chem. Chem. Phys.* **2013,** *15*, 4888-4891.

Chapter 3: Energetic Performances of ZIF-8 Derivatives: Impact of the Substitution (Me, Cl, or Br) on the Imidazolate Linker

In this chapter we aim at investigating the effect of both, the nature of the non-wetting liquid (water or aqueous electrolyte solutions) and the substituent borne by the imidazolate linker on the energetic behaviors of ZIF-8 derivatives during high-pressure intrusion−extrusion experiments. The first section is devoted to the description of the structure of ZIF-8 and two halogenated derivatives, i. e. ZIF-8_Cl and ZIF-8_Br. The second section is a summary of our first article (referred to as article 1), which deals with the materials' energetic performances (where ZIF-8 is named as ZIF-8_CH_3).[1] A copy of this article is provided afterwards. Finally, in Section III, additional comments are given in the light of recently published computational results concerning the intrusion of LiCl aqueous solution in ZIF-8.

I. ZIF-8 and its Halogenated Derivatives

A. Structures

Prior to this PhD work, two SOD-type materials, ZIF-8_Cl and ZIF-8_Br, were synthesized in the aim of studying the impact of the substitution on the imidazolate linker on the ZIFs' structural and adsorptive properties by comparing them to those of the well-known ZIF-8, also commercially labeled as Basolite® Z1200. These materials are constructed from Zn^{2+} cations bridged by imidazolate linkers that are substituted at the position 2 by a methyl (CH_3), chlorine (Cl), or bromine (Br) group/atom for ZIF-8, ZIF-8_Cl, and ZIF-8_Br, respectively. It is worthy to note that ZIF-8_Cl, and ZIF-8_Br are quite new variants of ZIF-8 as they were experimentally reported only once, where only the capacity of ZIF-8_Cl in the kinetic separation of propane and propene was evaluated.[2] Their structures were later elucidated, showing that the three ZIF materials are isoreticular, possessing a zeolitic SOD framework topology, with 4- and 6-membered ring pore apertures (Scheme 1).[3]

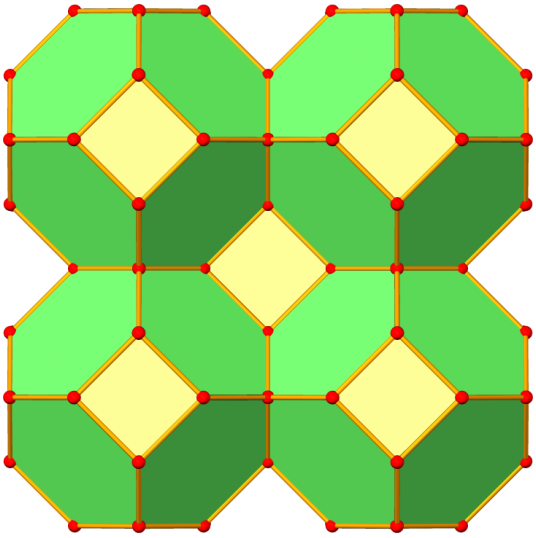

Scheme 1. Representation of the SOD topology of the ZIF-8 derivatives. In red, zinc cations. In yellow and green, the 4- and 6-membered ring pore apertures, respectively.

ZIF-8 and its derivatives crystallize in the cubic symmetry (space group *I*-43*m*), with the lattice constant $a \approx 17.01$,[4] 17.04,[3] and 17.08[3] Å for ZIF-8, ZIF-8_Cl, and ZIF-8_Br, respectively. The slight increase in the value of the lattice constant is related to the steric hindrance provided by the substituent on the imidazolate linker and which is more important for Br than for Cl and then CH_3. Another notable structural feature is the fact that the 2-chloroimidazolate (cim-2) and 2-bromoimidazolate (bim-2) linkers incorporated in the ZIF-8_Cl and ZIF-8_Br frameworks, respectively, are disordered. These linkers are indeed tilted around a fixed axis defined by the two nitrogen atoms. This results in two sets of atoms, with a site occupation factor of around 50 % for each set. Figures 1a and 1b represent the ZIF-8_Cl and ZIF-8_Br asymmetric units, whereas Figures 1c and 1d demonstrate the angles between the disordered (tilted) linkers in the two materials.

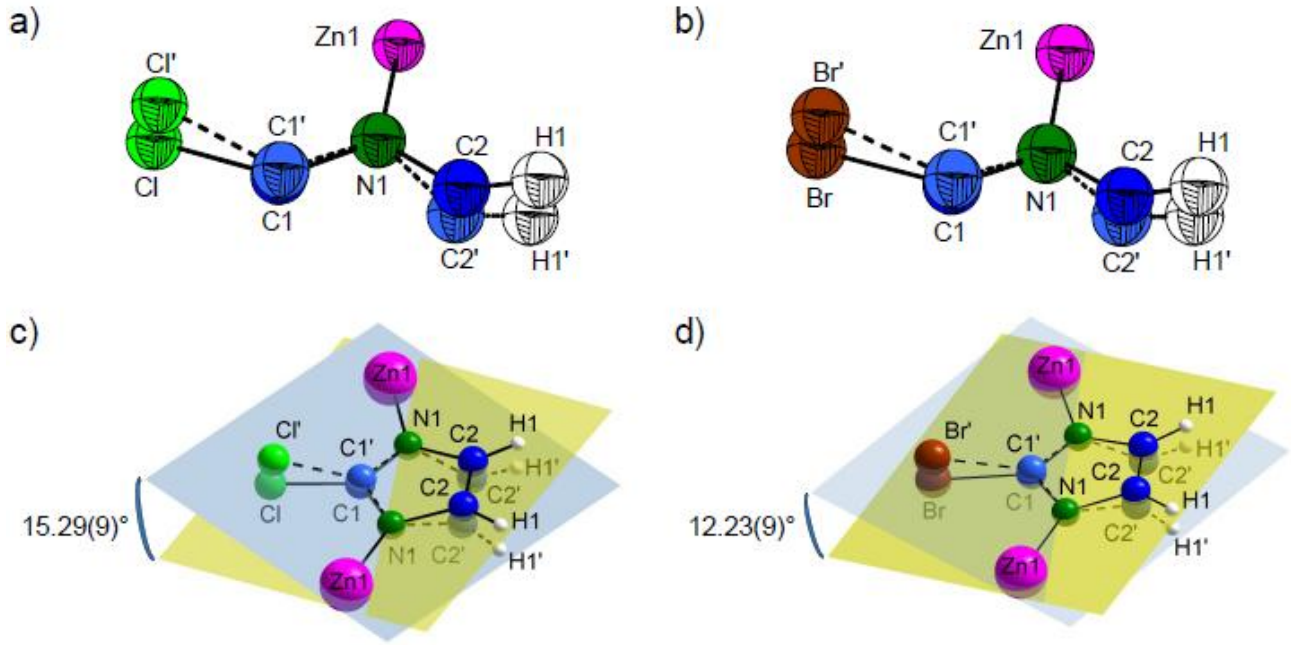

Figure 1. Asymmetric units of (a) ZIF-8_Cl and (b) ZIF-8_Br (50% of probability ellipsoid). Dihedral angles between the disordered imidazolate linkers of (c) ZIF-8_Cl and (d) ZIF-8_Br.[3]

B. Flexibility and Porosity

Remarkably, ZIF-8_Cl and more especially ZIF-8 are characterized by a framework flexibility, which is due to the swing of the imidazolate linkers under various stimuli. This phenomenon can be indicated from the profile of the N_2 sorption isotherms of both ZIF materials, where a step uptake is observed at a relative pressure around 0.005 (Figure 2b in attached article 1).[1] Previous and different studies have already highlighted this structural characteristic of ZIF-8. For example, Fairen-Jimenez *et al*. evidenced this peculiar phenomenon through a combined experimental-simulation study based on nitrogen sorption measurements combined with crystallographic data.[5] They assigned a step observed for relative pressure between 0.002 and 0.02 in the isotherm to the structural transition. Ania *et al*. used experimental and simulation studies in order to demonstrate that this swing effect is governed by the characteristics (polarizability, molecular size and shape) of the used gases (N_2, Ar, O_2, CO) and that the stepped adsorption behavior is defined by the guest packing inside the host.[6] Moggach *et al.* demonstrated the capability of ZIF-8 of undergoing a reversible structural transition when a pressure of 1.47 GPa is applied in the presence of methanol as the hydrostatic medium.[7] Such a structural transition of the imidazolate linkers under pressure can be highly advantageous in intrusion−extrusion experiments, as it is expected to allow the accommodation of a relatively larger amount of non-wetting liquid molecules. As for ZIF-8_Br, it displays a usual type Ia nitrogen sorption isotherm, with no sign of the flexibility of this material (characterized by stepped uptake at low relative pressure). The steric hindrance of Br substituent

may be the reason for the rigidity of the material's framework. Moreover, based on molecular dynamic simulation studies, it appears that the structural transition is triggered by a repacking of the nitrogen molecules, thereby inducing the swinging effect.[3] In this regard, the origin of the different sorption features observed for the three ZIF-8 derivatives can be assigned to the difference in pore size and shape, the pores in ZIF-8_Br being too small to enable a reordering of accommodated nitrogen molecules to occur.

Furthermore, the three ZIF-8 derivatives are characterized by a high degree of hydrophobicity and by high porosity (average microporous volume of 0.66, 0.57, and 0.35 $cm^3\ g^{-1}$ for ZIF-8, ZIF-8_Cl, and ZIF-8_Br, respectively) as revealed from water and N_2 adsorption-desorption measurements, respectively.[1] Therefore, these materials have been considered as good candidates for intrusion−extrusion experiments.

C. Context of the Study on Energetic Performances of ZIF-8 Derivatives

In previous work published by our team in 2013[8] and, later, in 2014[9], the energetic performances of ZIF-8 were explored using water, in addition to NaCl, KCl and LiCl aqueous solutions of concentrations ranging between 1- 4 M. Therefore, in the current study, we intend to complete this previous work performed on ZIF-8 by investigating the energetic behaviors of its derivatives using water, KCl 4 M aqueous solution, and LiCl 20 M aqueous solution. The aim is to analyze the influence of the substitution on the imidazolate linker on the energetic performances of the ZIF materials. As previously mentioned in Chapter 1, water is a nontoxic non-wetting liquid that has been extensively employed in intrusion−extrusion experiments. Moreover, the concentrations of both aqueous electrolyte solutions employed in this work (KCl 4 M and LiCl 20 M aqueous solutions) correspond to their maximum solubility at room temperature. This indicates the presence of less water molecules surrounding the alkaline cations (in the outer solvation shell and as free water molecules) and, thereby, a lower number of water molecules that could interact with/or create defects in the ZIF materials and, consequently, provoke an irreversible phenomenon during intrusion−extrusion experiments. Furthermore, it was shown that upon increasing the concentration of the LiCl aqueous solution, the energetic behavior of some zeosil-based LHSs can be modified from bumper to shock-absorber.[10]

II. Summary of the Article 1

Article 1 reports the intrusion−extrusion experiments performed on ZIF-8 (ZIF-8_CH_3 in the article), ZIF-8_Cl, and ZIF-8_Br using water, KCl 4 M, and LiCl 20M aqueous solutions as non-wetting liquids, whereby the experiments were realized up to a maximum pressure of 80 or 350

MPa and over three intrusion−extrusion cycles. The obtained results reveal that the intrusion pressure is enhanced with the addition of electrolytes to the non-wetting liquid, which is in agreement with the literature. Notably, for the three ZIF-8 derivatives, higher intrusion pressures are obtained with LiCl 20 M compared to the KCl 4 M aqueous solution. This confirms the results published by our team in 2014, where it was shown that for the same salt concentration of 4 M, higher intrusion pressures are attained with the LiCl (and NaCl) compared to the KCl aqueous solution during intrusion−extrusion experiments in ZIF-8.[9] This can be attributed to the larger hydrodynamic diameter of lithium compared to that of potassium[11] (or to the smaller size of the lithium cation compared to that of potassium[12]). Another explanation is the additional force needed to break down the solvation bonds, which are stronger in the case of lithium chloride than the case of potassium chloride salts.[13]

Our experimental results also prove that the intrusion pressure is always higher for the ZIF-8- and ZIF-8_Cl-based systems compared to the ZIF-8_Br-based systems, regardless of the nature of the non-wetting liquid. This can be explained by the additional pressure required to induce the swing of the imidazolate linkers and gate opening phenomenon in ZIF-8 and ZIF-8_Cl during the intrusion of the non-wetting liquid molecules, whereas, as previously mentioned in Section I, ZIF-8_Br is rigid.

Moreover, the obtained results show that the presence of an electron donating group on the imidazolate linker, such as the CH_3 group, can increase the interactions with the cations of the salt present in the non-wetting liquid (due to the increased electron density on the imidazolate linker), hence, preventing the complete extrusion of the non-wetting liquid molecules from the porosity at reduced pressures. This is particularly the case when a LiCl 20 M aqueous solution is used. In this respect, the "ZIF-8–LiCl 20 M aqueous solution" system displays bumper behavior with a remarkable value of absorbed energy of 104 J g^{-1}. These results are in agreement with the ones obtained very recently through molecular dynamic simulations[14] (which will be commented in Section III) and confirm that when confined in the porosity, the electrolyte from the non-wetting liquid may interact with the imidazolate linker.

Conversely, in the presence of an electron withdrawing group on the imidazolate linker, such as Cl or Br atoms, the interactions with the imidazolate linker are weakened (electron density on the imidazolate linker is decreased), which makes possible a complete extrusion of the non-wetting liquid molecules when the pressure is released and, thus, spring behavior is favored, as shown for the "ZIF-8_Cl–LiCl 20 M aqueous solution" and "ZIF-8_Br–LiCl 20 M aqueous solution" systems. Concerning the former system, it is important to highlight the outstanding value of the stored energy: 77 J g^{-1}. Indeed, until now, this is the highest value of stored energy registered for a spring system during intrusion−extrusion experiments.

We note that the high values of absorbed and stored energies obtained for the "ZIF-8−" and "ZIF-8_Cl−LiCl 20 M aqueous solution" systems, respectively, are ascribed to both the high intruded volumes (0.56 and 0.38 mL g^{-1} for the "ZIF-8−" and "ZIF-8_Cl−LiCl 20 M aqueous solution" systems, respectively) and intrusion pressures (186 and 201 MPa for the "ZIF-8−" and "ZIF-8_Cl−LiCl 20 M aqueous solution" systems, respectively).

When KCl 4 M aqueous solution is employed, the behaviors of all related systems are basically comparable to those of corresponding "ZIFs−water" systems. This could indicate weaker interactions of these electrolyte species with porous materials than those disclosed in "ZIFs−LiCl 20 M aqueous solution" systems.

Based on these results, it can be concluded that for a LHS consisting of a ZIF material and an aqueous electrolyte solution, the nature of the substituent present on the imidazolate linker can influence the energetic behavior of the system during intrusion−extrusion experiments, through host−guest (linker−aqueous electrolyte solution) interactions. The substituent can also affect the flexibility/rigidity of the ZIF material,[1] which consequently leads to higher/lower intrusion pressures, as demonstrated for the LHSs based on the three ZIF-8 derivatives of SOD topology. Finally, this study shows that the bulkier the substituent (i.e. the smaller the microporous volume), the smaller is the intruded volume.

The full text of article 1 entitled "Energetic Performances of ZIF-8 Derivatives: Impact of the Substitution (Me, Cl or Br) on Imidazolate Linker" and published in the Journal of Physical Chemistry C in 2018 is presented within next ten pages.

THE JOURNAL OF PHYSICAL CHEMISTRY C

Article

Cite This: J. Phys. Chem. C 2018, 122, 3846−3855

pubs.acs.org/JPCC

Energetic Performances of ZIF-8 Derivatives: Impact of the Substitution (Me, Cl, or Br) on Imidazolate Linker

Boushra Mortada, Gérald Chaplais,* Vasyl Veremeienko, Habiba Nouali, Claire Marichal, and Joël Patarin

Axe Matériaux à Porosité Contrôlée (MPC), Institut de Science des Matériaux de Mulhouse (IS2M), UMR CNRS 7361, Université de Strasbourg (UniStra), Université de Haute Alsace (UHA), ENSCMu, 3 bis rue Alfred Werner, Cedex 68093 Mulhouse, France

Supporting Information

ABSTRACT: The energetic performances of three isomorphic ZIF materials, i.e., ZIF-8_CH_3 (Basolite Z1200), ZIF-8_Cl, and ZIF-8_Br, of SOD topology are studied with high-pressure intrusion−extrusion experiments using water and aqueous electrolyte solutions (KCl 4 M and LiCl 20 M) as nonwetting liquids. This work represents an important progress in the field of energetic applications, as the "ZIF-8_Cl−LiCl 20 M" system exhibits a spring behavior with a stored energy of 77 J g^{-1}. To the best of our knowledge, this is the highest value for the stored energy obtained using intrusion−extrusion experiments. Experimental results reveal that the intrusion pressure increases with the addition of electrolytes. The systems evolve from a bumper to a shock-absorber or spring behavior with the decrease in the strength of the interactions between the cation of the salt and the imidazolate linker. This explains the bumper or rather the shock-absorber behavior observed for the "ZIF-8_Br−KCl 4 M" and "ZIF-8_CH_3−LiCl 20 M" systems compared to the spring behavior observed with the other systems reported in this work.

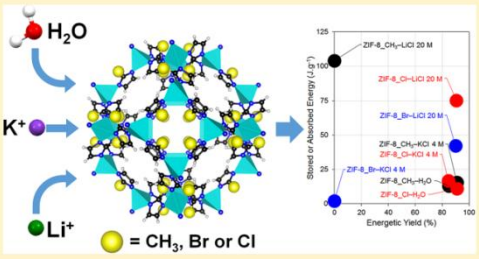

1. INTRODUCTION

In the field of new energetic applications, intrusion−extrusion experiments of nonwetting liquids in lyophobic porous materials have been widely carried out by Eroshenko, whose invention is illustrated by a lyophobic heterogeneous system (LHS) for accumulating or dissipating mechanical energy.[1−3] The system consists of a porous solid matrix that is characterized by open capillary porosity and controlled topology and a nonwetting liquid surrounding it. The latter component is characterized by a high surface tension at its interface with the solid and is selected to define a solid/liquid separation surface whose area varies isothermally and reversibly as a function of an external pressure applied on the system. According to Soulard et al.,[4] the phenomenon can be explained as follows: in order to spread a drop of a nonwetting liquid on the surface of a solid, a certain pressure must be applied. Similarly, to introduce a nonwetting liquid into a porous material, a hydraulic pressure, referred to as the intrusion pressure P_{int}, should be applied and should be at least equal to the capillary pressure P_c, which can be expressed by the Laplace−Washburn relation:

$$P_c = -(2\gamma \cos\theta)/r \quad (1)$$

where γ is the liquid−vapor interfacial tension, r the radius of the pores, and θ the contact angle between the liquid and the solid ($\theta > 90°$ for a nonwetting liquid).

In the first step, a mechanical energy is applied that provokes a forced penetration, also called intrusion, of the nonwetting liquid into the porous matrix. At the microscopic scale, this process results from the breaking of the intermolecular bonds in the bulk liquid to create new bonds with the solid, and a large solid−liquid interface ($\Delta\Omega > 0$) is developed. From a thermodynamic point of view, this phenomenon is associated with an increase in the Gibbs free energy of the system ($\Delta G > 0$), which is due to the unfavorable increased contact at the solid−liquid interface.[4,5]

In the second step, the pressure is progressively released, and depending on the nature of the heterogeneous system, the liquid is either totally/partially maintained in the pores or is completely expelled from the solid. The heterogeneous system can, thus, absorb, dissipate, or restore the supplied mechanical energy, hence behaving as a bumper, shock-absorber, or molecular spring, respectively.

Our group applied the process suggested by Eroshenko to strongly hydrophobic pure-silica zeolites (so-called zeosils) for the first time in 2001, which involved water as the nonwetting liquid.[6,7] Following this study, the energetic performances of numerous zeosils have been investigated.[6−15] Nevertheless, they are not sufficient for an industrial application, especially in terms of stored energy.

The stored energy can be enhanced by increasing the pore volume.[16,17] Another method involves increasing the applied

Received: September 9, 2017
Revised: January 17, 2018
Published: January 29, 2018

DOI: 10.1021/acs.jpcc.7b08999
J. Phys. Chem. C 2018, 122, 3846−3855

pressure during compression (i.e., by decreasing the tube size in channel systems or varying the nature of the nonwetting liquid).[18,19] In a first approach aiming to increase the stored energy, materials that are characterized by a porous volume that exceeds that of zeosils are desired. Zeolitic imidazolate frameworks (so-called ZIFs) constitute a class of metal−organic frameworks (MOFs), which are made of divalent metal ions (e.g., Zn^{2+} and Co^{2+}) bridged by ditopic imidazolate (Im) anions.[20−24] Each metal cation is tetrahedrally linked, through nitrogen atoms, to four imidazolate linkers, thus forming extended three-dimensional structures. ZIFs are known for being highly crystalline materials, displaying three-dimensional porous structures. They also display higher chemical and thermal stabilities as compared to other MOFs.[25] Intrusion−extrusion experiments for energetic applications require ZIF materials with highly hydrophobic pore surfaces. The energetic performances of ZIF materials based on water intrusion−extrusion experiments were first investigated by our group in 2013.[26] The first ZIF material successfully investigated for such experiments was ZIF-8 (hereafter-named ZIF-8_CH_3) of SOD topology, which showed a shock-absorber behavior during water intrusion−extrusion with a stored energy of 13 J g^{-1}.[26] Following this study, the energetic behaviors of various other ZIFs have been explored, and in addition to ZIF-8_CH_3, hydrophobic ZIF-71 of RHO topology also showed remarkable water intrusion properties. The "ZIF-71−water" system behaves as a perfect shock-absorber with stored energy of 26 J g^{-1}.[27,28] The hydrophilic character and steric hindrance in addition to the morphological parameters associated with a smaller crystal size are usually assumed to limit or even prevent the intrusion of water molecules in other ZIFs.[28,29]

The second approach toward enhancing the stored energy involves increasing the intrusion pressure. This can be accomplished by replacing pure water with aqueous electrolyte solutions. Different hypotheses have been suggested to explain the increase of the intrusion and extrusion pressures and, consequently, of the stored energy associated with the use of aqueous electrolyte solutions as nonwetting liquids instead of water. Based on studies performed on both zeolites and ZIFs, the enhanced energetic performances of the LHSs in the presence of electrolytes can be attributed to the increase in the liquid−vapor interfacial tension and/or an electrostatic repulsion that contributes to a higher transport resistant force or to electrification effects.[27,30−32] Other explanations include the additional force required to break down the solvation bonds of the solvated ions.[33−35] Arletti et al. investigated the energetic behavior of the pure-silica ferrierite-type zeolite (Si-FER) based on intrusion−extrusion experiments, using $MgCl_2{\cdot}21H_2O$ solution as the nonwetting liquid. The Rietveld refinement performed on the XRD pattern collected at 280 MPa, a pressure close to the intrusion value, revealed that the composition of the intruded species was $MgCl_2{\cdot}10H_2O$. This indicates that both water molecules and ions of the aqueous electrolyte solution were intruded in the zeolite pores. However, the lower solvation degree of the intruded ions compared to the initial solution ($MgCl_2{\cdot}10H_2O$ compared to $MgCl_2{\cdot}21H_2O$) indicates a partial desolvation of both magnesium and chloride ions.[35] Finally, the increased intrusion pressure may be due to the osmotic pressure, that is, the additional pressure needed to partially or totally provoke the infiltration of the liquid through the cage apertures.[36]

In this work, ZIF-8_Cl and ZIF-8_Br materials, in addition to the commercially available ZIF-8_CH_3, also known as Basolite Z1200, are investigated in high-pressure intrusion−extrusion experiments. The energetic behaviors of these different LHSs are explored based on different combinations of the porous materials and nonwetting liquids. The effect of both the nature of the linker and the nonwetting liquid on the intrusion pressure and, hence, on the energetic performance of the LHS is studied using both water and aqueous electrolyte solutions (LiCl 20 M and KCl 4 M). In order to study the influence of the intrusion−extrusion experiments on the ZIF-8 structures, the samples are characterized before and after such experiments using powder X-ray diffraction, N_2 physisorption, and chemical (ICP-OES) and thermogravimetric analyses.

2. EXPERIMENTAL SECTION

2.1. Materials. *Reagents and ZIF Materials.* The reagents, zinc nitrate hexahydrate ($Zn(NO_3)_2{\cdot}6H_2O$, 99%), 2-chloroimidazole (Hcim-2, 97%), and 2-bromoimidazole (Hbim-2, 95%) were purchased from Alfa Aesar, whereas ethanol (EtOH, 99.9%) was supplied from Carlo Erba. All the reagents were used without further purifications. Basolite Z1200 (ZIF-8_CH_3) was commercially purchased from Sigma-Aldrich and used in intrusion−extrusion experiments as supplied. ZIF-8_Br and ZIF-8_Cl were prepared by altering the synthesis procedure described by Li et al.[37] in terms of solvent, linker-to-metal molar ratio, and heating duration.

Synthesis of ZIF-8_Br. In a PTFE-lined stainless-steel autoclave, 1.36 g (4.57 mmol) of $Zn(NO_3)_2{\cdot}6H_2O$ was dissolved in 73.84 g (1602.78 mmol) of EtOH by stirring for 10 min. 1.35 g (9.20 mmol) of Hbim-2 was added, and the mixture was stirred for further 10 min, resulting in the formation of a yellow suspension. Therefore, the molar composition of the starting synthesis suspension was 1 Zn: 2 Hbim-2:350 EtOH:6 H_2O. The reaction mixture was then heated in a preheated oven at 100 °C for 72 h. The resulting yellow microcrystalline powder was separated from the solvent through vacuum filtration. The collected yellow powder was then washed with fresh EtOH (120 mL), and the powder was left to dry in air. Postsynthetic treatment of the product involved suspending the powder in ethanol (40 mL), followed by sonicating for 3 min. The powder was then filtered, washed with 20 mL of fresh ethanol, and dried in air.

Synthesis of ZIF-8_Cl. A similar synthesis procedure was used to prepare ZIF-8_Cl. Hcim-2 (0.95 g, 9.23 mmol) was introduced in the starting mixture instead of Hbim-2, while maintaining the molar composition of the starting synthesis solution as follows: 1 Zn: 2 Hcim-2:350 EtOH: 6 H_2O.

The obtained materials are called hereafter ZIF-8_X materials (X = Br, Cl).

2.2. Characterization Techniques. *Powder X-ray Diffraction.* X-ray diffraction (XRD) patterns of the different samples were recorded in transmission mode on a STOE STADI-P diffractometer equipped with a curved germanium (111), primary monochromator, and a linear position-sensitive detector (6° in 2θ) using Cu Kα_1 radiation (λ = 1.5406 Å). Measurements were achieved for 2θ angle values in the 5°−50° range, with a step of 0.04° in 2θ.

Nitrogen Adsorption−Desorption Measurements. Nitrogen adsorption−desorption isotherms were performed at 77 K using a Micromeritics ASAP 2420 apparatus. Prior to the adsorption measurements, the samples were outgassed at 473 K overnight under vacuum. The specific surface area (S_{BET}) was calculated according the criteria given in the literature and thereby using the BET method applied[38,39] in the $0.0004 \leq p/$

DOI: 10.1021/acs.jpcc.7b08999
J. Phys. Chem. C 2018, 122, 3846−3855

$p^\circ \leq 0.0028$ range for ZIF-8_CH_3, in the $0.0003 \leq p/p^\circ \leq 0.0035$ range for ZIF-8_Cl, and in the $0.0007 \leq p/p^\circ \leq 0.0200$ range for ZIF-8_Br. The microporous volumes (V_μ) were determined according to the *t*-plot method.

Water Adsorption–Desorption Measurements. Water adsorption–desorption isotherms were measured at 298 K on a Triflex Micromeritics equipment. Prior to the water adsorption measurements, water (analyte) was flash frozen under liquid nitrogen and then evacuated under dynamic vacuum at least five times to remove any gases in the water reservoir. The samples were outgassed at 473 K for 12 h.

Intrusion–Extrusion Experiments. The LiCl 20 M and KCl 4 M aqueous solutions were prepared by dissolving the corresponding amounts of salts in distilled water. The intrusion–extrusion experiments of water and aqueous electrolyte solutions in the ZIF materials were performed at room temperature over three cycles using a modified mercury porosimeter (Micromeritics Model Autopore IV).[8] The intruded and extruded volumes (V_{int}, V_{ext}) and pressures (P_{int}, P_{ext}) were determined as follows: $V_{int} = V_{inte} - V_{intb}$ and $V_{ext} = V_{extb} - V_{exte}$, where V_{intb} and V_{inte} refer to the volume values at the beginning and end of the intrusion step, respectively. Similarly, V_{extb} and V_{exte} correspond to the volume values at the beginning and end of the extrusion step, respectively. The values P_{int} and P_{ext} correspond to the pressure at half total volume variation. Pressure is expressed in megapascals (MPa) and volume in milliliters per gram of sample (mL g^{-1}). In this work, the energetic behavior of a LHS is classified as shock-absorber or spring based on a complete extrusion of the intruded liquid from the solid with an energy yield lower or higher than 80%, respectively. Systems that involve no extrusion of the liquid are referred to as bumpers.

Thermogravimetric Analyses (TGA). TGA were carried out on a TG Mettler Toledo STARe apparatus, under air flow, with a heating rate of 2 °C/min from 30 to 650 °C.

Inductively Coupled Plasma Optical Emission Spectroscopy (ICP-OES). The analysis was carried out using a Thermo Model 6300DUO spectrometer. 50 mg of ZIF-8_CH_3 powder, recovered after intrusion with 20 M LiCl aqueous electrolyte solution, was digested in 2 mL of hydrofluoric acid by stirring overnight at room temperature. The obtained solution was diluted to 20 mL with ultrapure water and then filtered. The wavelength of the corresponding spectrometric lines that were used for the Li analysis was 670.784 nm.

3. RESULTS AND DISCUSSION

3.1. Characterization of the ZIF Materials. We report in this article the high-pressure intrusion–extrusion experiments for ZIF-8_Br and ZIF-8_Cl materials. For comparison, commercially available ZIF-8_CH_3 (Basolite Z1200) is also investigated. The three ZIF materials are made of zinc cations that are linked through methyl-, chloro-, and bromo-2-substituted imidazolate linkers for ZIF-8_CH_3, ZIF-8_Cl, and ZIF-8_Br, respectively. The XRD patterns of the ZIF-8 samples are given in Figure 1. All three materials crystallize in the cubic symmetry (space group *I*-43*m*) and display a SOD-type topology with a lattice constant $a \approx 17$ Å, in agreement with values of unit cell parameters given in the literature.[37,40] It is worthy to note the inversion of the intensities of some XRD peaks in particular in the 2θ range 10°–14°. This can be explained by the nature of the substituents on the imidazolate linker, which display different X-ray diffusion factors.

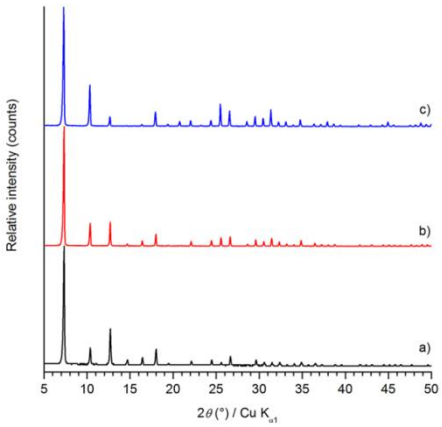

Figure 1. XRD patterns of the (a) ZIF-8_CH_3, (b) ZIF-8_Cl, and (c) ZIF-8_Br samples.

The N_2 adsorption–desorption isotherms of the three studied ZIF-8 materials are reported in Figures 2a and 2b. The isotherm of ZIF-8_CH_3 is mainly characterized by a two-step uptake ca. $p/p^\circ \approx 0.005$ and a hysteresis loop indicating a reversible crystal-sized-dependent structural transition leading to an increase of the porous volume due to the reorientation (swing) of the imidazolate linkers.[41−44] The microporous volume is 0.64 $cm^3\ g^{-1}$, which is consistent with the literature.[29] A similar feature for the first step, even though narrower, is noticed at the same relative pressure for ZIF-8_Cl, revealing presumably the flexibility of this ZIF material. This noticeable uptake is accompanied by a second one, more diffuse, occurring above ca. $p/p^\circ \approx 0.10$ and up to $p/p^\circ \approx 0.97$. The corresponding volumes are 0.53 $cm^3\ g^{-1}$ at $p/p^\circ \approx 0.03$ and 0.55 $cm^3\ g^{-1}$ at $p/p^\circ \approx 0.97$. In contrast, no abrupt uptake is observed at low relative pressure for ZIF-8_Br. This highlights the stiffness of this latter that might be explained by the steric hindrance or/and electrostatic repulsion due to the presence of the bromine substituent on the imidazolate linker. The related microporous volume is 0.34 $cm^3\ g^{-1}$.

The influence of the hydrophilic/hydrophobic nature of the linker in intrusion–extrusion experiments has already been investigated by our team.[28] The study showed that ZIFs constituted from organic linkers bearing polar (hydrophilic) substituents are capable of adsorbing water at low pressures, which reduces their ability to further adsorb water molecules at higher pressures during the process. In this regard, water adsorption measurements were performed on the three studied ZIF materials at room temperature, and their water uptake capacities were compared to that of ZIF-90 (synthesized from imidazole-2-carboxaldehyde) that is known to be hydrophilic due to the presence of a polar aldehyde substituent on the imidazolate linker.[45] Water adsorption isotherms displayed in Figure 3 indicate almost negligible water uptake for ZIF-8_CH_3, ZIF-8_Cl, and ZIF-8_Br, whereas, as expected, ZIF-90 is capable of adsorbing water. The hydrophobic character of the other ZIF materials is attributed to the nonpolar methyl, bromine, and chlorine substituents borne by the imidazolate ligands. Thus, characterized by their high crystallinity and porosity as well as their hydrophobic character, ZIF-8_CH_3, ZIF-8_Cl, and ZIF-8_Br are considered as very attractive

DOI: 10.1021/acs.jpcc.7b08999
J. Phys. Chem. C 2018, 122, 3846−3855

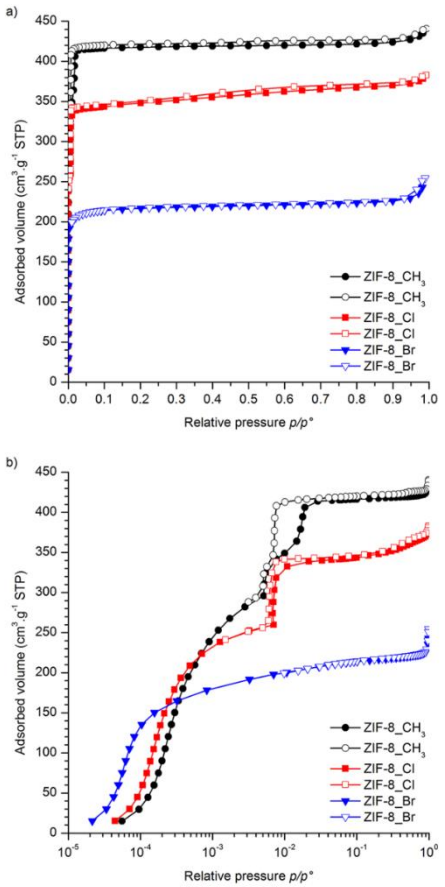

Figure 2. N_2 adsorption−desorption isotherms at 77 K of the ZIF-8_CH_3, ZIF-8_Cl, and ZIF-8_Br samples. Plots are given with (a) a linear scale and (b) a logarithmic scale of the relative pressure. Filled and empty symbols correspond to the adsorption and desorption branches, respectively.

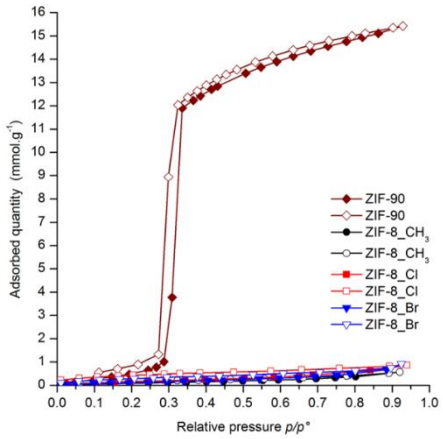

Figure 3. Water adsorption−desorption isotherms of the ZIF-8_CH_3, ZIF-8_Cl, ZIF-8_Br, and ZIF-90 samples. Filled and empty symbols correspond to the adsorption and desorption branches, respectively.

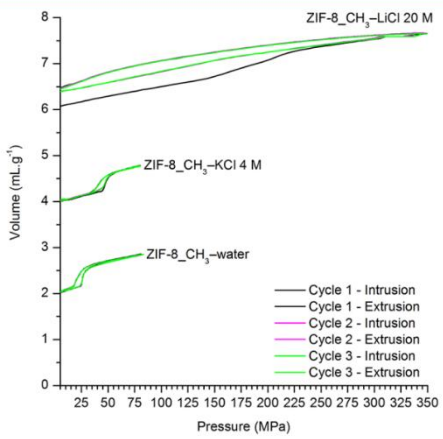

Figure 4. Pressure−volume diagrams of the "ZIF-8_CH_3−water" and "ZIF-8_CH_3−aqueous electrolyte solution" systems. For clarity, the diagrams are shifted on the *y*-axis. The pressure range 0−5 MPa (corresponding to compression of the ZIF particles and filling of the interparticular porosity) is not reported.

candidates for the investigation of their energetic performances in high-pressure intrusion−extrusion experiments.

3.2. Intrusion−Extrusion Experiments. The intrusion−extrusion experiments were performed using three different nonwetting liquids: water, lithium chloride (20 M), and potassium chloride (4 M) aqueous solutions. The concentrations of both aqueous electrolyte solutions correspond to their maximum solubility at room temperature. The pressure−volume ($P-V$) diagrams for the different systems after three consecutive intrusion−extrusion cycles are demonstrated in Figures 4−6. The corresponding characteristics data are listed in Table 1. In the $P-V$ diagrams, and as previously reported,[26,27] the volume variation in the low pressure range (0−5 MPa) corresponds to the compression of the ZIF particles and to the filling of the interparticular porosity. This pressure range is not shown in the $P-V$ diagrams presented in Figures 4−6. However, Figure S1 represents the volume variation between 0 and 5 MPa in the case of the "ZIF-8_CH_3−LiCl 20 M" system.

ZIF-8_CH_3-Based Systems. The "ZIF-8_CH_3−water" and "ZIF-8_CH_3−KCl 4 M" systems were already described in our previous work, by Ortiz et al.[32] For comparison with the "ZIF-8_CH_3−LiCl 20 M" system, the intrusion−extrusion curves and the characteristics of these two systems are also reported in Figure 4 and in Table 1, respectively.

For the "ZIF-8_CH_3−LiCl 20 M" system, the intrusion curve of the first intrusion−extrusion cycle exhibits one main step from 150 to 230 MPa, corresponding to the intrusion of the liquid in the ZIF pores, with an intrusion pressure of ca. 186 MPa. This pressure is higher than those obtained for the first intrusion−extrusion cycle in the case of the "ZIF-8_CH_3−

DOI: 10.1021/acs.jpcc.7b08999
J. Phys. Chem. C 2018, 122, 3846−3855

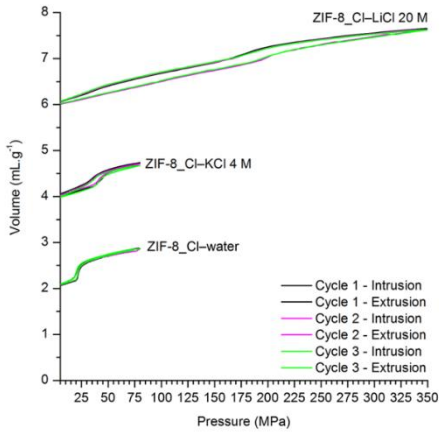

Figure 5. Pressure−volume diagrams of the "ZIF-8_Cl−water" and "ZIF-8_Cl−aqueous electrolyte solution" systems. For clarity, the diagrams are shifted on the *y*-axis. The pressure range 0−5 MPa is not reported (compression of the ZIF particles and filling of the interparticular porosity).

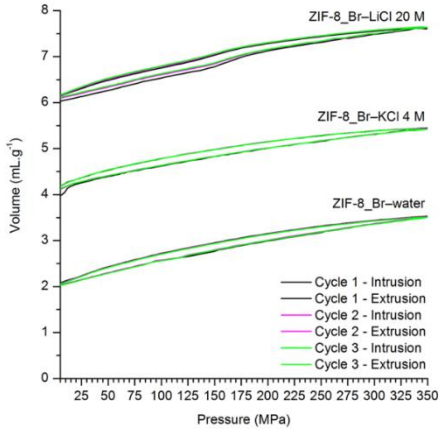

Figure 6. Pressure−volume diagrams of the "ZIF-8_Br−water" and "ZIF-8_Br−aqueous electrolyte solution" systems. For clarity, the diagrams are shifted on the *y*-axis. The pressure range 0−5 MPa (corresponding to compression of the ZIF particles and filling of the interparticular porosity) is not reported.

water" (27 MPa) and "ZIF-8_CH_3−KCl 4 M" (31 MPa) systems. For the same electrolyte concentration (4 M), it was shown in a previous study that the intrusion pressure is higher for the LiCl compared to KCl aqueous electrolyte solution.[32] This can be explained by the larger diameter of the hydrated lithium species compared to the hydrodynamic diameter of potassium[46] or by the smaller size of the lithium cation compared to that of potassium ($r_{Li+} < r_{Na+} < r_{K+} < r_{Cs+}$).[47] Moreover, an additional force is required to break down the solvation bonds that are stronger in the case of lithium chloride than in the case of potassium chloride salts.[48] The intruded volume is approximately equal to 0.56 mL g^{-1}, which is less than the microporous volume of ZIF-8_CH_3 obtained from nitrogen sorption measurements (0.64 cm^3 g^{-1}). This difference between the intruded and microporous volumes was previously observed with "ZIF-8_CH_3−water" and numerous "zeosil−water" systems and was attributed to a bulk water density lower than 1.[26] In the decompression step, the liquid seems to be not expelled and to remain in the porosity. Indeed, no further intrusion occurs in the second and third cycles, and the observed volume variations are only due to the compression−decompression of the nonwetting liquid in the cell. Consequently, the system appears to behave as a bumper with an absorbed energy near 104 J g^{-1}. However, according to the TG curves and ICP-OES analysis (section 3.3), most of the intruded liquid is expelled from the solid probably in the 0−5 MPa pressure range. The fact that the liquid is not completely expelled may be attributed to the strong interaction between Li^+ ions and the imidazolate linker.[49] Therefore, the "ZIF-8_CH_3−LiCl 20 M" system behaves rather as a shock-absorber working only once. The high absorbed energy (104 J g^{-1}) is the product of both the high intrusion pressure and intruded volume. The latter is attributed to the high microporous volume observed for this sample due to the swing of the imidazolate linker that is clearly observed from the N_2 adsorption−desorption measurements (section 3.1).

ZIF-8_Cl-Based Systems. In the case of the "ZIF-8_Cl−water" system (Figure 5), the three intrusion−extrusion curves corresponding to the three intrusion−extrusion cycles are completely superimposable. The intrusion curves exhibit one main step at P_{int} = 22 MPa that corresponds to the water intrusion into the ZIF pores. In the extrusion step, the liquid is completely expelled ($V_{int} \approx V_{ext} \approx$ 0.48 mL g^{-1}) at a pressure slightly lower than that of the intrusion step ($P_{ext} \approx$ 20 MPa), resulting in a very small hysteresis. The energy yield is close to 90%, and thus the "ZIF-8_Cl−water" system behaves as a spring.

For the "ZIF-8_Cl−KCl 4 M" system, the intrusion curves of the three intrusion−extrusion cycles show one main step at a pressure of 41−44 MPa that corresponds to the intrusion in the ZIF pores (compared to 22 MPa for "ZIF-8_Cl−water" system). When the pressure is reduced, the liquid is completely expelled ($V_{int} \approx V_{ext} \approx$ 0.40 mL g^{-1}) at a lower pressure (P_{ext} ranging from 34 to 36 MPa) than the intrusion one. The phenomenon is therefore completely reversible, and the system shifts from a shock-absorber behavior (energy yield = 78%) in the first cycle to a spring behavior in the second and third cycles (energy yield = 88%).

For the "ZIF-8_Cl−LiCl 20 M" system, the intrusion and extrusion curves of the three intrusion−extrusion cycles exhibit one main step with an intrusion pressure in the order of 200 MPa, which is remarkably higher than those obtained in the cases of the "ZIF-8_Cl−water" and "ZIF-8_Cl−KCl 4 M" systems. These results are in agreement with previous data showing an increase in the intrusion pressure when using electrolytes and especially with LiCl 20 M aqueous solution.[32,33] The intruded volume is around 0.38 cm^3 g^{-1} and is equal to the extruded volume. For ZIF-8_Cl, the intrusion−extrusion process of the LiCl 20 M aqueous solution is thus completely reversible. The extrusion occurs at a slightly lower pressure, resulting in a small gap between the intrusion and extrusion curves. Another small step is observed on the extrusion curve at lower pressure (40 MPa). Depending on the temperature, a one- or two-step extrusion process was reported by Grosu et al. during the extrusion of water in "ZIF-8−water" systems.[50,51] In our case, this step is probably due to the LiCl

DOI: 10.1021/acs.jpcc.7b08999
J. Phys. Chem. C 2018, 122, 3846−3855

Table 1. Characteristics of the Different "ZIF−Nonwetting Liquid" Systems: Intrusion (P_{int}) and Extrusion (P_{ext}) Pressures, Intruded (V_{int}) and Extruded (V_{ext}) Volumes, Stored (E_s), Absorbed (E_a), and Restored (E_r) Energies, and Energy Yield

system	cycle	P_{int}[a] (MPa)	P_{ext}[a] (MPa)	V_{int}[a] (mL g^{-1})	V_{ext}[a] (mL g^{-1})	E_s or E_a[b] (J g^{-1})	E_r[b] (J g^{-1})	yield[c] (%)	behavior[d]
ZIF-8_CH_3−water	1	27	22	0.50	0.50	13	11	85	S
	2	27	22	0.50	0.50	13	11	85	S
	3	27	22	0.50	0.50	13	11	85	S
ZIF-8_CH_3−KCl 4 M	1	32	28	0.50	0.50	16	14	88	S
	2	31	28	0.50	0.50	15	14	93	S
	3	31	28	0.50	0.50	15	14	93	S
ZIF-8_CH_3−LiCl 20 M	1	186		0.56		104		0	B or SA[e]
	2								
	3								
ZIF-8_Cl−water	1	22	20	0.48	0.48	11	10	91	S
	2	22	20	0.48	0.48	11	10	91	S
	3	22	20	0.48	0.48	11	10	91	S
ZIF-8_Cl−KCl 4 M	1	44	34	0.40	0.40	18	14	78	SA
	2	41	36	0.40	0.40	16	14	88	S
	3	41	36	0.40	0.40	16	14	88	S
ZIF-8_Cl−LiCl 20 M	1	202	180	0.38	0.38	77	68	88	S
	2	200	185	0.37	0.37	74	68	92	S
	3	200	185	0.37	0.37	74	68	92	S
ZIF-8_Br−water	1	*f*	*f*	*f*	*f*				
	2	*f*	*f*	*f*	*f*				
	3	*f*	*f*	*f*	*f*				
ZIF-8-Br−KCl 4 M	1	11		0.16		2			B or SA[e]
	2								
	3								
ZIF-8_Br−LiCl 20 M	1	167	152	0.25	0.25	42	38	90	S
	2	166	150	0.25	0.25	42	38	90	S
	3	166	150	0.25	0.25	42	38	90	S

[a]Determined from the intrusion−extrusion diagrams. [b]Corresponding to the area of the relevant intrusion or extrusion curve, respectively, and given by $E = \int_{V_0}^{V_f} P\,dV$, where V_0 is the initial volume and V_f is the final volume. [c]Energy yield (%) = $E_r/E_s \times 100$. [d]B (bumper), SA (shock-absorber), and S (spring) behaviors. [e]SA (shock-absorber) according to the TG and ICP-OES results. [f]Indicates that the value could not be determined from the intrusion−extrusion curve.

20 M aqueous solution, as it is also clearly visible in the $P-V$ diagram of this solution (without porous solid) (Figure S2). Such a step might correspond to the dissolution of LiCl, which might crystallize under high pressure. Accordingly, the system exhibits a spring behavior with a stored energy between 74 and 77 J g^{-1}. This value of stored energy is the highest that has been recorded until now in intrusion−extrusion experiments.

ZIF-8_Br-Based Systems. In the case of both the "ZIF-8_Br−water" and "ZIF-8_Br−KCl 4 M" systems, the intrusion curves exhibit one main steep step, each, at very low pressure (<5 MPa (not visible on the curve) and 11 MPa, respectively (Figure 6). This step for the "ZIF-8_Br−water" system either may correspond to the compression of the ZIF particles and intrusion in the interparticular porosity, which are the common phenomena that occur in the low pressure range (0−5 MPa) during intrusion−extrusion experiments, or may correspond, in addition, to the intrusion of the liquid in the pores of the SOD structure. One of the above hypotheses can be confirmed by the experiment carried out using LiCl 20 M as the nonwetting liquid (Figure 6).

For the "ZIF-8_Br−LiCl 20 M" system, the intrusion and extrusion curves of the three intrusion−extrusion cycles are stackable and exhibit one main step each at a pressure in the order of 166 MPa. This pressure is much higher than that observed with the "ZIF-8_Br−water" and "ZIF-8_Br−KCl 4 M" systems and corresponds to the intrusion of the liquid in the ZIF pores, which is clearly recognized from the shape of the intrusion−extrusion curves. However, it is worthy to note that this pressure is lower than those observed for the "ZIF-8_CH_3−LiCl 20 M" and "ZIF-8_Cl−LiCl 20 M" systems (186 and 202 MPa, respectively). The difference ranges between 20 and 40 MPa. By taking into account such a difference, the intrusion of the nonwetting liquid for the "ZIF-8_Br−water" and "ZIF-8_Br−KCl 4 M" systems is expected to be observed at a lower pressure than those of the corresponding ZIF-8_CH_3−nonwetting liquid" (i.e., 27 and 31 MPa, respectively) and "ZIF-8_Cl−nonwetting liquid" systems (i.e., 22 and 41 MPa, respectively). This is effectively noted experimentally. Hence, the volume variation observed at low pressure for the "ZIF-8_Br−water" system (<5 MPa) can correspond to the intrusion of the liquid in the ZIF pores in addition to the compression of the ZIF particles and intrusion of the liquid in the interparticular porosity.

In the case of the "ZIF-8_Br-KCl 4 M" system, the pressure−volume diagram reveals a bumper behavior in the first cycle. The volume variations in the second and third cycles can be attributed to the compression/decompression of the nonwetting liquid. However, as mentioned above for the "ZIF-8_CH_3−LiCl 20 M" system, the intruded liquid might also be expelled from the solid in the 0−5 MPa pressure range. Therefore, this system can also possibly behave as a shock-absorber working once. We note that the intruded volumes are

DOI: 10.1021/acs.jpcc.7b08999
J. Phys. Chem. C 2018, 122, 3846−3855

higher for the ZIF-8_CH_3 and ZIF-8_Cl than for the ZIF-8_Br-based systems (Table 1). This is in agreement with the N_2 adsorption/desorption measurements (Figure 2a,b) and may be attributed to the swing of the imidazolate ligands which leads to larger pore apertures for the first two systems and, thus, to higher intruded volumes. The higher intrusion/extrusion pressures observed for these systems characterized by larger pore apertures may be attributed to the additional pressure needed to increase the cage aperture by swinging of the imidazolate linkers.

The "ZIF-8_Br–LiCl 20 M", similar to the "ZIF-8_Cl–LiCl 20 M" system, shows a complete extrusion of the liquid from the ZIF pores and thereby behaves as a spring, unlike the case of the "ZIF-8_CH_3–LiCl 20 M" system, in which the liquid is not completely expelled. This may be explained by the higher electron-withdrawing effect of the chlorine and bromine substituents compared to the electron-donating effect of the methyl group,[52] which results in a less partial negative charge borne by the halogenated imidazolate linkers. Consequently, stronger interactions with the lithium ions are expected to occur in the case of ZIF-8_CH_3 rather than in the case of ZIF-8_Cl and ZIF-8_Br, interpreting, thus, the partial bumper behavior for the "ZIF-8_CH_3–LiCl 20 M" system.

3.3. Characterizations of ZIF Materials after Intrusion–Extrusion Experiments. In order to assess potential damages in host material structures generated by the intrusion–extrusion experiments under high pressure, XRD characterizations and nitrogen sorption measurements were undertaken for the postintruded samples. Thermogravimetric and ICP-OES analyses were also performed on the ZIF-8_CH_3 sample after intrusion with LiCl 20 M aqueous solution.

XRD Characterizations. The XRD patterns of the samples before and after intrusion–extrusion experiments are reported in Figure 7. It is worth noting that the intrusion–extrusion experiments were generally realized up to 80 MPa when water and KCl 4 M aqueous solution are used (except for ZIF-8_Br for which the highest pressures attained 350 MPa in both systems) and up to 350 MPa with LiCl 20 M aqueous solution. Compared to the nonintruded samples, the crystallinity of the intruded samples is maintained, revealing that the ZIF-8 structures are preserved whatever the nonwetting liquid and the associated limit pressure.

Thermogravimetric (TG) and ICP-OES Analyses. The TG curves of the nonintruded ZIF-8_CH_3, ZIF-8_Cl, and ZIF-8_Br materials are supplied in the Supporting Information (Figure S3). TG analyses of the nonintruded and LiCl 20 M intruded-extruded ZIF-8_CH_3 samples are also compared (Figure 8), since a bumper behavior was expected from the P–V diagrams. In order not to affect the sample, after the intrusion–extrusion experiment, it was gently washed with a small quantity of distilled water and then dried at room temperature for 24 h. The TG curve of the nonintruded sample shows one main decomposition step with a total mass loss of 64% that corresponds to the degradation of the framework, leading to the formation of ZnO. This value is in perfect agreement with the calculated one (64%). For the LiCl 20 M intruded sample, the TG curve displays a first mass loss below 70 °C (ca. 6%) corresponding to traces of water molecules trapped in the interparticular porosity and resulting from the drying at room temperature. Another mass loss occurring between 150 and 300 °C (ca. 7%) can be assigned to traces of the intruded liquid. Finally, the main mass loss (50%) corresponds to the degradation of the framework. Such a

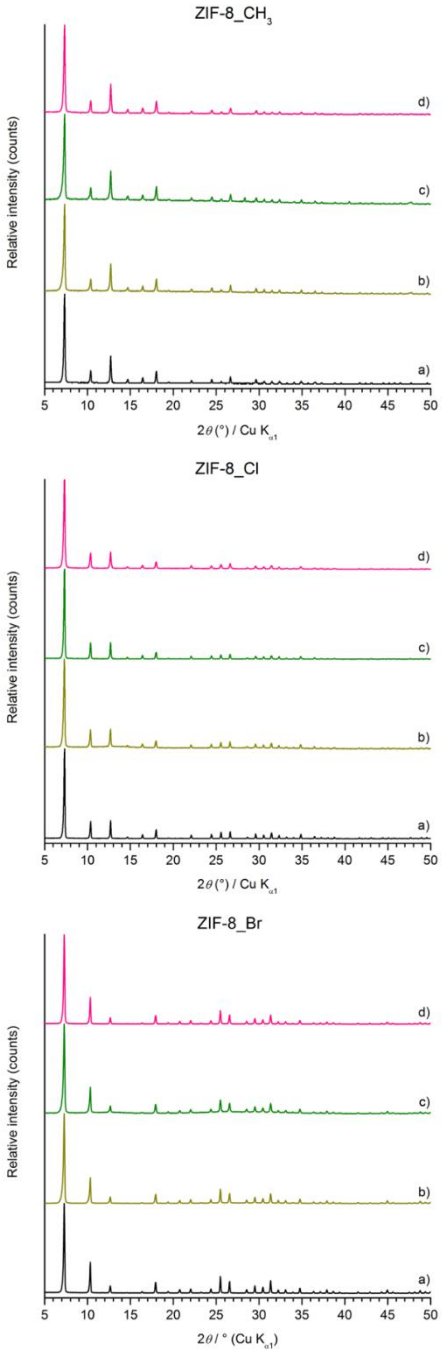

Figure 7. XRD patterns of (a) the nonintruded ZIF-8 samples and intruded ZIF-8 samples with (b) water, (c) KCl 4 M, and (d) LiCl 20 M.

DOI: 10.1021/acs.jpcc.7b08999
J. Phys. Chem. C 2018, 122, 3846–3855

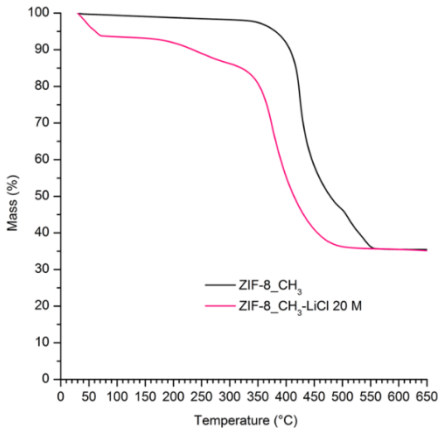

Figure 8. TG curves of the ZIF-8_CH_3 samples before and after intrusion with LiCl 20 M aqueous electrolyte solution.

mass loss, calculated for 100% of the ZIF-8_CH_3 sample, is slightly lower (58%) than the one observed for the nonintruded sample (i.e., 64%). The slight difference observed might be due to the breaking down of some organic linkers during the intrusion−extrusion process. From this experiment, the mass loss assigned to the intruded liquid (ca. 7%) is low compared to what is expected for the intruded volume (ca. 40%), indicating that most of the intruded liquid is expelled from the solid at atmospheric pressure. Thereby, the "ZIF-8_CH_3−LiCl 20 M" system behaves rather as a shock-absorber working only once. An ICP-OES analysis performed on the same sample confirms this result, suggesting that most of the liquid (between 80 and 90%) is expelled at very low pressure. Indeed, the amount of lithium found in the solid (7 mg of Li per gram of ZIF) is considerably lower than that expected (78 mg g^{-1}).

N_2 Sorption Analyses. Figure 9 represents the N_2 sorption isotherms for the ZIF materials before and after intrusion−extrusion experiments, except those of ZIF-8_CH_3 materials arising from "ZIF-8_CH_3−water" and "ZIF-8_CH_3−KCl 4 M" systems that were published elsewhere.[26,32] As previously mentioned in the Experimental Section, the activation procedure is performed at 200 °C under vacuum in all cases; therefore, no traces of remaining intruded liquid are present in the solids. For each given material, all the nonintruded and intruded samples adopt the same profile. The most significant differences are observed after intrusion with LiCl 20 M aqueous solution. After three intrusion−extrusion cycles, the textural properties of ZIF-8_CH_3 (P_{int} = 186 MPa) decrease from 1342 to 1191 $m^2 g^{-1}$ for the BET surface area (S_{BET}) and from 0.64 to 0.57 $cm^3 g^{-1}$ in terms of microporous volume (V_μ). A similar trend (decrease of S_{BET} and V_μ from 1138 to 972 $m^2 g^{-1}$ and 0.55 to 0.46 $cm^3 g^{-1}$, respectively) is observed for the ZIF-8_Cl sample intruded with the LiCl 20 M aqueous solution (P_{int} = 202 MPa). In contrast, the variation of the textural properties is much less pronounced even negligible for ZIF-8_Br (P_{int} = 167 MPa) with S_{BET} evolving from 914 to 874 $m^2 g^{-1}$ and V_μ from 0.34 to 0.33 $cm^3 g^{-1}$. These decreases can be related to the intrusion pressure and might be explained by a partial degradation of the SOD structure even if, according to the recorded XRD patterns, no structural changes are observed at

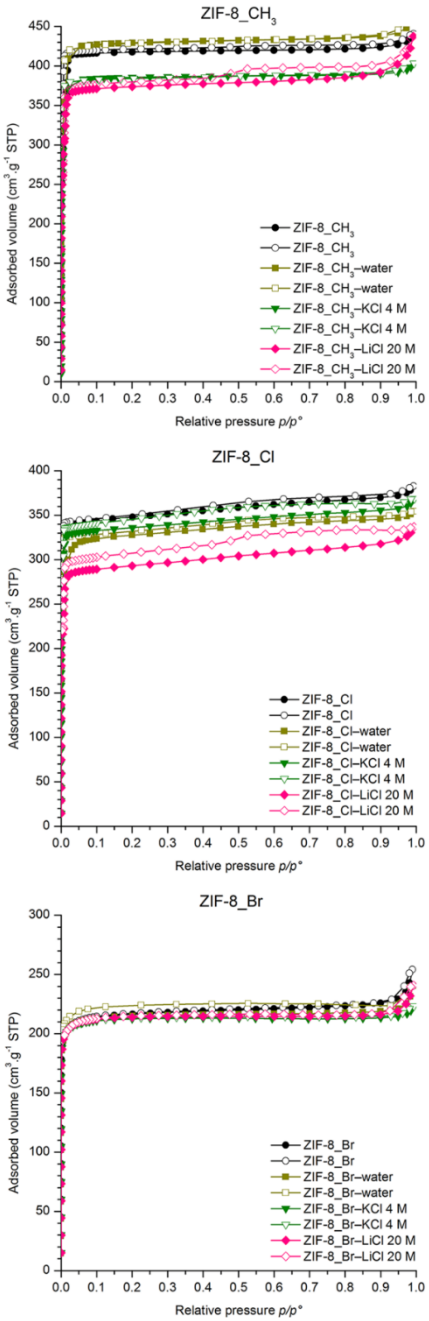

Figure 9. N_2 adsorption−desorption isotherms at 77 K of the ZIF-8 samples before and after intrusion of the different nonwetting liquids. Filled and empty symbols correspond to the adsorption and desorption branches, respectively.

DOI: 10.1021/acs.jpcc.7b08999
J. Phys. Chem. C 2018, 122, 3846−3855

the long-range order. It appears that the higher the intrusion pressure, the higher the decrease in pore volume and surface area for the intruded samples even if it remains negligible for ZIF-8_Br. The stiffness of the latter compared to the flexibility of the two other ZIFs might be another factor.

4. CONCLUSIONS

Three ZIF-8 materials of SOD topology (ZIF-8_CH_3, ZIF-8_Br, and ZIF-8_Cl) have been studied in intrusion−extrusion experiments under high pressure. These latter were carried out using water and aqueous electrolyte solutions (KCl 4 M and LiCl 20 M) as the nonwetting liquids. The "ZIF-8_Cl−LiCl 20 M" exhibits a spring behavior with a stored energy of 77 J g^{-1}, which is to the best of our knowledge the highest value recorded until now. It is also worthy to note the remarkable absorbed energy of 104 J g^{-1} observed for the "ZIF-8_CH_3−LiCl 20 M" system, which displays mainly a shock-absorber behavior. As for the other lyophobic heterogeneous systems, they exhibit a spring behavior primarily. Experimental results obtained from pressure−volume curves indicate the increase in intrusion pressure with the addition of electrolytes. By comparing our results to those obtained in a previous study, for the same electrolyte concentration (4 M), the increase in intrusion pressure is more pronounced with LiCl than KCl, which is ascribed to the larger hydrodynamic diameter of the lithium compared to potassium ions. Moreover, the obtained results show the impact of the nature of the substituent present on the imidazolate linker on the intrusion pressure, intruded volume, and behavior of the system. The presence of electron-withdrawing (Cl and Br) or -donating (CH_3) groups on the imidazolate linker decreases or increases, respectively, the partial negative charge borne by the substituted linker. This is believed to affect the host (linker)−guest (aqueous salt solution) interactions and enable the modulation of the energetic performances of the studied lyophobic heterogeneous systems.

■ ASSOCIATED CONTENT

Supporting Information

The Supporting Information is available free of charge on the ACS Publications website at DOI: 10.1021/acs.jpcc.7b08999.

Volume variation in the 0−5 MPa pressure range for the "ZIF-8_CH_3−LiCl 20 M" system, pressure−volume diagram of LiCl 20 M aqueous electrolyte solution, thermogravimetric analyses (TG curves of ZIF-8_CH_3, ZIF-8_Cl and ZIF-8_Br parent materials) (PDF)

■ AUTHOR INFORMATION

Corresponding Author

*(G.C.) E-mail gerald.chaplais@uha.fr; tel +33 389 33 68 87.

ORCID

Gérald Chaplais: 0000-0003-2756-4896

Joël Patarin: 0000-0002-6511-5357

Notes

The authors declare no competing financial interest.

■ ACKNOWLEDGMENTS

XRD analyses, nitrogen sorption measurements. and thermal (TG) analyses were performed on the technical plateforms of IS2M.

■ REFERENCES

(1) Eroshenko, V. Unusual Properties of One Complex Thermodynamic System. *Dopov. Akad. Nauk Ukr. RSR, Ser. A: Fiz.-Tekh. Mater. Nauki* **1990**, 77−80.

(2) Eroshenko, V. Heterogeneous Energy Accumulation or Dissipation Structure, Methods for Using Such Structure and Associated Apparatus. Int. Patent WO/1996/018040, June 13, 1996.

(3) Eroshenko, V. Adiabatic Incompressibility and Non-Dilatation in a Complex Thermodynamic System. *Entropie* **1996**, *32*, 17−23.

(4) Soulard, M.; Patarin, J.; Eroshenko, V.; Regis, R. C. Molecular Spring or Bumper: a New Application for Hydrophobic Zeolitic Materials. *Stud. Surf. Sci. Catal.* **2004**, *154*, 1830−1837.

(5) Zhao, J.; Culligan, P. J.; Germaine, J. T.; Chen, X. Experimental Study on Energy Dissipation of Electrolytes in Nanopores. *Langmuir* **2009**, *25*, 12687−12696.

(6) Eroshenko, V.; Regis, R. C.; Soulard, M.; Patarin, J. Energetics: a New Field of Applications for Hydrophobic Zeolites. *J. Am. Chem. Soc.* **2001**, *123*, 8129−8130.

(7) Eroshenko, V.; Regis, R. C.; Soulard, M.; Patarin, J. The Heterogeneous Systems "Water-Hydrophobic Zeolites": New Molecular Springs. *C. R. Phys.* **2002**, *3*, 111−119.

(8) Trzpit, M.; Soulard, M.; Patarin, J. The Pure Silica Chabazite: a High Volume Molecular Spring at Low Pressure for Energy Storage. *Chem. Lett.* **2007**, *36*, 980−981.

(9) Trzpit, M.; Rigolet, S.; Paillaud, J. L.; Marichal, C.; Soulard, M.; Patarin, J. Pure Silica Chabazite Molecular Spring: a Structural Study on Water Intrusion-Extrusion Processes. *J. Phys. Chem. B* **2008**, *112*, 7257−7266.

(10) Tzanis, L.; Trzpit, M.; Soulard, M.; Patarin, J. High Pressure Water Intrusion Investigation of Pure Silica 1D Channel AFI, MTW and TON-type Zeolites. *Microporous Mesoporous Mater.* **2011**, *146*, 119−126.

(11) Saada, M. A.; Soulard, M.; Marler, B.; Gies, H.; Patarin, J. High-Pressure Water Intrusion Investigation of Pure Silica RUB-41 and S-SOD Zeolite Materials. *J. Phys. Chem. C* **2011**, *115*, 425−430.

(12) Tzanis, L.; Trzpit, M.; Soulard, M.; Patarin, J. Energetic Performances of Channel and Cage-type Zeosils. *J. Phys. Chem. C* **2012**, *116*, 20389−20395.

(13) Ryzhikov, A.; Khay, I.; Nouali, H.; Daou, T. J.; Patarin, J. Energetic Performances of Pure Silica STF and MTT-type Zeolites under High Pressure Water Intrusion. *RSC Adv.* **2014**, *4*, 37655.

(14) Tzanis, L.; Trzpit, M.; Soulard, M.; Patarin, J. Energetic Performances of STT-type Zeosil: Influence of the Nature of the Mineralizing Agent Used for the Synthesis. *J. Phys. Chem. C* **2012**, *116*, 4802−4808.

(15) Ievtushenko, O. V.; Eroshenko, V.; Grosu, Y. G.; Nedelec, J. M.; Grolier, J. P. E. Evolution of the Energetic Characteristics of {Silicalite-1 + Water} Repulsive Clathrates in a Wide Temperature Range. *Phys. Chem. Chem. Phys.* **2013**, *15*, 4451.

(16) Gokulakrishnan, N.; Parmentier, J.; Trzpit, M.; Vonna, L.; Paillaud, J. L.; Soulard, M. Intrusion/Extrusion of Water into Organic Grafted SBA-15 Silica Materials for Energy Storage. *J. Nanosci. Nanotechnol.* **2013**, *13*, 2847−2852.

(17) Trzpit, M.; Soulard, M.; Patarin, J. Water Intrusion in Mesoporous Silicalite-1: an Increase of the Stored Energy. *Microporous Mesoporous Mater.* **2009**, *117*, 627−634.

(18) Cao, G. Working Mechanism of Nanoporous Energy Absorption System under High Speed Loading. *J. Phys. Chem. C* **2012**, *116*, 8278−8286.

(19) Guillemot, L.; Galarneau, A.; Vigier, G.; Abensur, T.; Charlaix, E. New Device to Measure Intrusion/Extrusion Cycles of Lyophobic Heterogeneous Systems. *Rev. Sci. Instrum.* **2012**, *83*, 105105.

(20) Furukawa, H.; Ko, N.; Go, Y. B.; Aratani, N.; Choi, S. B.; Choi, E.; Yazaydin, A. O.; Snurr, R. Q.; O'Keeffe, M.; Kim, J.; et al. Ultrahigh Porosity in Metal-Organic Frameworks. *Science* **2010**, *329*, 424−428.

(21) Furukawa, H.; Cordova, K. E.; O'Keeffe, M.; Yaghi, O. M. The Chemistry and Applications of Metal-Organic Frameworks. *Science* **2013**, *341*, 1230444.

DOI: 10.1021/acs.jpcc.7b08999
J. Phys. Chem. C 2018, 122, 3846−3855

(22) Kong, X.; Deng, H.; Yan, F.; Kim, J.; Swisher, J. A.; Smit, B.; Yaghi, O. M.; Reimer, J. A. Mapping of Functional Groups in Metal-Organic Frameworks. *Science* **2013**, *341*, 882−885.
(23) Banerjee, R.; Furukawa, H.; Britt, D.; Knobler, C.; O'Keeffe, M.; Yaghi, O. M. Control of Pore Size and Functionality in Isoreticular Zeolitic Imidazolate Frameworks and Their Carbon Dioxide Selective Capture Properties. *J. Am. Chem. Soc.* **2009**, *131*, 3875−3877.
(24) Li, Y.; Zhou, K.; He, M.; Yao, J. Synthesis of ZIF-8 and ZIF-67 Using Mixed-Base and Their Dye Adsorption. *Microporous Mesoporous Mater.* **2016**, *234*, 287−292.
(25) Phan, A.; Doonan, C. J.; Uribe-Romo, F. J.; Knobler, C. B.; O'Keeffe, M.; Yaghi, O. M. Synthesis, Structure, and Carbon Dioxide Capture Properties of Zeolitic Imidazolate Frameworks. *Acc. Chem. Res.* **2010**, *43*, 58−67.
(26) Ortiz, G.; Nouali, H.; Marichal, C.; Chaplais, G.; Patarin, J. Energetic Performances of the Metal-Organic Framework ZIF-8 Obtained Using High Pressure Water Intrusion-Extrusion Experiments. *Phys. Chem. Chem. Phys.* **2013**, *15*, 4888−4891.
(27) Ortiz, G.; Nouali, H.; Marichal, C.; Chaplais, G.; Patarin, J. Energetic Performances of "ZIF-71-Aqueous Solution" Systems: a Perfect Shock-Absorber with Water. *J. Phys. Chem. C* **2014**, *118*, 21316−21322.
(28) Khay, I.; Chaplais, G.; Nouali, H.; Ortiz, G.; Marichal, C.; Patarin, J. Assessment of the Energetic Performances of Various ZIFs with SOD and RHO Topology Using High Pressure Water Intrusion-Extrusion Experiments. *Dalton. Trans.* **2016**, *45*, 4392−4400.
(29) Khay, I.; Chaplais, G.; Nouali, H.; Marichal, C.; Patarin, J. Water Intrusion-Extrusion Experiments in ZIF-8: Impacts of the Shape and Particle Size on the Energetic Performances. *RSC Adv.* **2015**, *5*, 31514−31518.
(30) Grosu, Y.; Mierzwa, M.; Eroshenko, V. A.; Pawlus, S.; Chorążewski, M.; Nedelec, J.-M.; Grolier, J.-P. E. Mechanical, Thermal, and Electrical Energy Storage in a Single Working Body: Electrification and Thermal Effects upon Pressure-Induced Water Intrusion−Extrusion in Nanoporous Solids. *ACS Appl. Mater. Interfaces* **2017**, *9*, 7044−7049.
(31) Han, A.; Lu, W.; Kim, T.; Punyamurtula, V. K.; Qiao, Y. The Dependence of Infiltration Pressure and Volume in Zeolite Y on Potassium Chloride Concentration. *Smart Mater. Struct.* **2009**, *18*, 024005−024010.
(32) Ortiz, G.; Nouali, H.; Marichal, C.; Chaplais, G.; Patarin, J. Versatile Energetic Behavior of ZIF-8 upon High Pressure Intrusion-Extrusion of Aqueous Electrolyte Solutions. *J. Phys. Chem. C* **2014**, *118*, 7321−7328.
(33) Tzanis, L.; Nouali, H.; Daou, T. J.; Soulard, M.; Patarin, J. Influence of the Aqueous Medium on the Energetic Performances of Silicalite-1. *Mater. Lett.* **2014**, *115*, 229−232.
(34) Soulard, M.; Patarin, J. Procédé pour le Stockage d'Energie Haute Pression par Solvatation. Fr. Pat. FR1154707, 2011.
(35) Arletti, R.; Ronchi, L.; Quartieri, S.; Vezzalini, G.; Ryzhikov, A.; Nouali, H.; Daou, T. J.; Patarin, J. Intrusion-Extrusion Experiments of $MgCl_2$ Aqueous Solution in Pure Silica Ferrierite: Evidence of the Nature of Intruded Liquid by In Situ High Pressure Synchroton X-ray Powder Diffraction. *Microporous Mesoporous Mater.* **2016**, *235*, 253−260.
(36) Michelin-Jamois, M.; Picard, C.; Charlaix, E.; Vigier, G. Osmotic Pressure Effects Upon Intrusion of Liquid Electrolytes Inside Hydrophobic MOFs. *Phys. Chem.* **2014**, arXiv: 1404.5318v1 [physics. chem-ph].
(37) Li, K.; Olson, D. H.; Seidel, J.; Emge, T. J.; Gong, H.; Zeng, H.; Li, J. Zeolitic Imidazolate Frameworks for Kinetic Separation of Propane and Propene. *J. Am. Chem. Soc.* **2009**, *131*, 10368−10369.
(38) Rouquerol, J.; Llewellyn, P.; Rouquerol, F. Is the BET Equation Applicable to Microporous Adsorbents? *Stud. Surf. Sci. Catal.* **2007**, *160*, 49−56.
(39) Walton, K. S.; Snurr, R. Q. Applicability of the BET Method for Determining Surface Areas of Microporous Metal-Organic Frameworks. *J. Am. Chem. Soc.* **2007**, *129*, 8552−8556.
(40) Park, K. S.; Ni, Z.; Côte, A. P.; Choi, J. Y.; Huang, R.; Uribe-Romo, F. J.; Chae, H. K.; O'Keeffe, M.; Yaghi, O. M. Exceptional Chemical and Thermal Stability of Zeolitic Imidazolate Frameworks. *Proc. Natl. Acad. Sci. U. S. A.* **2006**, *103*, 10186−10191.
(41) Fairen-Jimenez, D.; Moggach, S. A.; Wharmby, M. T.; Wright, P. A.; Parsons, S.; Düren, T. Opening the Gate: Framework Flexibility in ZIF-8 Explored by Experiments and Simulations. *J. Am. Chem. Soc.* **2011**, *133*, 8900−8902.
(42) Ania, C. O.; García-Pérez, E.; Haro, M.; Gutiérrez-Sevillano, J. J.; Valdés-Solís, T.; Parra, J. B.; Calero, S. Understanding Gas-Induced Structural Deformation of ZIF-8. *J. Phys. Chem. Lett.* **2012**, *3*, 1159−1164.
(43) Tian, T.; Wharmby, M. T.; Parra, J. B.; Ania, C. O.; Fairen-Jimenez, D. Role of Crystal Size on Swing-Effect and Adsorption Induced Structure Transition of ZIF-8. *Dalton Trans.* **2016**, *45*, 6893−6900.
(44) Tanaka, S.; Fujita, K.; Miyake, Y.; Miyamoto, M.; Hasegawa, Y.; Makino, T.; Van der Perre, S.; Cousin Saint Remi, J.; Van Assche, T.; Baron, G. V.; et al. Adsorption and Diffusion Phenomena in Crystal Size Engineered ZIF-8 MOF. *J. Phys. Chem. C* **2015**, *119*, 28430−28439.
(45) Zhang, K.; Lively, R. P.; Dose, M. E.; Brown, A. J.; Zhang, C.; Chung, J.; Nair, S.; Koros, W. J.; Chance, R. R. Alcohol and Water Adsorption in Zeolitic Imidazolate Frameworks. *Chem. Commun.* **2013**, *49*, 3245−3247.
(46) Calleja, G.; Botas, J. A.; Martos, C.; Orcajo, G.; Villajos, J. A. Effect of Ion-Exchange Modification on Hydrogen and Carbon Dioxide Adsorption Behaviour of RhoZMOF Material. *Adsorpt. Sci. Technol.* **2012**, *30*, 793−806.
(47) Liu, L.; Chen, X.; Lu, W.; Han, A.; Qiao, Y. Infiltration of Electrolytes in Molecular-Sized Nanopores. *Phys. Rev. Lett.* **2009**, *102*, 184501−184504.
(48) Bostrom, M.; Ninham, B. W. Contributions from Dispersion and Born Self-Free Energies to the Solvation Energies of Salt Solutions. *J. Phys. Chem. B* **2004**, *108*, 12593−12595.
(49) Han, S. S.; Choi, S.-H.; Goddard, W. A. Improved H_2 Storage in Zeolitic Imidazolate Frameworks Using Li^+, Na^+, and K^+ Dopants, with an Emphasis on Delivery H_2 Uptake. *J. Phys. Chem. C* **2011**, *115*, 3507−3512.
(50) Grosu, Y.; Renaudin, G.; Eroshenko, V.; Nedelec, J.-M.; Grolier, J.-P. E. Synergetic Effect of Temperature and Pressure on Energetic and Structural Characteristics of {ZIF-8+ water} Molecular Spring. *Nanoscale* **2015**, *7*, 8803−8810.
(51) Grosu, Y.; Gomes, S.; Renaudin, G.; Grolier, J.-P. E.; Eroshenko, V.; Nedelec, J.-M. Stability of Zeolitic Imidazolate Frameworks: Effect of Forced Water Intrusion and Framework Flexibility Dynamics. *RSC Adv.* **2015**, *5*, 89498−89502.
(52) Rabasso, N. *Chimie Organique. Hétéroélements, Stratégies de Synthèse et Chimie Organométallique*; De Boeck: Bruxelles, 2006.

DOI: 10.1021/acs.jpcc.7b08999
J. Phys. Chem. C 2018, 122, 3846−3855

III. **Comments in the Light of Recently Published Results**

Fraux *et al*. studied, using molecular dynamic simulations, the properties of the LiCl aqueous solution when confined in the ZIF-8 nanopores.[14] The results obtained based on this study confirms that in the nanopores, the solvation degree of the ions is diminished (desolvation) and the formation of Li-Cl ion pairs is favored. Moreover, instead of being widely distributed in the porosity, the solvated ions are restricted to specific preferential locations, due to interactions with the imidazolate linker. This effect of preferential distribution is stronger for the Cl/water pairs than for the water/water (in the case of "pure" water intrusion−extrusion experiments) or Li/water pairs. The authors also note that the relatively small kinetic radius of lithium ions (2.1 Å) allows them to fit in smaller spaces, which results in even distribution of the cations in the nanopores and a consequent increase in the total entropy of the system. However, chlorine ions and water molecules are more polarizable than lithium, and interact more strongly with the aromatic linkers, which favors a highly organized arrangement. Finally, from a thermodynamic point of view, there is no free energy barrier for the intrusion of water molecules into the ZIF-8 pores. As for chlorine anions, the free energy profile reveals two barriers. These barriers can be correlated to the fact that there is not enough space inside the window to accommodate a Cl anion with 7 water molecules in the solvation shell, and the anion has to partially desolvate to pass through the 6-membered ring pore aperture of ZIF-8. Thus, it can be considered that the Cl anions have a kinetic barrier to entry in ZIF-8. Nevertheless, for Li cations, the results are different. Indeed, the solvation of Li cations by water is much stronger, and its solvation sphere is smaller in size compared to that of Cl anions. Therefore, lithium does not partially desolvate or rearrange to pass through the pores and the whole solvation sphere needs to go through a relatively small window, thus, making the barrier higher. In conclusion, molecular dynamic simulations give some very interesting insights into the intrusion of electrolytes, in particular LiCl, in ZIF-8 and confirm some of our assumptions of desolvation and the interaction of the electrolytes from the non-wetting liquid with the imidazolate linker.

References

1. Mortada, B.; Chaplais, G.; Veremeienko, V.; Nouali, H.; Marichal, C.; Patarin, J., Energetic Performances of ZIF-8 Derivatives: Impact of the Substitution (Me, Cl, or Br) on Imidazolate Linker. *J. Phys. Chem. C* **2018,** *122*, 3846-3855.

2. Li, K.; Olson, D. H.; Seidel, J.; Emge, T. J.; Gong, H.; Zeng, H.; Li, J., Zeolitic Imidazolate Frameworks for Kinetic Separation of Propane and Propene. *J. Am. Chem. Soc.* **2009,** *131*, 10368-10369.

3. Chaplais, G.; Fraux, G.; Paillaud, J.-L.; Marichal, C.; Nouali, H.; Fuchs, A. H.; Coudert, F.-X.; Patarin, J., Impacts of the Imidazolate Linker Substitution (CH_3, Cl, or Br) on the Structural and Adsorptive Properties of ZIF-8. *J. Phys. Chem. C* **2018,** *122*, 26945-26955.

4. Morris, W.; Stevens, C. J.; Taylor, R. E.; Dybowski, C.; Yaghi, O. M.; Garcia-Garibay, M. A., NMR and X-ray Study Revealing the Rigidity of Zeolitic Imidazolate Frameworks. *J. Phys. Chem. C* **2012,** *116*, 13307-13312.

5. Fairen-Jimenez, D.; Moggach, S. A.; Wharmby, M. T.; Wright, P. A.; Parsons, S.; Duren, T., Opening the Gate: Framework Flexibility in ZIF-8 Explored by Experiments and Simulations. *J. Am. Chem. Soc.* **2011,** *133*, 8900-8902.

6. Ania, C. O.; Garcia-Perez, E.; Haro, M.; Gutierrez-Sevillano, J. J.; Valdes-Solis, T.; Parra, J. B.; Calero, S., Understanding Gas-Induced Structural Deformation of ZIF-8. *J. Phys. Chem. Lett.* **2012,** *3*, 1159-1164.

7. Moggach, S. A.; Bennett, T. D.; Cheetham, A. K., The Effect of Pressure on ZIF-8: Increasing Pore Size with Pressure and the Formation of a High-Pressure Phase at 1.47 GPa. *Angew. Chem., Int. Ed.* **2009,** *48*, 7087-7089.

8. Ortiz, G.; Nouali, H.; Marichal, C.; Chaplais, G.; Patarin, J., Energetic Performances of the Metal–Organic Framework ZIF-8 Obtained Using High Pressure Water Intrusion–Extrusion Experiments. *Phys. Chem. Chem. Phys.* **2013,** *15*, 4888-4891.

9. Ortiz, G.; Nouali, H.; Marichal, C.; Chaplais, G.; Patarin, J., Versatile Energetic Behavior of ZIF-8 upon High Pressure Intrusion-Extrusion of Aqueous Electrolyte Solutions. *J. Phys. Chem. C* **2014,** *118*, 7321-7328.

10. Ryzhikov, A.; Khay, I.; Nouali, H.; Daou, T. J.; Patarin, J., Drastic Change of the Intrusion-Extrusion Behavior of Electrolyte Solutions in Pure Silica *BEA-Type Zeolite. *Phys. Chem. Chem. Phys.* **2014,** *16*, 17893-17899.

11. Calleja, G.; Botas, J. A.; Martos, C.; Orcajo, G.; Villajos, J. A., Effect of Ion-Exchange Modification on Hydrogen and Carbon Dioxide Adsorption Behaviour of RhoZMOF Material. *Adsorpt. Sci. Technol.* **2012,** *30*, 793-806.

12. Liu, L.; Chen, X.; Lu, W.; Han, A.; Qiao, Y., Infiltration of Electrolytes in Molecular-Sized Nanopores. *Phys. Rev. Lett.* **2009,** *102*, 184501/1-184501/4.

13. Bostroem, M.; Ninham, B. W., Contributions from Dispersion and Born Self-Free Energies to the Solvation Energies of Salt Solutions. *J. Phys. Chem. B* **2004,** *108*, 12593-12595.

14. Fraux, G.; Boutin, A.; Fuchs, A. H.; Coudert, F.-X., Structure, Dynamics, and Thermodynamics of Intruded Electrolytes in ZIF-8. *J. Phys. Chem. C* **2019,** *123*, 15589-15598.

Chapter 4: Synthesis and Study of the Energetic Performances of ZIFs of RHO Topology

The literature review of this thesis manuscript (Chapter 1) demonstrates the significant impact of the topology on the energetic performances of both zeolites and MOFs. The SOD topology has been widely studied in intrusion−extrusion experiments (Chapters 1 and 3), whereas the RHO topology was only studied for ZIF-71, where the "ZIF-71−water" system displays perfect shock-absorber behavior, with a stored energy value of 26 J g^{-1}, i.e. twice the value registered for the "ZIF-8–water" system.[1-2] Furthermore, the results obtained from the intrusion−extrusion experiments carried out on ZIF-8 derivatives of SOD framework-type topology (Chapter 3), reveal the effect of the substituent present on the imidazolate linker on the energetic performances of the corresponding lyophobic heterogeneous system (LHS).[3]

Thus, a part of this thesis work was devoted to the further investigation of RHO-type ZIF materials in intrusion−extrusion experiments, and the study of the influence of the substitution on the imidazolate linker on the energetic performances of the related systems. In this regard, two newly reported ZIFs, i.e. ZIF-25 and MAF-6,[4-6] were selected for this study. Our research also included ZIF-71, which was integrated into new LHSs that were not investigated in intrusion−extrusion experiments prior to this work, in addition to a new isoreticular analog of ZIF-71, MAF-6, and ZIF-25, named ZIF-71_Br_2, which was attempted to be prepared purely.

This chapter is divided into two parts. The first part is devoted to the study of the energetic performances of ZIF-71 and MAF-6 in water and LiCl 20 M aqueous solution intrusion−extrusion experiments, which evidences phase transformation phenomena that were not reported in the literature prior to our work. Consequently, owing to the novelty of the obtained results, they were published this year (Article 2).[7] On the other hand, Part II of this chapter is dedicated to the optimization of the syntheses of the porous ZIF-25 and ZIF-71_Br_2 materials, in the aim of exploring them in high-pressure intrusion−extrusion experiments of water and LiCl 20 M aqueous solution.

I. Phase Transformations of Metal-Organic Frameworks MAF-6 and ZIF-71 during Intrusion−Extrusion Experiments

Herein, we report the water and LiCl 20 M aqueous solution intrusion−extrusion experiments realized on MAF-6 and ZIF-71. Indeed, MAF-6, a recently reported (2016) ZIF material,[6] was

selected owing to its structural characteristics (large pore volume, pore size, and pore aperture) that were expected to lead to a large amount of stored/absorbed energy, together with a relatively low intrusion pressure (more suitable for practical applications). Furthermore, according to the literature, MAF-6 exhibits a strong hydrophobic character that is highly desired in water and aqueous solution intrusion−extrusion experiments.[6] In the aim of comparison, the energetic performance of the "ZIF-71−water" system is recalled, whereas that of the "ZIF-71−LiCl 20 M aqueous solution" system is investigated for the first time.

A. Summary of Article 2

This publication reports the synthesis and characterization of two hydrophobic zeolitic-imidazolate framework (ZIF) materials, MAF-6 and ZIF-71, which are prepared in the aim of studying their energetic behaviors in high pressure intrusion−extrusion experiments using water and LiCl 20 M aqueous solution as non-wetting liquids. The materials are made up of zinc cations bridged by 2-ethylimidazolate (eim) and 4,5-dichloroimidazolate (dcim) linkers for MAF-6 and ZIF-71, respectively. Both ZIF materials display a RHO framework topology with large cages (16.5-16.8 and 18.1 Å in diameter for ZIF-71 and MAF-6, respectively) delimited by 4-, 6-, and 8-membered ring pore apertures (4.2-4.8 and 7.6 Å in diameter for ZIF-71 and MAF-6, respectively) (Scheme 1).

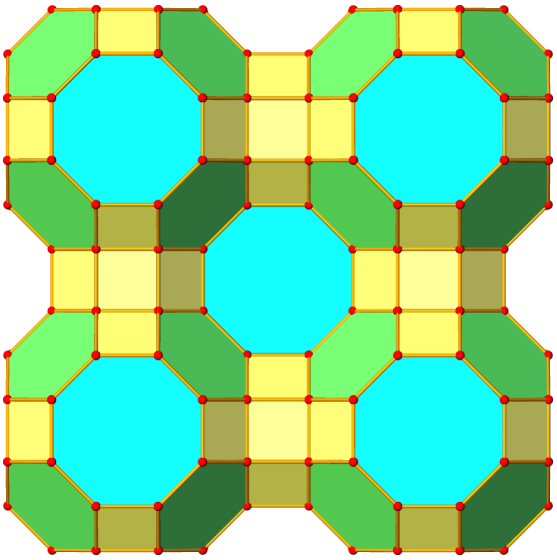

Scheme 1. Representation of the RHO framework topology. In red, zinc cations. In yellow, green, and blue; the 4-, 6-, and 8-membered ring pore apertures, respectively.

For both the MAF-6 and ZIF-71 materials, the intrusion−extrusion experiments were first realized up to a maximum pressure of 350 or 300 MPa, respectively. Nevertheless, in order to understand the effect of the applied pressure on the structure of the studied materials, complementary

experiments were conducted under lower pressures. In all cases, the post-intruded samples were characterized mainly using X-ray diffraction (XRD) and N_2 sorption analyses.

The "ZIF-71–water" system was already reported to display perfect shock-absorber behavior.[1] However, our study showed that with LiCl 20 M aqueous solution, ZIF-71 is transformed into the dense ZIF-72 phase; a ZIF-71 polymorph of lcs topology. This structural transformation was proven to occur under the combined effect of high pressure and the non-wetting liquid during intrusion−extrusion experiments. The phase transformation phenomenon was associated with a partial intrusion of the non-wetting liquid molecules into the porosity, where they seem to remain entrapped even after the release of the applied mechanical pressure, as revealed by thermogravimetric (TG) and inductively-coupled plasma (ICP) analyses (Section I. C.). On the pressure−volume ($P-V$) diagrams, only one volume variation step is observed on the intrusion curve of the first intrusion−extrusion cycle, which indicates the irreversibility of the phase transformation and intrusion phenomena.

As for the "MAF-6–water" and "MAF-6–LiCl 20 M aqueous solution" systems, the $P-V$ diagrams also reveal only one volume variation step (observed on the intrusion curve of the first intrusion−extrusion cycle), which based on TG and ICP analyses corresponds, in part, to the intrusion of the non-wetting liquid molecules into the porosity. Besides, similar to the case of the "ZIF-71−LiCl 20 M aqueous solution" system, for both the "MAF-6–water" and "MAF-6–LiCl 20 M aqueous solution" systems, the intrusion is associated with a phase transformation and, more precisely, with a partial collapse of the structure, resulting in the formation of a highly crystalline, but, nonporous phase that is called phase X. It is worthy to note that the phase X does not correspond to any of the MAF-6 polymorphs (MAF-32 or ZIF-14 (also called MAF-5) of quartz and ANA topologies, respectively) nor to the organic precursor molecules (Heim). The probable identity of the newly formed phase X and its formation mechanism will be further discussed in Section I. B.

Finally, it is important to highlight that this work confirms that the addition of electrolytes to the non-wetting liquid increases the intrusion pressure (higher intrusion pressure with LiCl 20 M aqueous solution compared to water). Moreover, for the first time, irreversible crystal phase transformation phenomenona are observed during intrusion−extrusion experiments, leading to a mixture of shock-absorber and bumper behaviors for the "MAF-6−water" system and bumper behavior for both the "MAF-6−" and "ZIF-71−LiCl 20 M aqueous solution" systems. The originality of this work is illustrated in proving that the detected volume variation on the $P–V$ diagram, usually related to the intrusion of the non-wetting liquid into the porosity of the material, can also be attributed, in some particular cases, to a complete or partial phase transformation, potentially associated to an intrusion phenomenon.

The full text and supporting information of Article 2 entitled “Phase Transformations of Metal-Organic Frameworks MAF-6 and ZIF-71 during Intrusion-Extrusion Experiments” that was published in the Journal of Physical Chemistry C in 2019 are presented within the next eighteen pages.

THE JOURNAL OF PHYSICAL CHEMISTRY C

Article

Cite This: J. Phys. Chem. C 2019, 123, 4319−4328

pubs.acs.org/JPCC

Phase Transformations of Metal−Organic Frameworks MAF-6 and ZIF-71 during Intrusion−Extrusion Experiments

Boushra Mortada,[†,‡] Gérald Chaplais,*[,†,‡] Habiba Nouali,[†,‡] Claire Marichal,[†,‡] and Joël Patarin[†,‡]

[†]Université de Haute-Alsace, CNRS, Institut de Science des Matériaux de Mulhouse (IS2M), UMR 7361, Axe Matériaux à Porosité Contrôlée (MPC), UMR 7361, F-68100 Mulhouse, France

[‡]Université de Strasbourg, 67000 Strasbourg, France

Supporting Information

ABSTRACT: In this work, the energetic behaviors of two zeolitic imidazolate framework (ZIF) materials, ZIF-71 and the highly porous MAF-6, of RHO topology are studied in high-pressure intrusion−extrusion experiments using LiCl 20 M aqueous solution and/or water as nonwetting liquids. During the intrusion−extrusion experiments, both MAF-6 and ZIF-71 structures undergo phase transformations under the combined effects of high pressure and the nonwetting liquid. For the "MAF-6−H_2O" system, the volume variation step observed on the intrusion curve of the first intrusion−extrusion cycle partially corresponds to the intrusion of water molecules inside the MAF-6 pores associated with a partial and irreversible phase transformation of MAF-6 into a nonporous and unidentified phase X. When the pressure is released, that is, when the experiment is stopped at the end of the volume variation step and the system returns to atmospheric pressure, the intruded water molecules are expelled from the porosity of the remaining MAF-6 material, and the "MAF-6−H_2O" system, therefore, displays a mixture of shock-absorber and bumper behaviors. In the case of both "MAF-6−" and "ZIF-71−LiCl 20 M aqueous solution" systems, the volume variation step is shifted to a higher pressure range, indicating that the intrusion of the nonwetting liquid molecules occurs at a higher pressure because of the presence of electrolytes. For the "MAF-6−LiCl 20 M aqueous solution" system, a mixture of MAF-6 and phase X is obtained at the end of the volume variation step, which probably indicates energetic behavior similar to the one observed for the "MAF-6−H_2O" system (i.e., a mixture of shock-absorber and bumper behaviors). In the case of the "ZIF-71−LiCl 20 M aqueous solution" system, the volume variation step observed on the intrusion curve of the first intrusion−extrusion cycle corresponds to a phase transformation. At the end of this step, the ZIF-71 structure is completely transformed into ZIF-72 (lcs). The "ZIF-71−LiCl 20 M aqueous solution" system, thus, displays bumper behavior, as the supplied mechanical energy is absorbed during the irreversible phase transformation phenomenon.

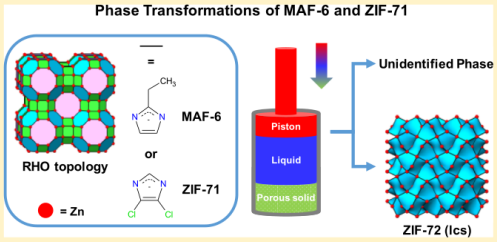

1. INTRODUCTION

Owing to the growing need for renewable energy sources, mechanical energy storage through intrusion−extrusion of nonwetting liquids under high pressure in lyophobic porous materials has been widely explored by Eroshenko.[1−3] Intrusion−extrusion phenomena in lyophobic heterogeneous systems (also known as LHS and consisting of the lyophobic porous material surrounded by the nonwetting liquid) involve two steps. In the intrusion step, an external pressure (mechanical energy) is applied to provoke the penetration (intrusion) of the nonwetting liquid molecules into the porosity of the material. During this step, the supplied mechanical energy is converted into interfacial energy (resulting from the interactions between the nonwetting liquid molecules and the pore walls of the solid material).[4,5] In the extrusion step, the applied pressure is progressively decreased, and depending on the nature of both the porous material and the nonwetting liquid, the latter is either totally/partially retained in the pores or is completely expelled from the solid. The system can, hence, absorb, dissipate, or restore the supplied mechanical energy, thereby behaving as a bumper, shock-absorber, or molecular spring, respectively.

The energetic performance of pure silica zeolites (zeosils) was first investigated in intrusion−extrusion experiments by our team in 2001.[6] Since then, numerous "zeosil−nonwetting liquid" systems have been studied.[7,8] With the aim of increasing the stored energy, materials that are characterized by a porous volume that exceeds that of zeosils are targeted. Among these materials, zeolitic imidazolate frameworks (ZIFs), a subclass of metal−organic frameworks, have already been proven to be efficient in intrusion−extrusion experiments.[9−14] ZIFs are made mainly from divalent metal cations (Zn^{2+}, Co^{2+}, etc.) that are tetrahedrally coordinated to anionic and ditopic imidazolate moieties or its derivatives.[15−20] ZIFs

Received: December 14, 2018
Revised: January 17, 2019
Published: January 30, 2019

DOI: 10.1021/acs.jpcc.8b12047
J. Phys. Chem. C 2019, 123, 4319−4328

are known for being highly crystalline and porous (with a porosity that exceeds that of zeolites), and they are also characterized by their high chemical and thermal stabilities compared to other MOF materials.[15,16,20] Our team was the first to investigate the energetic performance of ZIF material-based systems using intrusion−extrusion experiments, with the primary study of "ZIF-8−H_2O" system,[9] which has paved the way to complementary work.[21,22]

In addition to the high porosity and stability, the materials employed in intrusion−extrusion experiments must be characterized by a lyophobic character.[9] In the case where water or aqueous electrolyte solutions are used as nonwetting liquids, the intruded−extruded materials should exhibit hydrophobic pore surfaces, so as to prevent the adsorption of water molecules at low pressures.[13] In a recent study, we investigated in high-pressure intrusion−extrusion experiments, the energetic behaviors of three highly hydrophobic ZIF materials of SOD topology: ZIF-8_CH_3 (also commonly known as ZIF-8) and its halogenated derivatives, ZIF-8_Cl and ZIF-8_Br.[14] This work showed that the intrusion pressure increases when switching from water to aqueous electrolyte solutions, which is in agreement with the results previously published in the literature concerning the effect of addition of electrolytes to the nonwetting liquid on the intrusion pressure.[10,11,23,24]

On another note, MAF-6 and ZIF-71 are two other ZIF materials that are known for their very low water-adsorption capacities, indicating their hydrophobic character.[25−27] Both materials possess a RHO framework topology and are made from zinc cations that are bridged by 2-ethylimidazolate and 4,5-dichloroimidazolate linkers for MAF-6 and ZIF-71, respectively.[28,29] The energetic performance of ZIF-71 has already been studied by Ortiz et al. by carrying out intrusion−extrusion experiments of water and KCl aqueous electrolyte solutions (1 and 4 M).[11] However, the energetic behavior of this ZIF material was not investigated using LiCl solutions. In another study performed on ZIF-8, it was shown that the intrusion pressure is higher for LiCl 4 M aqueous electrolyte solution compared to that for KCl 4 M.[10] This could be attributed to the larger hydrated diameter of the lithium species compared to that of potassium or to the smaller size of the lithium cation compared to that of potassium ($r_{Li^+} < r_{Na^+} < r_{K^+}$).[30,31] Moreover, a higher pressure is needed to break the solvation bonds that are stronger in the case of LiCl than in the case of KCl salts.[32] As higher intrusion pressures imply generally higher energy values, employing LiCl aqueous solution as a nonwetting liquid in intrusion−extrusion experiments appears pertinent to obtain systems with high energy.

Herein, we study the energetic behavior of ZIF-71 using LiCl 20 M aqueous solution as the nonwetting liquid and report the results previously obtained from water intrusion−extrusion experiments.[11] We also study for the first time the energetic behavior of MAF-6, of high pore volume (0.61 $cm^3 g^{-1}$),[27] using both water and LiCl 20 M aqueous solution as nonwetting liquids.

2. EXPERIMENTAL SECTION

2.1. Materials. *2.1.1. Reagents and ZIF Materials.* Zinc oxide (ZnO, 99%) and the solvents, methanol (MeOH, 99.9%) and ethanol (EtOH, 99.9%), were purchased from Carlo Erba. Anhydrous zinc acetate ($Zn(O_2CCH_3)_2$, 99%), 4,5-dichloroimidazole (Hdcim, 98%), and 2-ethylimidazole (Heim, 98%) were supplied by Acros Organics, Alfa Aesar, and TCI, respectively. As for the ammonium hydroxide solution (NH_3, 31.5%) and cyclohexane (99%), they were provided by Sigma-Aldrich and Biosolve, respectively. Deionized water was also used in the synthesis of MAF-6. All reagents and solvents were used as supplied and without further purification. ZIF-71 was prepared based on the synthesis procedure described by Lively et al.,[25] nevertheless, by up-scaling 8 times, whereas MAF-6 was prepared based on the synthesis procedure described by He et al. by up-scaling 4 times.[27] Importantly, in the MAF-6 synthesis, we modified the metal source and used zinc oxide instead of zinc hydroxide. Ethanol was also substituted for methanol.

2.1.2. Synthesis of MAF-6. The synthesis was carried out at room temperature following a rapid solution mixing procedure. A solution of concentrated aqueous ammonia (31.5%, 3710 mmol, 200 g), water (54 g), and ZnO (14 mmol, 1.14 g) (S_1) was added into an ethanol solution (5162 mmol, 238 g) of Heim (28.20 mmol, 2.70 g) premixed with cyclohexane (129.76 mmol, 10.92 g) (S_2). The final molar composition of the reaction mixture is 1 Zn/2 Heim/265 NH_3/370 EtOH/750 H_2O/9.26 cyclohexane. S_1 was added to S_2 in a dropwise manner over a time period of 25 min and with continuous stirring. The reaction mixture was then stirred over a 45 min period, with manual shaking after 15 min and then after 30 min. The as-synthesized product (white powder, 38% yield, 1358 mg) was recovered by filtration, washed with methanol (100 mL), and then left to dry in air.

2.1.3. Synthesis of ZIF-71. Two solutions, S_3 and S_4, were prepared by dissolving anhydrous zinc acetate (3.20 mmol, 0.60 g) in methanol (6023.70 mmol, 96.50 g) (S_3) and Hdcim (12.80 mmol, 1.75 g) also in methanol (6023.70 mmol, 96.50 g) (S_4). The final molar composition of the reaction mixture is 1 Zn/4 Hdcim/1854 MeOH. S_3 was added to S_4, and the reaction mixture was let to stand for 24 h at room temperature. The as-synthesized product was recovered by filtration, washed with methanol (2000 mmol, 64 g), and then left to dry in air (white powder, 80% yield, 874 mg).

2.2. Characterization Techniques. *2.2.1. Powder X-ray Diffraction.* X-ray diffraction (XRD) patterns of the different samples were recorded in the transmission mode on a STOE STADI-P diffractometer equipped with a curved germanium (111) primary monochromator and a linear position-sensitive detector (6° in 2θ) using Cu Kα_1 radiation (λ = 1.5406 Å). Measurements were achieved for 2θ angle values in the 3−35° range, with a step of 0.04° in 2θ.

2.2.2. Nitrogen Adsorption−Desorption Measurements. Nitrogen adsorption−desorption isotherms were performed at 77 K using a Micromeritics ASAP 2420 apparatus. Prior to adsorption measurements, the samples were outgassed at 423 K for 12 h under vacuum. The specific surface area (S_{BET}) was calculated according to the criteria given in the literature[33,34] and by using the Brunauer−Emmett−Teller (BET) method applied in the $0.004 \le p/p^\circ \le 0.018$ and $0.005 \le p/p^\circ \le 0.010$ ranges for MAF-6 and ZIF-71, respectively. The microporous volumes (V_μ) were determined according to the *t*-plot method.

2.2.3. Intrusion−Extrusion Experiments. The LiCl 20 M aqueous solution was prepared by dissolving the corresponding amount of salt in deionized water. The intrusion−extrusion experiments of water and aqueous electrolyte solutions in the ZIF materials were performed at room temperature over three cycles (counting 532 measurement points for a duration of 3 h) by using a modified mercury porosimeter (Micromeritics

DOI: 10.1021/acs.jpcc.8b12047
J. Phys. Chem. C 2019, 123, 4319−4328

model AutoPore IV).[35] Some complementary experiments, on the other hand, were also realized and involved only one intrusion−extrusion cycle. The intruded and extruded volumes (V_{int}, V_{ext}) and pressures (P_{int}, P_{ext}) were determined as follows: $V_{int} = V_{inte} - V_{intb}$ and $V_{ext} = V_{extb} - V_{exte}$, where V_{intb} and V_{inte} refer to the volume values at the beginning and end of the intrusion step, respectively. Similarly, V_{extb} and V_{exte} correspond to the volume values at the beginning and end of the extrusion step, respectively. The values P_{int} and P_{ext} correspond to the pressure at half total volume variation. Pressure is expressed in megapascal (MPa) and volume in milliliter per gram of sample (mL g^{-1}). The energetic behavior of a LHS is classified as shock-absorber or spring based on complete extrusion of the intruded liquid from the solid with an energy yield lower or higher than 80%, respectively. Systems that involve no extrusion of the liquid are referred to as bumpers. After intrusion−extrusion experiments, the sample was recovered by filtration, washed with a few milliliters of water, and then dried in air.

2.2.4. Thermogravimetric Analyses. Thermogravimetric analyses (TGA) were carried out on a TG Mettler Toledo STARe apparatus, under air flow, with a heating rate of 2 °C min^{-1} from 30 to 900 °C.

3. RESULTS AND DISCUSSION

3.1. Characterization of the Parent MAF-6 and ZIF-71 Materials. The synthesized MAF-6 and ZIF-71 materials (parent materials) were characterized using XRD, N_2 adsorption−desorption, and TGA. The XRD patterns of the MAF-6 and ZIF-71 materials are given in Figure 1. For both materials, the experimental and theoretical XRD patterns (CCDC number/RefCode are 287182/MECWOH for MAF-6[28] and 671080/GITVIP for ZIF-71[29]) are similar. Both ZIF-71 and MAF-6 display a RHO topology and crystallize in the cubic symmetry. The structures are built from large cages (16.5−16.8 and 18.1 Å in diameter for ZIF-71 and MAF-6, respectively) with eight-membered ring cage apertures (diameter 4.2−4.8 and 7.6 Å for ZIF-71 and MAF-6, respectively), in addition to four- and six-membered ring pore apertures (Figure S1). On the basis of the results obtained from our data refinement, which are in agreement with those previously published in the literature,[28,29] MAF-6 belongs to the space group *Im*3*m* with a lattice constant $a \approx 29.3$ Å, whereas ZIF-71 belongs to the *Pm*3*m* space group with the lattice parameter $a \approx 28.6$ Å.

The N_2 adsorption−desorption isotherms of the two studied ZIF materials are reported in Figure 2. The isotherms of both parent materials adopt a Type I profile according to the IUPAC classification.[36] As expected (by referring to the literature), MAF-6 exhibits a higher microporous volume (of 0.61 cm^3 g^{-1}) than ZIF-71 (0.37 cm^3 g^{-1}). These results are consistent with the literature.[26,27]

The TG curves of the parent MAF-6 and ZIF-71 materials are reported in Figure 3. They show one main decomposition step at temperatures ranging between 350 and 530 °C for MAF-6 and between 380 and 670 °C for ZIF-71. These steps correspond to relative mass losses of 68 and 83% for MAF-6 and ZIF-71, respectively, and can be attributed to the degradation of the organic network, leading finally to the formation of ZnO. In the case of MAF-6, the total experimental and theoretical mass losses (determined based on the main decomposition step) are in agreement (68%), whereas for the case of ZIF-71, the total experimental mass loss

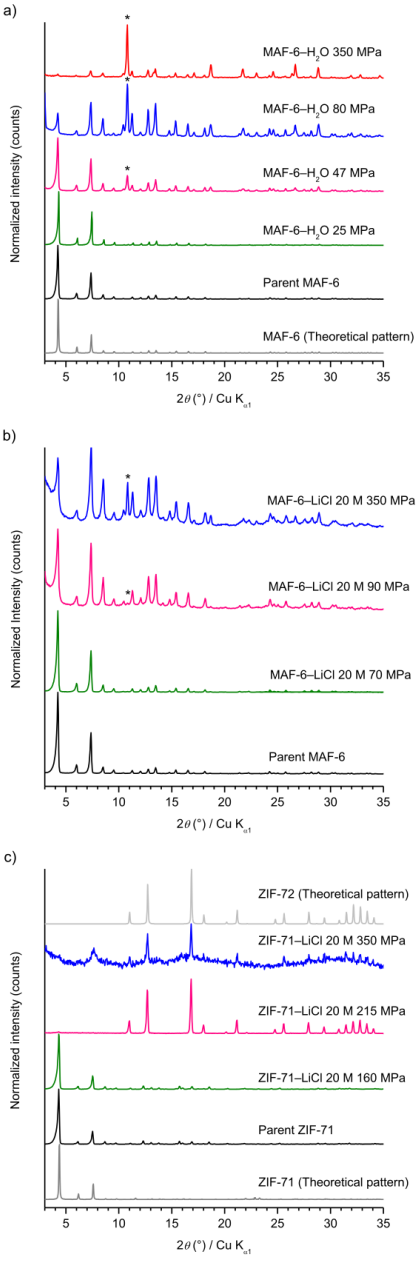

Figure 1. XRD patterns of the parent and postintruded MAF-6 samples at different pressures using (a) water and (b) LiCl 20 M aqueous solution as nonwetting liquids, and parent and postintruded ZIF-71 samples at different pressures using (c) LiCl 20 M aqueous solution as the nonwetting liquid. The theoretical XRD patterns of MAF-6, ZIF-71, and ZIF-72 are also reported for comparison. * denotes the main peak of the unidentified phase X.

DOI: 10.1021/acs.jpcc.8b12047
J. Phys. Chem. C 2019, 123, 4319−4328

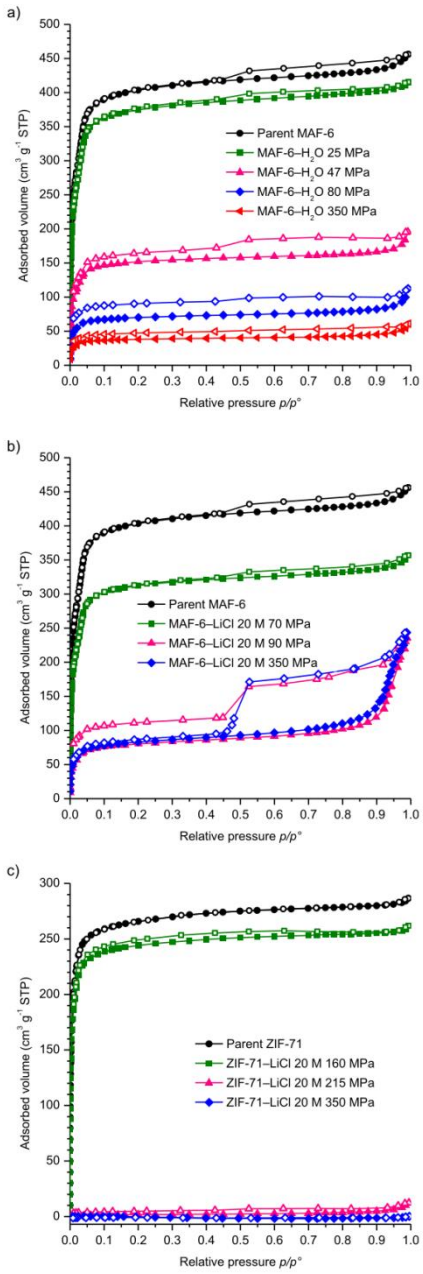

Figure 2. N_2 adsorption−desorption isotherms of the parent and postintruded MAF-6 samples at different pressures using (a) water and (b) LiCl 20 M aqueous solution as nonwetting liquids, and (c) parent and postintruded ZIF-71 samples at different pressures using LiCl 20 M aqueous solution as the nonwetting liquid. Filled and empty symbols correspond to the adsorption and desorption branches, respectively.

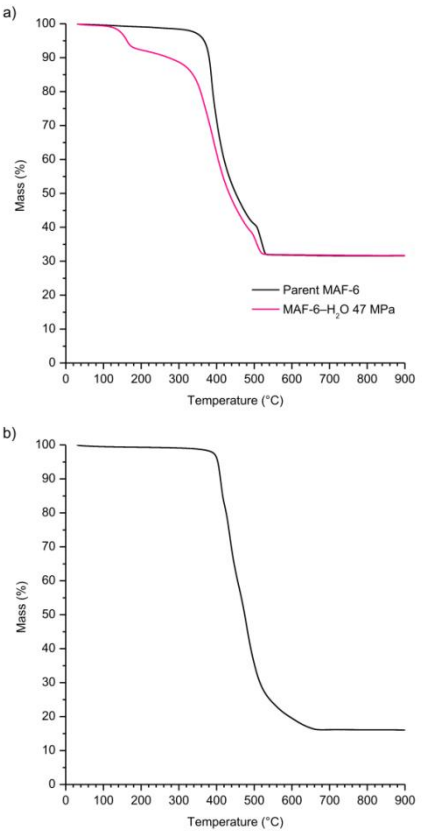

Figure 3. TG curves of (a) the parent and postintruded MAF-6 after intrusion of water at 47 MPa and (b) the parent ZIF-71 material.

(83%) is higher than the theoretical one (76%). It is important to note that similar behavior during TGA was observed previously for ZIF-71[11,13,37] and for the halogenated ZIF-8_Cl and ZIF-8_Br materials,[14] which could be attributed to the formation of volatile halogenated Zn species in addition to the ZnO residue at temperatures higher than 650 °C.

3.2. Intrusion−Extrusion Experiments. The intrusion−extrusion experiments were carried out using water and/or lithium chloride (20 M) aqueous solution as the nonwetting liquids. The concentration of the LiCl aqueous solution corresponds to its maximum solubility at room temperature. The pressure−volume ($P-V$) diagrams for the different systems after three consecutive intrusion−extrusion cycles are demonstrated in Figures 4 and 5. For both MAF-6 and ZIF-71 materials, the intrusion−extrusion experiments were first realized up to 300 or mainly 350 MPa, which was followed by complementary experiments that were performed under lower pressures to understand the effect of applied pressure on the structure of the studied materials. On the $P-V$ diagrams, and as previously reported,[9,11] the volume variation in the low-pressure range (0−5 MPa) corresponds to the compression of the ZIF particles and filling of the interparticular porosity. This

DOI: 10.1021/acs.jpcc.8b12047
J. Phys. Chem. C 2019, 123, 4319−4328

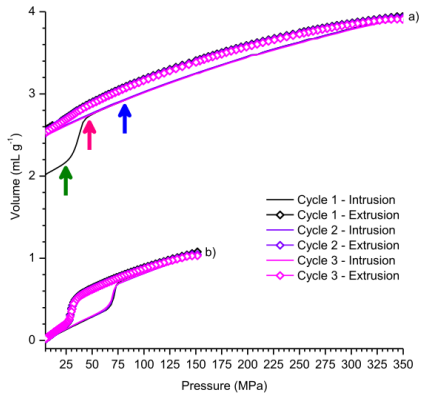

Figure 4. Pressure−volume diagrams of the (a) "MAF-6−H_2O" and (b) previously reported[11] "ZIF-71−H_2O" systems after intrusion−extrusion experiments realized up to 350 and 150 MPa, respectively. The arrows refer to the pressures at which the complementary experiments were stopped. For clarity, the *P*−*V* diagrams were shifted on the *y*-axis.

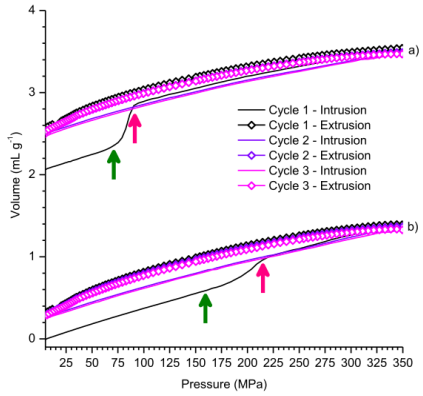

Figure 5. Pressure−volume diagrams of the (a) "MAF-6−LiCl 20 M aqueous solution" and (b) "ZIF-71−LiCl 20 M aqueous solution" systems after intrusion−extrusion experiments conducted up to 350 MPa. The arrows refer to the pressures at which the complementary experiments were stopped. For clarity, the *P*−*V* diagrams were shifted on the *y*-axis.

pressure range is not shown on the *P*−*V* diagrams presented in Figures 4 and 5.

3.2.1. "ZIF−H_2O" Systems. 3.2.1.1. Intrusion−Extrusion Experiments Carried Out Up To 300 or 350 MPa. In the case of the "MAF-6−H_2O" system, by referring to the *P*−*V* diagrams obtained from the intrusion−extrusion experiment carried out up to 350 MPa, the intrusion curve of the first intrusion−extrusion cycle exhibits one main steep step in the 25−50 MPa pressure range (Figure 4a). This step corresponds to a volume variation of 0.52 mL g^{-1} and may indicate the intrusion of the nonwetting liquid molecules in the porosity of MAF-6 at an intrusion pressure of 37 MPa. On the extrusion curve of the first intrusion−extrusion cycle, however, no steep step, corresponding to the extrusion of the nonwetting liquid molecules, is observed. Indeed, the intrusion and extrusion curves of the second and third cycles show no step, and the observed volume variations can be only attributed to the compression−decompression of water in the cell. These results suggest that water molecules are not expelled from the porosity at reduced pressures, and thus, the "MAF-6−H_2O" system displays bumper behavior. Another hypothesis is that the nonwetting liquid molecules are extruded from the porosity at atmospheric pressure, with no further intrusion occurring in the second and third intrusion cycles. In this case, the system behaves as a shock-absorber working only once. Finally, a third hypothesis could be that the volume variation observed in the intrusion step of the first intrusion−extrusion cycle corresponds to the collapse of the MAF-6 structure (under the effect of high pressure and/or the nonwetting liquid), which may be (or not) associated with the intrusion of water into the porosity. Scheme 1 shows the different phenomena that can take place when applying pressure to a "porous material−nonwetting liquid" system (water in the present case) during intrusion−extrusion experiments. The scheme demonstrates how the volume variation observed on the intrusion−extrusion curve during a water intrusion−extrusion experiment can be either attributed to the intrusion of water in the porosity (Scheme 1b), intrusion of water associated with a partial collapse (or partial phase transformation) (Scheme 1c), or complete collapse (or complete phase transformation) of the porous structure with the formation of a nonporous solid (Scheme 1d). It is worthy to note that in all cases, the observed volume variation is the same, regardless of the nature of the phenomenon that is taking place. In the case of the "MAF-6−H_2O" system, the volume variation (0.52 mL g^{-1}) is not very far from the microporous volume of the parent MAF-6 material (0.61 cm^3 g^{-1}), the difference being explained by the density of confined water that is lower than 1, as it was clearly shown for water molecules confined in silicalite-1 (MFI-type zeolite).[38]

The "ZIF-71−H_2O" system has already been studied by Ortiz et al.[11] The obtained results revealed a water intrusion step occurring around 71 MPa, with the extrusion step occurring at a much lower pressure of 36 MPa (Figure 4b). The process is completely reproducible over three intrusion−extrusion cycles, and the system displays perfect shock-absorber behavior with a stored energy of 26 J g^{-1}. Similar results were obtained for ZIF-71 with the water intrusion−extrusion experiment realized up to 300 MPa (Figure S2).

3.2.1.2. Post Intrusion−Extrusion Characterizations. The postintruded samples were analyzed by XRD and N_2 sorption measurements. This makes possible to assess any possible damages in the structure of the studied materials generated during intrusion−extrusion experiments (owing to the high pressure and/or the nonwetting liquid). In addition, TGA was performed on MAF-6 after the water intrusion−extrusion experiment was conducted up to 47 MPa.

XRD Characterizations: The XRD patterns of the samples before and after water intrusion−extrusion experiments are reported in Figure 1a. Compared to the parent MAF-6 material, when the limit pressure associated with water intrusion−extrusion experiments is equal to 350 MPa (sample MAF-6−H_2O 350 MPa), the intensities of the peaks corresponding to the MAF-6 phase become almost negligible (minor phase), while another crystallized phase is formed (major phase). It is important to note that this phase, characterized by a main high-relative-intensity peak at 10.8°

DOI: 10.1021/acs.jpcc.8b12047
J. Phys. Chem. C 2019, 123, 4319−4328

Scheme 1. Representation of the Volume Variation Occurring under the Effect of Applied Pressure during Intrusion–Extrusion Experiments: System (a) Before Intrusion, (b) Volume Variation Attributed to the Intrusion of Water in the Porosity, (c) Intrusion of Water Associated with a Partial Collapse (or Phase Transformation) of the Porous Structure, and (d) Complete Collapse (or Phase Transformation) of the Porous Structure

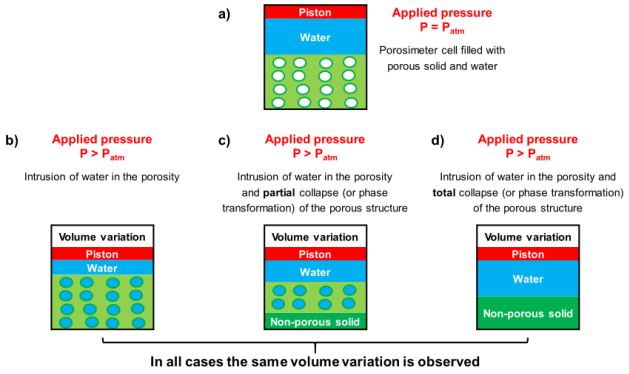

(2θ), still remains unidentified and is referred to as phase X. However, it does not correspond to any of the MAF-6 polymorphs (i.e., MAF-32[39,40] or MAF-5 (also called ZIF-14)[16,28,29,40] of quartz and ANA topologies, respectively), or to the organic precursor Heim. It also does not correspond to ZnO or $Zn(OH)_2$ that may have been formed by the partial collapse of the material during the intrusion step. This phase transformation of MAF-6 into phase X is irreversible, as the latter phase persists after the pressure is reduced and can be probably assigned to the combined effects of high pressure and the nonwetting liquid during intrusion–extrusion experiments. To shed light on these effects, we studied separately the influence of pressure and water (the nonwetting liquid) on the stability of the MAF-6 structure. On the basis of XRD measurements obtained after suspending MAF-6 in water for 24 h at room temperature and atmospheric pressure, the MAF-6 structure is completely maintained (Figure S3a). Even after extending the contact time with water to 4 days, according to XRD analyses, MAF-6 remains the major phase, with only two additional peaks of very low relative intensities at 13.84 and 10.85° (2θ) corresponding to MAF-32 (qtz) and phase X, respectively (Figure S3b). As the water stability tests were carried out using the same MAF-6-to-water mass ratio used in high-pressure intrusion–extrusion experiments, the obtained results reveal a negligible effect of water on the structure of MAF-6 at atmospheric pressure. The particular effect of the pressure on the MAF-6 structure was also investigated. In this aim, we subjected 100 mg of MAF-6 powder to a pressure of 38 MPa ($\approx P_{int}$). Indeed, the XRD pattern recorded after compression corresponds to that of MAF-6 (Figure S4). These results exclude a phase transformation from MAF-6 into phase X under the effects of pressure or water alone and confirm our hypothesis on the combined effects of both parameters during intrusion–extrusion experiments. A phase transformation phenomenon (an irreversible structural transition of ZIF-8 from the cubic to orthorhombic symmetry) has already been described by Grosu et al. during water intrusion–extrusion experiments in ZIF-8.[41]

In the case of ZIF-71, based on the results published by Ortiz et al., the structure is maintained after water intrusion–extrusion experiments were realized up to 150 MPa.[11] The similar profile of the $P-V$ diagrams obtained from the water intrusion–extrusion experiment realized on the "ZIF-71–H_2O" system up to 300 MPa (Figure S2) compared to the one obtained from the 150 MPa experiment, also implies the stability of the ZIF-71 structure at such an elevated pressure (300 MPa).

N_2 Sorption Analyses: Figure 2a represents the N_2 adsorption–desorption isotherms of MAF-6 before and after water intrusion–extrusion experiments were realized up to 350 MPa (sample MAF-6–H_2O 350 MPa). Both the parent and intruded MAF-6 materials exhibit a Type I adsorption–desorption isotherm. However, after three intrusion–extrusion cycles, the textural properties of the ZIF material are decreased compared to those of the parent material, from 1360 to 137 $m^2\ g^{-1}$ and from 0.61 to 0.05 $cm^3\ g^{-1}$ (91% decrease) in terms of the BET surface area and microporous volume, respectively. These results are in agreement with the ones obtained from XRD analyses confirming the transformation of the MAF-6 structure into a nonporous phase X at this higher pressure (350 MPa).

3.2.1.3. Complementary Water Intrusion–Extrusion Experiments. To better understand the effect of applied pressure on the formation of phase X during water intrusion–extrusion experiments performed on MAF-6, a complementary water intrusion–extrusion experiment was carried out under a lower pressure of 80 MPa, in addition to two experiments that were stopped at the beginning (at 25 MPa) and the end (at 47 MPa) of the volume variation step of the first intrusion–extrusion cycle (Figure 4a). The materials obtained after the diverse experiments were then analyzed by XRD (Figure 1a) and N_2 adsorption–desorption measurements (Figure 2a). Figure 1a reveals that as the limit pressure associated with the water intrusion–extrusion experiment increases, XRD peaks of the MAF-6 phase become less pronounced, whereas those corresponding to phase X become more prominent. At 25 MPa (beginning of the volume variation step), the XRD pattern (sample MAF-6–H_2O 25 MPa) corresponds to that of MAF-6, and the N_2 adsorption–desorption isotherms (Figure 2a) are quite close to those of the parent sample (only a slight decrease of porous volume (5–10%) is observed, may be due to the presence of phase X not detected by XRD).

DOI: 10.1021/acs.jpcc.8b12047
J. Phys. Chem. C 2019, 123, 4319–4328

This is no longer the case at the end of the volume variation step (47 MPa). Indeed, at this step, the diffraction peaks of phase X appear clearly on the XRD pattern and a large decrease in the pore volume (60%) is evidenced (Figure 2a, sample MAF-6–H_2O 47 MPa), which indicates a phase transformation of MAF-6 into phase X by 60%. This also means that at the end of the volume variation step, the resulting material consists of a mixture of 60% nonporous phase X and 40% water-intruded MAF-6. On the basis of these results (40% of remaining MAF-6 material) and also based on the profile of the *P*–*V* diagrams (bumper behavior), a relative mass loss of around 21% (between room temperature and 200 °C), corresponding to intruded water molecules, is expected from TGA. The TG curves of the parent MAF-6 material and the sample MAF-6–H_2O 47 MPa are reported in Figure 3a. After the first intrusion–extrusion cycle, the recovered sample was dried at room temperature. For this sample, the TG curve reveals a relative mass loss of only 7% between room temperature and 185 °C. This value is 3 times lower than the one expected and indicates that the intruded water molecules are almost completely expelled from the MAF-6 pores at atmospheric pressure (shock-absorber behavior). Also by referring to the TG curve of the postintruded material, a relative mass loss of 66% (determined between 185 and 800 °C) is observed and corresponds to the decomposition of the organic network. This value, being similar to the one observed for parent MAF-6 (68%), indicates that phase X is probably a hybrid organic–inorganic material.

As expected, at 80 MPa, based on XRD and N_2 sorption analyses, the related recovered sample corresponds mainly to phase X.

Therefore, by referring to the shape of the *P*–*V* diagrams and by combining the results obtained from XRD and N_2 adsorption–desorption measurements (for the samples obtained at different pressures during intrusion–extrusion experiments), we can conclude that the volume variation step observed on the intrusion curve of the first intrusion–extrusion cycle corresponds to the intrusion of water molecules into the MAF-6 pores, associated with the partial phase transformation of the MAF-6 structure into phase X (example given in Scheme 1c). According to TGA, most of the intruded water is expelled from the porosity at atmospheric pressure. Thus, the "MAF-6–H_2O" system displays a mixture of a shock-absorber and bumper behaviors. Indeed, the intruded water molecules are expelled from the porosity of the remaining MAF-6 (shock-absorber behavior), whereas the phase transformation into phase X is irreversible and does not allow for restoring the mechanical energy (bumper behavior).

3.2.2. "ZIF–LiCl 20 M Aqueous Solution" Systems. 3.2.2.1. Intrusion–Extrusion Experiments Carried Out Up To 350 MPa. In the case of both "MAF-6–LiCl 20 M aqueous solution" and "ZIF-71–LiCl 20 M aqueous solution" systems, the *P*–*V* diagrams obtained from the intrusion–extrusion experiments carried out up to 350 MPa (Figure 5a,b) exhibit a profile similar to the ones observed for the "MAF-6–H_2O" system (Figure 4a). According to the *P*–*V* diagrams, the intrusion curve of the first intrusion–extrusion cycle exhibits one main steep step (in the 70–90 and 185–215 MPa pressure ranges for the "MAF-6–LiCl 20 M aqueous solution" and "ZIF-71–LiCl 20 M aqueous solution" systems, respectively). This step corresponds to volume variations of 0.54 and 0.30 mL g^{-1} for the "MAF-6–LiCl 20 M aqueous solution" and "ZIF-71–LiCl 20 M aqueous solution" systems, respectively. For both systems, the magnitude of the volume variations is consistent with the pore volumes of the ZIF materials, that is, 0.61 and 0.41 cm^3 g^{-1}. Similar to the "MAF-6–H_2O" system, on the extrusion curve of the first intrusion–extrusion cycle and the intrusion and extrusion curves of the second and third intrusion–extrusion cycles, no steep step corresponding to the expected extrusion of the nonwetting liquid molecules is observed. In this case also, the obtained results can suggest that the nonwetting liquid molecules are not expelled from the porosity at reduced pressures, and thus, both "MAF-6–" and "ZIF-71–LiCl 20 M aqueous solution" systems display bumper behaviors and/or that the structures of both systems partially or totally collapse or undergo a phase transformation during the intrusion step under the effect of high pressure and/or the nonwetting liquid. It has to be recalled that in all cases, the same volume variation is expected according to Scheme 1.

3.2.2.2. Post Intrusion–Extrusion Characterizations. XRD Characterizations: The XRD patterns of the MAF-6 and ZIF-71 samples before and after intrusion–extrusion experiments with LiCl 20 M aqueous solution are reported in Figure 1b,c. In the case of ZIF-71, at an associated limit pressure during intrusion–extrusion equal to 350 MPa (sample ZIF-71–LiCl 20 M 350 MPa), the XRD analyses reveal the major collapse of the ZIF-71 structure with some peaks corresponding to traces of ZIF-71 and ZIF-72, a ZIF-71 polymorph with lcs topology.[29] As for MAF-6, the XRD pattern obtained after the intrusion–extrusion experiment was performed up to a pressure of 350 MPa (sample MAF-6–LiCl 20 M 350 MPa) shows an inversion in the relative peak intensities compared to the parent MAF-6 material, which can indicate a mixture of crystallized phases of MAF-6 and phase X under the effect of high pressure and/or the nonwetting liquid.

N_2 Sorption Analyses: Figure 2b,c represents the N_2 adsorption–desorption isotherms of the MAF-6 and ZIF-71 materials before and after intrusion–extrusion experiments with LiCl 20 M aqueous solution realized up to 350 MPa. The postintruded MAF-6 material displays a Type I sorption isotherm. After three intrusion–extrusion cycles conducted up to 350 MPa, the textural properties of MAF-6 decrease compared to those of the parent MAF-6 material from 1360 to 288 m^2 g^{-1} and from 0.61 to 0.10 cm^3 g^{-1} (84% decrease) in terms of the BET surface area and microporous volume, respectively. This indicates a major collapse or phase transformation of the MAF-6 porous structure into a nonporous structure. The N_2 adsorption–desorption isotherms of the sample MAF-6–LiCl 20 M 350 MPa also show a relative increase in the adsorbed volume at $p/p° = 0.9$ with a large hysteresis, indicating the presence of mesopores.

In the case of ZIF-71, the N_2 adsorption–desorption isotherms reveal that after the LiCl 20 M aqueous solution intrusion–extrusion experiment was performed up to 350 MPa, the material is nonporous, which confirms the XRD result and the complete collapse of the ZIF-71 structure after intrusion–extrusion under a pressure of 350 MPa. As mentioned above for the "ZIF–H_2O" systems (Scheme 1), these results are not sufficient to confirm the presence/absence of intrusion during the volume variation step observed on the LiCl 20 M aqueous solution intrusion–extrusion curves. More information is, thus, needed to specify whether the collapse (partial or complete) occurs during the volume variation step or later at higher pressures.

DOI: 10.1021/acs.jpcc.8b12047
J. Phys. Chem. C 2019, 123, 4319–4328

3.2.2.3. Complementary LiCl 20 M Aqueous Solution Intrusion–Extrusion Experiments. To better figure out the effect of applied pressure on MAF-6 and ZIF-71 structures during the LiCl 20 M aqueous solution intrusion–extrusion experiments, complementary experiments were undertaken and stopped at the beginning (70 and 160 MPa for "MAF-6– and ZIF-71–LiCl 20 M aqueous solution" systems, respectively) and at the end (90 and 215 MPa for MAF-6– and ZIF-71–LiCl 20 M aqueous solution" systems, respectively) of the volume variation step that is observed on the intrusion curve of the first intrusion–extrusion cycle (Figure 5a,b). The materials obtained after the different experiments were then analyzed by XRD (Figure 1b,c) and N_2 adsorption–desorption measurements (Figure 2b,c).

In the case of the "MAF-6–LiCl 20 M aqueous solution" system, at the beginning of the volume variation step (70 MPa), the XRD pattern corresponds to that of MAF-6. However, a decrease (20%) in the pore volume is clearly observed on the N_2 adsorption–desorption isotherms (Figure 2b). At the end of the volume variation step, that is, at an associated limit pressure of 90 MPa, the XRD pattern of the corresponding sample reveals large variations in the relative intensities of the peaks as well as the emergence of a new peak at 10.8° (2θ), assignable to the unidentified phase X (Figure 1b). At a maximum applied pressure of 350 MPa, this peak is clearly more pronounced indicating a mixture of the two crystallized phases. It is worthy to note that even if the XRD results highlight the presence of MAF-6 in the samples intruded at 90 and 350 MPa, the corresponding N_2 adsorption–desorption isotherms are very similar and characterized by an 84% decrease in the pore volume compared to the parent MAF-6 material. Therefore, during the volume variation step, most of the textural properties of MAF-6 are lost because of the irreversible phase transformation into the nonporous phase X. It is important to note that for MAF-6, as shown on the *P*–*V* diagrams, the pressure range of the volume variation step varies with the nature of the nonwetting liquid (water or LiCl 20 M aqueous solution), which further proves that the phase transformation phenomenon does not take place solely under the effect of pressure. Complementary experiments were conducted by suspending MAF-6 in a LiCl 20 M aqueous solution for 24 h at room temperature (using the same MAF-6-to-nonwetting liquid mass ratio used in high-pressure intrusion–extrusion experiments). MAF-6 structure is not damaged as shown by XRD measurements (Figure S3c). Consequently, in this case also, the phase transformation phenomenon is attributed to the combined effects of high pressure and the nonwetting liquid.

For the "ZIF-71–LiCl 20 M aqueous solution" system, Figure 1c reveals that at an associated limit pressure of 160 MPa, that is, before the beginning of the volume variation step, the ZIF-71 (RHO) structure is maintained at the long-range order. At the end of the volume variation step (at 215 MPa), the studied material displays an XRD pattern corresponding to ZIF-72 (lcs), which evidences that a phase transformation has taken place. Moreover, increasing the pressure to 350 MPa leads to a large collapse/amorphization of the ZIF-72 structure (Figure 1c, sample ZIF-71–LiCl 20 M aqueous solution 350 MPa). Besides, N_2 sorption measurements performed on the ZIF-71–LiCl 20 M 160 MPa sample reveal a 8% decrease in the pore volume compared to the parent material (Figure 2c), whereas for the ZIF-71–LiCl 20 M 215 MPa sample, no N_2 adsorption is noted, meaning that the material is, thus, nonporous using molecular nitrogen as a probe molecule. These results are consistent with the ones obtained from XRD analyses that confirm the phase transformation from ZIF-71 (RHO) to ZIF-72 (lcs), with the latter phase being mostly destroyed at pressures as high as 350 MPa. Here as well, to prove that the latter phenomenon does not occur because of the single effect of the nonwetting liquid, we suspended ZIF-71 in LiCl 20 M aqueous solution for 48 h at room temperature (using the same ZIF-71-to-water mass ratio used in high-pressure intrusion–extrusion experiments). The results obtained from XRD measurements reveal the absence of any peak corresponding to ZIF-72 (lcs) after 48 h of contact with the LiCl solution, with the XRD pattern corresponding to that of ZIF-71 (RHO) (Figure S5). To confirm the absence of a separate effect of pressure on the phase transformation phenomenon, we carried out a mercury porosimetry experiment, so as to subject the ZIF-71 material to high pressure in the absence of LiCl 20 M aqueous solution. No volume variation step is observed on the *P*–*V* diagrams (Figure S6), and the XRD pattern of the recovered material reveals the absence of any traces of ZIF-72 (lcs) (Figure S7). These results prove the absence of any separate effect of either the pressure or the nonwetting liquid on the phase transformation phenomenon and ascertain our hypothesis on the combined effects of both parameters.

Finally, the fact that the volume variation step in the case of both "MAF-6–" and "ZIF-71–LiCl 20 M aqueous solution" systems is shifted to a higher pressure range compared to the "corresponding porous material–H_2O" systems, probably indicates an intrusion of liquid into the pores of the MAF-6 and ZIF-71 materials. The intrusion pressure in this case is higher than that observed with water, which is due to the effect of addition of electrolytes to the nonwetting liquid.[10,11,14,23,24] Therefore, for both "MAF-6–" and "ZIF-71–LiCl 20 M aqueous solution systems," the volume variation step observed on the *P*–*V* diagrams can be explained according to Scheme 1c and corresponds to the intrusion of the nonwetting liquid molecules associated with a phase transformation into the nonporous phase X and ZIF-72 (lcs) in the case of MAF-6 and ZIF-71, respectively.

4. CONCLUSIONS

Two ZIF materials, MAF-6 and ZIF-71, of RHO topology are studied in high-pressure intrusion–extrusion experiments using LiCl 20 M aqueous solution and/or water as nonwetting liquids. The results reveal that both MAF-6 and ZIF-71 structures undergo phase transformations under the combined effects of high pressure and the nonwetting liquid. For the "MAF-6–H_2O" system, the volume variation step observed on the intrusion curve of the first intrusion–extrusion cycle corresponds, in part, to the intrusion of water molecules in the MAF-6 pores, associated with a partial collapse (60%) of the structure and resulting in the formation of a nonporous and unidentified phase X. When the system goes back to atmospheric pressure, the intruded water molecules are expelled from the pores of the remaining MAF-6 material. However, the structural transformation into phase X is irreversible (according to the *P*–*V* diagrams) and the absorbed mechanical energy is not restored. The "MAF-6–H_2O" system, thus, displays a mixture of shock-absorber and bumper behaviors. With LiCl 20 M aqueous solution, for both MAF-6 and ZIF-71, the volume variation step is shifted to a higher pressure compared to the case where water is used as the

DOI: 10.1021/acs.jpcc.8b12047
J. Phys. Chem. C 2019, 123, 4319–4328

nonwetting liquid, which again confirms the higher intrusion pressure associated with use of aqueous electrolyte solutions in intrusion−extrusion experiments. For the "MAF-6−LiCl 20 M aqueous solution" system, the material obtained after intrusion−extrusion is a mixture of MAF-6 and the nonporous phase X. The energetic behavior of the latter system is, thus, probably similar to that displayed by the "MAF-6−H_2O" system, that is, a mixture of shock-absorber and bumper behaviors. As for the "ZIF-71−LiCl 20 M aqueous solution" system, at the end of the volume variation step, the initial ZIF-71 (RHO) material is completely and irreversibly transformed into ZIF-72 (lcs). This system, thus, behaves as a bumper, as the supplied mechanical energy in the intrusion step is absorbed by the ZIF material when undergoing irreversible phase transformation.

■ ASSOCIATED CONTENT

Supporting Information

The Supporting Information is available free of charge on the ACS Publications website at DOI: 10.1021/acs.jpcc.8b12047.

Representation of the RHO topology, pressure−volume diagrams of the "ZIF-71−H_2O" system up to 300 MPa, XRD patterns of MAF-6 samples subjected to separate effects of the nonwetting liquid and the pressure, XRD patterns of a ZIF-71 sample subjected to LiCl 20 M aqueous solution for 2 days, pressure−volume diagrams obtained from a mercury porosimetry experiment on a ZIF-71 sample, and XRD pattern of the resulting material (PDF)

■ AUTHOR INFORMATION

Corresponding Author

*E-mail: gerald.chaplais@uha.fr. Phone: +33 389 33 68 87.

ORCID

Gérald Chaplais: 0000-0003-2756-4896

Joël Patarin: 0000-0002-6511-5357

Notes

The authors declare no competing financial interest.

■ ACKNOWLEDGMENTS

XRD analyses and nitrogen sorption measurements were performed on the technical platforms of IS2M.

■ REFERENCES

(1) Eroshenko, V. A. Unusual Properties of One Complex Thermodynamic System. *Dopov. Akad. Nauk Ukr. RSR, Ser. A: Fiz.-Tekh. Mat. Nauki* **1990**, 77−80.

(2) Eroshenko, V. A. Adiabatic Incompressibility and Non-Dilatation in a Complex Thermodynamic System. *Entropie* **1996**, *32*, 17−23.

(3) Eroshenko, V. Heterogeneous Energy Accumulation or Dissipation Structure, Methods for Using Such Structure and Associated Apparatus. WO 9618040, June 13, 1996.

(4) Soulard, M.; Patarin, J.; Eroshenko, V.; Regis, R. Molecular Spring or Bumper: a New Application for Hydrophobic Zeolitic Materials. *Stud. Surf. Sci. Catal.* **2004**, *154*, 1830−1837.

(5) Zhao, J.; Culligan, P. J.; Germaine, J. T.; Chen, X. Experimental Study on Energy Dissipation of Electrolytes in Nanopores. *Langmuir* **2009**, *25*, 12687−12696.

(6) Eroshenko, V.; Regis, R.-C.; Soulard, M.; Patarin, J. Energetics: a New Field of Applications for Hydrophobic Zeolites. *J. Am. Chem. Soc.* **2001**, *123*, 8129−8130.

(7) Eroshenko, V.; Regis, R.-C.; Soulard, M.; Patarin, J. The Heterogeneous Systems "Water-Hydrophobic Zeolites". *Compt. Rendus Phys.* **2002**, *3*, 111−119.

(8) Tzanis, L.; Trzpit, M.; Soulard, M.; Patarin, J. Energetic Performances of Channel and Cage-Type Zeosils. *J. Phys. Chem. C* **2012**, *116*, 20389−20395.

(9) Ortiz, G.; Nouali, H.; Marichal, C.; Chaplais, G.; Patarin, J. Energetic Performances of the Metal-Organic Framework ZIF-8 Obtained Using High Pressure Water Intrusion-Extrusion Experiments. *Phys. Chem. Chem. Phys.* **2013**, *15*, 4888−4891.

(10) Ortiz, G.; Nouali, H.; Marichal, C.; Chaplais, G.; Patarin, J. Versatile Energetic Behavior of ZIF-8 upon High Pressure Intrusion-Extrusion of Aqueous Electrolyte Solutions. *J. Phys. Chem. C* **2014**, *118*, 7321−7328.

(11) Ortiz, G.; Nouali, H.; Marichal, C.; Chaplais, G.; Patarin, J. Energetic Performances of "ZIF-71-Aqueous Solution" Systems: a Perfect Shock-Absorber with Water. *J. Phys. Chem. C* **2014**, *118*, 21316−21322.

(12) Khay, I.; Chaplais, G.; Nouali, H.; Marichal, C.; Patarin, J. Water Intrusion-Extrusion Experiments in ZIF-8: Impacts of the Shape and Particle Size on the Energetic Performances. *RSC Adv.* **2015**, *5*, 31514−31518.

(13) Khay, I.; Chaplais, G.; Nouali, H.; Ortiz, G.; Marichal, C.; Patarin, J. Assessment of the Energetic Performances of Various ZIFs with SOD or RHO Topology Using High Pressure Water Intrusion-Extrusion Experiments. *Dalton Trans.* **2016**, *45*, 4392−4400.

(14) Mortada, B.; Chaplais, G.; Veremeienko, V.; Nouali, H.; Marichal, C.; Patarin, J. Energetic Performances of ZIF-8 Derivatives: Impact of the Substitution (Me, Cl or Br) on Imidazolate Linker. *J. Phys. Chem. C* **2018**, *122*, 3846−3855.

(15) Banerjee, R.; Furukawa, H.; Britt, D.; Knobler, C.; O'Keeffe, M.; Yaghi, O. M. Control of Pore Size and Functionality in Isoreticular Zeolitic Imidazolate Frameworks and their Carbon Dioxide Selective Capture Properties. *J. Am. Chem. Soc.* **2009**, *131*, 3875−3877.

(16) Phan, A.; Doonan, C. J.; Uribe-Romo, F. J.; Knobler, C. B.; O'Keeffe, M.; Yaghi, O. M. Synthesis, Structure, and Carbon Dioxide Capture Properties of Zeolitic Imidazolate Frameworks. *Acc. Chem. Res.* **2010**, *43*, 58−67.

(17) Furukawa, H.; Ko, N.; Go, Y. B.; Aratani, N.; Choi, S. B.; Choi, E.; Yazaydin, A. O.; Snurr, R. Q.; O'Keeffe, M.; Kim, J.; et al. Ultrahigh Porosity in Metal-Organic Frameworks. *Science* **2010**, *329*, 424−428.

(18) Furukawa, H.; Cordova, K. E.; O'Keeffe, M.; Yaghi, O. M. The Chemistry and Applications of Metal-Organic Frameworks. *Science* **2013**, *341*, 1230444.

(19) Kong, X.; Deng, H.; Yan, F.; Kim, J.; Swisher, J. A.; Smit, B.; Yaghi, O. M.; Reimer, J. A. Mapping of Functional Groups in Metal-Organic Frameworks. *Science* **2013**, *341*, 882−885.

(20) Li, Y.; Zhou, K.; He, M.; Yao, J. Synthesis of ZIF-8 and ZIF-67 Using Mixed-Base and Their Dye Adsorption. *Microporous Mesoporous Mater.* **2016**, *234*, 287−292.

(21) Grosu, Y.; Gomes, S.; Renaudin, G.; Grolier, J.-P. E.; Eroshenko, V.; Nedelec, J.-M. Stability of Zeolitic Imidazolate Frameworks: Effect of Forced Water Intrusion and Framework Flexibility Dynamics. *RSC Adv.* **2015**, *5*, 89498−89502.

(22) Michelin-Jamois, M.; Picard, C.; Vigier, G.; Charlaix, E. Giant Osmotic Pressure in the Forced Wetting of Hydrophobic Nanopores. *Phys. Rev. Lett.* **2015**, *115*, 036101.

(23) Grosu, Y.; Mierzwa, M.; Eroshenko, V. A.; Pawlus, S.; Chorążewski, M.; Nedelec, J.-M.; Grolier, J.-P. E. Mechanical, Thermal, and Electrical Energy Storage in a Single Working Body: Electrification and Thermal Effects upon Pressure-Induced Water Intrusion-Extrusion in Nanoporous Solids. *ACS Appl. Mater. Interfaces* **2017**, *9*, 7044−7049.

(24) Han, A.; Lu, W.; Kim, T.; Punyamurtula, V. K.; Qiao, Y. The Dependence of Infiltration Pressure and Volume in Zeolite Y on Potassium Chloride Concentration. *Smart Mater. Struct.* **2009**, *18*, 024005.

DOI: 10.1021/acs.jpcc.8b12047
J. Phys. Chem. C 2019, 123, 4319−4328

(25) Lively, R. P.; Dose, M. E.; Thompson, J. A.; McCool, B. A.; Chance, R. R.; Koros, W. J. Ethanol and Water Adsorption in Methanol-Derived ZIF-71. *Chem. Commun.* **2011**, *47*, 8667−8669.
(26) Zhang, K.; Lively, R. P.; Dose, M. E.; Brown, A. J.; Zhang, C.; Chung, J.; Nair, S.; Koros, W. J.; Chance, R. R. Alcohol and Water Adsorption in Zeolitic Imidazolate Frameworks. *Chem. Commun.* **2013**, *49*, 3245−3247.
(27) He, C.-T.; Jiang, L.; Ye, Z.-M.; Krishna, R.; Zhong, Z.-S.; Liao, P.-Q.; Xu, J.; Ouyang, G.; Zhang, J.-P.; Chen, X.-M. Exceptional Hydrophobicity of a Large-Pore Metal-Organic Zeolite. *J. Am. Chem. Soc.* **2015**, *137*, 7217−7223.
(28) Huang, X.-C.; Lin, Y.-Y.; Zhang, J.-P.; Chen, X.-M. Ligand-Directed Strategy for Zeolite-Type Metal-Organic Frameworks: Zinc(II) Imidazolates with Unusual Zeolitic Topologies. *Angew. Chem., Int. Ed.* **2006**, *45*, 1557−1559.
(29) Banerjee, R.; Phan, A.; Wang, B.; Knobler, C.; Furukawa, H.; O'Keeffe, M.; Yaghi, O. M. High-Throughput Synthesis of Zeolitic Imidazolate Frameworks and Application to CO_2 Capture. *Science* **2008**, *319*, 939−943.
(30) Calleja, G.; Botas, J. A.; Martos, C.; Orcajo, G.; Villajos, J. A. Effect of Ion-Exchange Modification on Hydrogen and Carbon Dioxide Adsorption Behaviour of RhoZMOF Material. *Adsorpt. Sci. Technol.* **2012**, *30*, 793−806.
(31) Liu, L.; Chen, X.; Lu, W.; Han, A.; Qiao, Y. Infiltration of Electrolytes in Molecular-Sized Nanopores. *Phys. Rev. Lett.* **2009**, *102*, 184501.
(32) Boström, M.; Ninham, B. W. Contributions from Dispersion and Born Self-Free Energies to the Solvation Energies of Salt Solutions. *J. Phys. Chem. B* **2004**, *108*, 12593−12595.
(33) Rouquerol, J.; Llewellyn, P.; Rouquerol, F. Is the BET Equation Applicable to Microporous Adsorbents? *Stud. Surf. Sci. Catal.* **2007**, *160*, 49−56.
(34) Walton, K. S.; Snurr, R. Q. Applicability of the BET Method for Determining Surface Areas of Microporous Metal-Organic Frameworks. *J. Am. Chem. Soc.* **2007**, *129*, 8552−8556.
(35) Trzpit, M.; Soulard, M.; Patarin, J. The Pure Silica Chabazite: a High Volume Molecular Spring at Low Pressure for Energy Storage. *Chem. Lett.* **2007**, *36*, 980−981.
(36) Thommes, M.; Kaneko, K.; Neimark, A. V.; Olivier, J. P.; Rodriguez-Reinoso, F.; Rouquerol, J.; Sing, K. S. W. Physisorption of Gases, with Special Reference to the Evaluation of Surface Area and Pore Size Distribution (IUPAC Technical Report). *Pure Appl. Chem.* **2015**, *87*, 1051−1069.
(37) Schweinefuß, M. E.; Springer, S.; Baburin, I. A.; Hikov, T.; Huber, K.; Leoni, S.; Wiebcke, M. Zeolitic Imidazolate Framework-71 Nanocrystals and a Novel SOD-Type Polymorph: Solution Mediated Phase Transformations, Phase Selection via Coordination Modulation and a Density Functional Theory Derived Energy Landscape. *Dalton Trans.* **2014**, *43*, 3528−3536.
(38) Desbiens, N.; Demachy, I.; Fuchs, A. H.; Kirsch-Rodeschini, H.; Soulard, M.; Patarin, J. Water Condensation in Hydrophobic Nanopores. *Angew. Chem., Int. Ed.* **2005**, *44*, 5310−5313.
(39) Beldon, P. J.; Fábián, L.; Stein, R. S.; Thirumurugan, A.; Cheetham, A. K.; Friščić, T. Rapid Room-Temperature Synthesis of Zeolitic Imidazolate Frameworks by Using Mechanochemistry. *Angew. Chem., Int. Ed.* **2010**, *49*, 9640−9643.
(40) Zhu, A.-X.; Lin, R.-B.; Qi, X.-L.; Liu, Y.; Lin, Y.-Y.; Zhang, J.-P.; Chen, X.-M. Zeolitic Metal Azolate Frameworks (MAFs) from ZnO/$Zn(OH)_2$ and Monoalkyl-Substituted Imidazoles and 1,2,4-Triazoles: Efficient Syntheses and Properties. *Microporous Mesoporous Mater.* **2012**, *157*, 42−49.
(41) Grosu, Y.; Renaudin, G.; Eroshenko, V.; Nedelec, J.-M.; Grolier, J.-P. E. Synergetic Effect of Temperature and Pressure on Energetic and Structural Characteristics of {ZIF-8 + water} Molecular Spring. *Nanoscale* **2015**, *7*, 8803−8810.

DOI: 10.1021/acs.jpcc.8b12047
J. Phys. Chem. C 2019, 123, 4319−4328

Phase Transformations of Metal-Organic Frameworks MAF-6 and ZIF-71 During Intrusion-Extrusion Experiments

Boushra Mortada,[1, 2] Gérald Chaplais,[1, 2*] Habiba Nouali,[1, 2] Claire Marichal,[1, 2] and Joël Patarin[1, 2]

[1] *Université de Haute-Alsace, CNRS, Institut de Science des Matériaux de Mulhouse (IS2M), UMR 7361, Axe Matériaux à Porosité Contrôlée (MPC), UMR 7361, F-68100 Mulhouse, France*

[2] *Université de Strasbourg, France*

* Corresponding author: gerald.chaplais@uha.fr, tel. +33 389 33 68 87

Table of Contents

1. Structure: RHO Topology

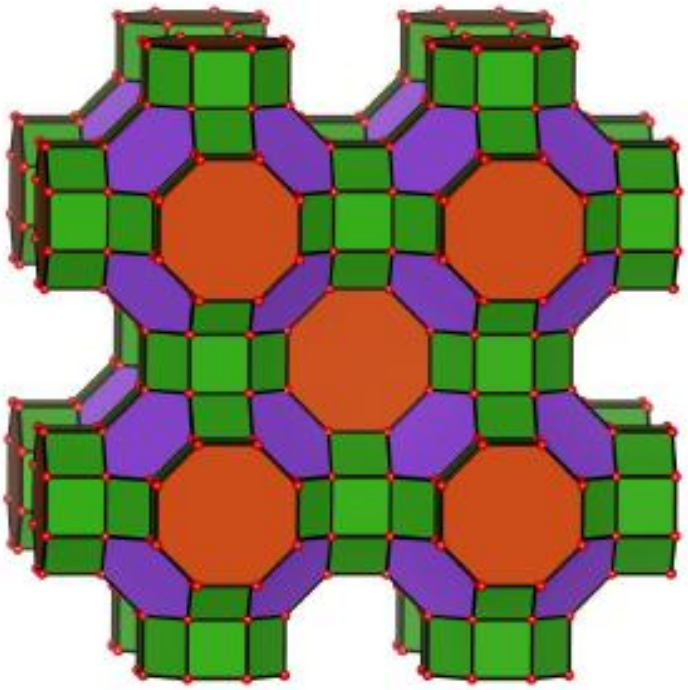

Figure S1. Representation of the structure adopting the RHO topology with 4-, 6-, and 8-membered ring cage apertures in green, violet, and rust-colored, respectively. The red spheres represent the metal cation, whereas the black edges represent the linker.

2. "ZIF-71–H_2O" System: Intrusion-Extrusion Experiments Up to 300 MPa

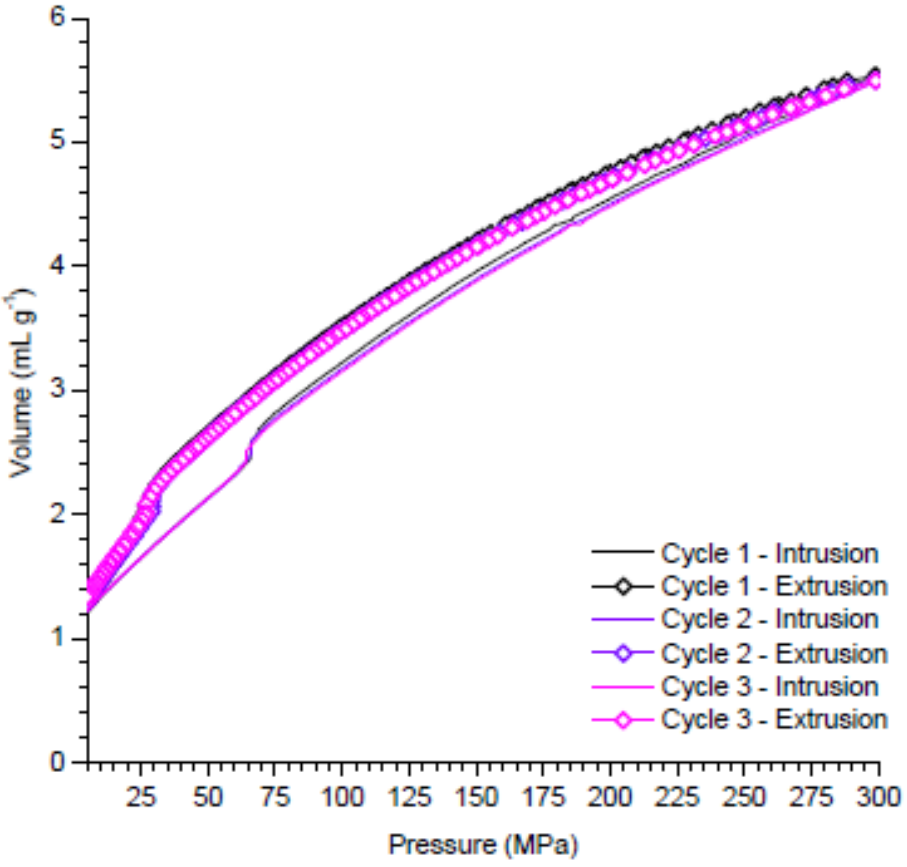

Figure S2. Pressure-volume diagrams of the "ZIF-71–H_2O" system conducted up to 300 MPa.

3. MAF-6 Structure: Effect of the Nonwetting Liquid

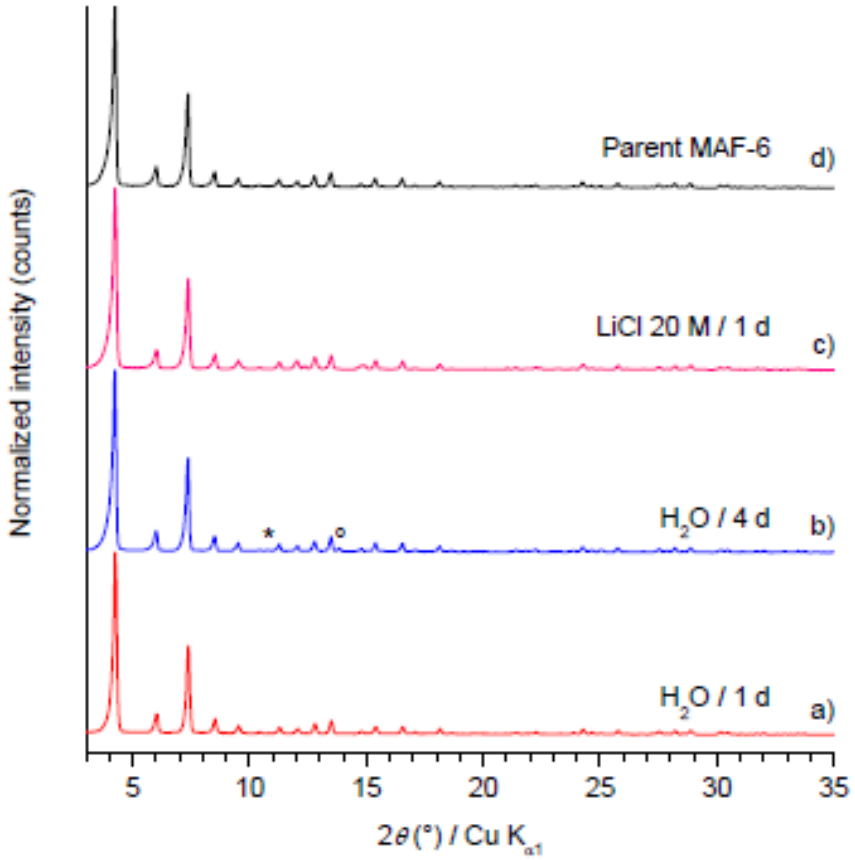

Figure S3. XRD patterns of MAF-6 after suspending in water for (a) 1 day and (b) 4 days, and (c) after suspending in LiCl 20 M aqueous solution for 1 day. For comparison (d) the XRD pattern of parent MAF-6 is also included. ° and * refer to the peaks corresponding to MAF-32 and the unidentified phase X, respectively.

4. MAF-6 Structure: Effect of the Pressure

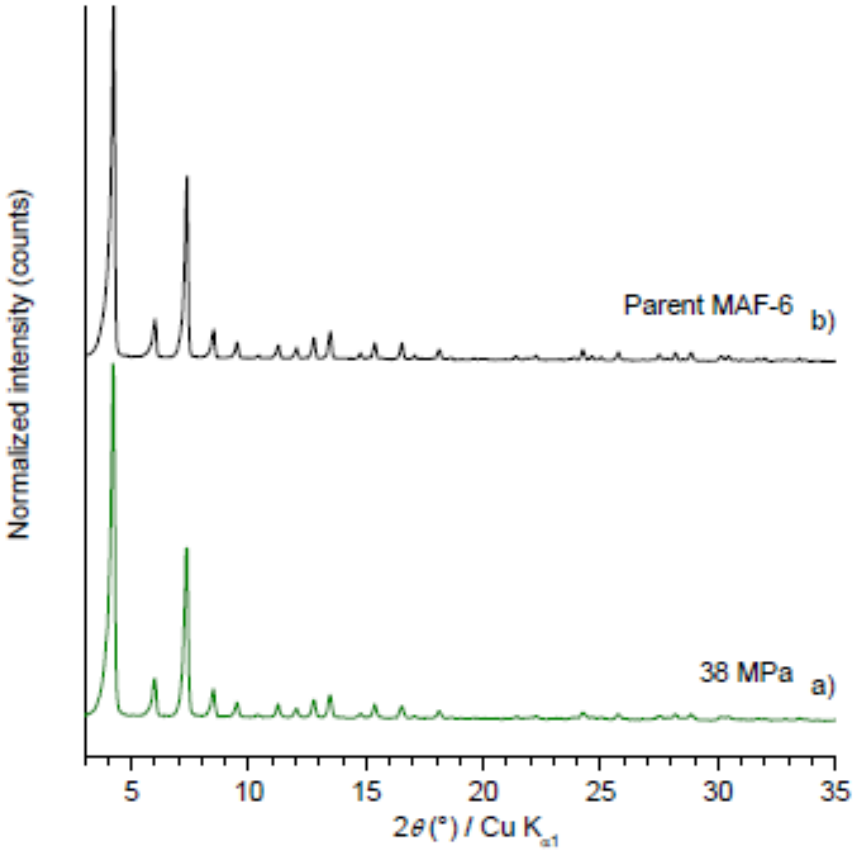

Figure S4. XRD patterns of (a) MAF-6 after subjecting it to a pressure of 38 MPa and (b) the parent MAF-6 material.

5. ZIF-71 Structure: Effect of the Nonwetting Liquid

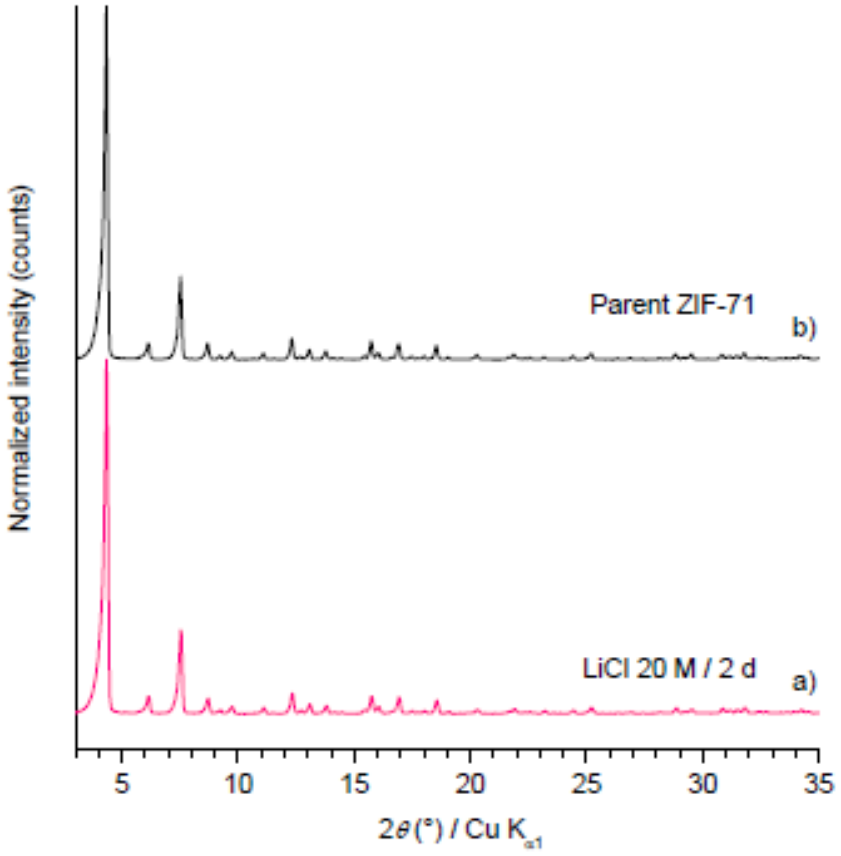

Figure S5. XRD patterns of (a) ZIF-71 after suspending in LiCl 20 M aqueous solution for 2 days and (b) the parent ZIF-71 material.

6. ZIF-71 Structure: Effect of the Pressure

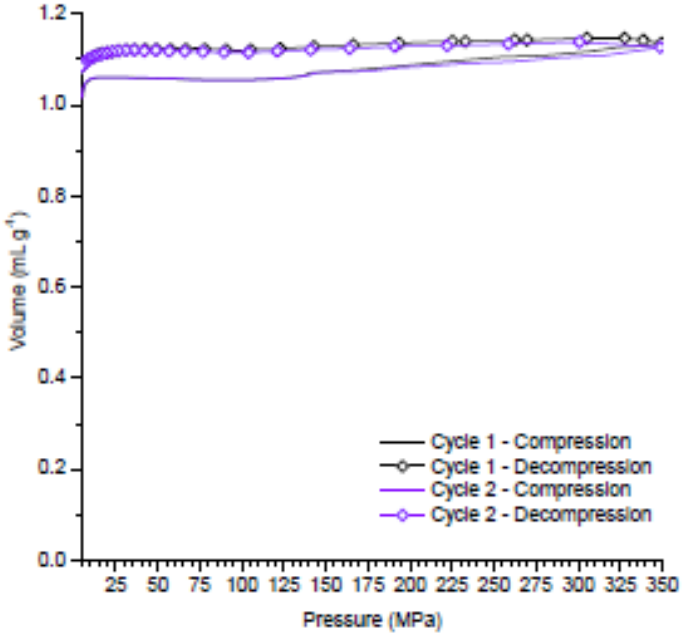

Figure S6. Pressure-volume diagrams obtained from mercury porosimetry experiment performed on ZIF-71.

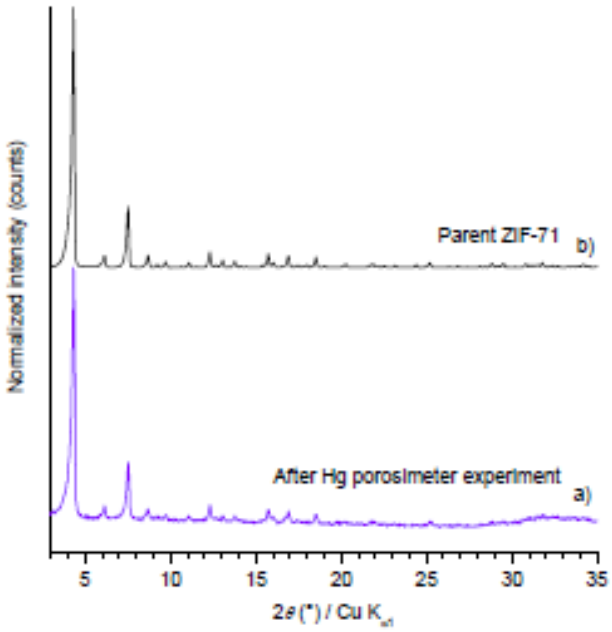

Figure S7. XRD patterns of (a) ZIF-71 after mercury porosimetry experiment and (b) the parent ZIF-71 material.

B. Identification of Phase X

When Article 2 was accepted for publication, the identification of phase X was still in progress. Phase X still remains unidentified, but does not correspond to any of the MAF-6 polymorphs (MAF-32 or ZIF-14/MAF-5), or the organic precursor (Heim), or the plausible zinc-based hydroxide/oxide species; $Zn(OH)_2$ or ZnO, respectively. As previously mentioned, phase X is obtained from MAF-6 *via* a phase transformation process during intrusion−extrusion experiments of water and LiCl 20 M aqueous solution. This phase transformation is clearly more prominent in the case of water. Moreover, phase X is nonporous, as revealed with N_2 sorption analyses, while, according to TG analysis, it is a hybrid organic-inorganic material. Besides, as shown in Figure 1, Scanning Electron Microcopy (SEM) analyses reveal a different morphology for the post-intruded samples (spherical shaped crystals shown in Figures 1b and 1c) compared to the parent MAF-6 material (dodecahedral crystals shown in Figure 1a).

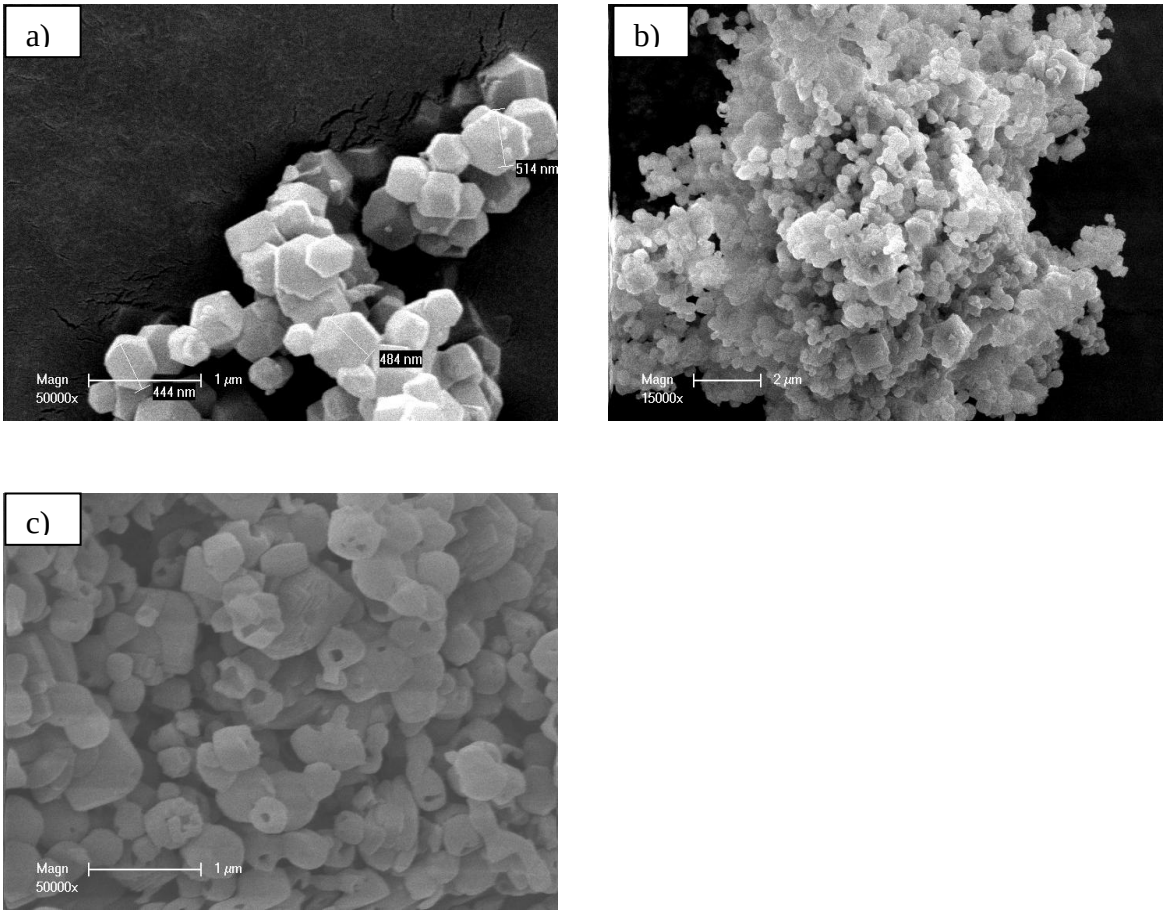

Figure 1. SEM images of (a) parent MAF-6 sample, and (b) samples recovered after three cycles of water and (c) LiCl 20 M aqueous solution intrusion−extrusion experiments realized up to 350 MPa.

Based on these results, one hypothesis would be that MAF-6 is capable of undergoing a partial hydrolysis-condensation phenomenon in the presence of water molecules, which results in the formation of phase X. Even though stability tests performed at room pressure and temperature, by suspending MAF-6 samples in water and LiCl 20 M aqueous solution (with a MAF-6 / water and MAF-6 / LiCl 20 M aqueous solution mass ratios of 10 and 4.8 %, respectively), reveal that the ZIF structure is maintained (Figure 2 and Figure S3 of the supporting information of Article 2), however, it seems that hydrolysis can take place under the combined effect of high pressure and the non-wetting liquid.

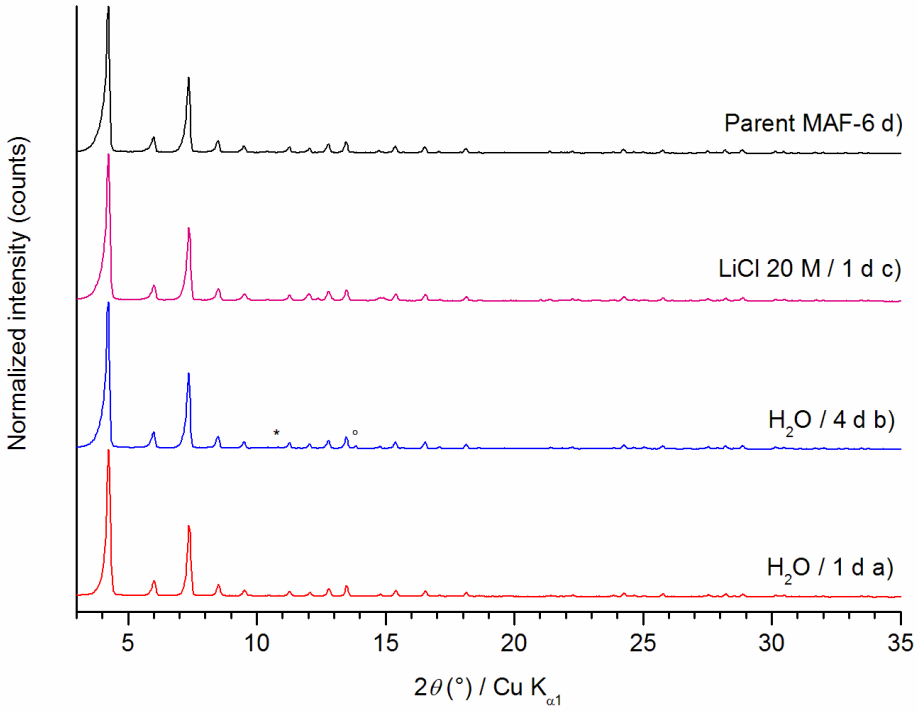

Figure 2. XRD patterns of MAF-6 after suspending in water for (a) 1 d and (b) 4 d and (c) after suspending in LiCl 20 M aqueous solution for 1 d. For comparison, the XRD pattern of parent MAF-6 is also included. ° and * refer to the peaks corresponding to MAF-32 and phase X, respectively.[7]

Indeed, by referring to the XRD and N_2 sorption analyses (Figures 1 and 2 of the Article 2) performed on the ZIF materials after the complementary intrusion−extrusion experiments, at the pressure corresponding to the beginning of the intrusion step, hydrolysis probably only occurs at the surface, as the non-wetting liquid molecules have not yet entered the porosity. Consequently, a slight decrease in the textural properties of MAF-6 is observed at 25 and 70 MPa with water and LiCl 20 M aqueous solution, respectively. This could be assigned to a rising pore blocking caused by the superficial hydrolysis, while the MAF-6 structure is preserved at long range order. When the

pressure reaches P_{int}, water/electrolyte aqueous solution is intruded into the ZIF pores and the effect of hydrolysis starts increasing. This results in further degradation of the framework and, hence, in a lower microporous volume at the end of the intrusion step. Finally, when the applied pressure continues to increase during water intrusion for example, the aqueous medium becomes more "harsh", leading to some further hydrolysis, as indicated from the XRD patterns and N_2 sorption isotherms of the "MAF-6−water" system obtained at 80 and 350 MPa. It is important to note that with both water and the LiCl 20 M aqueous solution, hydrolysis appears mainly when the non-wetting liquid molecules are present inside the porosity, which explains the significant decrease in the textural properties of MAF-6 between the beginning and end pressures of the intrusion step. As the pressure continues to increase, a small decrease in the textural properties of MAF-6 is observed in the case of water, whereas no further decrease is noted with the LiCl 20 M aqueous solution. The fact that the phase transformation of MAF-6 into phase X is more prominent (91% transformation based on nitrogen sorption experiments) during water intrusion−extrusion experiments than in the case of the LiCl 20 M aqueous solution (84% transformation based on nitrogen sorption experiments), can be attributed to the smaller amount of water molecules available for hydrolysis in the case of the highly concentrated aqueous electrolyte solution. Indeed, in the case of the "MAF-6−water" system, part of the water molecules that were intruded into the MAF-6 pores was probably used to hydrolyze the ZIF material. However, the hydrolysis (and the formation of phase X) remains partial (40% of water-intruded MAF-6 remains at the end of the intrusion step, as revealed by the N_2 sorption isotherms obtained after water intrusion−extrusion experiments realized up to 47 MPa) and the water molecules entrapped in the pores of the remaining MAF-6 material seem to be mainly extruded at atmospheric pressure, as indicated from TG analysis. Thus, the **"MAF-6−water" system is said to display a mixture of shock-absorber and bumper behaviors**.

Notably, a hydrolysis-condensation mechanism that is similar to the one proposed to explain the formation of phase X was reported in the case of ZIF-8 in a very recent study published in 2019.[8] Indeed, Zhang *et al*. shed light on the transformation of the ZIF-8 structure into another crystalline phase through a partial hydrolysis-condensation mechanism. When ZIF-8 is suspended in a dilute aqueous medium (ZIF-8 / water mass ratio of ≈ 0.02%) for 24 h at room temperature, with continuous stirring, the authors demonstrated that ZIF-8 is partially hydrolyzed. During the hydrolysis step, a Zn-N coordination bond is cleaved. Consequently, a hydroxyl group from a water molecule substitutes a 2-methylimidazolate linker molecule, whereas the remaining hydrogen atom bonds to the nitrogen of the initially coordinating 2-methylimidazolate. In order to recover the product of hydrolysis, water is evaporated by heating the suspension at 40°C in a convection oven. This step is referred to as the condensation step, during which the clusters and ions reunite and then stack, through hydrogen bonding, to form the new phase. The phase transformation of ZIF-8 is

confirmed through XRD, N_2 sorption, SEM, energy-dispersive X-ray spectroscopy (EDS), and TG analyses. Furthermore, the hydrolysis-tested phase is a hybrid organic-inorganic material with the same C: N: Zn ratio as ZIF-8, however, with an increased oxygen content that is ascribed to the coordinating hydroxyl groups. Therefore, all these characterizations allow concluding that the phase obtained through hydrolysis is a new pseudo-polymorph of ZIF-8, which is dense, nonporous, and has a different morphology (leaf-like) compared to the parent ZIF-8 material (octahedral crystals).

Notably, the results obtained from the characterizations performed on the post-intruded MAF-6 samples are closely related with those obtained by Zhang *et al* for the pseudo-polymorph of ZIF-8.[8] For instance, an analogy can be made up between the mechanisms leading to the formation of the pseudo-polymorph of ZIF-8 and phase X, as both ZIF-8 and MAF-6 are Zn-based materials that are made up of linkers substituted at the position 2 (2-methylimidazolate and 2-ethylimidazolate, respectively). Moreover, similar to the hydrolysis-tested ZIF-8 material, phase X is also nonporous and dense, with the main high relative-intensity peak centered at 10.8° (2θ). It also seems to be a hybrid organic-inorganic material. Besides, a different morphology is revealed for the post-intruded samples (spherical shaped crystals) compared to the parent MAF-6 material (dodecahedral crystals). **Therefore, it can be assumed that, as in the case of ZIF-8, in the presence of water molecules, MAF-6 is capable of undergoing hydrolysis, which is followed by the connection of the ions and clusters and stacking of the framework through hydrogen bonding, finally resulting in the formation of a probably new pseudo-polymorph of MAF-6; denoted as phase X.** It is important to note that Fourier-transform infrared spectroscopy (FTIR) analyses could be used in a comparative study between the parent and post-intruded MAF-6 samples in order to confirm the presence of newly formed hydroxyl groups, in addition to the presence of intermolecular hydrogen bonds between these groups and protons in phase X (which lead to stacking of the framework). Moreover, the oxygen content of phase X could be determined by elementary analyses.

Finally, in order to be able to determine the structure of phase X, a pure phase X sample should be obtained, i. e. no peaks corresponding to traces of the MAF-6 phase should be visible on the XRD pattern of the hydrolyzed sample. In this respect, a complementary water intrusion−extrusion experiment was realized up to 350 MPa and by increasing the number of intrusion−extrusion cycles from 3 to 10. It was expected that continuous loading would eventually lead to the formation of pure phase X. Nevertheless, Figure 3 clearly demonstrates the similarity between the XRD patterns of the post-intruded samples obtained after 3 and 10 consecutive water-intrusion−extrusion cycles. Indeed, this indicates the persistence of a mixture of MAF-6 and phase X and sheds light on the high stability of the latter phase, which was not destroyed over continuous loading.

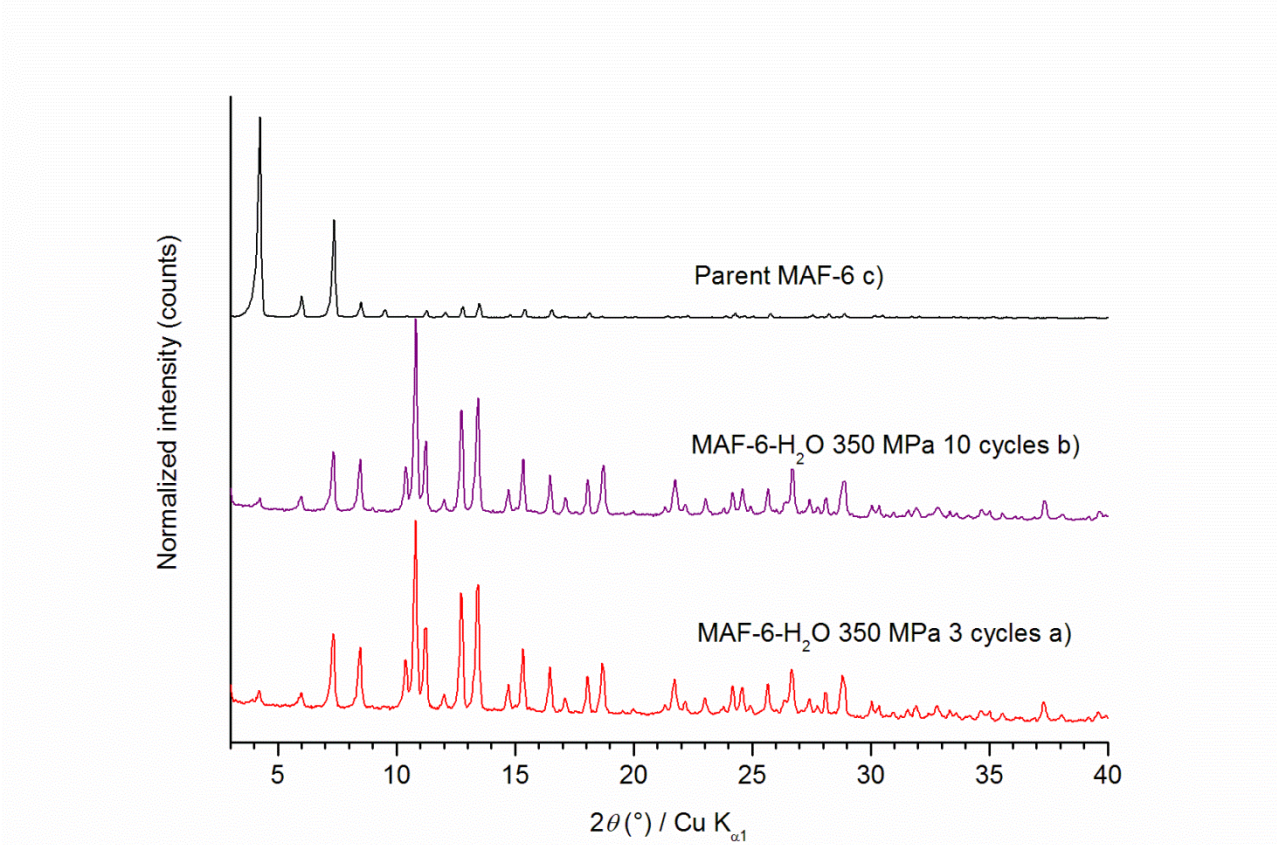

Figure 3. XRD patterns of the "MAF-6−water" system after (a) 3 and (b) 10 intrusion−extrusion cycles realized up to 350 MPa. For comparison, (c) the XRD pattern of the parent MAF-6 material is also represented.

C. Composition of the Post-Intruded MAF-6 and ZIF-71 Samples: ICP and TG Analyses

In the aim of confirming the presence/absence of entrapped LiCl salt ions and/or water molecules in the post-intruded samples after LiCl 20 M aqueous solution intrusion−extrusion experiments realized up to 350 MPa, ICP and TG analyses were carried out and their results were combined so as to determine the composition of the post-intruded samples.

In the case of the ZIF-71 and MAF-6 samples recovered after the LiCl 20 M aqueous solution intrusion−extrusion experiments, ICP analyses indicate a mass percentage of 0.7 and 0.2%, respectively, corresponding to Li cations present in the post-intruded samples' pores. Furthermore, TG analyses reveal a mass loss of 14.6 and 7% for the post-intruded ZIF-71 and MAF-6 samples, respectively, between room temperature and 200°C. Assuming that the salt ions detected with ICP analyses are surrounded by water solvation shells and/or free water inside the ZIF pores, the mass losses observed in this low temperature range can be entirely assigned to the desorption of entrapped water molecules. Indeed, **the results obtained based on ICP and TG analyses do**

confirm the intrusion of both water and electrolytes into the ZIF pores. Moreover, it seems that the non-wetting liquid molecules remain in the porosity even when the pressure is released, which indicates **bumper behavior of both the "ZIF-71−" and "MAF-6−LiCl 20 M aqueous solution" systems**.

Finally, by following the calculation method mentioned in Section III. C. of Chapter 2, the composition of the post-intruded ZIF-71 sample (i.e. ZIF-72) is determined to be: $Zn(dcim)_2 \cdot 0.42LiCl \cdot 3.37H_2O$. It is important to note that the calculations were done based on the fact that ZIF-71 and ZIF-72 (the ZIF-71 polymorph) have the same molar mass.

As for the post-intruded MAF-6 sample, its composition cannot be definitely determined, as supplementary analyses are required, mainly in order to determine the oxygen content resulting from the coordinating hydroxyl groups in the hydrolyzed sample. In this respect, EDS analyses may be carried out (however, after having degassed the post-intruded sample, so as to desorb the entrapped water molecules from intrusion and avoid confusion between the different oxygen sources). Nevertheless, by analogy with what was suggested by Zhang *et al*.,[8] the formula of the post-intruded MAF-6 sample (pure MAF-6 and phase X) can be denoted as follows: $Zn_{((n + m) / 2)}(Heim)_n(eim)_m(OH)_n$. Furthermore, ICP analysis revealed the presence of 0.00207 g of Li per 1 g of the post-intruded sample.

D. Conclusions

In this section, the energetic performances of two ZIF materials; MAF-6 and ZIF-71, were investigated in water and LiCl 20 M aqueous solution intrusion−extrusion experiments. This is the first time that an irreversible phase transformation is observed during intrusion−extrusion experiments, which is attributed to the combined effect of high pressure and the non-wetting liquid. This was highlighted for the "ZIF-71−LiCl 20 M aqueous solution" system, where ZIF-71 undergoes a complete and irreversible crystal phase transformation into the dense and nonporous ZIF-72 phase; a ZIF-71 polymorph of lcs topology, leading, thus, to bumper behavior. Therefore, for the latter system, the volume variation step observed on the $P-V$ diagrams corresponds, in part to the intrusion of the non-wetting liquid molecules into the porosity, associated with the phase transformation into ZIF-72. In contrast, the "ZIF-71−water" system behaves as a perfect shock-absorber. As for MAF-6, the intrusion of water or LiCl 20 M aqueous solution leads to the formation of a new pseudo-polymorph. This new phase, referred to herein as phase X, is probably the result of a partial hydrolysis-condensation mechanism that occurs during both water and LiCl 20 M aqueous solution intrusion−extrusion experiments, however, to a higher extent with water. Even if its chemical composition and structure still need to be resolved, nevertheless, it was evidenced that this new phase is nonporous. In addition, the "MAF-6−water" system displays a mixture of shock-absorber and bumper behaviors, as even though the phase transformation into phase X is irreversible (bumper behavior), however, most of the intruded water molecules are extruded from the porosity at reduced pressure (according to TG analysis). As for the "MAF-6−LiCl 20 M aqueous solution" system, in addition to the fact that the applied mechanical energy is mainly used to induce the irreversible phase transformation, both ICP and TG analyses reveal the persistence of the non-wetting liquid molecules in the porosity of the post-intruded material after the pressure has been reduced. Therefore, the latter system behaves as a bumper.

II. Syntheses, Characterization and Energetic Performances of ZIF-25 and ZIF-71_Br_2

In the aim of studying the influence of the substituent present on the imidazolate linker on the energetic performances of RHO-type ZIF materials during intrusion−extrusion experiments, two ZIF materials of RHO topology; ZIF-25 and ZIF-71_Br_2 (with two CH_3 and Br atoms in positions 4 and 5, respectively) were chosen to be compared with ZIF-71 (two Cl atoms in position 4 and 5).
To this end, herein, the syntheses of ZIF-25 and ZIF-71_Br_2 are optimized prior to studying their energetic performances in high-pressure intrusion−extrusion experiments of water and LiCl 20 M aqueous solution. The syntheses conditions of both materials are developed by varying several compositional (reaction mixture composition and solvent) and process (synthesis duration and temperature) parameters. We note that the synthesis of ZIF-25 has already been reported in the literature,[4-5] whereas, to the best of our knowledge, that of ZIF-71_Br_2 has never been published. In Section II. A., the optimization procedure for the synthesis of ZIF-25 is detailed together with its structure and properties. This section also includes the results obtained from water intrusion−extrusion experiments performed on ZIF-25. Section II. B. is devoted to the optimization of the ZIF-71_Br_2 synthesis.

A. ZIF-25

ZIF-25 is made up of zinc cations that are tetrahedrally coordinated by 4,5-dimethylimodazolate (dmim) linkers. Similar to the MAF-6 and ZIF-71 materials, ZIF-25 possesses a RHO framework topology, with 4-, 6-, and 8-membered ring pore apertures (Section I. A.). The synthesis of ZIF-25 was first reported in the literature by Yaghi and coworkers.[4] The corresponding synthesis conditions involve dissolving anhydrous zinc acetate and 4,5-dimethylimidazole (Hdmim) in *N*,*N*-dimethylformamide (DMF), resulting in the formation of two separate solutions of the metal and organic precursors. The two solutions are then mixed together and the molar composition of the starting reaction mixture is, therefore, 1 Zn: 3 Hdmim: 260 DMF. The reaction mixture is then heated at 125°C for 12 h, finally yielding ZIF-25 powder (Table 1). Even though, according to the literature, the synthesis protocol followed by Yaghi and coworkers successfully yields ZIF-25 crystals of RHO topology, however, by repeating the synthesis under the exact same conditions, only a gel-like material was obtained (**Sample 1** in Table 1). In this regard, the optimization of the synthesis of ZIF-25 was necessary. The corresponding synthesis conditions of significant attempts are represented in Table 1, whereas Section II. A. 1. details the process of optimization of the ZIF-25 synthesis.

Table 1. Synthesis conditions of the ZIF-25 samples synthesized with and without modulators.

Sample	Solvent	Acid	Zn: Hdmim: solvent: acid molar ratio	Temperature (°C)	Duration (h)	Container	Aspect	Experimental mass (mg)	Experimental yield (%)
according to Ref. [4]	DMF	-	1: 3: 260: 0	125	12	Scintillation vial (20 mL)	Powder	27	76
1	DMF	-	1: 3: 260: 0	125	12	Glass bottle	Yellow gellish material	-	-
2	DMF	-	1: 3: 260: 0	125	48	Glass bottle	Yellow gellish material	-	-
3	DMF	-	1: 3: 260: 0	125	19	T-20 autoclave	White powder	52	24
4	DMF	-	1: 3: 260: 0	140	48	T-50 autoclave	Pale yellow powder	240	62
5	DMF	-	1: 3: 260: 0	140	48	T-50 autoclave	Dark brown suspension	456	116
6	DMF	AA	1: 3: 260: 3	140	48	T-50 autoclave	Yellow suspension	123	39
7	DMF	AA	1: 3: 260: 12	140	48	T-50 autoclave	No precipitation	-	-
8	DMF	AA	1: 3: 260: 7.5	140	48	T-50 autoclave	Yellow precipitate	35	12
9	DMF	AA	1: 3: 260: 7.5	140	72	T-50 autoclave	Yellow precipitate	107	36
according to Ref. [5]	MeOH	FA	*1: 3: 370:3	120	24	T-30 autoclave	Powder		
10	EtOH	FA	1: 3: 370: 3	120	24	T-50 autoclave	Brown powder	14	7
11	EtOH	FA	1: 3: 370: 3	100	48	T-50 autoclave	Brown powder	4	4
12	EtOH	FA	1: 3: 370: 3	110	41	T-50 autoclave	Brown powder	10	3

In all cases, the metal source used is anhydrous zinc acetate (except in the case of reference 5). * indicates that zinc acetate dihydrate is used as the metal source. AA and FA refer to acetic acid and formic acid, respectively.

1. Optimization of the Synthesis Protocol

In the first approach towards optimizing the synthesis conditions of ZIF-25, while keeping the same compositional and process parameters as those employed in the protocol followed by Yaghi and coworkers,[4] only the synthesis duration was extended to 48 h, as we assumed that 12 h (as denoted in the literature) are probably not enough to crystallize the material. Nonetheless, this resulted again in the formation of a gel-like material (**Sample 2**). To this end, in the next synthesis, both the synthesis duration and nature of the container were varied . The reaction mixture was heated in a PTFE-lined stainless-steel autoclave (instead of a glass bottle) for 19 h (an intermediate duration between 12 and 48 h). By referring to Figure 1, the powder X-ray diffraction (PXRD) pattern of **Sample 3** could be indexed in the RHO topology, which indicates the successful formation of ZIF-25 crystals. However, the experimental yield was low (≈ 24%) and the obtained mass (≈ 52 mg) was also insufficient for an intrusion−extrusion experiment where around 100 mg of the ZIF material are required. Therefore, further optimization of the synthesis of ZIF-25 was needed. In order to increase the yield of the reaction, two process parameters were varied compared to the previous synthesis. In this regard, the synthesis temperature and duration were increased from 125 to 140°C and from 19 to 48 h, respectively (Table 1). In addition, we attempted to scale up (by a factor of 2) the synthesis by increasing the masses of the metal and organic precursors and the solvent, while maintaining the same molar composition of the reaction mixture as the one used in the previous syntheses. Following this protocol, around 240 mg of ZIF-25 were successfully obtained with a yield of 62% (**Sample 4**). It is important to note that **Sample 4** was used to fully determine the structure of ZIF-25, from which the ZIF's theoretical XRD pattern was, consequently, generated (Section II. A. 2.). Nevertheless, this recipe for the synthesis of ZIF-25 was not reproducible, as it later led to the formation of aggregations of nanocrystals of indefinite shape, as revealed by the scanning electron microscopy (SEM) analysis performed on **Sample 5** (Figure 2). The formation of nanocrystals could also be indicated from the broad shape of the corresponding PXRD peaks compared to the theoretical pattern (Figure 1). The very high synthesis yield obtained for **Sample 5** (116%) may be probably attributed to the presence of solvent molecules entrapped in the interparticular porosity of the formed aggregations. It is also important to note that nanosized ZIF materials were shown to display a larger number of defects compared to microcrystals, which was associated with lower intrusion pressures and irreversible phenomena during water intrusion−extrusion experiments.[9] Indeed, this makes microcrystals more desired for energetic applications.

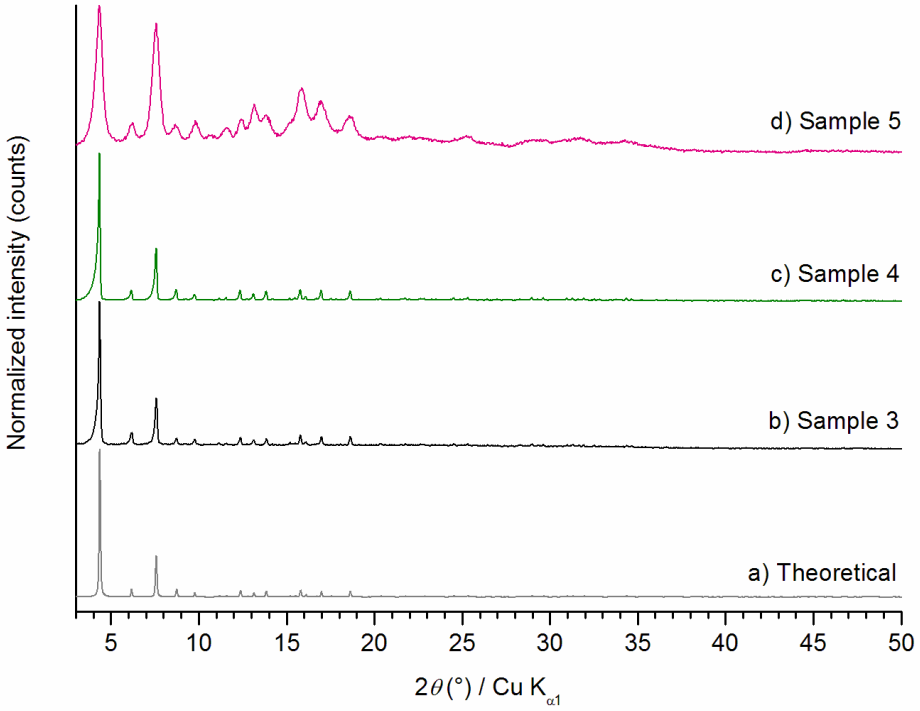

Figure 1. (a) Theoretical XRD pattern of ZIF-25 and the experimentally obtained PXRD patterns corresponding to Samples (b) 3, (c) 4, and (d) 5.

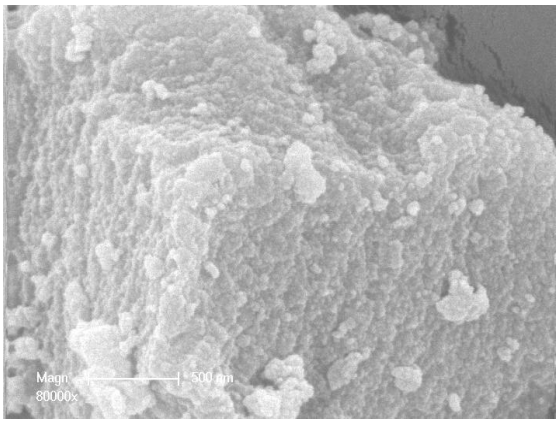

Figure 2. SEM image of Sample 5.

Given these results, it was important to enhance the crystal growth so as to obtain ZIF-25 on the micrometer scale. One way for increasing the crystal size of MOFs, is through employing modulators, such as organic acids.

In Section II. A. 1. a., the role of the modulator in MOF synthesis is defined and the two different modulator-assisted synthesis routes, that were followed in the aim of optimizing the synthesis of ZIF-25, are discussed.

a. Optimization of the ZIF-25 synthesis Protocol by Using Modulators

In fact, a modulator can be viewed as both, a crystal growth inhibitor or promoter.[10] In the former case, the modulator acts as a capping agent as it terminates the crystal by coordinating to the metal center at the site where a polydentate framework linker should exist.[10] The capping agent is monodentate and lacks further binding sites. Thus, no further assembly of the network can take place and MOFs of smaller particle size are expected to be formed.[10] Nonetheless, when competing with the ligand on coordination to the metal cation, a monodentate modulator decreases the nucleation rate and, consequently, increases the MOF particle size.[10] Moreover, the lower the pK_a of the modulator, the more deprotonated i.e. more acidic it is, which implies stronger competition with the ligands on coordinating to the metal center. For instance, using 30 equivalents of benzoic acid, as a modulator, in the synthesis of UiO-68-NH_2, yielded microcrystals of 100 μm in size.[11]

In this work, two organic acids; acetic and formic acids, were employed as modulators in two separate synthesis protocols towards the optimization of the ZIF-25 synthesis by increasing the particle size. Acetic acid was used as it is the conjugate acid of acetate in zinc acetate; the metal precursor, whereas formic acid was employed in order to mimic the synthesis protocol reported by Gao *et al*.[5]

i. The Acetic Acid Synthesis Route

A first modulator-assisted ZIF-25 synthesis trial was carried out using acetic acid (CH_3COOH) of pK_a value ≈ 4.8. Assuming that each mole of acetic acid will compete with one mole of the organic precursor, 3 molar equivalents of CH_3COOH were employed in the first synthesis trial. Indeed, the compositional and process parameters were maintained similar to the previous synthesis (**Samples 4 and 5**), with the only difference being the addition of the modulator to the reaction mixture (**Sample 6**) (Table 1). A fine yellow powder was obtained, which, based on XRD analyses, corresponded to ZIF-25 of RHO topology (Figure 3). Moreover, compared to **Sample 5**, the XRD peak widths were remarkably diminished after the addition of acetic acid (Figure 3). Nonetheless, employing 12 molar equivalents of acetic acid did not lead to the precipitation of the product, probably due to the highly acidic pH of the reaction medium (**Sample 7**). However, with an optimized molar composition, using 7.5 molar equivalents of the modulator, narrower peaks were revealed from the corresponding XRD pattern (**Sample 8**) (Figure 3). Furthermore, dodecahedral-shaped microcrystals of 2-6 μm in size were obtained, i.e. similar to was obtained by Gao *et al.*,[5] albeit a slightly smaller particle size and presenting a wider size distribution (Figure 4a). These results are in agreement with the hypothesis on the role of the modulator in decreasing the nucleation rate, while enhancing crystal growth. The acetic acid synthesis route was also further optimized by increasing the synthesis duration to 72 h, so as to enhance the synthesis yield (**Sample**

9) (Table 1). The optimized protocol yielded 104 mg of pure ZIF-25 material of RHO framework topology, as indicated in Figure 3, with the synthesis yield increasing from 12 to 36% for **Samples 8 and 9**, respectively. Furthermore, SEM analysis shows that increasing the synthesis duration does not affect the morphology of the ZIF-25 crystals, as, similar to **Sample 8**, crystals of **Sample 9** also show a dodecahedral shape, with the particle size ranging between 2-6 µm (Figure 4b) and again revealing a wide distribution in crystals size.

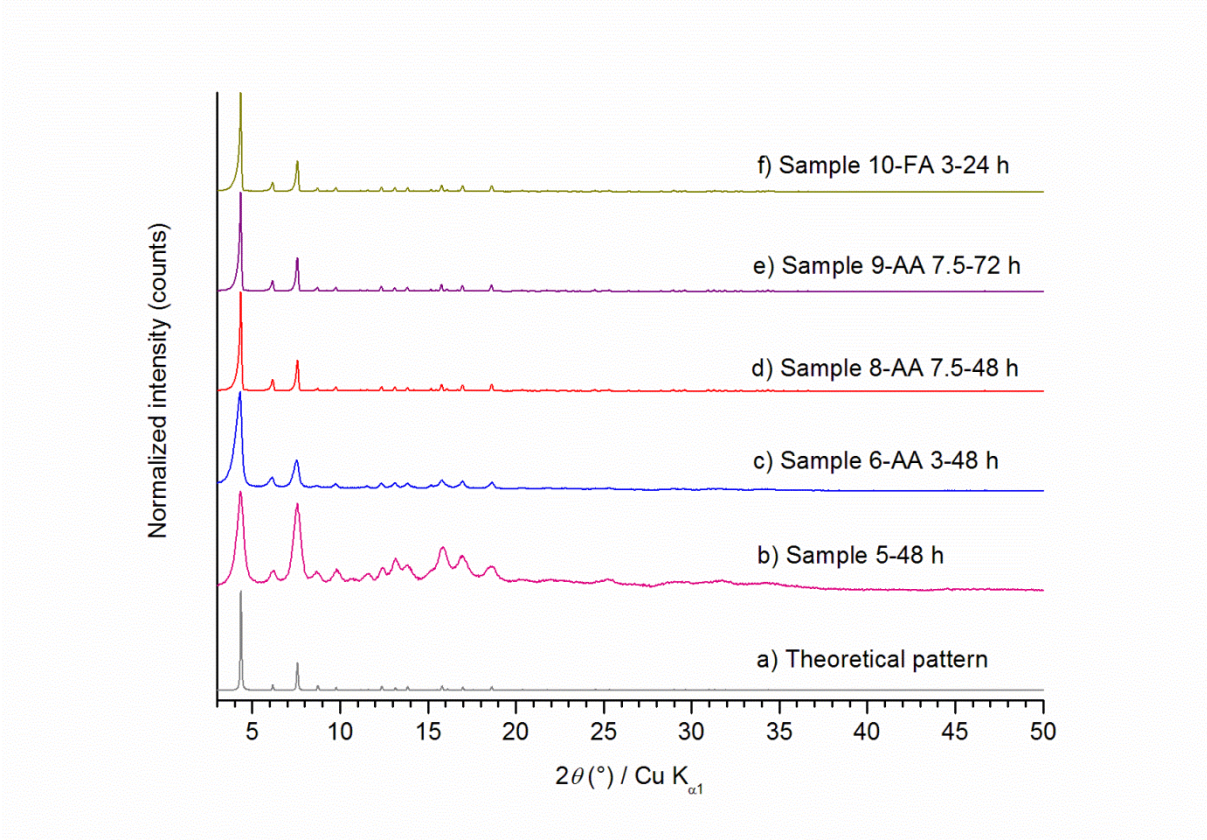

Figure 3. (a) Theoretical XRD pattern of ZIF-25 and the experimentally obtained XRD patterns corresponding to Samples (b) 5 (c) 6, (d) 8, (e) 9, and (f) 10. AA and FA are the abbreviations for acetic and formic acids, respectively. The number noted next to the acid name's abbreviation indicates the corresponding number of molar equivalents of the acid (ex: AA 3 corresponds to three molar equivalents of acetic acid).

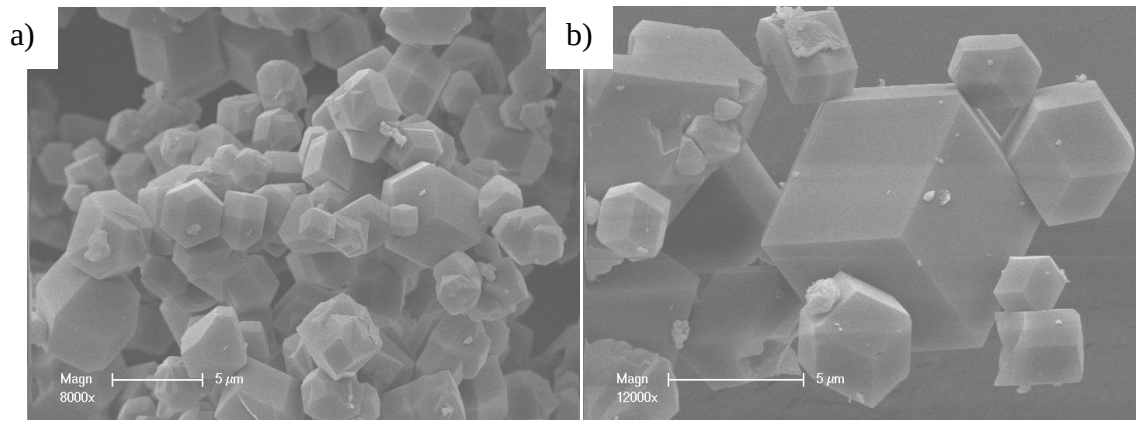

Figure 4. SEM image of Samples (a) 8 and (b) 9.

The optimized synthesis protocol of ZIF-25 (Sample 9) is the following:

In a PTFE-lined stainless steel autoclave (T-50 mL), anhydrous zinc acetate ($Zn(C_2H_3O)_2$, 0.2093 g, 1.1412 mmol) was dissolved in DMF (21.70 g, 296.85 mmol). 4,5-dimethylimidazole (Hdmim, 0.3278, 3.4100 mmol) was added and the reaction mixture was stirred for 10 minutes (a white solution was obtained). Then, acetic acid ($C_2H_4O_2$, 0.514 mg, 8.56 mmol) was added to the reaction mixture, which was stirred for 3 minutes, resulting in the formation of a clear solution. The molar composition of the starting reaction mixture was, therefore, 1 Zn: 3 Hdmim: 260 DMF: 7.5 $C_2H_4O_2$. The autoclave was sealed and heated in an oven at 140°C for 72 h.
Crude ZIF-25 was recovered by Büchner filtration on a grade 5 Whatman filter paper. The retained powder was washed with MeOH (≈ 40 mL) and then dried in air.

ii. The Formic Acid Synthesis Route

In 2018, Gao *et al*. reported a new synthesis protocol for ZIF-25,[5] which is based on the same Zn precursor: organic precursor molar ratio used in the work of Yaghi and coworkers (i.e., 3),[4] however, while employing 4,5-dimethylimidazole formate as the organic precursor (instead of 4,5-dimethylimidazole) and methanol as a solvent (instead of DMF). We note that the pK_a value of formic acid is ≈ 3.75, which is lower than that of acetic acid (≈ 4.8). This indicates a higher acidity of formic acid, which can probably lead to an enhanced growth-promoting effect.[10] The synthesis protocol also requires heating the reaction mixture at 120°C for 24 h.
In the aim of obtaining the best-quality ZIF-25 sample, we intended to mimic Gao *et al*.'s synthesis protocol and compare its results to those obtained from the optimized protocol (following the acetic acid route). To this end, a 1: 1 molar ratio of Hdmim and formic acid were used (giving a zinc precursor: formic acid molar ratio of 1: 3). In addition, methanol was substituted by ethanol for safety reasons (**Sample 10**). A well crystallized sample of ZIF-25 was successfully obtained, as indicated with XRD analysis (Figure 3), nevertheless, in a very low yield (7 %), with only 14 mg

that are, indeed, insufficient for going further with the characterization of the material and for performing intrusion−extrusion experiments. It is also important to note that modifying the process parameters, such as the duration and temperature did not improve the synthesis yield (**Samples 11 and 12**) (Table 1).

Therefore, these results indicate that, compared to acetic acid, the formic acid route is less efficient in the synthesis of ZIF-25, as it is associated with much lower synthesis yields.

In conclusion, after varying several process and compositional parameters, the synthesis of ZIF-25 of RHO-type framework topology was optimized. The best conditions (Sample 9) were obtained by using acetic acid as a modulator.

The next sections involve a description of the structure of the ZIF-25 material and its main properties. Note that the work concerning the structure was performed by Dr. Jean-Louis Paillaud (IS2M, MPC).

2. Structural Analysis Based on Rietveld Refinement

ZIF-25 and ZIF-71 are two isoreticular materials, where the crystal structure of the latter ZIF material is already known. Therefore, the XRD pattern of ZIF-25 can be simulated from the single crystal structure of ZIF-71, by substituting the two chlorine atoms in the latter material by two methyl groups. By comparing the simulated (calculated) XRD pattern to that obtained from PXRD analysis, a Rietveld refinement can be performed, which allows refining the structure.[12]

As previously mentioned, the synthesis of ZIF-25 was first reported by Yaghi and coworkers in 2010.[4] Based on experimental data and simulation analysis, the latter team indexed the PXRD pattern of ZIF-25 in the *F*-centered cubic lattice ($a \approx 28.76$ Å, *Fd*-3*m* space group).[4] However, surprisingly, the authors did not report any Rietveld refinement data. Later in 2018, based only on simulation analysis, Gao *et al*. reinvestigated the structure of ZIF-25.[5] Nevertheless, unlike the results reported by Yaghi and coworkers,[4] ZIF-25 crystallizes in the primitive cubic lattice ($a \approx$ 28.55 Å, *Pm*-3*m* space group,) according to Gao *et al*.[5] Surprisingly, the authors did not publish the simulated atomic coordinates.

To this end, using Rietveld refinement, we intended to resolve the crystal structure of ZIF-25 from the powdered sample. Thus, the PXRD pattern of ZIF-25 (**Sample 4**) was compared to that calculated based on the single crystal structure of ZIF-71.[13] The starting model, including hydrogen atoms, was constructed from ZIF-71 in the space group *Pm*-3*m* and the structure was minimized with the Universal force field available in the Cerius2 package. Then, during Rietveld refinement, all the atoms were refined isotropically and soft restraints (bonds, angles, planars) were added to the ZnN_4 tetrahedra and 4,5-dimethylimidazolate linkers in order to maintain their suitable geometries. Consequently, the final Rietveld refinement gave acceptable reliability factors. Figure 5 represents

the final Rietveld plot, whereas the crystal and Rietveld refinement parameters and the atomic parameters are listed in Tables 2 and 3, respectively.

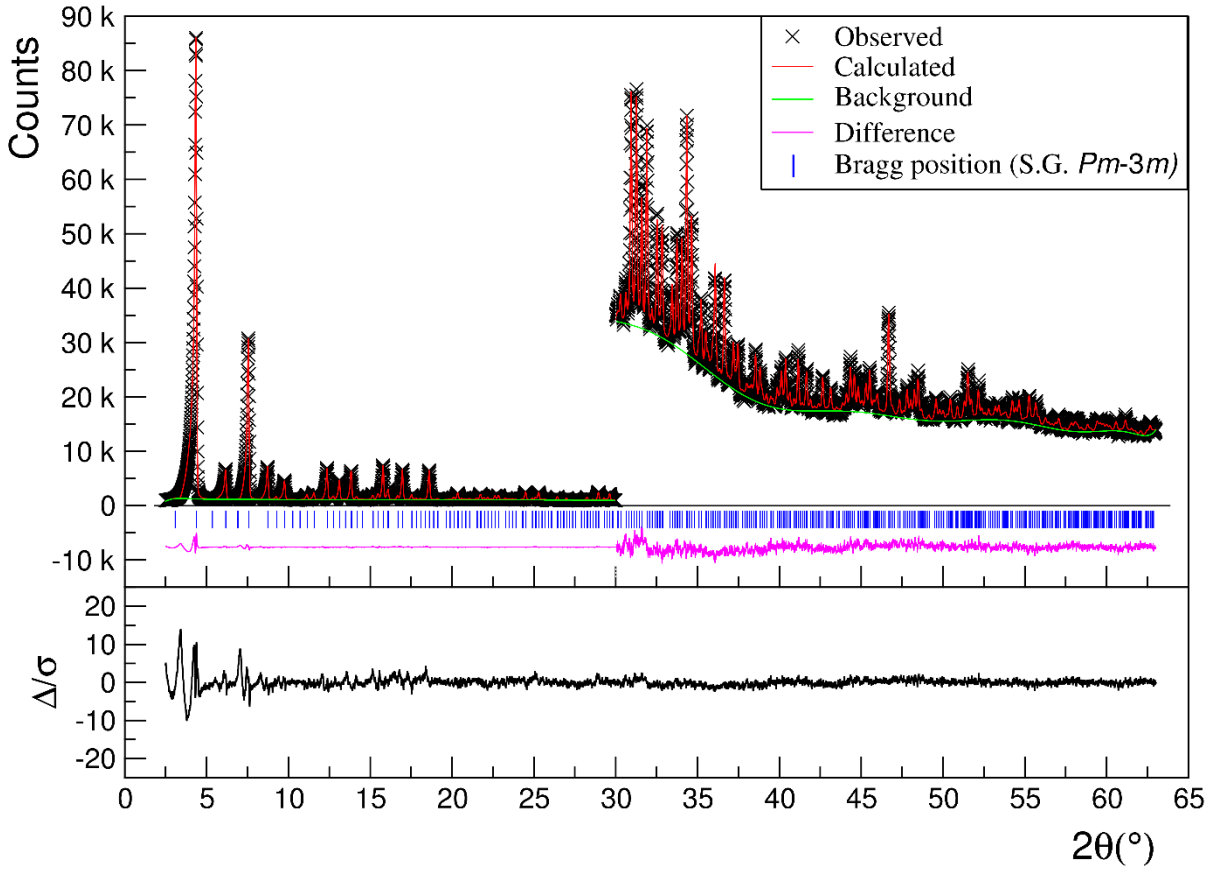

Figure 5. Rietveld plot of ZIF-25. The high-angles range (30-63 in 2θ (°)) is magnified by a factor of 35. Δ/σ is the weighted difference between the experimental and calculated diffraction patterns; the square of this weighted difference is what is actually minimized.

Table 2. Crystal and Rietveld refinement data of ZIF-25.

Chemical formula	$C_{20}H_{28}N_8Zn_2$
Space group	*Pm*-3*m* (# 221)
λ (Å), CuK$_{α1}$	1.5406
Data collection temperature (°C)	20
***a* (Å)**	28.5639(3)
***V* (Å^3)**	23305.2(8)
Z	24
Computing Rietveld software	GSAS-II[14]
Number of data points, 2θ range (°) (step (° (2θ))	6051, 2.5-63.0, 0.01
Number of contributing reflections	829
Number of structural variables	20
Number of profile parameters	5
Total number of restraints (bonds, angles, planars)	78 (32, 42, 4)
Total number of constraints	4
R_p	0.0253
wR_p	0.0378
wR_{exp}	0.0262
R_F	0.0499
R_F^2	0.0441
R_B	0.0260
wR_B	0.0357
Goodness of fit	1.468
Largest differences peak and hole (ē/Å^3)	0.386, -0.244

Table 3. Atomic parameters of ZIF-25.

Atom	Wyckoff positions	x	y	z	U (Å^2)[a]
Zn1	48n	0.39477(16)	0.10328(17)	0.25195(20)	0.1137(15)
C1A	24k	0.3921(7)	0	0.2575(8)	0.120(7)
H1A	24k	0.4210(26)	0	0.276(4)	0.1200
N1A	48n	0.3708(5)	0.03923(30)	0.2423(7)	0.1200
C2A	48n	0.3327(6)	0.02367(15)	0.2184(7)	0.1200
C3A	48n	0.2986(4)	0.0557(4)	0.1948(5)	0.1200
H2A	48n	0.301(4)	0.0883(16)	0.208(4)	0.1200
H3A	48n	0.2654(9)	0.043(3)	0.200(5)	0.1200
H4A	48n	0.306(4)	0.057(5)	0.1599(12)	0.1200
C1B	24l	1/2	0.1090(13)	0.2506(7)	0.089(7)
H1B	24l	1/2	0.1198(15)	0.2177(10)	0.0890
N1B	48n	0.46047(29)	0.0995(7)	0.2752(5)	0.0890
C2B	48n	0.47629(15)	0.0859(7)	0.3186(5)	0.0890
C3B	48n	0.4458(4)	0.0714(6)	0.3587(5)	0.0890
H2B	48n	0.4127(13)	0.083(4)	0.3534(22)	0.0890
H3B	48n	0.4583(26)	0.085(3)	0.3883(11)	0.0890
H4B	48n	0.446(4)	0.0356(10)	0.3616(27)	0.0890
C1C	24m	0.3180(6)	0.1120(7)	0.31800	0.138(7)
H1C	24m	0.3057(11)	0.0819(12)	0.30570	0.1380
N1C	48n	0.3544(5)	0.1357(5)	0.2986(5)	0.1380
C2C	48n	0.3596(5)	0.1743(6)	0.3257(5)	0.1380
C3C	48n	0.3973(5)	0.2082(4)	0.3142(5)	0.1380
H2C	48n	0.3830(11)	0.2390(18)	0.305(5)	0.1380
H3C	48n	0.416(3)	0.1958(25)	0.288(4)	0.1380
H4C	48n	0.4180(31)	0.213(4)	0.3419(18)	0.1380
C1D	24m	0.3899(9)	0.1794(5)	0.17940	0.120(7)
H1D	24m	0.3753(22)	0.2022(10)	0.20220	0.1200
N1D	48n	0.3962(7)	0.1332(4)	0.1885(5)	0.1200
C2D	48n	0.4174(6)	0.11609(32)	0.1493(3)	0.1200
C3D	48n	0.4307(5)	0.0667(4)	0.1423(6)	0.1200
H2D	48n	0.4051(26)	0.0500(16)	0.125(5)	0.1200
H3D	48n	0.435(5)	0.0516(16)	0.173(1)	0.1200
H4D	48n	0.4607(31)	0.0651(9)	0.124(5)	0.1200

[a] The atomic displacement parameters (ADPs) of same values were constrained to be equal.

Figure 6 represents the asymmetric unit of ZIF-25, where there is one crystallographically distinct Zn atom and four distinct linkers' moieties.

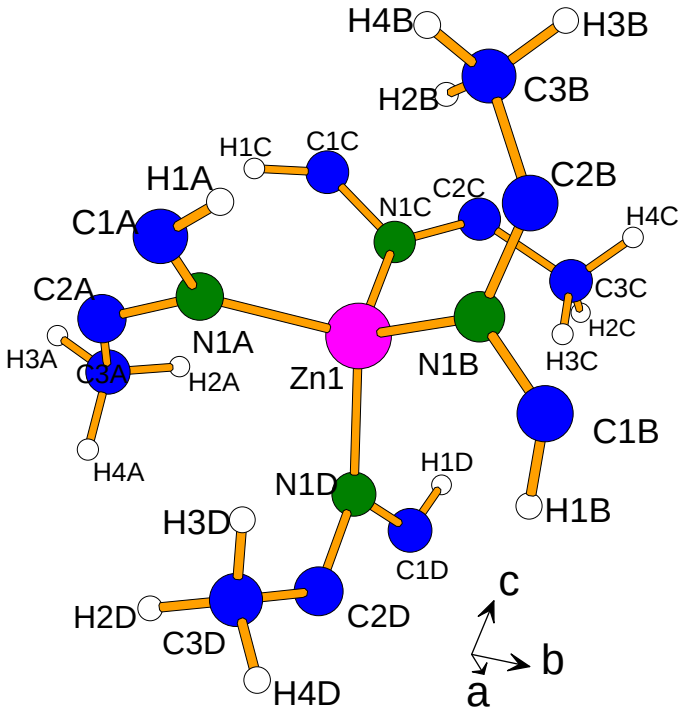

Figure 6. Asymmetric unit of ZIF-25.

3. Textural Properties and Thermal Stability

In addition to the high crystallinity and phase purity of the obtained ZIF-25 material, N_2 adsorption-desorption measurements revealed that the optimized ZIF-25 sample (**Sample 9**) exhibits a type I sorption isotherm (Figure 7) and that its textural properties are comparable to those reported in the literature,[4-5] with the experimentally determined microporous volume and BET surface area (determined in the 0.00263- 0.00616 p/p^0 range) in the order of 0.55 $cm^3\ g^{-1}$ and 964 $m^2\ g^{-1}$, respectively.

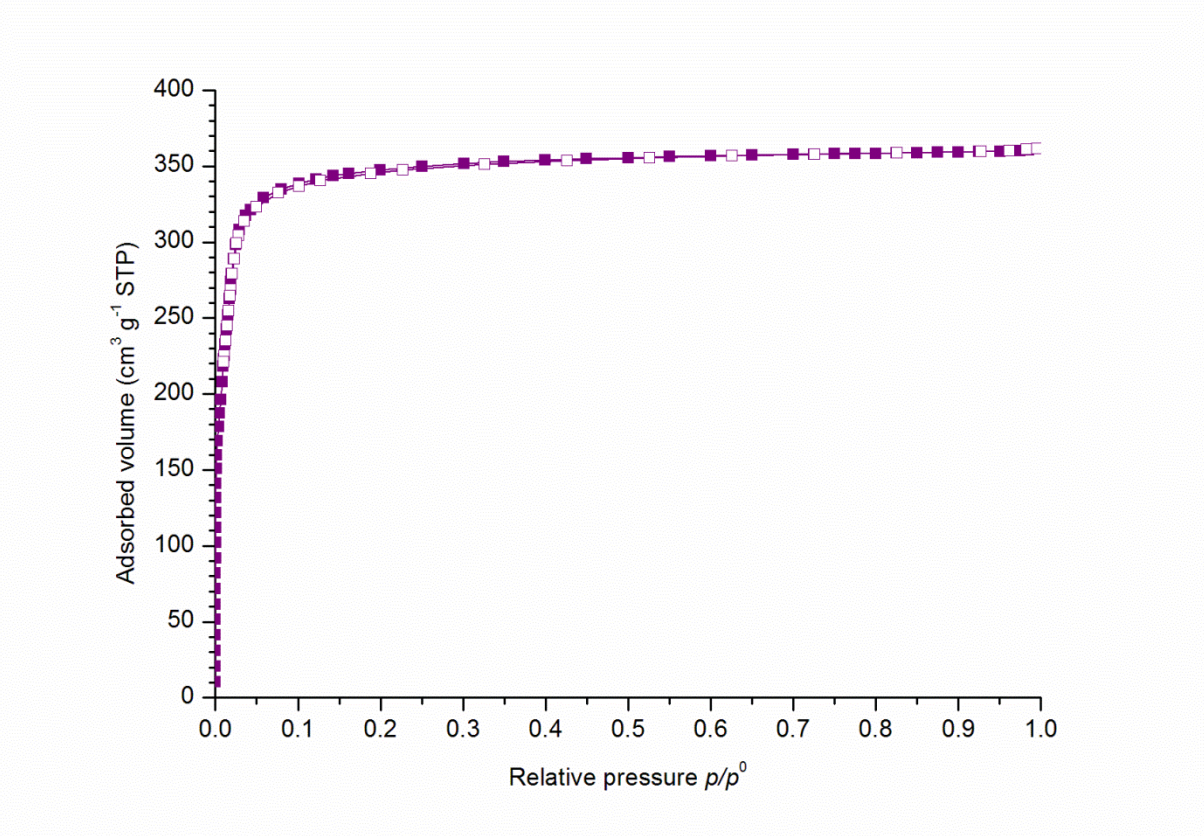

Figure 7. N_2 adsorption-desorption isotherm of Sample 9. Filled and empty symbols correspond to the adsorption and desorption branches, respectively.

Moreover, TGA performed on the optimized ZIF-25 sample (**Sample 9**) after activation, reveals that the ZIF material is thermally stable up to around 300°C (Figure 8), proving again the relatively high thermal stability of ZIF materials. Only one main decomposition step is observed on the TG curve between 300-650°C, corresponding to a mass loss of 69 %, and indicating the degradation of the organic framework. Indeed, this value is in agreement with the calculated mass loss (68 %) assigned to the transformation of ZIF-25 into ZnO (i.e. the degradation of the organic network). The absence of a mass loss between room temperature and 300°C reveals that the ZIF pores are liberated and that ZIF-25 is hydrophobic (absence of organic solvent in the porosity and/or water molecules in the porosity and on the crystal surface). The hydrophobic character of ZIF-25 had also been confirmed through water vapor adsorption-desorption measurements carried out by Gao *et al.*[5] Indeed, the corresponding simulated and experimentally obtained water vapor sorption isotherms (at 298 K) indicate that the water uptake remains almost negligible with the increase in water's relative pressure.

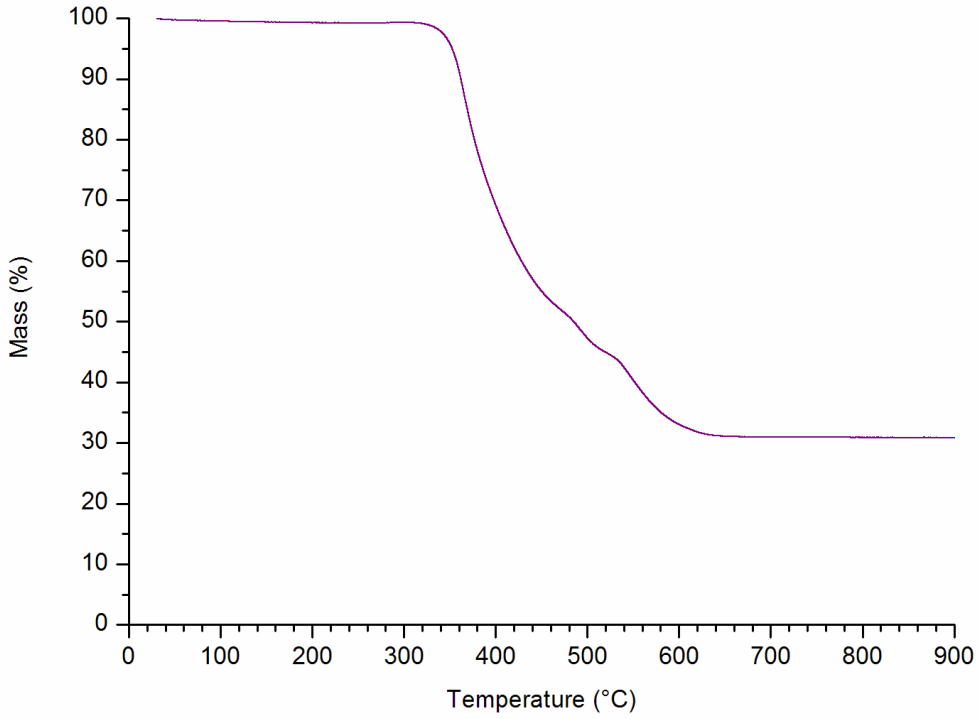

Figure 8. TG curve of Sample 9.

Therefore, the optimized ZIF-25 sample (**Sample 9**), obtained *via* the acetic acid route, shows high crystallinity and phase purity as indicated by the corresponding XRD pattern. The textural characteristics deduced from N_2 sorption measurements are similar to the ones reported in the literature. TG and water sorption analyses also reveal the relatively high thermal stability and hydrophobicity of ZIF-25. Furthermore, SEM images show the formation of microcrystals, which are, indeed, desired in intrusion−extrusion experiments. Thus, all these characteristics of ZIF-25 make it an interesting candidate for the investigation of its energetic performances in high-pressure water and LiCl 20 M aqueous solution intrusion–extrusion experiments.

In Section II. A. 4., the results obtained from the water intrusion−extrusion experiment performed on ZIF-25 are described. The intrusion−extrusion experiments carried out using LiCl 20 M aqueous solution are still in progress.

4. Water Intrusion−Extrusion Experiments

a. Pressure−Volume Diagrams

A water intrusion−extrusion experiment was carried out on ZIF-25 up to 350 MPa and over three consecutive cycles. The corresponding pressure−volume ($P-V$) diagrams are represented in Figure

9. On the diagrams, the 0-5 MPa pressure range, which is related to the compression of the ZIF particles and intrusion of water in the interparticular porosity, is not shown.

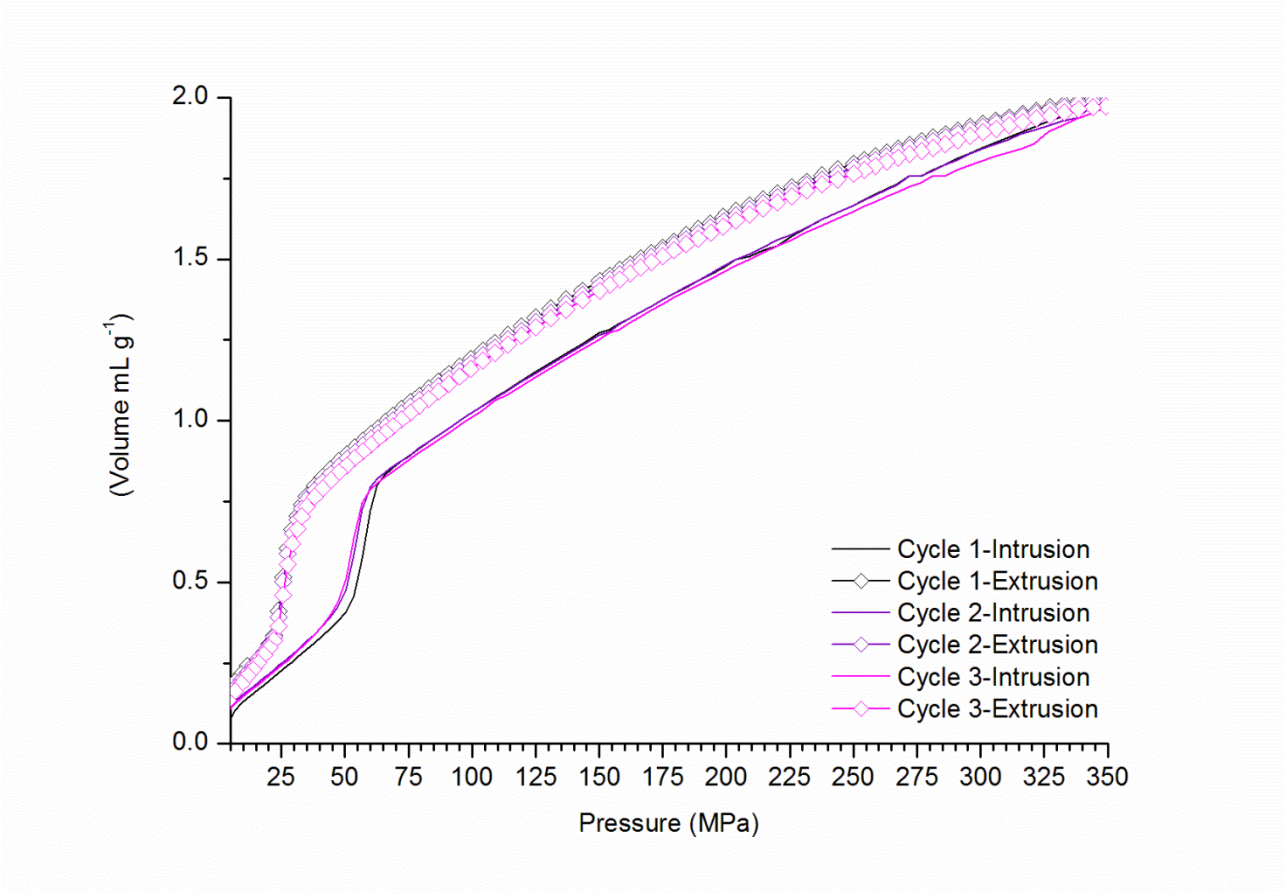

Figure 9. P−V diagrams of the "ZIF-25−water" system.

The intrusion curve of the first intrusion−extrusion cycle exhibits one main steep step that corresponds to the intrusion of water molecules into the ZIF-25 pores, with an intrusion pressure in the order of 58 MPa that is lower than the P_{int} value registered for the "ZIF-71−water" system (P_{int} = 71 MPa).

The intruded water volume is 0.53 mL g^{-1}, which is higher than that in the case of ZIF-71 (0.36 mL g^{-1}). Such a difference in the intruded volumes between both materials is in agreement with their microporous volumes ($V_{microporous}$ = 0.55 and 0.37 cm^3 g^{-1} for ZIF-25 and ZIF-71, respectively). The calculated water density values (or occupation factor of water in the space accessible by nitrogen) are 0.96 and 0.97 for ZIF-25 and ZIF-71, respectively. This is in contrast with what is observed for ZIF-8 and ZIF-8_Cl, with the corresponding water density values being lower and in the order of 0.76 and 0.84, respectively. The *P*−*V* diagrams of the "ZIF-25−water" system reveal that the phenomenon is completely reversible, as the extrusion curve also exhibits a steep volume variation step, corresponding to 0.53 mL g^{-1} (V_{ext}) and, thus, implying the complete extrusion of the non-

wetting liquid molecules from the porosity. However, this step occurs at a lower pressure (≈ 25 MPa) compared to the intrusion step, with a large hysteresis between the intrusion and extrusion curves. In the second and third cycles, the *P*−*V* diagrams of the "ZIF-25−water" system reveal a slight decrease in the intruded volume from 0.53 mL to 0.51 mL g^{-1}, which can be probably attributed to an experimental error. Nevertheless, the phenomenon is also reversible in both cycles (complete extrusion of water molecules from the porosity). The calculated energy yield is 42-45%, which indicates that the "ZIF-25−water" system behaves as a perfect shock-absorber, with a stored energy value of 29-31 J g^{-1}.

The intrusion−extrusion parameters and energetic behavior of the "ZIF-25−water" system are listed in Table 4. For comparison, the energetic characteristics of the "ZIF-71−water" system are also listed

Table 4. Energetic characteristics of the "ZIF-25−" and "ZIF-71−water" systems.

System	Cycle	P_{int} (MPa)	P_{ext} (MPa)	V_{int} (mL g^{-1})	V_{ext} (mL g^{-1})	E_s (J g^{-1})	E_r (J g^{-1})	Energy yield (%)	Energetic behavior
ZIF-25−water	1	58	25	0.53	0.53	31	13	42	SA
	2	56	25	0.51	0.51	29	13	45	SA
	3	56	25	0.51	0.51	29	13	45	SA
ZIF-71−water	1	71	30	0.36	0.36	26	11	42	SA
	2	71	30	0.36	0.36	26	11	42	SA
	3	71	30	0.36	0.36	26	11	42	SA

Intrusion (P_{int}) and extrusion (P_{ext}) pressures, intruded (V_{int}) and extruded (V_{ext}) volumes, stored (E_s) and restored (E_r) energies. SA refers to shock-absorber behavior.

These results show that both **ZIF-25 and ZIF-71 (of RHO-type framework topology) display similar energetic behaviors (shock-absorber), with the amount of stored energy for both systems being similar, ranging between 26-31 J g^{-1}.** It is also important to note that, similar to the case of SOD-type ZIFs, **the nature of the substituent (CH_3 or Cl) present on the imidazolate linker in a RHO-type ZIF material does not seem to affect the type of behavior of the corresponding LHS when water is used as the non-wetting liquid.** Indeed, both the **"ZIF-25−" and "ZIF-71−water" systems behave as shock-absorbers, whereas the "ZIF-8−" and "ZIF-8_Cl−water" systems, of SOD-type ZIFs, display spring behavior.**

b. Post-Intrusion Characterizations

The recovered post-intruded ZIF-25 sample was analyzed with XRD and N_2 sorption analyses. Figure 10 reveals that the ZIF-25 structure is retained after the water intrusion−extrusion experiment, as the XRD patterns of the parent (**Sample 9**) and post-intruded ZIF-25 samples are similar.

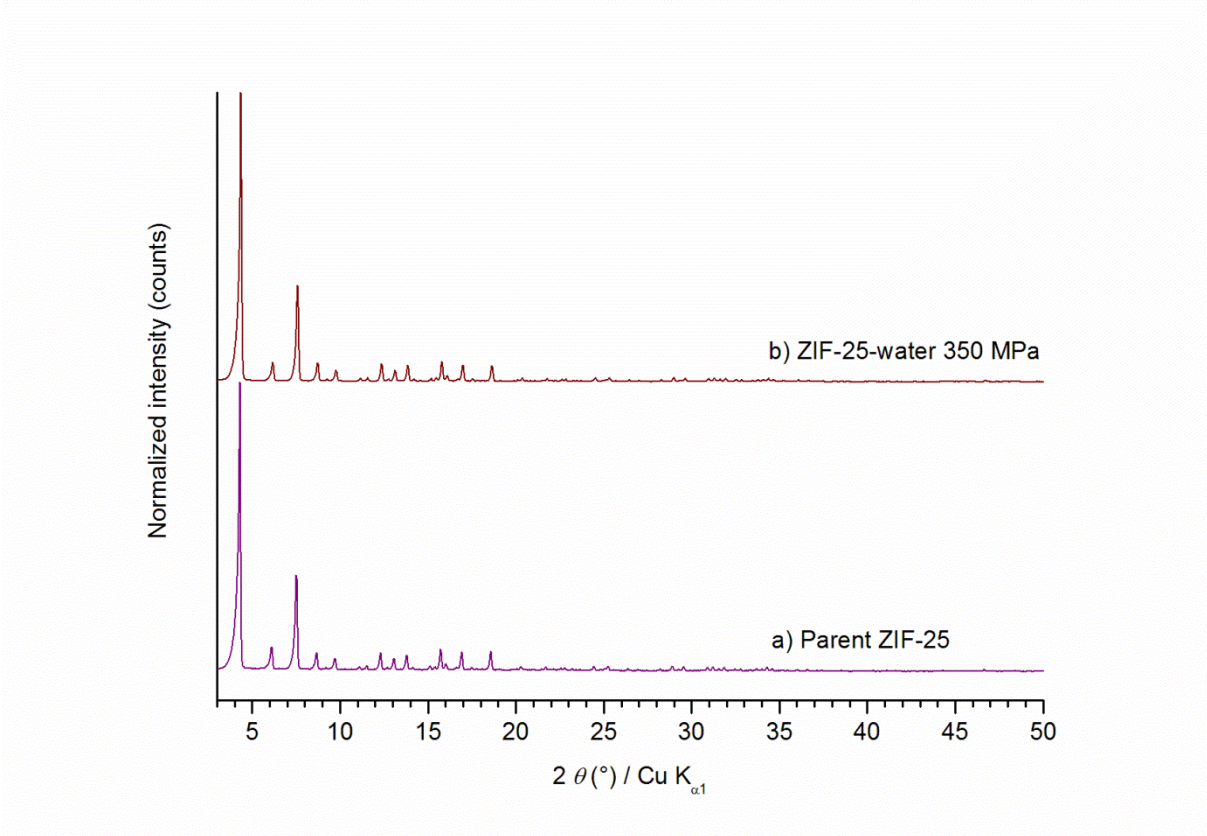

Figure 10. XRD patterns of the (a) parent (Sample 9) and (b) post-intruded ZIF-25 materials.

However, N_2 adsorption-desorption measurements show a small decrease in the textural properties of ZIF-25 after water intrusion compared to the parent material (Figure 11). The BET surface area (determined in the 0.00206 - 0.00689 p/p^0 range) and microporous volume decrease from 949 to 846 $m^2\ g^{-1}$ and from 0.55 to 0.48 $cm^3\ g^{-1}$ (13% decrease), respectively, which can be probably attributed to a partial degradation of the framework under the combined effect of high pressure and the non-wetting liquid during intrusion−extrusion experiments. The effect of pressure on the partial degradation of the ZIF-25 framework is planned to be verified by carrying out a supplementary intrusion−extrusion experiment, up to a lower pressure, i.e. 100 MPa.

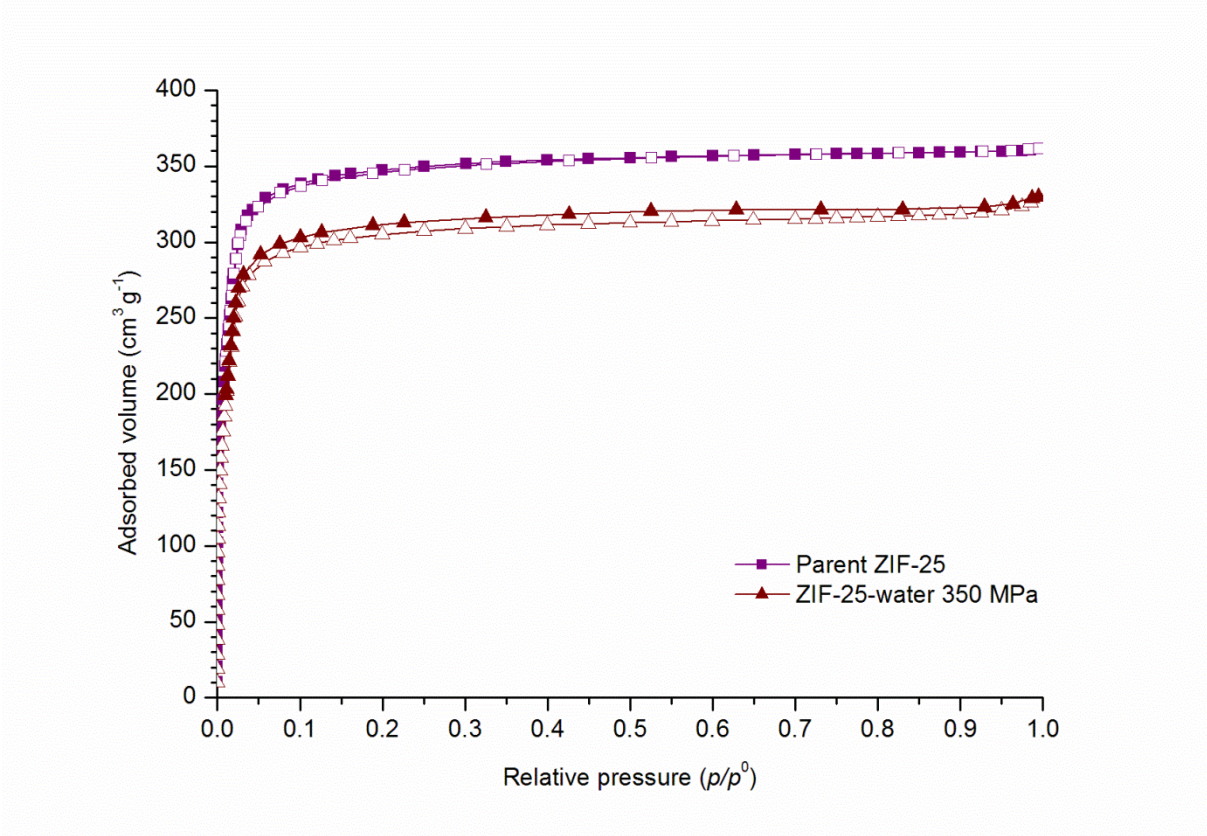

Figure 11. N_2 adsorption-desorption isotherms of the parent (Sample 9) and the post-intruded ZIF-25 materials. Filled and empty symbols correspond to the adsorption and desorption branches, respectively.

5. Conclusions

After following different synthesis routes and varying several process and compositional parameters, the synthesis of ZIF-25 was successfully optimized by employing acetic acid as a modulator. The acetic acid synthesis route leads to the formation of highly crystalline ZIF-25 material in a yield of 36% and with a mass that is sufficient for intrusion−extrusion experiments. The obtained product also exhibits relatively high porosity (0.55 cm^3 g^{-1}), thermal stability (up to 300°C), and hydrophobicity. Furthermore, microcrystalline ZIF-25 particles are obtained, which should theoretically exhibit less defects compared to nanocrystals and are, thus, more desired in intrusion−extrusion experiments. It is also important to note that herein, the structure of ZIF-25 is refined through Rietveld refinement and fully reported for the first time in *Pm*-3*m* space group. The novelty of this work is also attributed to the study of ZIF-25 in water intrusion−extrusion experiments for the first time, whereby the "ZIF-25−water" system, similar to the "ZIF-71−water" system, displays perfect shock-absorber behavior, with a stored energy value close to 30 J g^{-1}. Nevertheless, the intrusion pressure is lower in the case of ZIF-25 compared to the ZIF-71−water" system, which could not be attributed to the flexibility of the former material.

It also appears that, similar to the case of SOD-type ZIFs, the nature of the substituent present on the imidazolate linker (considering CH_3 and Cl) in a RHO-type ZIF material does not influence the energetic behavior of the corresponding LHS when water is used as the non-wetting liquid. In contrast, the energetic behavior seems to be affected by the topology as shock-absorber behavior is observed for both the "ZIF-25−" and "ZIF-71−water" systems, based on RHO-type ZIFs, whereas both the "ZIF-8−" and "ZIF-8_Cl−water" systems, based on SOD-type ZIF materials, display spring behavior. Moreover, post-intrusion characterizations reveal only a partial degradation of the framework (based on N_2 sorption measurements) during intrusion−extrusion experiments, which is probably due to the combined effect of water and high pressure. We note that as a future perspective, a supplementary water intrusion−extrusion experiment up to a maximum pressure of 100 MPa has to be undertaken, so as to verify the effect of pressure on the partial degradation of the ZIF-25 framework. Finally, the energetic performance of ZIF-25 using LiCl 20 M aqueous solution is to-be investigated, so as to compare the ZIF-25-based system's behavior to that of the "ZIF-71−LiCl 20 M aqueous solution" system.

B. ZIF-71_Br_2

In this work, we also intended to synthesize a new bromated and isoreticular analogue of ZIF-71 material of formula $Zn(dcim)_2$,[13] exceptionally denoted in the following sections as ZIF-71_Cl_2 (in order to avoid any confusion), so as to investigate its energetic performances in water and LiCl 20 M aqueous solution intrusion−extrusion experiments. This targeted ZIF material is expected to be constituted of Zn cations bridged through 4,5-dibromoimidazolate (dbim) ions and is referred to herein as ZIF-71_Br_2. Indeed, being isoreticular to ZIF-71 (ZIF-71_Cl_2) and ZIF-25, ZIF-71_Br_2 should also exhibit an RHO framework-type topology. In the following sections, we present the different synthesis protocols and the associated process and compositional parameters that were varied in the aim of obtaining a pure phase ZIF-71_Br_2 material. Nevertheless, XRD analyses revealed that the product of the syntheses was always a mixture of the targeted RHO phase and another unknown phase, which will be referred to in the following sections as phase Y, where the latter's abundance varies with the syntheses conditions.

1. Synthesis of ZIF-71_Br_2

a. Effect of the Synthesis Duration

In the first approach towards obtaining ZIF-71_Br_2, **Samples 13** and **14** were synthesized by mimicking the synthesis conditions of ZIF-71_Cl_2 [15] i.e. the metal and organic precursors; zinc acetate and Hdbim, respectively, were dissolved in MeOH, unlike the ZIF-71_Cl_2 protocol, which involves preparing two separate solutions; a metal and an organic precursor solution, after which

the former solution is added to the latter. Similar to the case of ZIF-71_Cl_2, the final molar composition of the reaction mixture was: 1 Zn: 4 organic precursor: 1854 MeOH. The reaction mixture was then left to stand at room temperature until the formation of a precipitate. The corresponding synthesis conditions are further detailed in Table 5. Based on our frequent observation of the reaction medium, precipitation first occurred after 9 d (**Sample 13**), that is, after a significant longer duration compared to ZIF-71_Cl_2. Nevertheless, we extended the synthesis duration for the second sample (**Sample 14**) to 11 d. Both samples were recovered by Büchner filtration over a Whatman 5 filter paper, washed with a few milliliters of fresh MeOH, and then left to dry in air. The obtained white powders were analyzed with XRD and the experimental patterns were compared to the theoretical XRD pattern of ZIF-71_Br_2 (Figure 12). The latter was simulated from the crystal structure of ZIF-71_Cl_2, by substituting the chlorine atoms with bromine. For both **Samples 13** and **14**, XRD analysis reveals the formation of ZIF-71_Br_2 of RHO topology. However, the presence of an extra peak at 5.5° in 2θ (Figure 12) that cannot be indexed in the RHO phase indicates the formation of another unknown phase, denoted herein as phase Y. Table 6 displays the lattice parameters of **Samples 13** and **14** obtained from the refinement of the corresponding PXRD patterns using the *Pm*-3*m* space group. In order to estimate the evolution of phase Y with the synthesis duration, for each sample, the areas A_1 and A_2 under the peaks centered around 4.3 and 5.5° in 2θ, corresponding to the RHO and Y phases, respectively, were determined (by using the integrate function of Origin software in the 3.28 - 4.76° and 4.96 - 5.84° in 2θ ranges of the corresponding XRD patterns, respectively). Preferential orientation can be excluded owing to the Debye-Scherrer mode used for the registering of XRD patterns as well as the supposed cubic system of ZIF-71_Br_2 and phase Y structures. The ratios of A_2 / A_1 were then calculated and the corresponding values are represented in Figure 15 and Table 5. The obtained results reveal a decrease in the A_2 / A_1 ratio with the decrease in the synthesis duration. Indeed, the lower the A_2 / A_1 ratio, the less prominent is phase Y with respect to the ZIF-71_Br_2 phase.

Table 5. Synthesis conditions of the ZIF-71_Br_2 samples.

Sample	Zn: linker: MeOH: HCOONa molar ratio	Duration (d)	Aspect	Experimental mass (mg)	Experimental pseudo yield (%)	A_2 / A_1 ratio
ZIF-71_Cl_2 according to ref [15]	1:4: 1852: 0	1	Pale pink powder	1022	94	-
13	1:4: 1852: 0	9	White powder	121	58	0.111
14	1:4: 1852: 0	11	White powder	151	73	0.247
15	1:4: 300: 0	1	White powder	58	63	-
16	1:4: 300: 0	4.7	White powder	70	77	0.079
17	1:4: 300: 4	4.7	White powder	53	59	0.020
18	1:4: 300:8	4.7	White powder	50	56	0.002
19	1:4: 300: 4	3.8	White powder	44	48	0.288
20	1:4: 300:8	3.8	White powder	54	59	0.055
21	1:4: 300:8	2.7	White powder	75	81	0.006
22	1:4: 300: 4	4.7	White powder	16	17	1.005
23	1:4: 300: 4	4.7	White powder	37	40	1.760
24	1:4: 300: 4	4.7	White powder	41	45	0.098

For comparison, the synthesis conditions of ZIF-71_Cl_2 are also recalled in the first line. A_1 and A_2 values were determined by using the integrate function of Origin software in the 3.28 - 4.76° and 4.96 - 5.84° ranges of the corresponding XRD patterns, respectively. Note that the term "pseudo yield" is used in the table, as the obtained products in all cases are not pure (ex: ZIF-71_Br2 + phase Y).

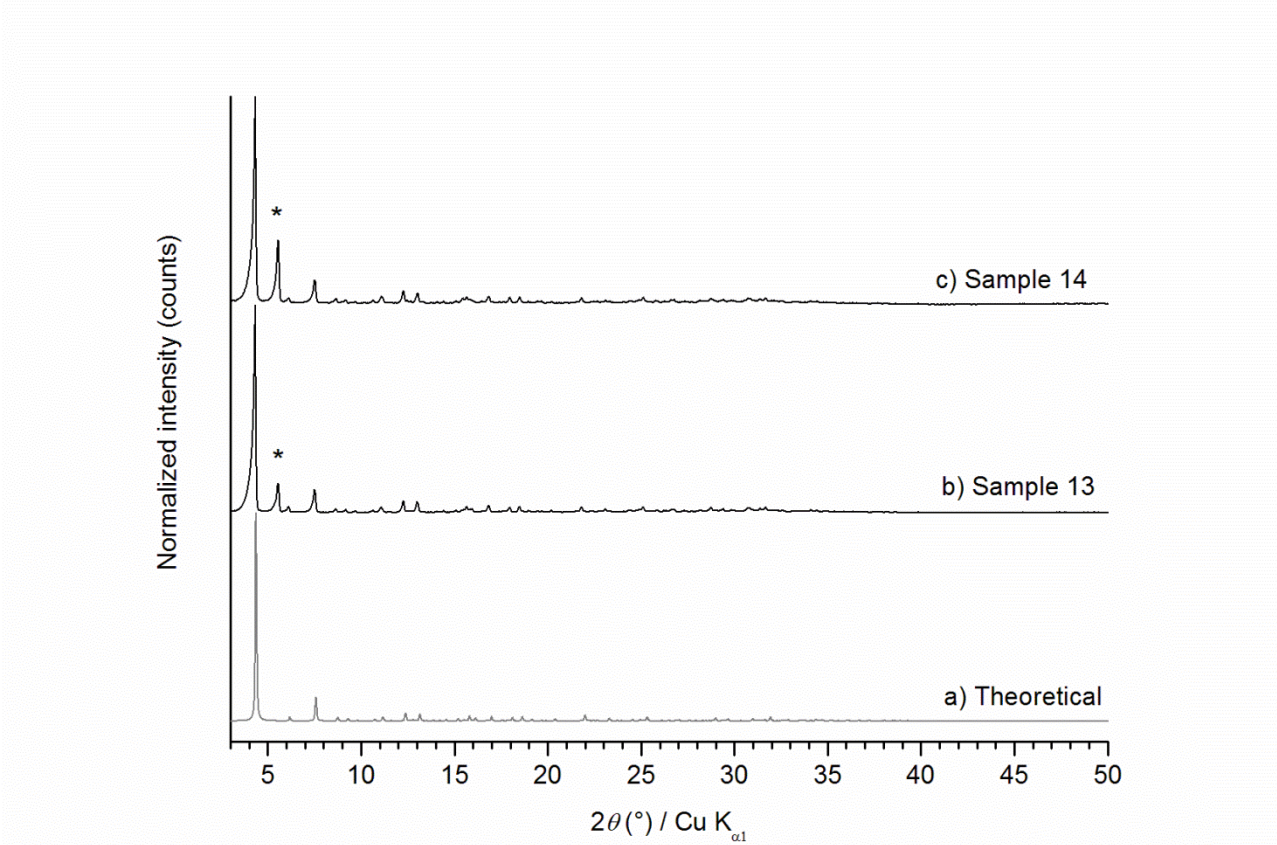

Figure 12. (a) Theoretical XRD pattern of ZIF-71_Br_2 and XRD patterns of Samples (b) 13 and (c) 14. * denotes the extra peak corresponding to phase Y.

Table 6. Lattice parameters of Samples 13 and 14 obtained from the refinement of the corresponding PXRD patterns.

Sample	**Crystal system**	***a* (Å)**	***V* (Å^3)**	**Space group**	**Figures of merit F(30)**
13	cubic	28.55(4)	23280.4(542)	*Pm*-3*m*	11.5
14	cubic	28.50(4)	23139.1(621)	*Pm*-3*m*	11.1

The extra peak at 5.5° is not taken into account when indexing.

Interestingly also, SEM images of both samples clearly show a mixture of two types of particles; dodecahedral microcrystals of 5-8 µm in size, which constitute the majority of the particles and probably correspond to ZIF-71_Br_2, in addition to larger crystals of a very-well defined shape and a particle size reaching up to 50 µm, which may be associated to the phase Y (Figure 13).

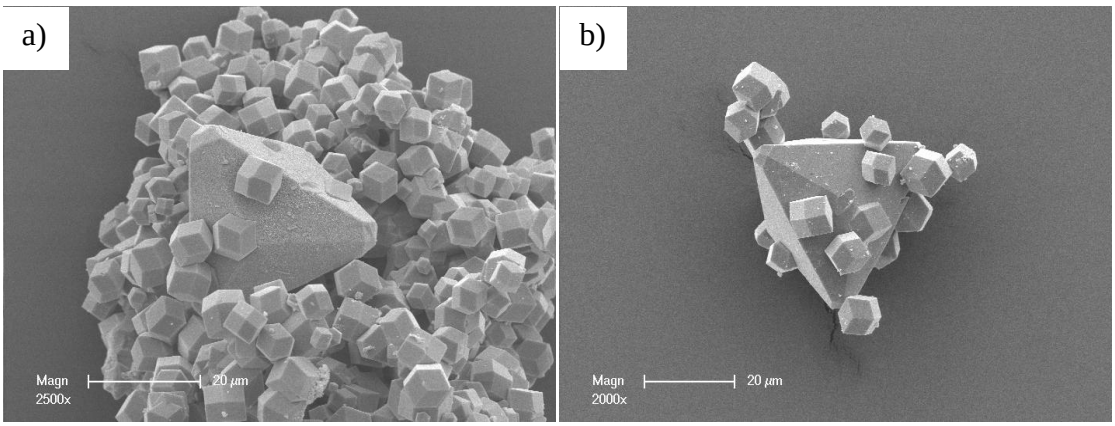

Figure 13. SEM images of Samples (a) 13 and (b) 14.

Based on these results, the optimization of the synthesis of ZIF-71_Br_2 was necessary in order to obtain a pure RHO-phase material, however, in a shortened duration. Therefore, in the second approach, we study the effect of increasing the concentrations of the metal and organic precursors on the rate of precipitation and purity of the targeted product.

b. Effect of the Concentration of the Precursors

The concentrations of the metal and organic precursors in the reaction mediums of **Samples 15** and **16** were increased by around 6 times with respect to those of **Samples 13** and **14**, while maintaining the Hdbim / anhydrous zinc acetate molar ratio in all cases (Table 5). Based on frequent observations of the reaction medium, the formation of a precipitate was first indicated after 1.1 d for **Sample 15**. However, according to the XRD analysis, the obtained product is mostly amorphous (Figure 14). Thus, we increased the synthesis duration for **Sample 16** to 4.7 d, which, based on XRD analysis is enough to obtain a highly crystalline material (Figure 14). Nonetheless, similar to **Samples 13** and **14**, the PXRD pattern of **Sample 16** also reveals an extra peak at 5.5° in 2θ, thereby, indicating the formation of phase Y during the synthesis. Interestingly, however, Figure 15 and Table 5 show that the A_2 / A_1 ratio decreases with respect to **Sample 14** (from 0.247 to 0.079 for **Samples 14** and **16**, respectively). Therefore, by increasing the concentration of the reaction medium, it was possible to decrease the synthesis duration, while enhancing the selectivity towards the targeted product with respect to the previously synthesized samples (**Samples 13** and **14**).

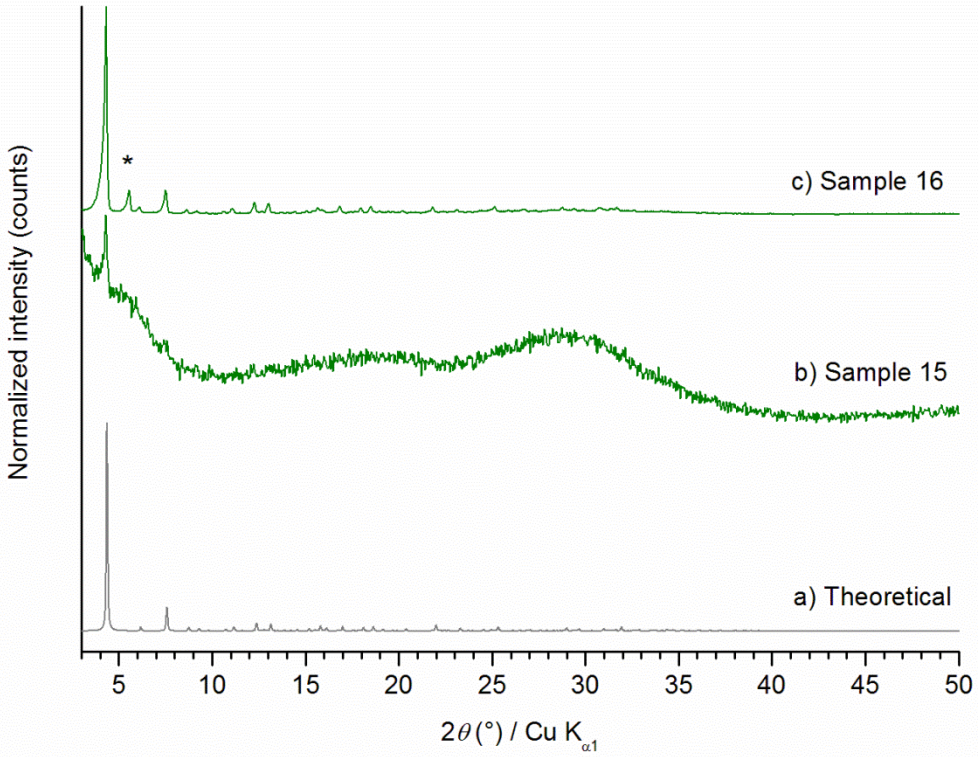

Figure 14. (a) Theoretical XRD pattern of ZIF-71_Br_2, XRD patterns of Samples (b) 15 and (c) 16. * denotes the extra peak corresponding to phase Y.

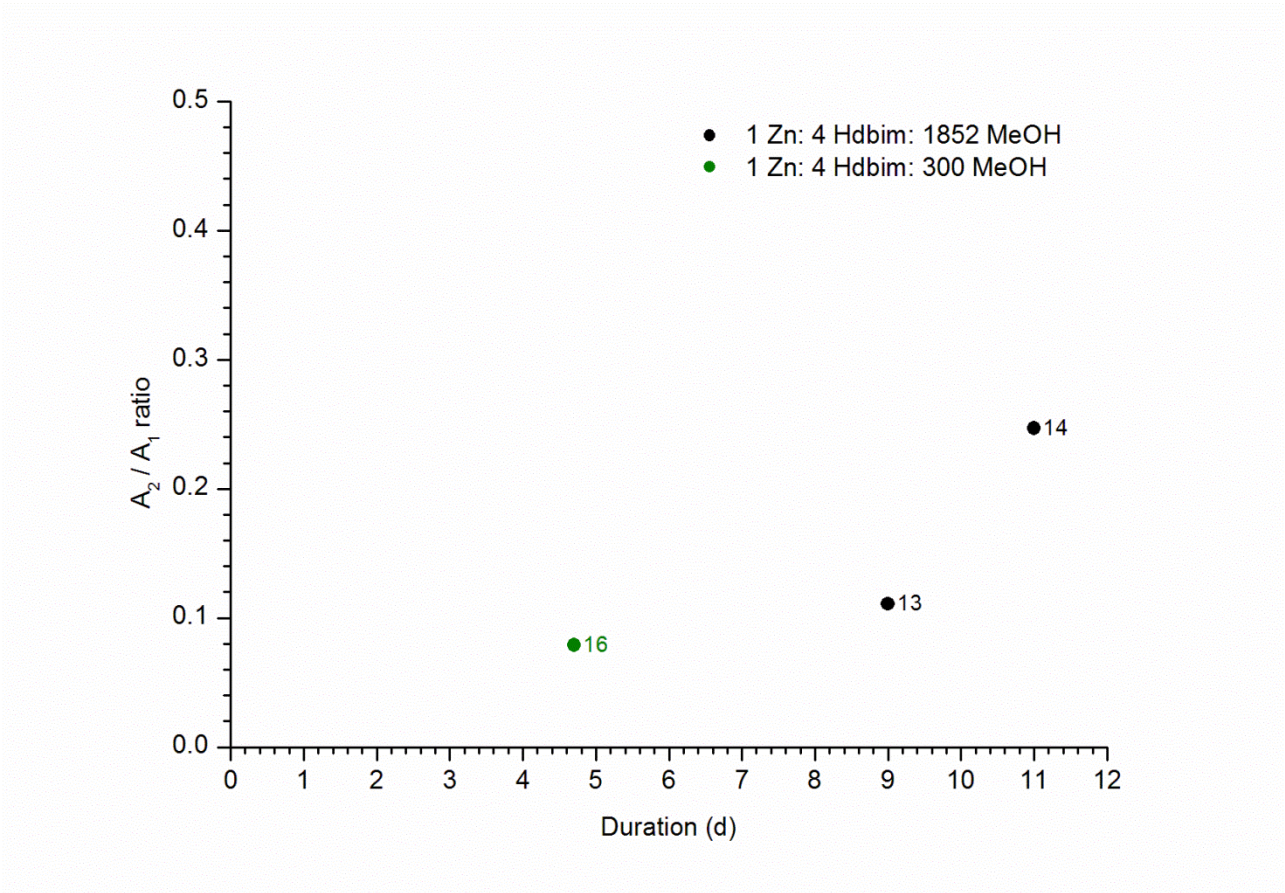

Figure 15. Variation of the A_2 / A_1 ratio as a function of the synthesis duration. The samples' numbers are indicated next to the symbols.

By referring to the results obtained for **Samples 13-16**, it may be concluded that**: i) the shorter the synthesis duration, the less prominent is phase Y, as long as the duration is sufficient for the crystallization of the product, ii) the high concentrations of the metal and organic precursors seem to enhance the selectivity towards ZIF-71_Br$_2$**.

In the quest of obtaining pure material, we attempted, in another approach, to increase the rate of formation of the product by employing an additive in the synthesis of ZIF-71_Br$_2$.

c. Effect of an Additive

In the syntheses of MOFs, employing a base allows/facilitates the deprotonation of the linker (especially in room-temperature syntheses, where amide-based solvents such as DMF and DEF cannot be thermally decomposed to yield amines as weak bases to deprotonate the linker).[16] Consequently, the kinetics of the reaction is enhanced by promoting nucleation and, thus, accelerating the crystal formation. The use of additives leads to higher yields. However, smaller crystals (nanocrystals) may be expected following this strategy, as the base favors nucleation over crystal growth.[17-18]

Herein, and as mentioned in Section II. B. 1. b., the aim is to increase the rate of formation of the product, as this parameter seems to be related to the final product's purity (i.e. the formation of pure RHO phase). In other words, **the target is to enhance the kinetics of the reaction**, as **ZIF-71_Br$_2$ may be considered as the kinetic product, whereas phase Y may be the thermodynamic product that becomes more prominent with the increase in the synthesis duration.** Therefore, an additive-assisted protocol for the synthesis of ZIF-71_Br$_2$ was followed, by employing sodium formate (HCOONa). Various syntheses were carried out, using 4 and 8 molar equivalents of HCOONa, while keeping the same concentrations of organic and metal precursors. The synthesis duration was fixed at 4.7 d (**Samples 17** and **18**), similar to the case of **Sample 16**. The XRD analysis reveals the formation of ZIF-71_Br$_2$ (Figure 16A), along with a decrease in the A_2 / A_1 ratio with the addition of HCOONa to the reaction medium (**Samples 17** and **18**). This ratio decreases to almost zero with 8 molar equivalents of the additive, as shown for **Sample 18** (Figure 21 and Table 5). However, an additional peak of low relative intensity appears on the XRD pattern at 44° in 2θ, which is not assignable to HCOONa (Figure 16B). Our assumption of the absence of HCOONa in **Sample 18** is attributed to the fact that the high-relative-intensity peaks corresponding to the base do not exist in the sample's experimentally obtained XRD pattern (Figure 16B).

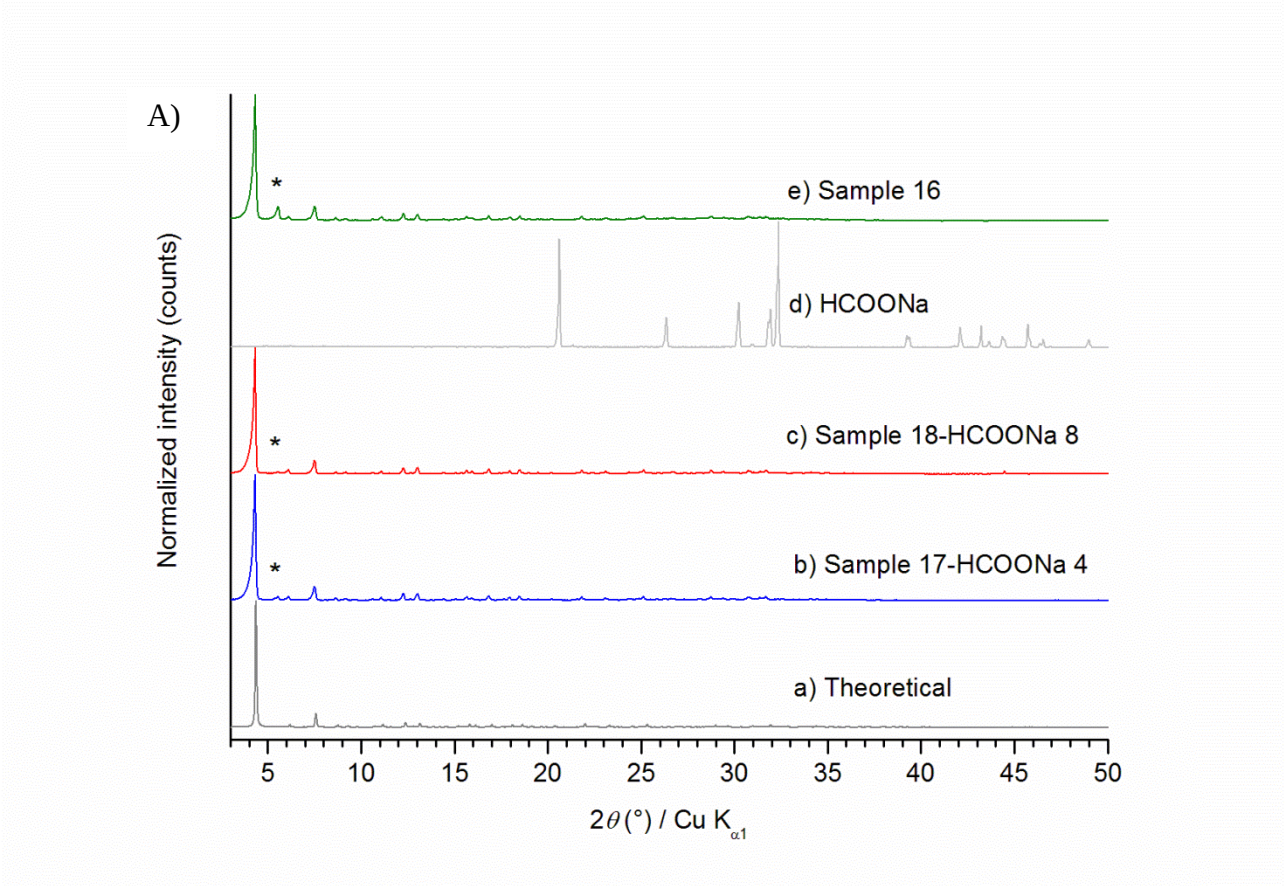

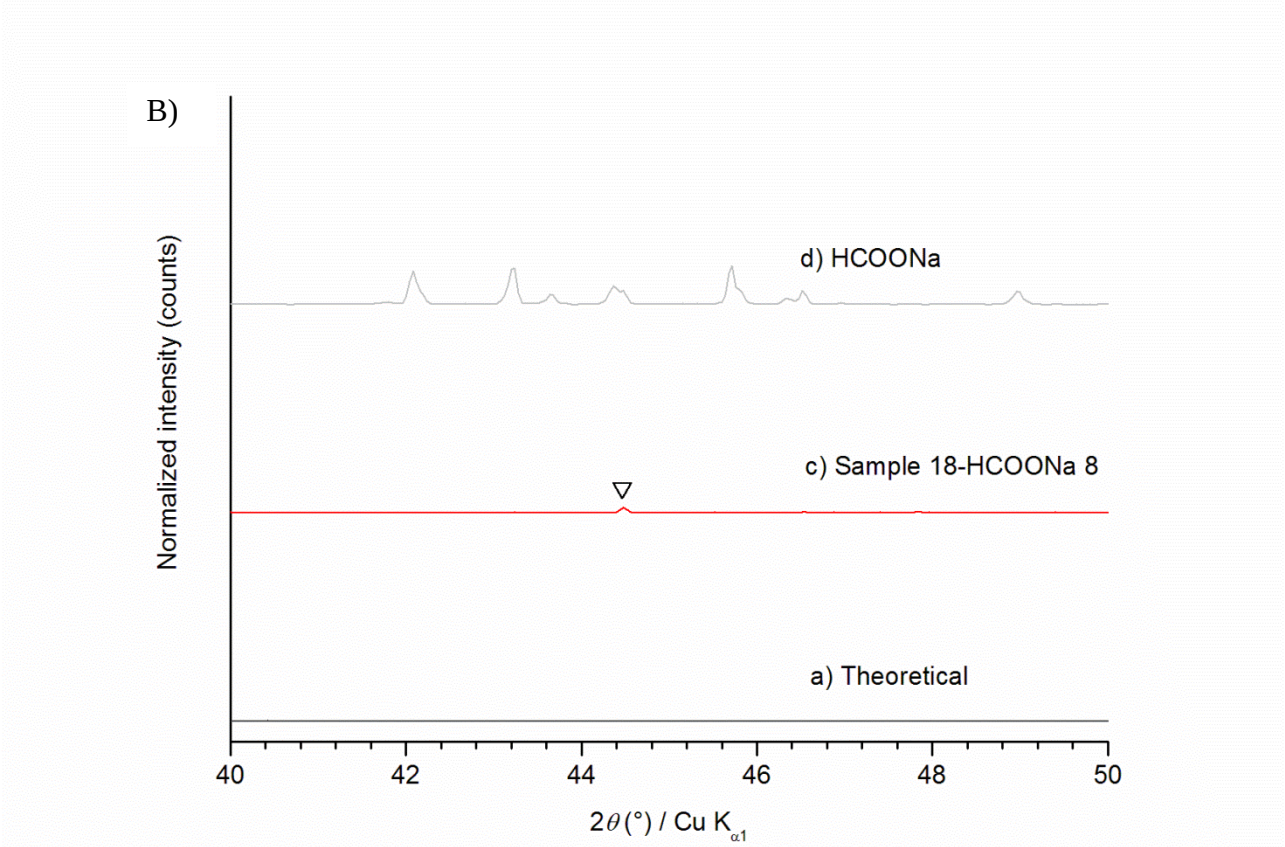

Figure 16. (A) (a) Theoretical XRD pattern of ZIF-71_Br_2, XRD patterns of Samples (b) 17 and (c) 18, (d) experimentally XRD pattern of sodium formate. For comparison, (e) XRD pattern of Sample 16 is recalled. * denotes the extra peak corresponding to phase Y. (B) A closer view of the XRD patterns of Sample (c) 18 and (d) sodium formate in the 40-50° in 2θ range. ▽ Indicates the additional and unidentified peak. The number noted next to HCOONa indicates the corresponding number of molar equivalents of the additive (ex: HCOONa 4 corresponds to four molar equivalents of HCOONa).

SEM analyses were carried out on **Samples 17** and **18**. For both samples, the pictures depicted in Figure 17 show the presence of dodecahedral crystals of an average size of 2 µm, in addition to the larger crystals that were previously observed for **Samples 13** and **14** and assigned to phase Y. However, in the case of **Samples 17** and **18**, the number of these crystals seems to be less prominent than in the previous cases.

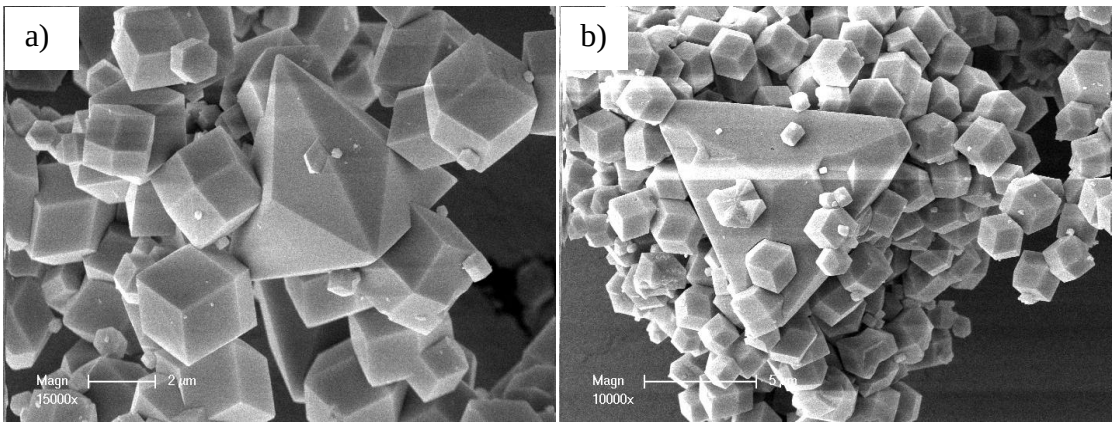

Figure 17. SEM images of Samples (a) 17 and (b) 18.

Samples 17 and **18** were also analyzed with N_2 adsorption-desorption measurements. The obtained N_2 sorption isotherms display a type I profile that is characteristic of microporous materials (Figure 18). Based on the experimental isotherms, the BET surface areas were determined to be 602 and 558 $m^2\ g^{-1}$ (in the 0.00122 - 0.00620 p/p^0 range), whereas the microporous volumes ranged between 0.26 and 0.24 $cm^3\ g^{-1}$ for **Samples 17** and **18**, respectively.

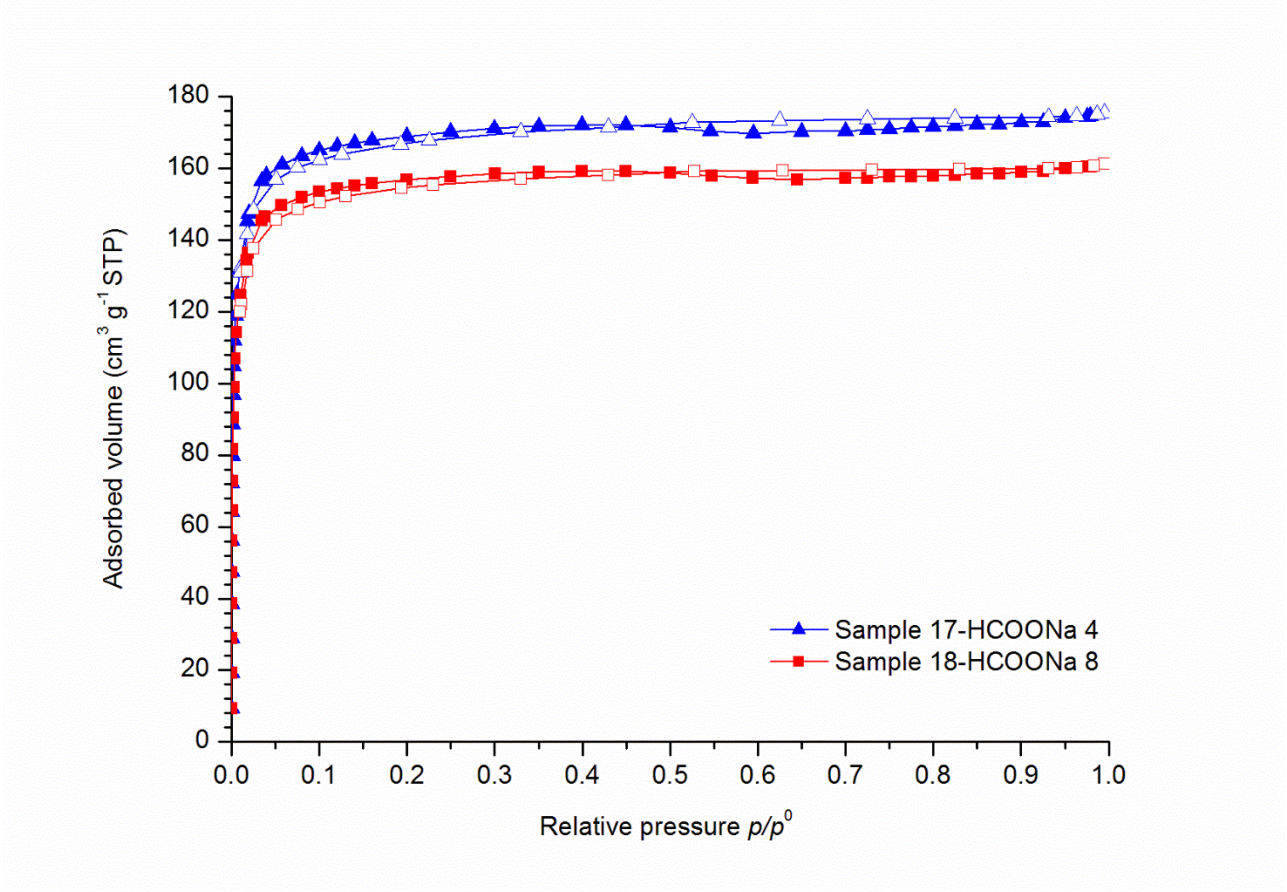

Figure 18. N_2 adsorption-desorption isotherm of Samples 17 and 18. Filled and empty symbols refer to the adsorption and desorption branches, respectively. The number noted next HCOONa indicates the corresponding number of molar equivalents of the additive (ex: HCOONa 4 corresponds to four molar equivalents of HCOONa).

The experimentally obtained value of the microporous volume is in agreement with the theoretical value (0.26 $cm^3\ g^{-1}$). The latter was calculated by referring to the microporous volumes of both ZIF-71_Cl_2 and ZIF-25 as follows: by multiplying the microporous volume of ZIF-71_Cl_2 or ZIF-25 (0.41 and 0.54 $cm^3\ g^{-1}$, respectively) by the corresponding molar mass (337.302 and 255.630 g mol^{-1}, respectively), the quantity of adsorbed molecular nitrogen can be determined in $cm^3\ mol^{-1}$. Then, the obtained value is divided by the molar mass of ZIF-71_Br_2 (515.103 g mol^{-1}), which finally leads to the theoretical microporous volume of ZIF-71_Br_2 (around 0.26 $cm^3\ g^{-1}$ or 165 $cm^3\ g^{-1}$ STP).

Therefore, for **Samples 17** and **18**, N_2 sorption analyses, in addition to the XRD analyses, confirm the formation of ZIF-71_Br_2 and the porosity of the material, in spite of the presence of, probably, traces of phase Y, as could be indicated from XRD and SEM analyses. The slightly lower textural properties of **Sample 18** (558 $m^2\ g^{-1}$ and 0.24 $cm^3\ g^{-1}$ for the BET surface area and microporous volume, respectively) compared to **Sample 17** (602 $m^2\ g^{-1}$ and 0.26 $cm^3\ g^{-1}$ for the BET surface area and microporous volume, respectively) may be attributed to the third phase detected from XRD analysis by the peak at 44° in 2θ.

TGA performed on **Sample 17,** after N_2 adsorption-desorption measurements, revealed that the ZIF material is thermally stable up to 300°C (Figure 19), thus, indicating the absence of solvent and organic precursor molecules in the porosity On the TG curve, a main decomposition step is observed between 300-540°C, with a global mass loss of 89 %, indicating the degradation of the organic framework. This value is higher than the calculated mass loss contributing to the degradation of the organic network (84 %). This trend appears to be common in the case of halogenated ZIFs, i.e. where the organic linker possesses one or more halogens as substituents.[19] Typical examples of ZIFs displaying a similar phenomenon include ZIF-71_Cl_2,[1] ZIF-8_Cl, and ZIF-8_Br.[3] It is also worthy to note that the absence of a mass loss between room temperature and 200°C reveals that the ZIF pores are liberated. Nevertheless, in order to confirm the hydrophobic character of ZIF-71_Br_2, water adsorption-desorption measurements are required.

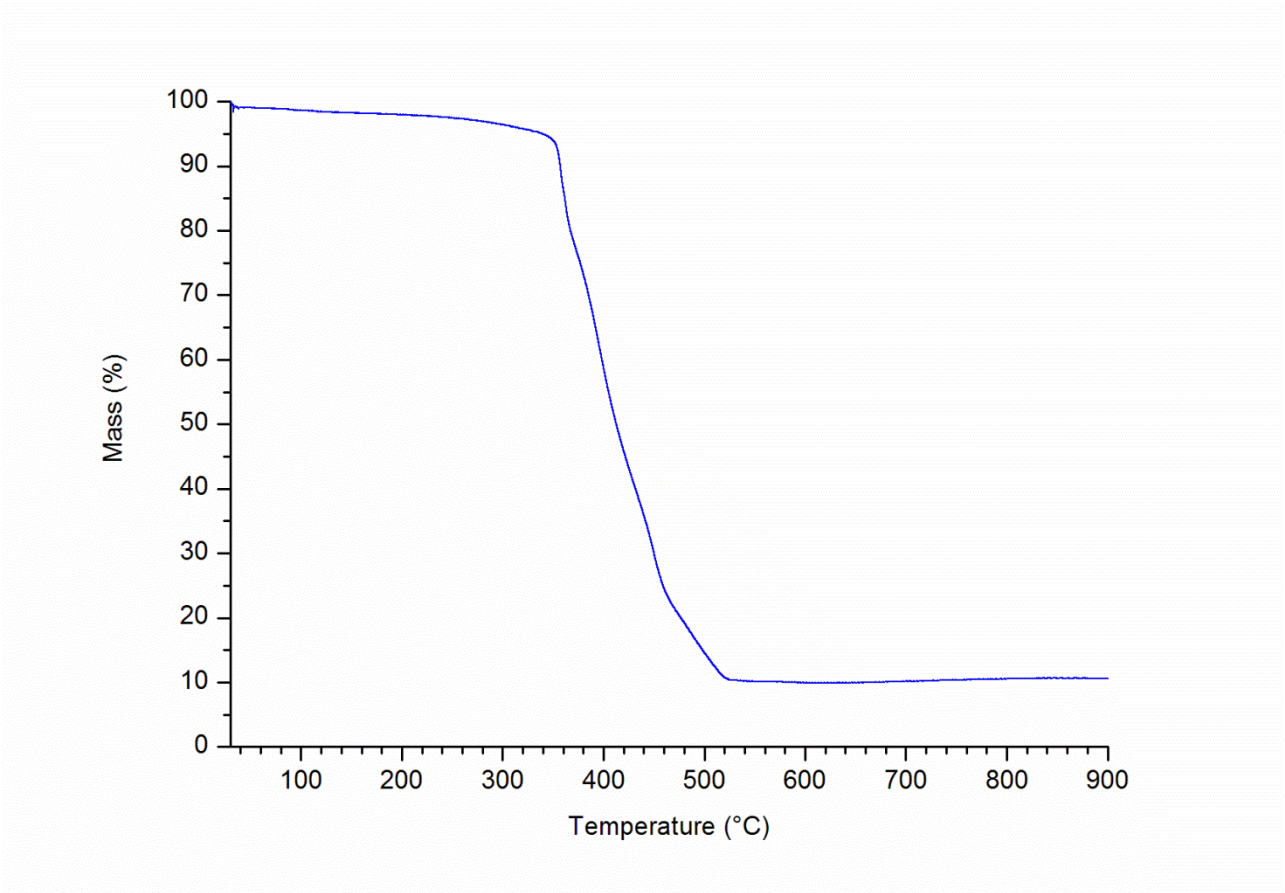

Figure 19. TG curve of Sample 17.

In another approach towards further optimizing the synthesis of ZIF-71_Br_2, we aimed at decreasing the synthesis duration. Among all the prepared samples, **Samples 17** and **18** (obtained using HCOONa as an additive) have shown the lowest A_2 / A_1 ratios (Table 5). Therefore, the new synthesis protocols were inspired by those of the two latter samples, however, by only decreasing the synthesis duration. Table 5 presents the synthesis conditions for **Sample 19**, synthesized using 4 molar equivalents of HCOONa (inspired by **Sample 17**), with the synthesis duration decreased to 3.8 d. As for **Samples 20** and **21** (inspired by **Sample 18**), obtained by employing 8 molar equivalents of the additive, the synthesis duration was decreased to 3.8 and 2.7 d, respectively. Figure 20 demonstrates the XRD patterns of **Samples 19**, **20**, and **21**.

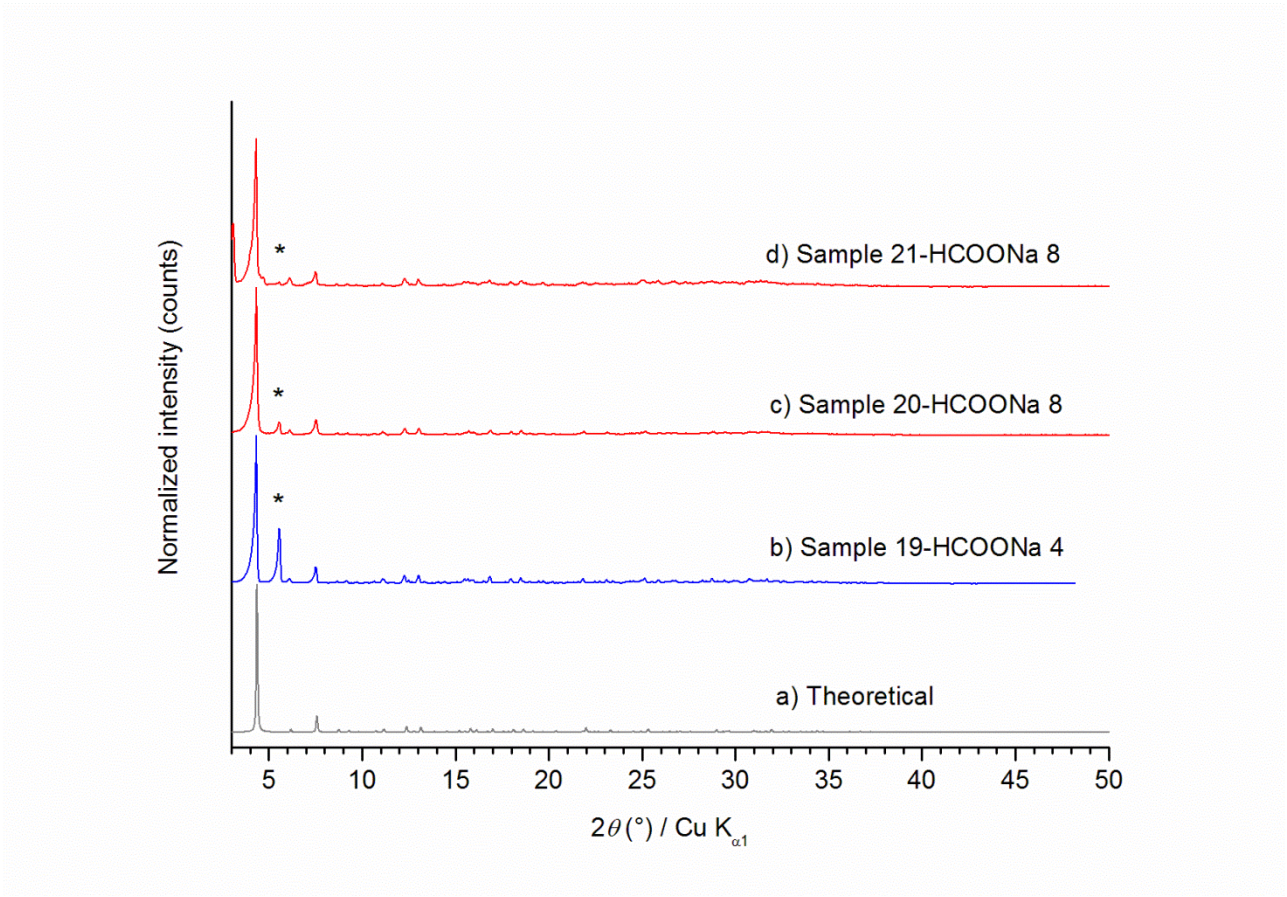

Figure 20. (a) Theoretical XRD pattern of ZIF-71_Br_2, XRD patterns of Samples (b) 19, (c) 20, and (d) 21. * denotes the extra peak corresponding to phase Y. The number noted next to HCOONa indicates the corresponding number of molar equivalents of the additive (ex: HCOONa 4 corresponds to four molar equivalents of HCOONa).

Surprisingly, PXRD analyses reveal unexpected results. It seems that regardless of the number of molar equivalents of the additive used, decreasing the synthesis duration increases back the A_2 / A_1 ratio for a given number of HCOONa molar equivalents, as shown in Table 5 and Figure 21.

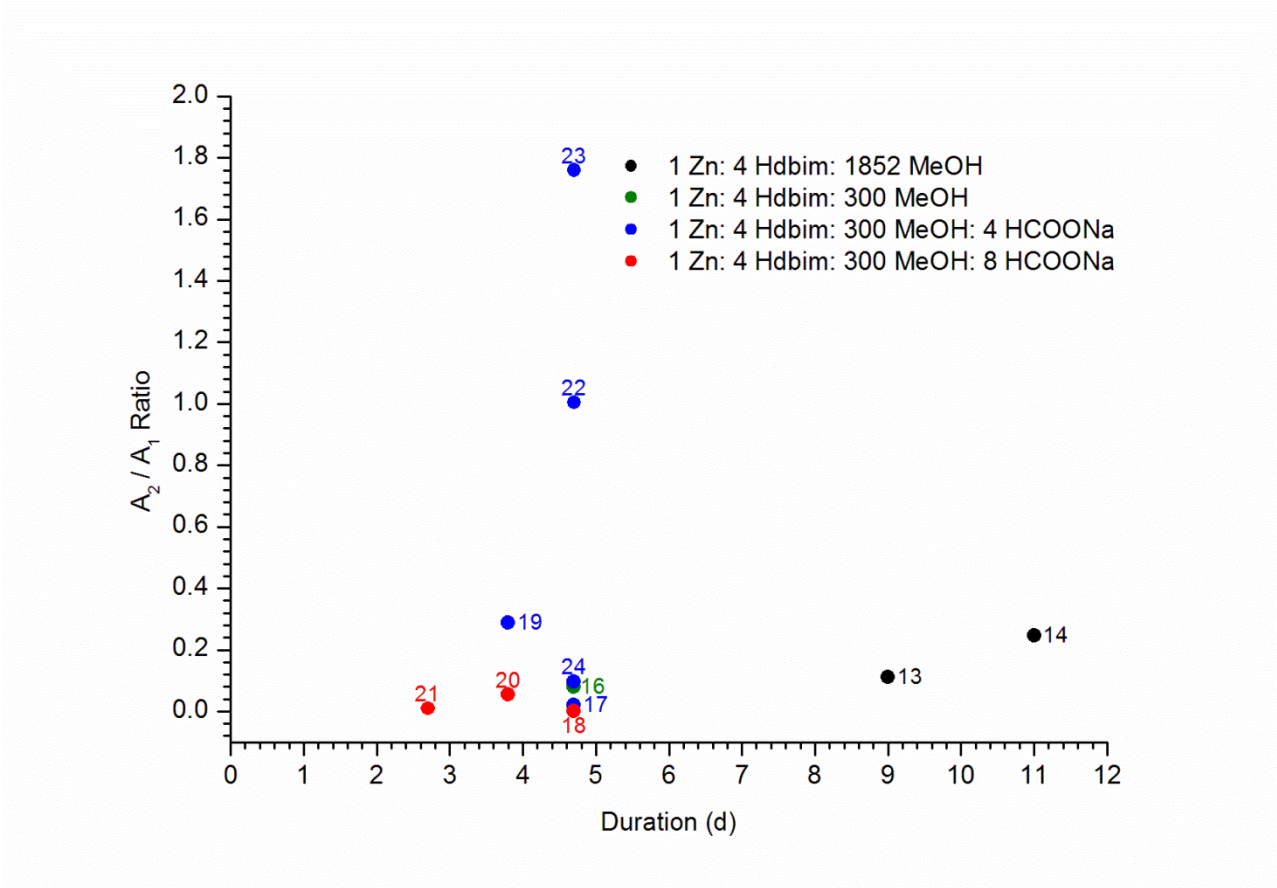

Figure 21. Variation of the A_2 / A_1 ratio as a function of the synthesis duration. The samples' numbers are indicated next to the symbols.

These results disagree with our hypothesis on the probability of ZIF-71_Br_2 and phase Y being the kinetic and thermodynamic products, respectively. As if it were the case, then the A_2 / A_1 ratio should decrease with the decrease in the synthesis duration.

Based on these results, it was decided to go no further with the optimization of the ZIF-71_Br_2 synthesis and to follow, instead, the protocol used to synthesize **Sample 17**. Even though **Sample 17** (synthesized by employing only 4 molar equivalents of HCOONa) exhibits an A_2 / A_1 ratio that is higher than that exhibited by **Sample 18** (synthesized by employing 8 molar equivalents of HCOONa), nevertheless, the latter seems to include more impurities compared to **Sample 17** that are indicated by the presence of the extra peak at 44° in 2θ and a lower microporous volume.

Therefore, it was first necessary to check the reproducibility of this synthesis protocol. In this respect, three separate syntheses were carried out, yielding **Samples 22**, **23**, and **24** (Table 5). The corresponding XRD patterns are displayed in Figure 22, whereas Table 5 and Figure 21 represent the A_2 / A_1 ratios. Surprisingly also, the values obtained from peak integration reveal the irreproducibility of the synthesis, with the A_2 / A_1 ratios being different and all higher than the value obtained for **Sample 17** (Figure 21).

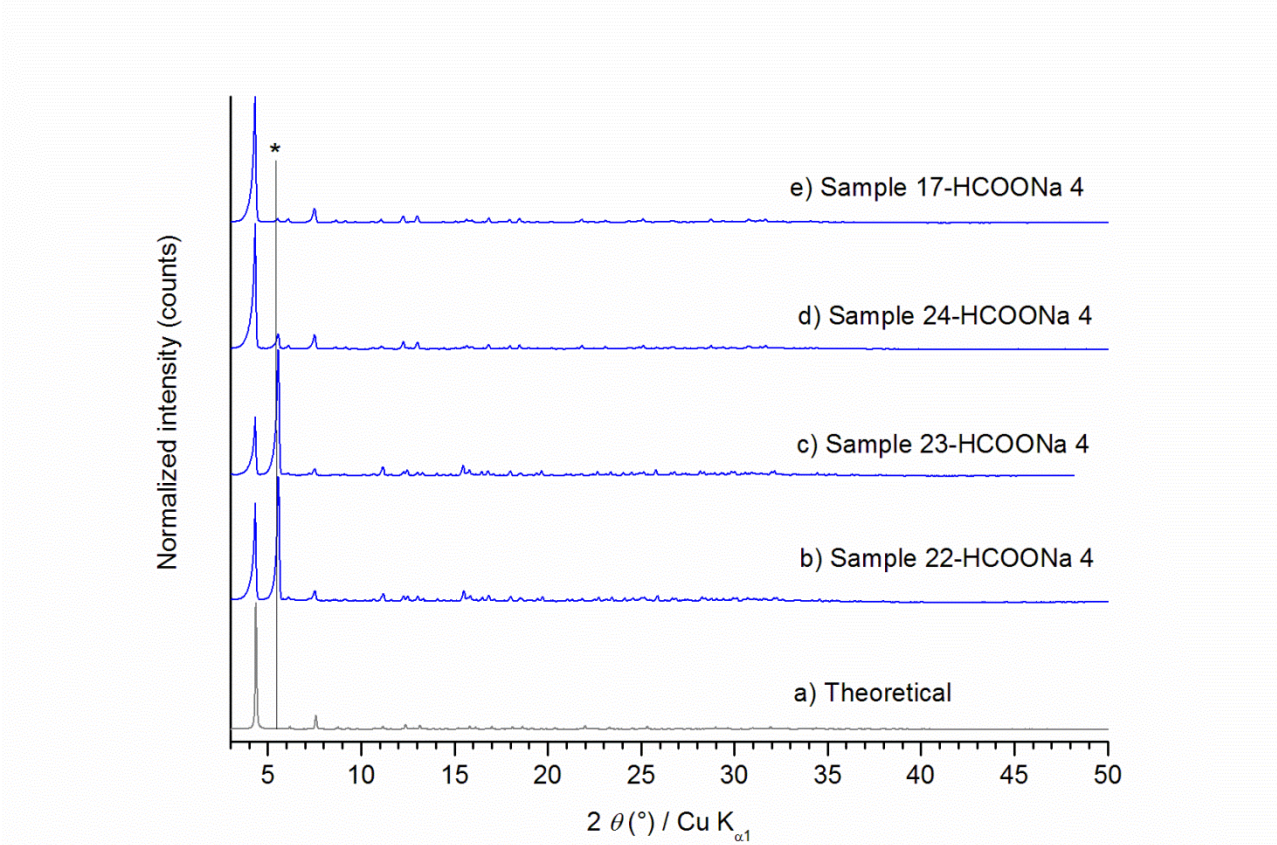

Figure 22. (a) Theoretical XRD pattern of ZIF-71_Br_2, XRD patterns of Samples (b) 22, (c) 23, (d) 24. For comparison, the XRD pattern of (e) Sample 17 is recalled. * denotes the extra peak corresponding to phase Y. The number noted next to HCOONa indicates the corresponding number of molar equivalents of the additive (ex: HCOONa 4 corresponds to four molar equivalents of HCOONa).

Therefore, to this moment, the preparation of pure ZIF-71_Br_2 has not yet been achieved. Another strategy that may be followed to synthesize ZIF-71_Br_2 of RHO topology, can be through the solvent-assisted ligand exchange process (SALE)[19] that has been previously employed in the synthesis of $Zn(dcim)_2$ of SOD topology (a polymorph of ZIF-71_Cl_2).[19-20] In this case, RHO-type ZIF-71_Cl_2 crystals can be used as the templates and suspended in a solution with 4,5-dibromoimidazole. The SALE route may be considered as one of our future perspectives in the aim of obtaining pure phase ZIF-71_Br_2 material.

2. Conclusions

The synthesis of ZIF-71_Br_2 of RHO framework-type topology has never been reported in the literature prior to this work. Herein, we intended to synthesize this latter material and to investigate its energetic performances in high-pressure intrusion−extrusion experiments using water and LiCl 20 M aqueous solution as non-wetting liquids. In this aim, several synthesis parameters were varied

(concentration of the reactants, synthesis duration, and use of additives). Even though, based on XRD and N_2 sorption analyses, ZIF-71_Br_2 was obtained, however, the product was not pure and a mixture of the ZIF material and another unknown phase, referred to as phase Y, was obtained in all cases. Furthermore, according to XRD analyses, the ratio of the latter phase to ZIF-71_Br_2 (A_2 / A_1) does not follow a linear trend and is difficult to control. In addition, the synthesis yielding one of the lowest A_2 / A_1 ratios (0.020) is not reproducible, which represents another limitation to the synthesis of the target ZIF material. Finally, one possible route for the synthesis of a pure phase RHO-type ZIF-71_Br_2 material may be the SALE process, which can be considered as one of our team's perspectives. In addition, another perspective is the identification of the phase Y. As for water and LiCl 20 M aqueous solution intrusion−extrusion experiments, they are intended to be carried out on the optimized ZIF-71_Br_2 sample, once obtained.

C. Conclusions

In Section II of this chapter, the syntheses of two RHO-type ZIF materials; ZIF-25 and ZIF-71_Br_2, were intended to be optimized for energetic applications. After numerous trials, whereby several synthesis parameters were varied, ZIF-25 was successfully obtained using acetic acid as a modulator. The optimized protocol leads to the formation of a pure-phase microcrystalline ZIF-25 material, which exhibits high porosity and hydrophobicity. Furthermore, the structure of ZIF-25 was resolved through Rietveld refinement and fully reported for the first time in the *Pm*-3*m* space group. The optimized ZIF-25 sample was also studied in high-pressure water intrusion–extrusion experiments, whereby the corresponding LHS shows perfect shock-absorber behavior. It is important to note that both the "ZIF-25–" and "ZIF-71–water" systems display similar energetic behaviors (perfect shock-absorber), with the amount of stored energy ranging between 26-30 J g^{-1}. This indicates the absence of the effect of the substitution on the imidazolate linker (in the case of Cl atoms or CH_3 groups) on the energetic behavior of RHO-type-ZIF-based LHSs during water intrusion–extrusion experiments, which is also the case for the SOD-type ZIFs (as both the "ZIF-8–" and "ZIF-8_Cl–water" systems display spring behavior). However, this effect has to be studied during LiCl 20 M aqueous solution intrusion–extrusion experiments in ZIF-25, so as to compare the obtained results to those corresponding to the "ZIF-71–LiCl 20 M aqueous solution" system. On another note, the water intrusion pressure is lower in the case of ZIF-25 compared to ZIF-71 (58 compared to 71 MPa, for the ZIF-25- and -71-based LHSs, respectively), which could not be attributed to an enhanced flexibility of the former material. As for the ZIF-71_Br_2 material, regardless of the various synthesis trials that have been carried out, while modifying several process and compositional parameters, the obtained product is still impure not completely pure and consists of a mixture of the RHO phase and another unknown phase Y. Moreover, even for one of the most

promising samples (with a low phase Y/ZIF-71_Br_2 ratio, i. e. 0.02), the synthesis is irreproducible. Therefore, further optimization of the synthesis conditions is required in the aim of obtaining a pure-RHO phase material. To this end, one possibility may be the SALE route. Indeed, similar to ZIF-25, the optimized ZIF-71_Br_2 material is intended to be employed in high-pressure intrusion–extrusion experiments of water and LiCl 20 M aqueous solution.

III. **Conclusions**

In this chapter, the energetic performances of four RHO-type ZIF materials; MAF-6, ZIF-71, ZIF-25, and ZIF-71_Br_2, were intended to be investigated in high-pressure intrusion–extrusion experiments of water and LiCl 20 M aqueous solution. The work aimed at exploring the effect of both the topology of the ZIF material and the substitution on the imidazolate linker (Cl or Br atoms, as well as methyl or ethyl groups) on the energetic behaviors of LHSs. The first part of this study involved MAF-6 and ZIF-71, which both display mainly bumper behaviors due to the intrusion phenomena that are associated with irreversible crystal phase transformations during LiCl 20 M aqueous solution intrusion–extrusion experiments. For instance, ZIF-71 (RHO) is transformed into ZIF-72; one of the former's dense polymorphs of lcs topology, while MAF-6 undergoes a partial hydrolysis-condensation process, which results in the formation of a new pseudo-polymorph, referred to as phase X. A similar partial phase transformation into phase X, but to a higher extent compared to the case of the LiCl 20 M aqueous solution, is also highlighted for the "MAF-6−water" system. This system displays a mixture of shock-absorber and bumper behaviors. In all cases, the phase transformation is assigned to the combined effect of the high pressure and non-wetting liquid. It is also important to note that the structure of phase X has not yet been determined, due to the difficulty of obtaining it in a pure phase, nevertheless, it is proven to be a crystalline and nonporous phase, with a spherical-like morphology. As for ZIF-71, it displays perfect shock absorber behavior with water. On another note, after numerous trials, the synthesis of ZIF-25 was successfully optimized using acetic acid as a modulator. The optimized sample exhibits high phase purity, crystallinity, and porosity, in addition to a hydrophobic character. Furthermore, similar to ZIF-71, ZIF-25 also displays shock-absorber behavior during water intrusion–extrusion experiments, with an amount of stored energy ranging between 26-30 J g^{-1}. Nevertheless, the "ZIF-25–water" system exhibits a lower intrusion pressure compared to the "ZIF-71–water" system, which does not appear to be due to a more pronounced flexibility of ZIF-25. Therefore, **it seems that the topology of the ZIF material possesses a more prominent effect compared to the functionalization (when Cl and CH_3 substituents are considered) on the energetic behavior of the LHS system during water intrusion–extrusion experiments**, which may explain the spring behavior displayed in the case of the SOD-type ZIFs, compared to a shock-absorber behavior for the RHO-type materials. Nevertheless, the effects of the ZIF topology and the substitution on the imidazolate linker still need to be investigated using LiCl 20 M aqueous solution. Finally, despite numerous synthesis trials that involved varying several process and compositional parameters, the synthesis of ZIF-71_Br_2 still needs to be optimized so as to obtain a pure RHO-phase material for applications in water and aqueous solution intrusion−extrusion experiments. The main obstacles facing the synthesis of ZIF-

71_Br_2 are the impurity of the final product, due to the presence of another unknown phase that is referred to as phase Y, and the irreproducibility of the syntheses. In this respect, the SALE process may be an alternative route for the synthesis of a pure phase RHO-type ZIF-71_Br_2 material. In addition, other perspectives concern the identification of phases X and Y.

In order to complete these intermediate results evidencing a more pronounced impact of the topology compared to the functionalization of the linker on the energetic behaviors of LHSs, Chapter 5 includes different prospective studies aiming to enlarge the fields of investigation based on these two parameters. For example, the synthesis and characterization of ZIFs with new topologies such as LTA, displaying the same types of membered-ring pore apertures (4-, 6- and 8-membered rings) as the RHO type, as well as AFI and CAN, with larger cage apertures (including12-membered rings) will be addressed. The attempts to elaborate a ZIF from a NO_2-funtionnalized linker will be also described.

References

1. Ortiz, G.; Nouali, H.; Marichal, C.; Chaplais, G.; Patarin, J., Energetic Performances of "ZIF-71-Aqueous Solution" Systems: A Perfect Shock-Absorber with Water. J. Phys. Chem. C 2014, 118, 21316-21322.

2. Ortiz, G.; Nouali, H.; Marichal, C.; Chaplais, G.; Patarin, J., Energetic Performances of the Metal–Organic Framework ZIF-8 Obtained Using High Pressure Water Intrusion–Extrusion Experiments. Phys. Chem. Chem. Phys. 2013, 15, 4888-4891.

3. Mortada, B.; Chaplais, G.; Veremeienko, V.; Nouali, H.; Marichal, C.; Patarin, J., Energetic Performances of ZIF-8 Derivatives: Impact of the Substitution (Me, Cl, or Br) on Imidazolate Linker. J. Phys. Chem. C 2018, 122, 3846-3855.

4. Morris, W.; Leung, B.; Furukawa, H.; Yaghi, O. K.; He, N.; Hayashi, H.; Houndonougbo, Y.; Asta, M.; Laird, B. B.; Yaghi, O. M., A Combined Experimental-Computational Investigation of Carbon Dioxide Capture in a Series of Isoreticular Zeolitic Imidazolate Frameworks. J. Am. Chem. Soc. 2010, 132, 11006-11008.

5. Gao, M.; Wang, J.; Rong, Z.; Shi, Q.; Dong, J., A Combined Experimental-Computational Investigation on Water Adsorption in Various ZIFs with the SOD and RHO Topologies. RSC Adv. 2018, 8, 39627-39634.

6. He, C.-T.; Jiang, L.; Ye, Z.-M.; Krishna, R.; Zhong, Z.-S.; Liao, P.-Q.; Xu, J.; Ouyang, G.; Zhang, J.-P.; Chen, X.-M., Exceptional Hydrophobicity of a Large-Pore Metal-Organic Zeolite. J. Am. Chem. Soc. 2015, 137, 7217-7223.

7. Mortada, B.; Chaplais, G.; Nouali, H.; Marichal, C.; Patarin, J., Phase Transformations of Metal-Organic Frameworks MAF-6 and ZIF-71 during Intrusion-Extrusion Experiments. J. Phys. Chem. C 2019, 123, 4319-4328.

8. Zhang, H.; Zhao, M.; Yang, Y.; Lin, Y. S., Hydrolysis and Condensation of ZIF-8 in Water. Microporous Mesoporous Mater. 2019, 288, 109568.

9. Khay, I.; Chaplais, G.; Nouali, H.; Marichal, C.; Patarin, J., Water Intrusion-Extrusion Experiments in ZIF-8: Impacts of the Shape and Particle Size on the Energetic Performances. RSC Adv. 2015, 5, 31514-31518.

10. McGuire, C. V.; Forgan, R. S., The Surface Chemistry of Metal-Organic Frameworks. Chem. Commun. 2015, 51, 5199-5217.

11. Schaate, A.; Roy, P.; Godt, A.; Lippke, J.; Waltz, F.; Wiebcke, M.; Behrens, P., Modulated Synthesis of Zr-Based Metal-Organic Frameworks: From Nano to Single Crystals. Chem. - Eur. J. 2011, 17, 6643-6651.

12. Rietveld, H. M., Profile Refinement Method for Nuclear and Magnetic Structures. J. Appl. Crystallogr. 1969, 2, 65-71.

13. Banerjee, R.; Phan, A.; Wang, B.; Knobler, C.; Furukawa, H.; O'Keeffe, M.; Yaghi, O. M., High-Throughput Synthesis of Zeolitic Imidazolate Frameworks and Application to CO2 Capture. Science 2008, 319, 939-943.

14. Toby, B. H.; Von Dreele, R. B., GSAS-II: the Genesis of a Modern Open-Source all Purpose Crystallography Software Package. J. Appl. Crystallogr. 2013, 46, 544-549.

15. Lively, R. P.; Dose, M. E.; Thompson, J. A.; McCool, B. A.; Chance, R. R.; Koros, W. J., Ethanol and Water Adsorption in Methanol-Derived ZIF-71. Chem. Commun. 2011, 47, 8667-8669.

16. Tian, Y.-Q.; Zhao, Y.-M.; Chen, Z.-X.; Zhang, G.-N.; Weng, L.-H.; Zhao, D.-Y., Design and Generation of Extended Zeolitic Metal-Organic Frameworks (ZMOFs): Synthesis and Crystal Structure of zinc(II) Imidazolate Polymers with Zeolitic Frameworks. Chem. - Eur. J. 2007, 13, 4146-4154.

17. Peralta, D.; Chaplais, G.; Simon-Masseron, A.; Barthelet, K.; Pirngruber, G. D., Synthesis and Adsorption Properties of ZIF-76 Isomorphs. Microporous Mesoporous Mater. 2012, 153, 1-7.

18. Huang, L.; Wang, H.; Chen, J.; Wang, Z.; Sun, J.; Zhao, D.; Yan, Y., Synthesis, Morphology Control, and Properties of Porous Metal-Organic Coordination Polymers. Microporous Mesoporous Mater. 2003, 58, 105-114.

19. Schweinefuss, M. E.; Springer, S.; Baburin, I. A.; Hikov, T.; Huber, K.; Leoni, S.; Wiebcke, M., Zeolitic Imidazolate Framework-71 Nanocrystals and a Novel SOD-Type Polymorph: Solution Mediated Phase Transformations, Phase Selection Via Coordination Modulation and a Density Functional Theory Derived Energy Landscape. Dalton Trans. 2014, 43, 3528-3536.

20. Khay, I.; Chaplais, G.; Nouali, H.; Ortiz, G.; Marichal, C.; Patarin, J., Assessment of the Energetic Performances of Various ZIFs with SOD or RHO Topology using High Pressure Water Intrusion-Extrusion Experiments. Dalton Trans. 2016, 45, 4392-4400.

Chapter 5: Highly Porous MOF Materials for Intrusion−Extrusion Experiments

In our quest for higher stored energy values and, thus, for more accessible porous volumes, two new highly porous MOFs, namely AFI- and CAN-type ZIFs,[1] appear as interesting candidates for high-pressure intrusion−extrusion experiments. Moreover, it was proven in Chapters 3 and 4, where the SOD[2] and RHO[3] topologies were widely investigated, that the topology of the MOF material (among other parameters) has a significant impact on the energetic behavior of the LHS in which the MOF is incorporated. In this respect, herein, new ZIF topologies, such as CAN, AFI, and LTA, are intended to be investigated in intrusion−extrusion experiments. Notably, the CAN- and AFI-$Zn(im)_2$ and ZIF-76 materials, displaying CAN, AFI, and LTA topologies, respectively, are assumed to exhibit a hydrophobic character. Furthermore, we were also interested in investigating the energetic performances of three highly porous, however, hydrophilic MOFs; NOF-1[4] (SOD) and the two mesoporous materials; MIL-101(Cr)[5] and the more-recently reported MOF-919(Sc/Cu).[6] Indeed, their hydrophilic character prevents the application of these materials in water or diluted aqueous electrolyte solutions intrusion−extrusion experiments. Nonetheless, it may be possible to investigate the energetic behaviors of hydrophilic MOFs using a highly concentrated aqueous electrolyte solution, such as LiCl 20 M. However, this remains a hypothesis that needs to be verified through experiments. Another possibility that allows taking advantage of the high porosity of the mesoporous MIL-101(Cr) and MOF-919(Sc/Cu) materials in intrusion−extrusion experiments may be through post-synthetic modification (PSM), i.e. by removing the metal-coordinated water molecules and substituting them for hydrophobic capping agents, as suggested by Hong *et al.*[7] This route is expected to consequently enable employing the post-synthetically modified hydrophobic materials to water and aqueous electrolyte solutions intrusion−extrusion experiments. However, with such mesoporous materials exhibiting also relatively large pore apertures, it can be wondered whether there is an upper limit for the pore aperture, above which the intrusion pressure is too low to be observed on $P-V$ diagrams, or the non-wetting liquid spontaneously enters the pores. Therefore, the aim of this chapter is to perform a preliminary study in order to broaden the scope of work in the field of energetic applications and open up the door for future research on various parameters that can control the energetic behaviors and performances of ZIF-based LHSs. In this regard, all of the above mentioned MOF/ZIF materials were synthesized and fully characterized, in order to explore their energetic behaviors in intrusion−extrusion experiments of water and/or LiCl 20 M aqueous solution. It is also important to highlight the

novelty of this work, as the MOFs/ZIFs discussed herein were never explored in intrusion−extrusion experiments prior to our work.

I. New ZIFs for Intrusion−Extrusion Experiments

A. NOF-1 (SOD)

1. Description

NOF-1 (also known as ZIF-108[8]) is a ZIF material made up from zinc cations tetrahedrally coordinated to 2-nitroimidazolate (nim) linkers leading to a 3D porous framework. Similar to ZIF-8 and its derivatives (ZIF-8_Cl and ZIF-8_Br), which we have previously discussed in Chapter 3 of this manuscript, NOF-1 possesses a SOD framework topology, with *sod* cages of 5.0 Å in diameter (determined by N_2 sorption analysis using the Horvath-Kawazoe method) delimited by 4- and 6-membered ring cage apertures as displayed on Scheme 1.

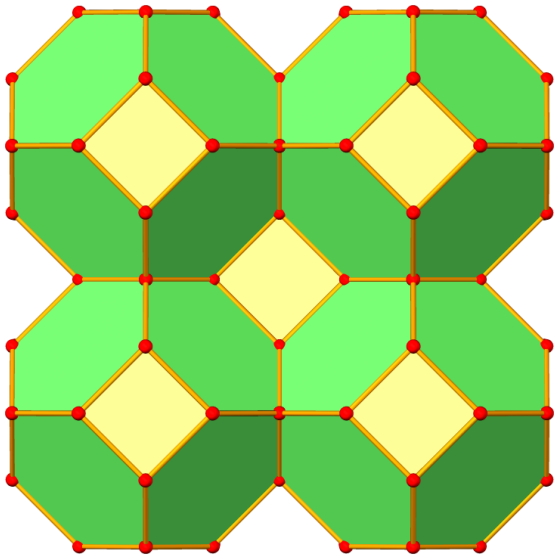

Scheme 1. Representation of the SOD topology of NOF-1. In red, zinc cations. In yellow and green, the 4- and 6-membered ring pore apertures, respectively.

The presence of nitro groups on the imidazolate linker is expected to render the ZIF material hydrophilic, which can, indeed, limit its application to water intrusion−extrusion experiments. However, in such cases, a highly concentrated aqueous electrolyte solution, for example LiCl 20 M, can be a promising alternative to water. Therefore, herein, we aimed at synthesizing, activating, and fully characterizing NOF-1 so as to study its energetic behavior using LiCl 20 M aqueous solution as a non-wetting liquid. Moreover, as NOF-1 displays a SOD topology, the presence of the nitro group on the imidazolate linker offers the opportunity to complete our study on the effect of the

nature of the substituent present on the imidazolate linker of the ZIF material on the energetic performance of the related LHS, by comparing the energetic behavior of NOF-1 to those of ZIF-8 and its halogenated derivatives.

2. Synthesis and Activation

NOF-1 was prepared according to the synthesis protocol reported by Diring *et al.*[4] 2-nitroimidazole (Hnim, 113 mg, 1.0 mmol) and sodium formate (HOOCNa, 136 mg, 2.0 mmol) were dissolved in a DMF/H_2O (v/v, 10/1) mixture (5 mL) and a solution (S_1) is obtained. Sodium formate is used to facilitate the deprotonation of the organic source, thus, increasing the nucleation rate.[9] A solution (S_2) of $Zn(NO_3)_2 \cdot 6H_2O$ (149 mg, 0.5 mmol) in H_2O (5 mL) was also prepared and added to S_1. The reaction mixture was then stirred vigorously at room temperature. The reaction mixture became cloudy within a few minutes after the addition of S_1. The starting molar composition was 1.00 $Zn(NO_3)_2$: 2.00 Hnim: 4.00 HOOCNa: 612.00 H_2O: 117.00 DMF. After 18 h of stirring, the precipitate was centrifuged and washed with water (2*15 mL) and DMF (3*15 mL) and then dried in air for 48 h, to yield 70.8 mg of a pale yellow powder that corresponds to the crude material.

According to Diring *et al.*, the activation of NOF-1 involves a solvent-exchange step, whereby the powder is soaked in fresh MeOH (5*15 mL over 48 h), so as to remove the entrapped water and DMF molecules, followed by heating at 80 °C under reduced pressure (10 mbar) for 18 h. In our case, the product was activated by solvent (MeOH) exchange, but we did not go further to heating it under vacuum.

3. Characterizations

The XRD pattern of the crude material is presented in Figure 1, together with the theoretical pattern obtained based on the published NOF-1 structural parameters.[4] Despite the differences in relative intensities, presumably due to the presence of guest molecules, the peak positions indicate that the synthesized material corresponds to NOF-1. Refinement of the experimental XRD data confirms that the material crystallizes in the cubic symmetry, with a lattice constant $a \approx 17.3$ Å and belongs to the space group *I*-43*m*, which is in agreement with the literature.[4]

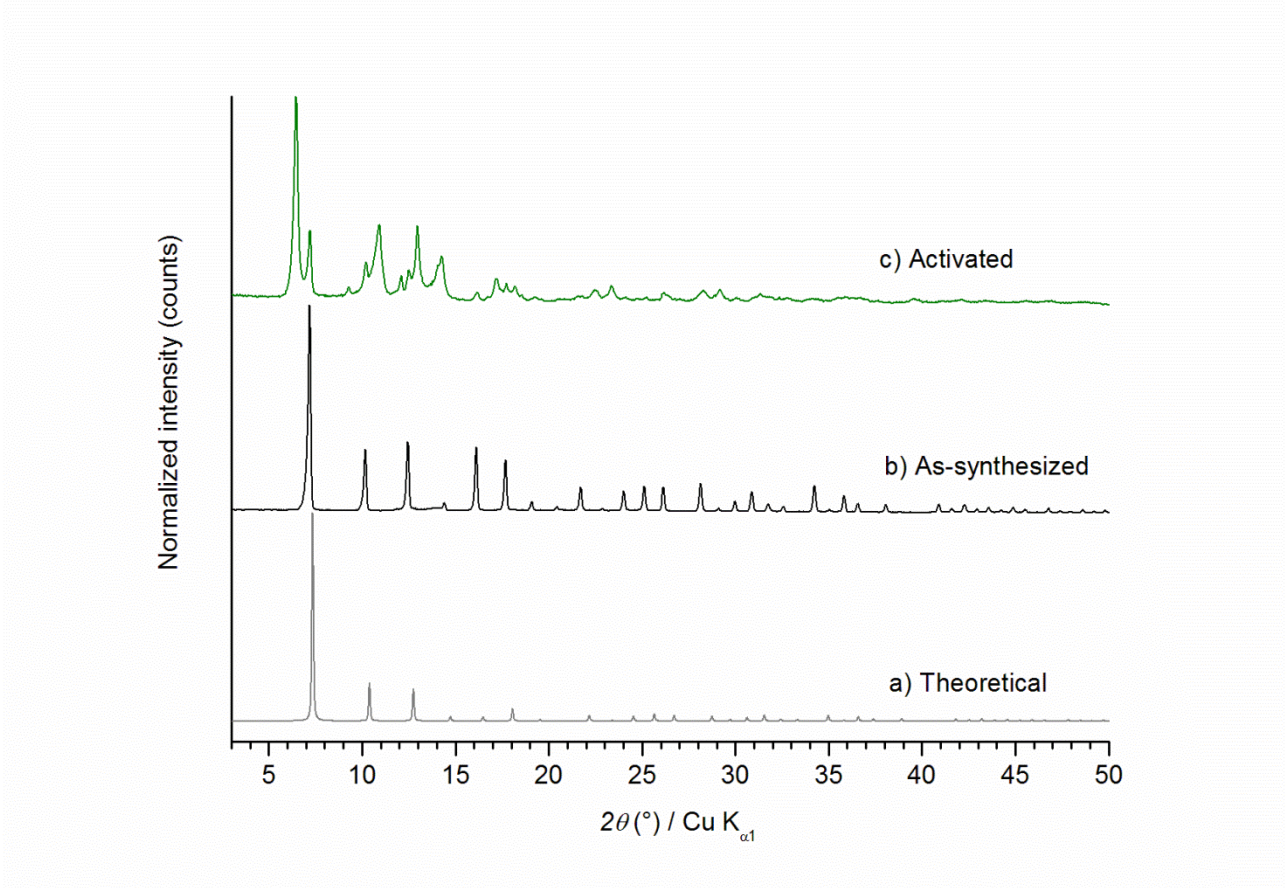

Figure 1. (a) Theoretical XRD pattern of NOF-1 and XRD patterns of the (b) as-synthesized and (c) methanol-activated NOF-1 samples.

The experimentally obtained XRD pattern of the powder recovered after the activation by soaking in MeOH is also represented in Figure 1. Surprisingly, the presence of additional peaks with respect to the crude material clearly indicates that NOF-1 is unstable in MeOH and partially loses crystallinity during the soaking process. The new peaks correspond neither to the organic precursor molecules nor to NOF-3, where the latter is a 2D nonporous polymorph formed of nim linkers and Zn^{2+} ions[4]. Furthermore, an attempt to heat the activated sample at 70 °C during 2 h (results not shown) did not allow recovering the NOF-1 structure indicating a presumably irreversible phase transformation.

Therefore, according to these results, and due to the lack of time required to optimize the activation step of NOF-1, we decided, at least for the meantime, to stop the work on this material. Nevertheless, NOF-1 remains an interesting candidate for LiCl 20 M aqueous solution intrusion−extrusion experiments and in this regard, optimizing the activation process can be considered as one of our team's future perspectives.

B. ZIF-76 (LTA)

1. Description

The zinc-based ZIF-76 material of formula; $Zn(im)_x(cbim)_y$ (where im and cbim stand for imidazolate and 5-chlorobenzimidazolate, respectively) is one of the few existing ZIF materials that combine both relatively large pore apertures and pore volumes.[10] ZIF-76 has an LTA framework topology that consists of *lta* cages, with 4-, 6-, and 8-membered ring pore apertures as well as *sod* cages of 4- and 6-membered ring pore windows that are linked together through d4r (double 4-membered rings) (Scheme 2). According to the literature, the average estimated values of the largest pore aperture and pore diameter in ZIF-76 are 5.4 and 12.2 Å, respectively.[11]

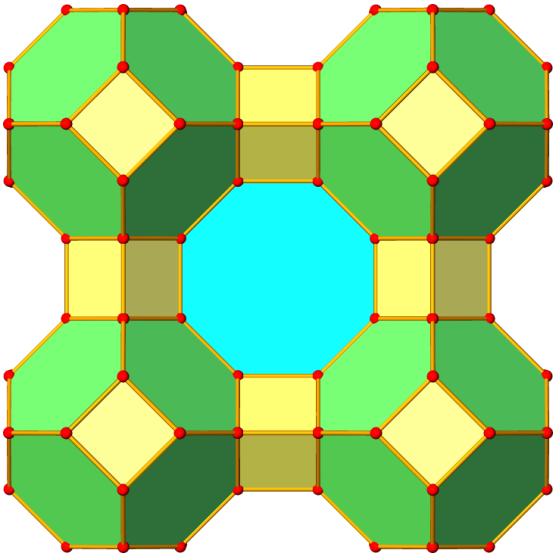

Scheme 2. Representation of the LTA topology of ZIF-76. In red, zinc cations. The 8-, 6- and 4-membered ring facets are represented in blue, green and yellow, respectively.

Moreover, ZIF-76 displays high thermal stability (up to 350 °C in air) and can be stored under ambient atmosphere without being degraded. All these characteristics of ZIF-76 have made it an attractive candidate for applications in the fields of separation and adsorption.[10, 12] Indeed, the advantage of high porosity associated with large pore apertures is also of huge interest in the field of energetic applications, as this combination allows for higher intruded volumes (due to high porosity), while maintaining a relatively low intrusion pressure (large pore apertures), which is required for some practical applications.[13] Thus, in the aim of studying its energetic behavior in intrusion−extrusion experiments, ZIF-76 was synthesized.

2. Synthesis and Activation

Five samples of ZIF-76 were prepared following the optimized synthesis protocol published by Peralta *et al.*, that is inspired by the protocol suggested by Yaghi *et al.*,[10-11] however, using NaOH as a base. In general, a base is employed in order to deprotonate the organic source,[9] especially in room temperature syntheses (where amide-based solvents such as DMF and DEF cannot be thermally decomposed to yield amines as weak bases to deprotonate the organic precursor). This speeds up the kinetics of the reaction by promoting nucleation, thus, accelerating the crystal formation and leading to higher yields.[10, 14] However, smaller crystals (nanocrystals) are expected following this strategy, as the base favors nucleation over crystal growth.[10, 14]

The typical synthesis protocol of ZIF-76 is the following: in a 23 mL polypropylene bottle, the organic precursors imidazole (Him, 0.1258 g, 1.8478 mmol) and 5-chlorobenzimidazole (Hcbim, 0.1379 g, 0.9038 mmol) were dissolved in a DMF/DEF mixture (DMF, 5.83 g, 79.8000 mmol and DEF, 5.46 g, 53.9792 mmol). A yellow solution was obtained. Later, the metal precursor $Zn(NO_3)_2 \cdot 6H_2O$ (0.2728 g, 0.9170 mmol) was added and the reaction mixture was stirred for 10 minutes. NaOH (0.55 mL, 1.3750 mmol) was finally added to the reaction mixture, which was stirred for 5 minutes resulting in the formation of a yellow suspension. The initial molar composition was 1.0 $Zn(NO_3)_2$: 1.0 Hcbim : 2.0 Him : 58 DEF : 86.0 DMF : 1.4 NaOH : 6.0 H_2O. The reaction mixture was then heated in an oven at 90 °C for 5 d. After cooling the bottle to room temperature, the product (yellow powder) was recovered by filtration, washed with a few milliliters of EtOH, and left to dry in air. In order to remove any entrapped solvent molecules and liberate the porosity, the as-synthesized ZIF-76 material was activated by degassing at 250 °C for 12 h under vacuum.

3. Characterizations

In order to verify that the desired structure is obtained and to determine the material's phase purity, the as-synthesized samples were analyzed with XRD and the obtained patterns were compared to the pattern simulated from the corresponding single crystal structure.[11] Figure 2 reveals that the typical experimental (corresponding to the as-synthesized material) and theoretical XRD patterns are similar, indicating the formation of a highly crystalline material of an LTA structure. Furthermore, based on the results obtained from our data refinement, ZIF-76 crystallizes in the cubic symmetry, with the refined unit cell parameters $a = b = c = 22.693(3)$ Å and belongs to the *P*-43*m* space group. Indeed, these results are in agreement with the data obtained for the corresponding single crystal structure (crystallographic published data: $a = b = c = 22.6702(2)$ Å).[11] The XRD pattern of the activated ZIF-76 samples (Figure 2) is similar to the as-synthesized ones, thus, indicating that the framework is maintained after activation. It is also important to note that

around 5 batches of ZIF-76 were synthesized and activated and that the results obtained from XRD analyses revealed a high reproducibility of both the synthesis and activation process.

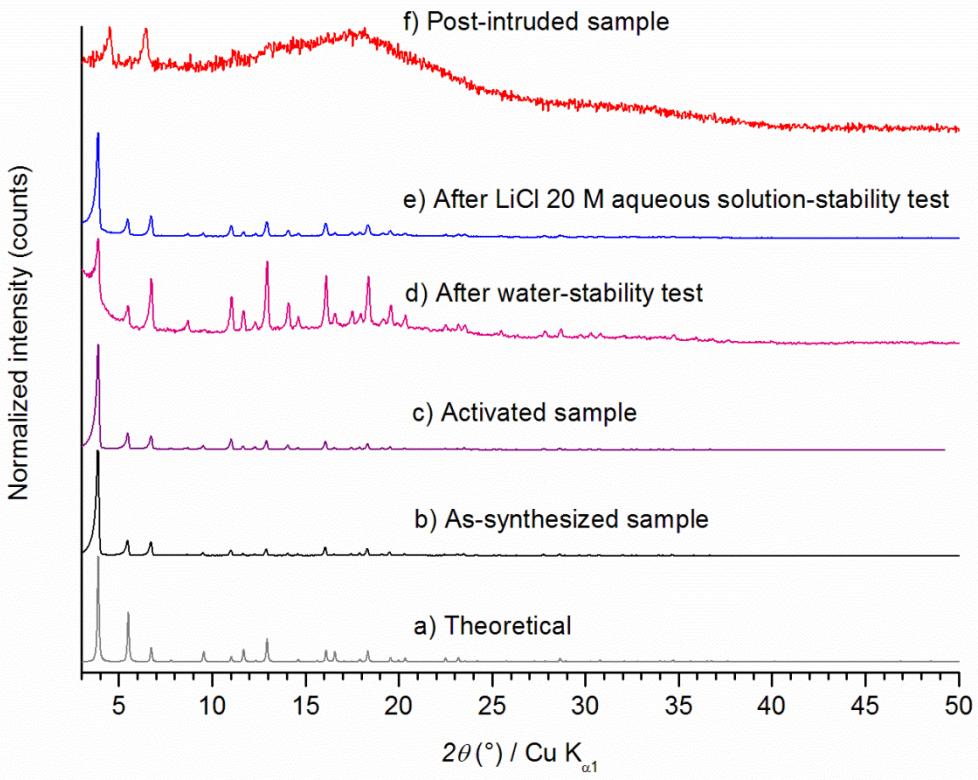

Figure 2. (a) Theoretical XRD pattern of ZIF-76 and XRD patterns of the (b) as-synthesized, (c) activated ZIF-76 samples. The XRD patterns of the ZIF-76 samples obtained after (d) the LiCl 20 M aqueous solution and (e) water and stability tests are also presented. (f) XRD pattern of the LiCl 20 M-intruded ZIF-76 sample.

In order to determine the chemical composition of the activated ZIF-76 sample, and more precisely the ratio between the two constituting linkers (i.e. im and cbim), ^{1}H NMR spectroscopy analysis was carried out. The corresponding ^{1}H NMR spectrum is displayed in Figure 3. The resonances detected at 9.15 (H2) and 7.93 (H4) ppm are assigned to Him, whereas those at 9.63 (H2), 8.37 (H4), 8.27 (H7), 8.25 (H7), 8.07 (H6), and 8.05 (H6) ppm correspond to Hcbim. From the relative intensities of the resonance peaks it is possible to deduced a chemical composition of $Zn(im)_{1.17}(cbim)_{0.83}$ for the ZIF-76 sample, which is close to the composition reported in the literature; $Zn(im)_{1.25}(cbim)_{0.75}$.[10] The ^{1}H NMR spectrum also shows the absence of resonance corresponding to DMF and/or DEF solvent molecules, expected around 7.90 and 8 ppm, respectively, which is in agreement with the results obtained from TG analysis displayed hereafter.

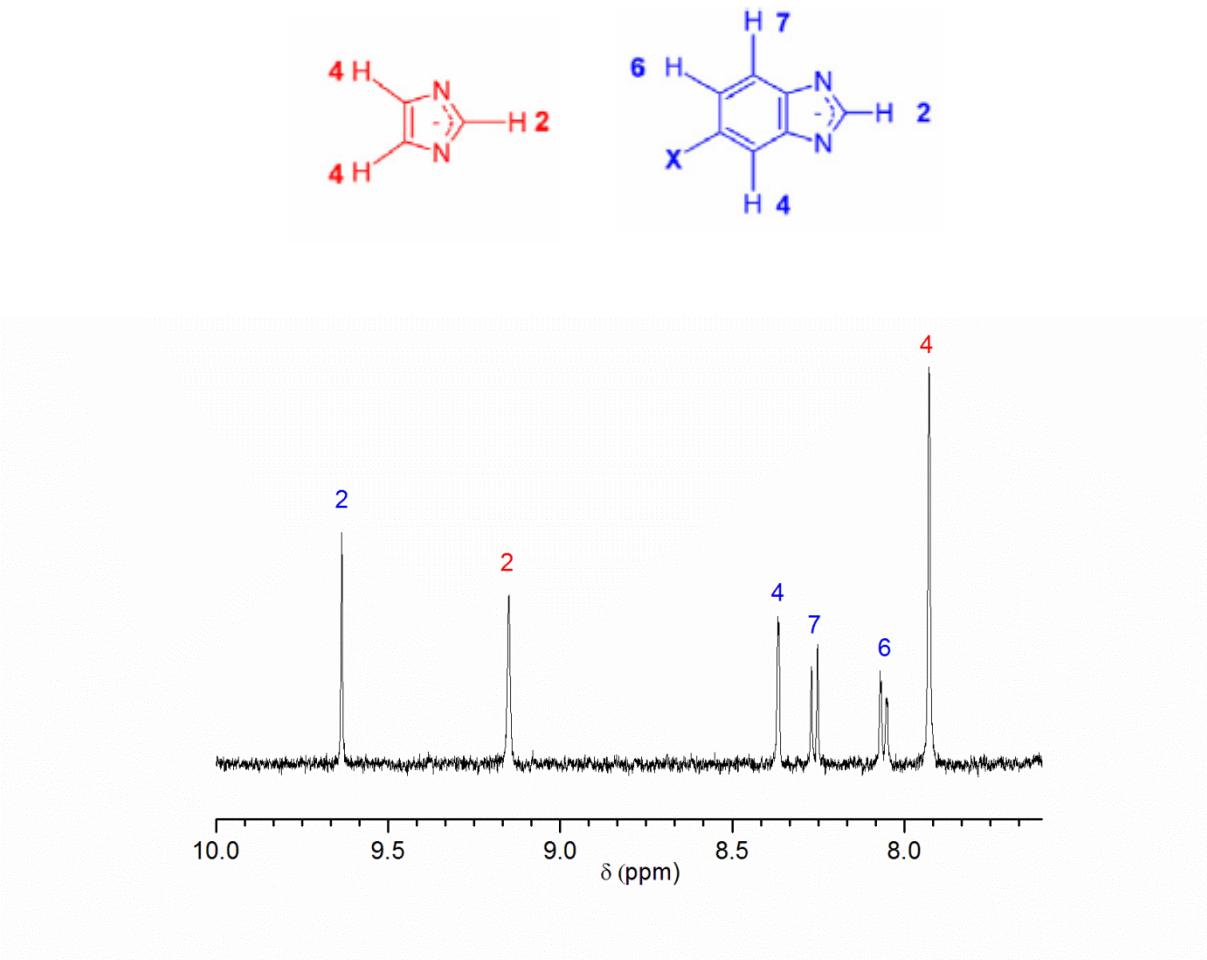

Figure 3. ^{1}H NMR spectrum of the activated ZIF-76 sample. The number denoted above each resonance (in red for imidazole and in blue for 5-chlorobenzimidazole) corresponds to the position of the hydrogen atom in the organic precursor.

Moreover, the activated material was analyzed with TGA, and according to Figure 4, no mass loss is observed between room temperature and 200 °C, which proves that the activation step is sufficient to remove the solvent molecules from the pores. The TG curve of the activated ZIF-76 sample also displays a main decomposition step between 400 and 660 °C, which is attributed to the degradation of the organic network. The mass loss between 200 and 800 °C is 75.8 % and is higher than the expected mass loss, which is 69.8 %. Similar to the cases of ZIF-8_Cl and ZIF-71,[2-3] prepared with chlorine-substituted organic precursors, this small difference between the experimental and theoretical mass losses for ZIF-76 can be explained by the presence of the chlorine substituent on the cbim linker, which could lead to the formation of a gaseous $ZnCl_2$ residue at high temperatures.

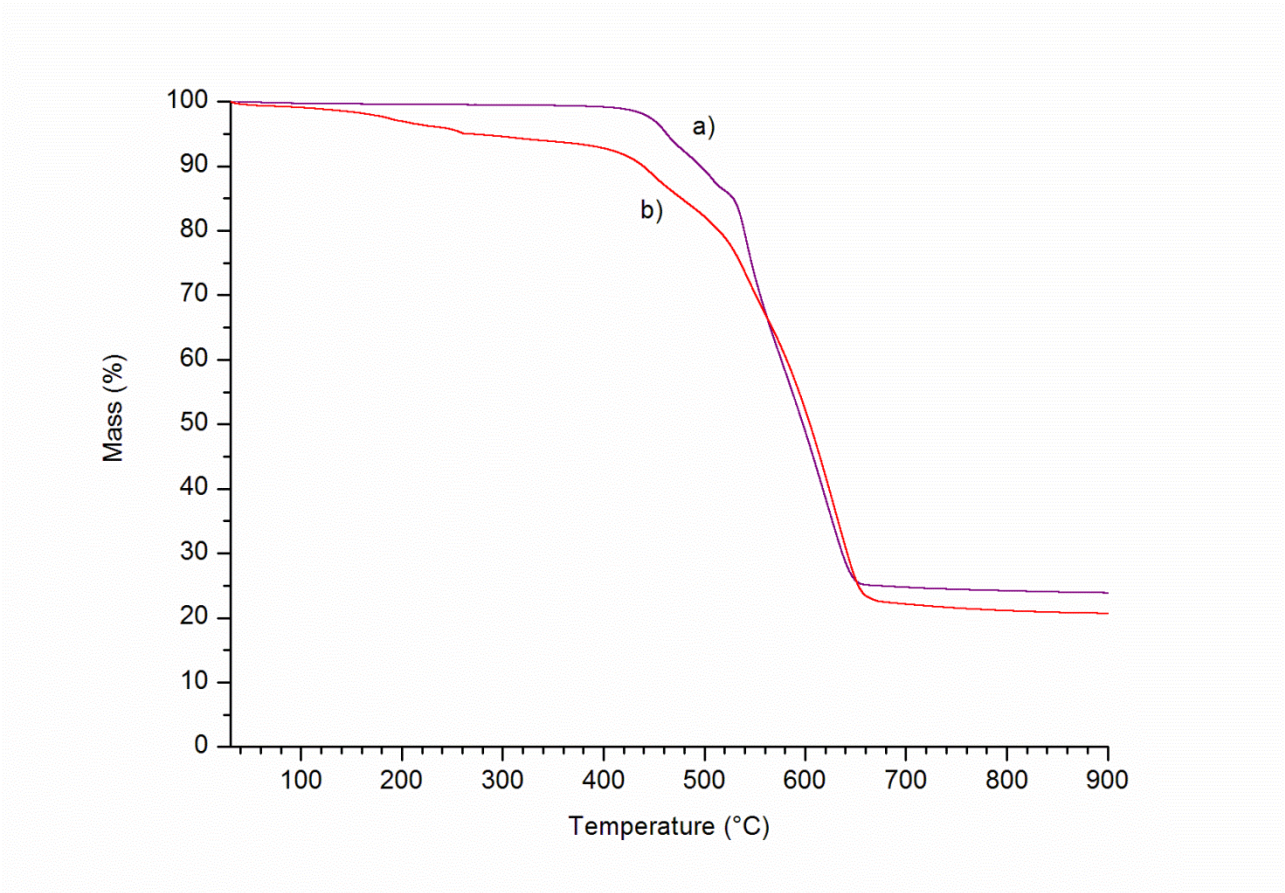

Figure 4. TG curves of the (a) activated and (b) post-intruded ZIF-76 samples.

The textural properties of ZIF-76 were determined *via* N_2 adsorption-desorption measurements. Figure 5 shows the N_2 adsorption-desorption isotherms of ZIF-76. The material displays a Type I sorption isotherm, with an average BET surface area of 1398 m^2 g^{-1} (determined in the 0.00384-0.00970 pressure range) and a microporous volume of 0.56 cm^3 g^{-1}. These values are comparable to the ones reported in the literature.[10]

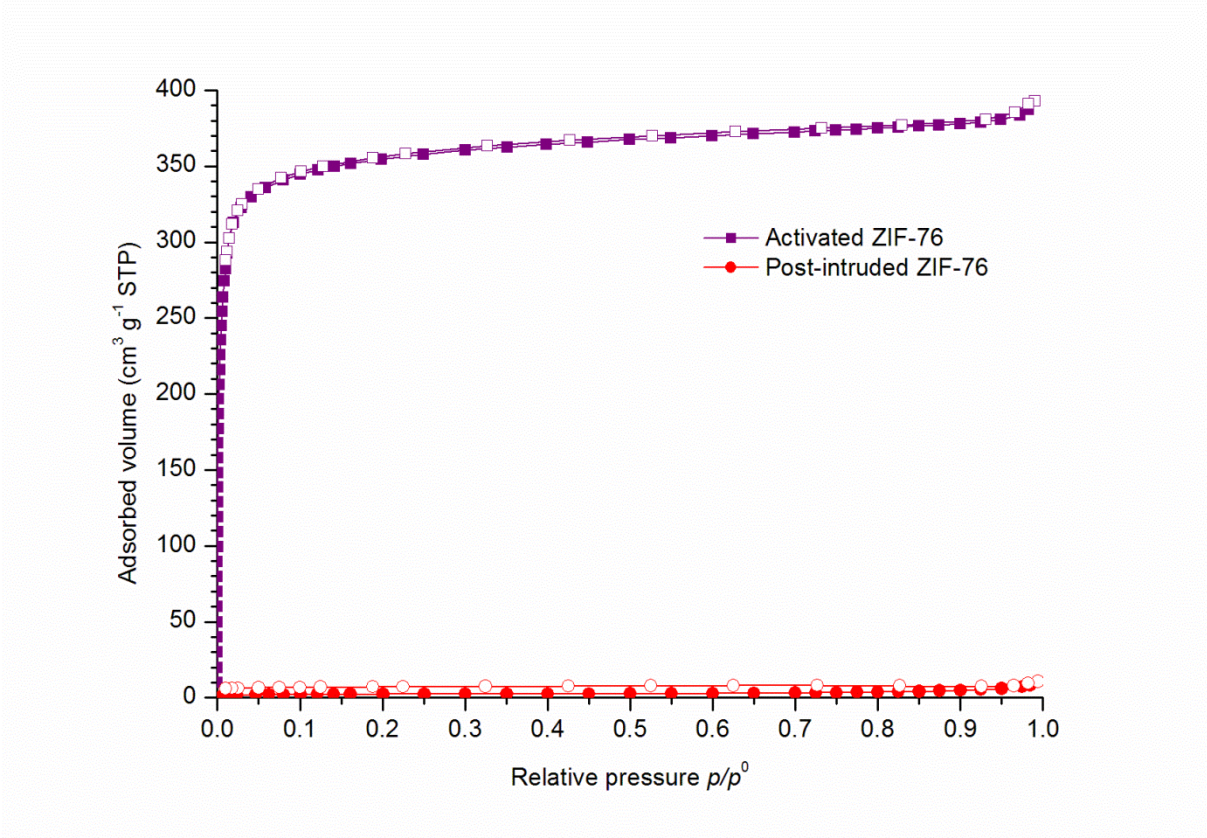

Figure 5. N_2 adsorption-desorption isotherms of the (purple) activated and (red) post-intruded ZIF-76 samples. Filled and empty symbols refer to the adsorption and desorption branches, respectively.

Furthermore, SEM images of the activated ZIF-76 sample indicate that the ZIF-76 crystals do not possess a definite shape and that the crystal size distribution is broad, ranging between 500 nm and 2 µm (Figure 6), which is also in agreement with the literature.[10]

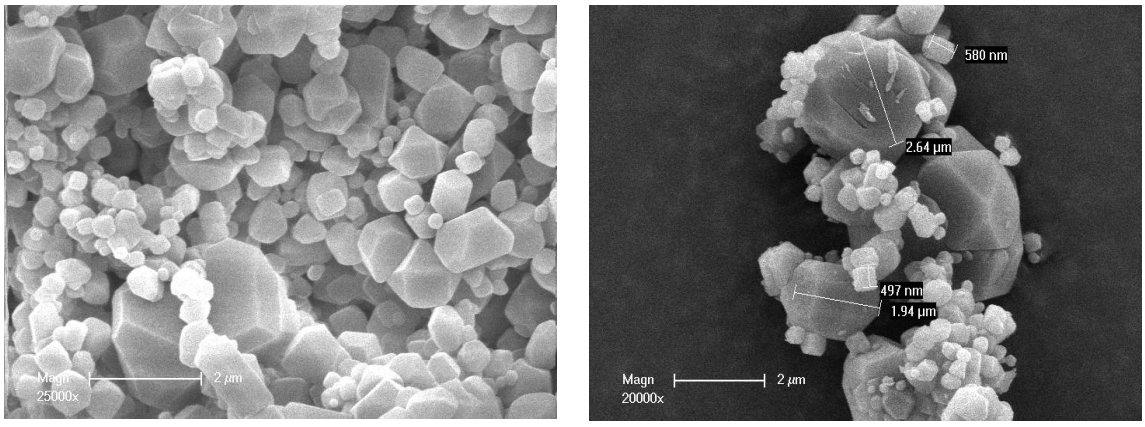

Figure 6. SEM images of the activated ZIF-76 sample.

In conclusion, ZIF-76 could be successfully synthesized and activated, as indicated by XRD, TGA, N_2 sorption, and SEM analyses, which reveal structural and textural properties of the synthesized and activated samples that are comparable to the literature.

4. Intrusion–Extrusion Experiments

Before proceeding to intrusion−extrusion experiments, the stability of the ZIF-76 framework in water and LiCl 20 M aqueous solution (the non-wetting liquids to-be employed in intrusion-extrusion experiments) was studied. Stability tests involved suspending crude ZIF-76 material in water and in LiCl 20 M aqueous solution for 24 h at room temperature. A ZIF/non-wetting liquid mass ratio similar to the one usually involved in intrusion−extrusion experiments was used. The XRD patterns of both materials are reported in Figure 2. After contact with water, a loss of crystallinity of the ZIF structure is indicated by a broad component centered around 18° in 2θ. Nevertheless, Figure 2 reveals that the LTA topology of ZIF-76 is conserved after suspending the powder in the LiCl 20 M aqueous solution, with the XRD patterns of the parent ZIF-76 and the sample recovered after the LiCl 20 M aqueous solution stability test being superimposable. Based on these results, the ZIF-76 framework was proven to be unstable in water, nonetheless, stable in a LiCl 20 M aqueous solution. Consequently, an intrusion−extrusion experiment was performed up to 350 MPa and over three intrusion−extrusion cycles, using LiCl 20 M aqueous solution as a non-wetting liquid. Such a high pressure was chosen in a first approach in order to screen the whole pressure range, even if a low intrusion pressure is expected according to the large pore aperture.

The *P*−*V* diagrams of the "ZIF-76–LiCl 20 M aqueous solution" system is presented in Figure 7. It reveals the presence of a volume variation step on the intrusion curve of the first intrusion-extrusion cycle, whereas no volume variation is observed during the first extrusion cycle or the second and third intrusion−extrusion cycles. This suggests bumper behavior of the system, with P_{int} = 50 MPa and V_{int} = 0.42 mL g^{-1} and, therefore, an absorbed energy of 22 J g^{-1}. Nevertheless, complementary experiments such as those performed in the cases of MAF-6- and ZIF-71-based LHSs must be realized in order to discriminate between intrusion or partial/total framework collapse. Indeed, the volume variations observed during the second and third cycles correspond to the compression-decompression of the liquid as already proven in previous work (Chapter 3).[2] It is worthy to note that **the intrusion pressure in this case is lower than the intrusion pressures obtained with the SOD topology** (for the "ZIF-8_X–LiCl 20 M aqueous solution" systems, with intrusion pressures in the 166-200 MPa range). **These results could be in agreement with the hypothesis suggesting the decrease in intrusion pressure with the increase in the size of the window opening** (4-, 6- and 8 membered rings for the LTA topology, compared to 4- and 6 membered rings for the SOD topology), even if the linker functionalization is different in each case. At last, the volume variation is significantly lower than the microporous volume (0.57 mL g^{-1}), as encountered in the "ZIF-8_X–LiCl 20 M aqueous solution" systems (Chapter 3).

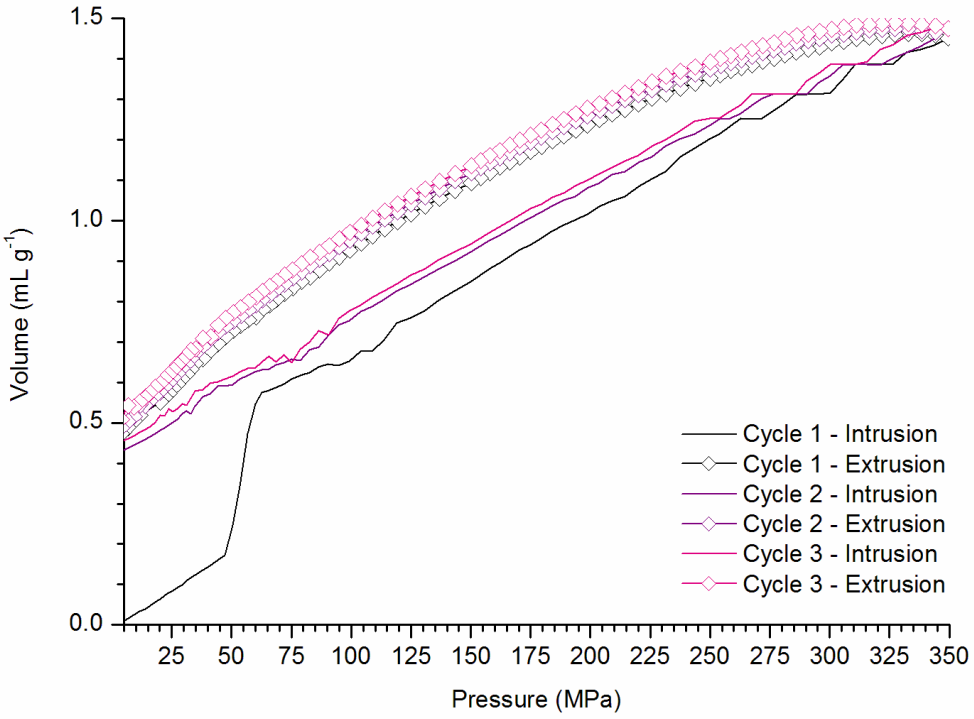

Figure 7. Pressure−volume diagrams of the "ZIF-76−LiCl 20 M aqueous solution" system.

As previously discussed in Chapter 3, bumper behavior of a system can have several explanations[3] and in order to understand the nature of the phenomenon taking place during intrusion−extrusion experiments, post-intrusion−extrusion characterizations are required. According to XRD analyses (Figure 2), the post-intruded-extruded sample is essentially amorphous. Moreover, the N_2 adsorption-desorption isotherms of the post-intruded ZIF-76 material, shown in Figure 5, indicates that it is non-porous. In addition, the TG curve of the corresponding sample (Figure 3) reveals a small mass loss (of 4 %) between room temperature and 250 °C that may be attributed to the evaporation of water molecules intruded in the porosity of the ZIF sample. Moreover, similar to the profile of the TG curve obtained for the parent (non-intruded) ZIF-76 material, the TG curve of the post-intruded sample reveals a mass loss of 78 % (compared to around 76 % for the parent material) in the 250-800 °C temperature range, corresponding to the degradation of the organic framework. This indicates that the post-intruded sample is a hybrid organic-inorganic material of similar chemical composition as the parent material. Therefore, the volume variation step observed on the intrusion curve of the first intrusion−extrusion cycle presumably results from the intrusion of the non-wetting liquid molecules into the ZIF-76 pores, associated with the amorphization of the ZIF framework. In other words, the framework seems to collapse as the non-wetting liquid molecules are being intruded, which prevents further intrusion and explains the very small mass loss of only 4

% observed on the TG curve and corresponding to the loss of water molecules. However, the current data are not enough to claim at which stage the amorphization occurs (i.e. before, during, or after the intrusion of the non-wetting liquid molecules) and the nature of the non-wetting liquid molecules intruded into the porosity (water or water and LiCl). Consequently, complementary intrusion−extrusion experiments must be realized up to various pressures, followed by characterizing the post-intruded samples (with XRD, N_2 sorption, TG and ICP analyses).

In conclusion, this preliminary study demonstrates for the first time the potential feasibility of intrusion−extrusion experiments in the case of LTA-type ZIF materials. Indeed, the collapse of the ZIF-76 framework may be avoided by lowering the pressure applied during the experiments. Thus, **complementary experiments** (realized under lower pressures, i.e 80 MPa), **in addition to post-intrusion−extrusion characterizations are required in order to gain better insight into the energetic performances of the "ZIF-76−LiCl 20 M aqueous solution" system.**

C. AFI-[Zn(im)$_2$] and CAN-[Zn(im)$_2$]

1. Description

Large-pore crystalline materials have always been interesting in both the academic and industrial fields for their potential ability to accommodate bulky molecules.[16] Most of the ZIF structures reported to date possess topologies, with cage windows consisting of 8-membered rings (including also, most of the time, 4- and 6-membered ring facets). Examples include the zeolitic topologies: ACO,[17] AFX,[18] ANA,[19-20] CHA,[18, 21] BCT,[22] LTA,[23] MER,[19] and RHO, [19, 24-25] in addition to non-zeolitic topologies, such as frl,[11] qtz,[20] and yqt.[19, 26] To the best of our knowledge, only a few ZIF topologies (including zeolitic and non-zeolitic topologies) have large, i.e. > 8-membered ring, pore windows. Among these topologies are the zec topology,[9] with 10-membered ring pore windows, and the AFI,[1] CAN,[1] GME,[18] moz,[18] poz,[27] ucb,[18] and zea topologies,[28] with 12-membered ring pore apertures. Furthermore, topologies with 14, 18, and even 24-membered ring pore windows also exist and include the ykh,[18] gcc,[18] and bam topologies,[18] respectively. It is important to note that more than 70 zeolite topologies display large/extra large pore apertures (≥ 12-membered ring pore apertures),[1] which are typically obtained using bulky organic molecules as structure-directing agents (SDA). As for the few existing ZIFs of topologies displaying 12-membered ring pore apertures, they have been synthesized following the ligand-directed strategy, i.e. using large-size substituted imidazolate linkers.[18, 29] Nevertheless, unfortunately, the presence of bulky substituents can have the disadvantage of blocking the ZIF apertures. In 2016, Shi *et al.* demonstrated an alternative way for obtaining ZIF materials with both large and accessible pore openings, which is through using large solvent molecules as SDAs and imidazolate groups as linkers.[1] They

synthesized, for the first time, two $Zn(im)_2$ ZIF materials of 12-membered ring channel apertures, with AFI- and CAN-type zeolite topologies, using the bulky amides *N*,*N*-dipropylformamide (DPF) and *N*,*N*-dibutylformamide (DBF) as SDAs (and solvents), respectively.

In the aim of investigating the influence of the pore aperture size and the pore dimensionality (cage- versus channel systems) on the energetic performances of ZIF-based LHSs, we chose to prepare the AFI- and CAN-$Zn(im)_2$ materials and study them in high-pressure intrusion−extrusion experiments. For instance, both ZIFs possess topologies that were not explored in intrusion−extrusion experiments prior to this work. Furthermore, they display a channel-pore system. Knowing that ZIF materials displaying 1D channels are not very common, the synthesis of CAN-[$Zn(im)_2$] and AFI-[$Zn(im)_2$] materials of channel systems represents a breakthrough in the world of ZIFs. In addition, these materials can be interesting candidates for intrusion−extrusion experiments as part of the study of the effect of the pore dimensionality on the intrusion pressure, by comparing them to ZIFs of cage systems having comparable pore volumes. Moreover, in their paper published in 2016, Shi *et al*.,[1] claimed that the CAN and AFI-type ZIFs exhibited the largest pore apertures reported to that date for ZIF materials. Indeed, both materials display larger pore apertures compared to SOD- (ZIF-8_X), -RHO (ZIF-71, MAF-6, ZIF-25), and LTA-type (ZIF-76) ZIFs. In addition, regardless of the absence of water sorption analyses results, the CAN- and AFI-$Zn(im)_2$ materials are expected to exhibit a hydrophobic character (in the absence of polar hydrophilic substituents on the imidazolate linker). Therefore, all these properties of AFI-[$Zn(im)_2$] and CAN-[$Zn(im)_2$] have made them interesting candidates for the investigation of their energetic behaviors in intrusion−extrusion experiments, using water and aqueous electrolyte solutions.

On another note, the GME-type materials could have also been implicated in the prospective work dealing with the influence of the pore aperture (and topology) on the energetic performances of ZIF-based LHSs. Nevertheless, they are mainly/partially constructed from linkers such as nim (2-nitroimidazolate) and ica (imidazolate-2-carboxaldehyde), which possess substituents that render the ZIF materials hydrophilic and, thereby, less promising for water and aqueous solutions intrusion−extrusion experiments. We also recall that the influence of the presence of a nitro group on the imidazolate linker on the energetic performances of the related systems was considered with the preparation of NOF-1. However, having failed in the activation of this ZIF (Section I. A.), the study could not be completed.

The structure of the CAN-[$Zn(im)_2$] material of CAN topology is made up of *can* cages of 4- and 6-membered ring pore openings.[1] The connection of these cages around a 3-fold axis leads to the formation of 1D channels (formed by *ato* cages) of 12-membered ring pore apertures with a diameter of 13.2 Å (Scheme 3a). CAN-[$Zn(im)_2$] has an orthorhombic symmetry and belongs to the space group *Pnma* with the lattice parameters a = 9.6256(8) Å, b = 23.436(2) Å, and c = 41.593(3)

Å.[1] As for the AFI-[Zn(im)$_2$] structure, the 4- and 6-membered rings are related to three types of tiles/cages: the *kah*, *lov* and *afi*. 1D large 12-membered ring channels (materialized by *apf* tiles) of 15.6 Å in diameter are obtained when the former cages are connected by shared 6-membered rings (Scheme 3b).[1] The AFI-type ZIF material crystallizes in the hexagonal symmetry and belongs to the space group *P6/mcc*, with the cell parameters $a = b = 26.437$ Å and $c = 16.632$ Å. The reported N_2 adsorption-desorption analyses reveal microporous volumes of 0.64 and 0.54 $cm^3\ g^{-1}$ for the AFI-[Zn(im)$_2$] and CAN-[Zn(im)$_2$] materials, respectively, which, indeed, make these two ZIFs attractive candidates for intrusion−extrusion experiments.

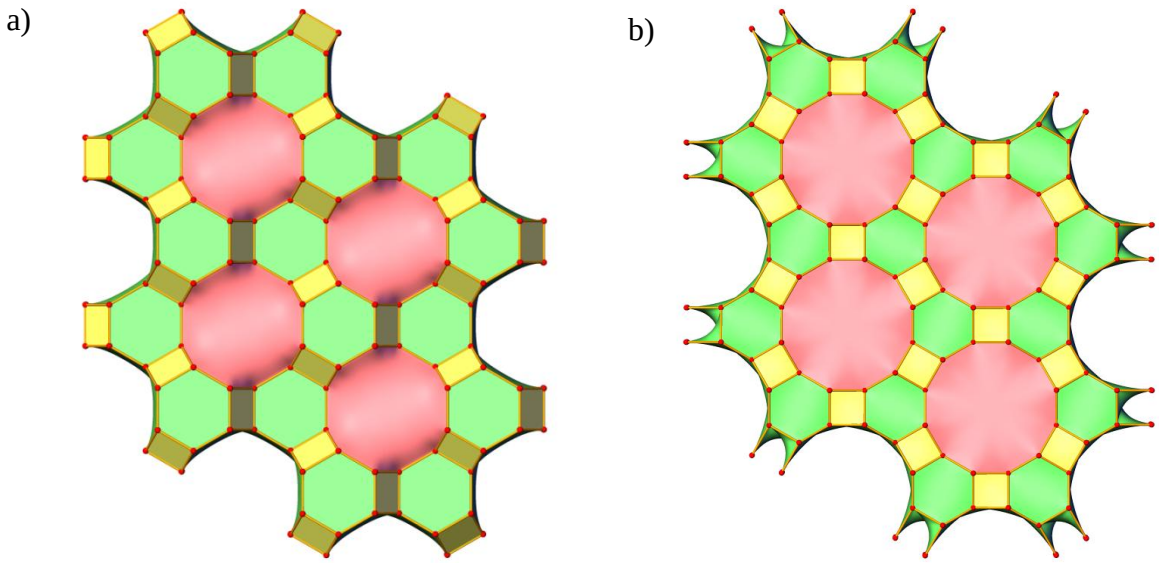

Scheme 3. Representation of the (a) CAN-[Zn(im)]$_2$ framework, with 4- and 6-membered rings (in yellow and green, respectively) of the *can* tiles and 12-membered rings of 13.2 Å in diameter (in pink) of the *ato* tiles and (b) AFI-[Zn(im)]$_2$ framework, with 4- and 6-membered rings (in yellow and green, respectively) of the *kah*, *lov*, and *afi* tiles, respectively and 12-membered rings of 15.6 Å in diameter (in pink) of the *apf* tiles.

2. Synthesis and Activation

The CAN- and AFI-[Zn(im)$_2$] materials were prepared following the synthesis protocols reported by Shi *et al.*[1] However, for the latter material the synthesis conditions were optimized by increasing the synthesis duration from 3 (reported in the literature) to 4 d, as the first attempt (3 d) led to a partially amorphous material. As for CAN-[Zn(im)$_2$], the synthesis was successfully scaled up 4 times. Nevertheless, in the aim of enhancing the material's crystallinity, compared to the literature,[1] the nature of the container was varied, by using a polypropylene bottle instead of an autoclave, and the synthesis duration was increased from 3 to 4 d. The optimized synthesis conditions of both ZIF materials are shown in Table 1.

Table 1. Synthesis conditions of the CAN-[$(im)_2$] and AFI-[$(im)_2$] ZIF materials.

ZIF	$Zn(ac)_2$ •$2H_2O$ (g)	Him (g)	Solvent/SDA (g)	H_2O (g)	Molar composition (in order)	Container	T (°C)	Duration (days)	Mass (mg)	Yield (%)
CAN-[$Zn(im)_2$]	0.367	0.573	(DBF) 29	-	1: 5: 110: 2	PP 125 mL	40	4	345	96*
AFI-[$Zn(im)_2$]	0.234	0.286	(DPF) 14.13	-	1: 4: 103: 2	T-20	60	4	182	85

PP: polypropylene bottle. T-20: 20 mL Teflon-lined autoclave. The noted masses of the samples correspond to those obtained for the as-synthesized product (before soaking in dry acetone and degassing). The symbol (*) indicates that the yield is calculated according to TGA, by taking into consideration the amount of solvent/SDA entrapped in the porosity.

CAN-[$Zn(Im)_2$] was prepared by dissolving zinc acetate dihydrate, $Zn(ac)_2$•$2H_2O$, (the metal precursor) in DBF, which was followed by the addition of Him (the organic precursor). The reaction mixture was stirred for 10 minutes at room temperature and then heated in an oven at 40 °C for 4 d.

As for the synthesis of AFI-[$Zn(im)_2$], a solution (S_1) was prepared by dissolving Him (the organic precursor) in 2/3 of the total quantity of DPF. Another solution (S_2) was prepared by dissolving $Zn(ac)_2$•$2H_2O$ (the metal precursor) in the remaining quantity of DPF (1/3 of the total quantity of the solvent). S_2 was added to S_1 and the reaction mixture was stirred at room temperature for 5 minutes, which was followed by heating at 60 °C for 4 d. The as-synthesized products were then collected by filtration over Whatman grade 5 filter papers, washed with a few milliliters of acetone, and dried at room temperature.

In order to liberate the pores and remove the entrapped solvent/SDA molecules, the as-synthesized CAN and AFI-$Zn(im)_2$ samples were soaked in dry acetone (4*10 mL) over 48 h.

3. Characterizations

Figures 8 and 9A show the XRD patterns of the as-synthesized and acetone-activated CAN-[$Zn(im)_2$] and AFI-[$Zn(im)_2$] materials, respectively, in addition to the corresponding simulated patterns. Indeed, for both ZIFs, the as-synthesized materials display the targeted topologies and the XRD patterns of the powdered samples are comparable to the corresponding simulated patterns (Figures 8 and 9A). Refinements of the experimental patterns reveal that CAN-[$Zn(im)_2$] crystallizes in the orthorhombic symmetry, with the lattice parameters a = 9.61(5) Å, b = 23.27(9) Å, and c = 41.49(6) Å and the space group *Pnma*. As for the AFI-[$Zn(im)_2$] material, it crystallizes

in the hexagonal symmetry, with the unit cell parameters $a = b = 26{,}5(9)$ Å and $c = 16{,}58(5)$ Å and the space group *P6/mcc*. These results are in agreement with literature.[1]

However, after soaking in dry acetone, contrary to what is mentioned in the literature,[1] both the CAN-[Zn(im)$_2$] and AFI-[Zn(im)$_2$] materials exhibit a partial loss of crystallinity that is indicated by the appearance of a hump between 14 and 18° in 2θ and 12 and 20° in 2θ, respectively (as indicated by Figures 8 and 9B, respectively). This can be attributed to the removal of the entrapped DBF and DPF template/solvent molecules, which may have led to the partial degradation of the framework, which is more pronounced for CAN than for the AFI topology. Nevertheless, the activated samples still exhibit the CAN and AFI topologies.

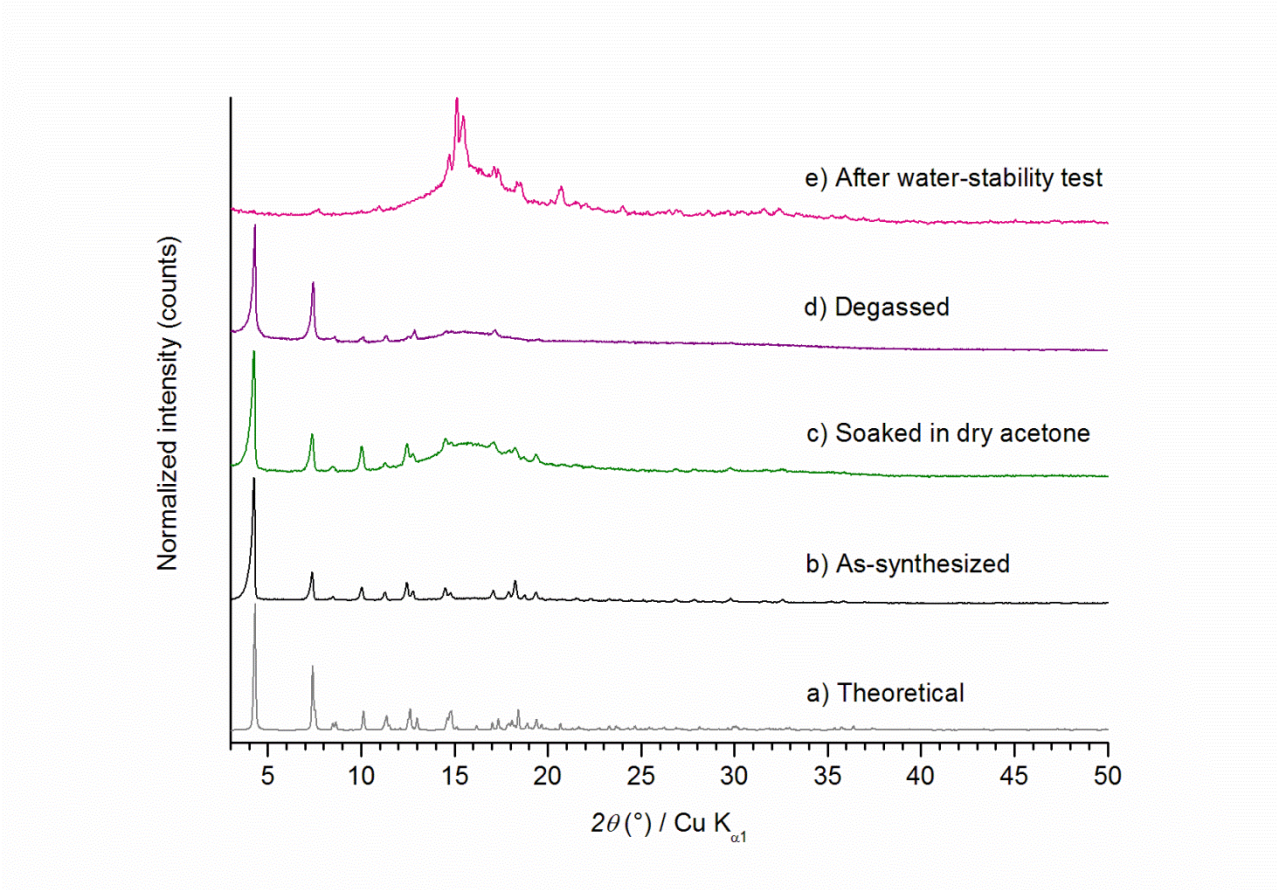

Figure 8. (a) Theoretical XRD pattern of CAN-[Zn(im)$_2$] and XRD patterns of the (b) as-synthesized CAN-[Zn(im)$_2$] sample, (c) CAN-[Zn(im)$_2$] activated with dry acetone, and (d) CAN-[Zn(im)$_2$] degassed at 125 °C for 6 h. (e) The XRD pattern of the CAN-[Zn(im)$_2$] sample obtained after water stability test is also presented.

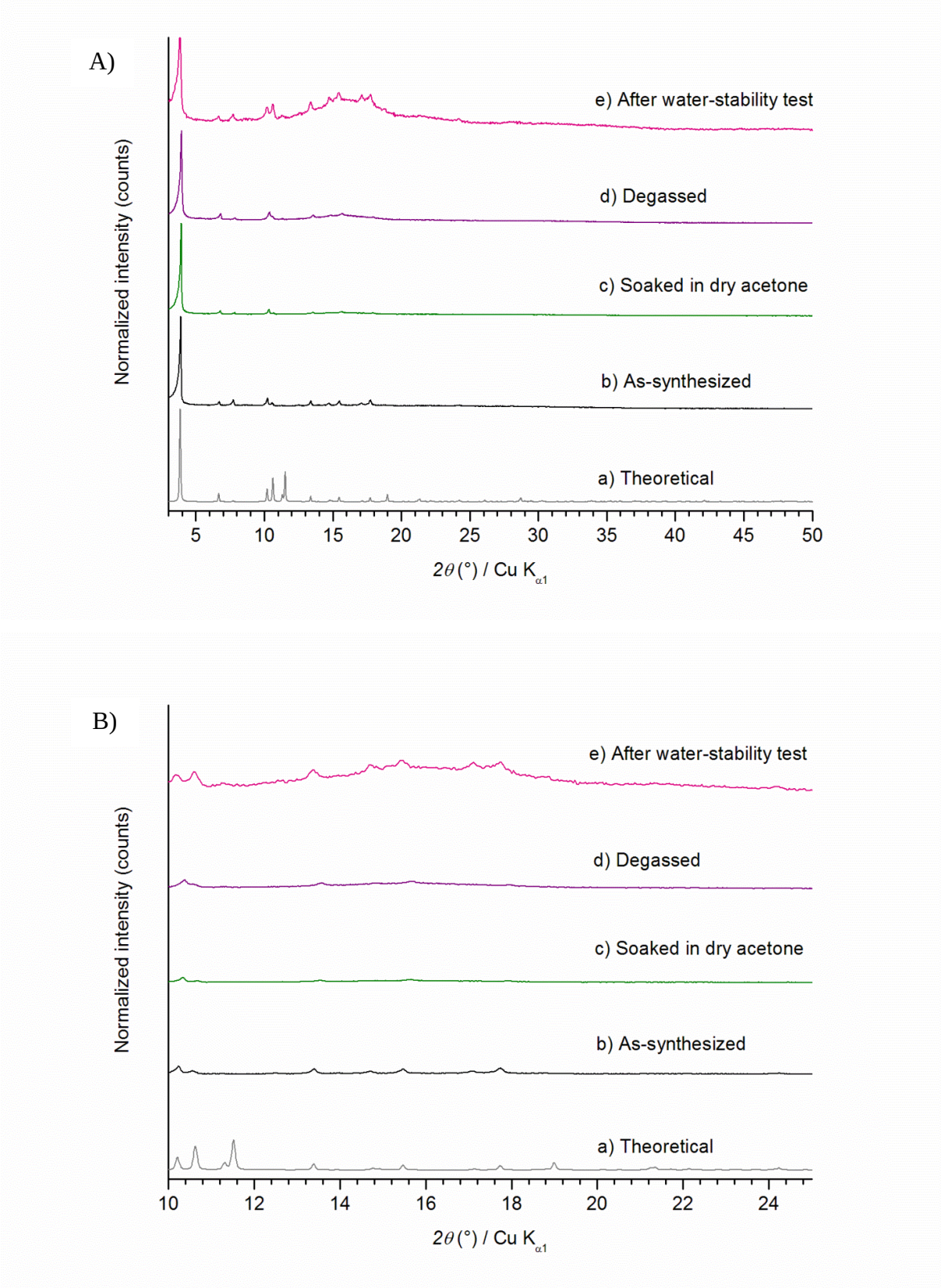

Figure 9. (A) XRD pattern of AFI-[Zn(im)$_2$] (a) Theoretical (b) as-synthesized sample, (c) sample activated with dry acetone (d) sample degassed at 125 °C for 6 h (e) sample recovered after water stability test (B) A closer view (in the 10-25 ° in 2θ range) of the XRD pattern of AFI-[Zn(im)$_2$] (a) theoretical (b) as-synthesized sample, (c) sample activated with dry acetone (d) sample degassed at 125 °C for 6 h (e) sample recovered after water-stability test.

Figures 10A and 10B represent the TG curves of the as-synthesized, acetone-activated, and degassed CAN-[$Zn(im)_2$] and AFI-[$Zn(im)_2$] samples. For both ZIFs, the TG curves of the as-synthesized samples reveal a mass loss between room temperature and 200 °C of 17 and 4 % for CAN-[$Zn(im)_2$] and AFI-[$Zn(im)_2$], respectively, which is assigned to the release of solvent molecules entrapped in the porosity. As for the corresponding samples that were activated with dry acetone, a small mass loss still exists in the low-temperature range, corresponding to 4 % for both CAN-[$Zn(im)_2$] and AFI-[$Zn(im)_2$], indicating the persistence of some solvent molecules in the ZIF pores and, thus, an incomplete activation process. These results prove that soaking in acetone is not sufficient for the complete removal of the template (DPF and DBF) molecules from the porosity of the AFI- and CAN-type ZIFs. Nonetheless, the latter activation process seems to be more efficient in the case of AFI-[$Zn(im)_2$] compared to CAN-[$Zn(im)_2$]. However, the TG curves of the CAN- and AFI-type ZIF materials that were degassed following their activation in acetone show that both materials are thermally stable up to 260 °C (a thermal plateau associated with a negligible mass loss between room temperature and 260 °C). This is followed by a main decomposition step between 260-800 °C, consisting of multiple sub-steps that can be all attributed to the decomposition of the organic network and correspond to a mass loss of 60 % in the case of both the CAN- and AFI-type ZIF materials. These results are similar to the ones reported in the literature,[1] which reveal a thermal stability up to 300 °C, after which the decomposition of the organic network occurs, resulting in a mass loss of ≈ 59 % for both CAN-[$Zn(im)_2$] and AFI-[$Zn(im)_2$].

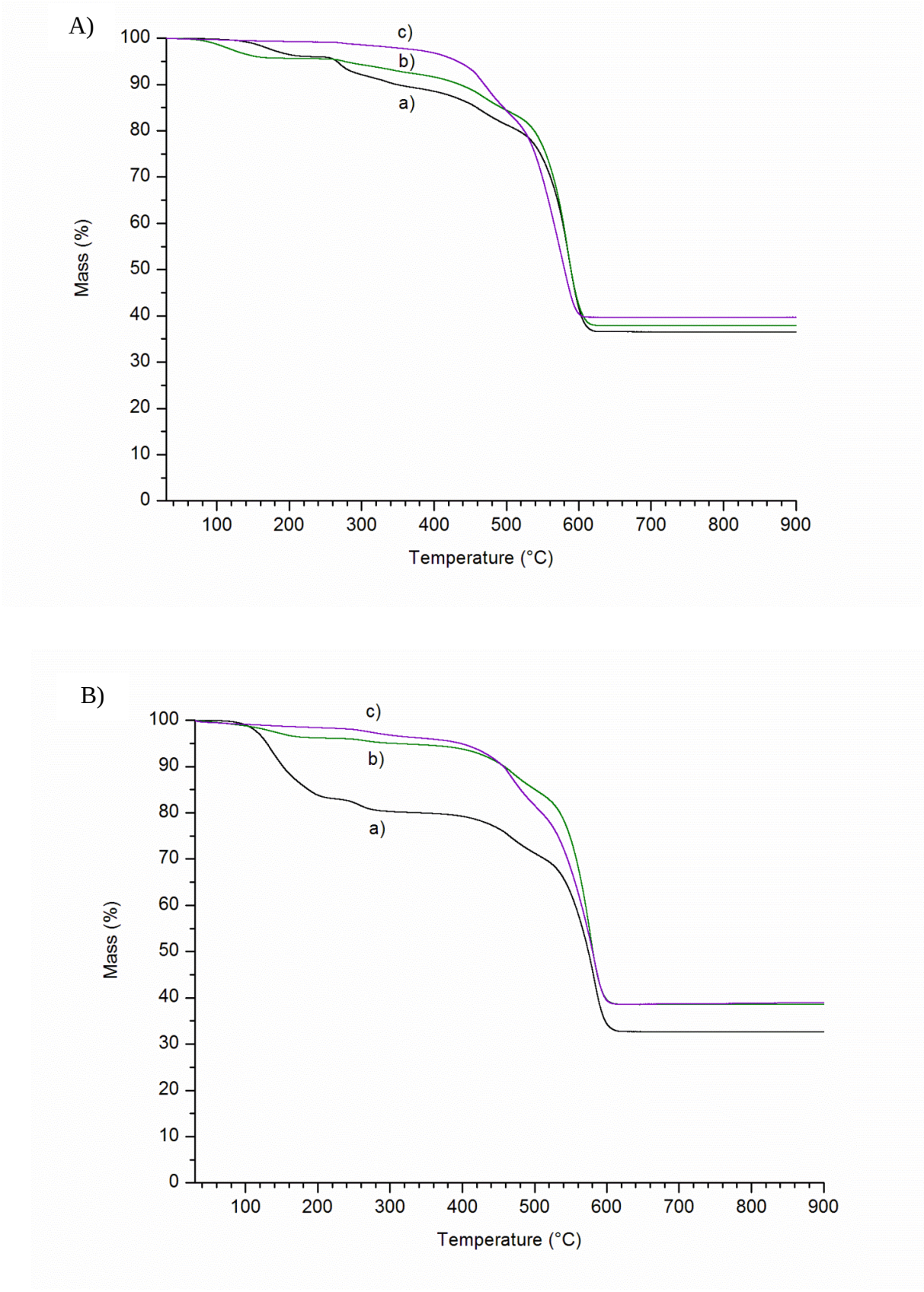

Figure 10. (A) TG curves of (a) the as-synthesized CAN-[$Zn(im)_2$], and the CAN-[$Zn(im)_2$] samples (b) activated with dry acetone and (c) degassed at 125 °C for 6 h. (B) TG curves of (a) as-synthesized AFI-[$Zn(im)_2$] and the AFI-[$Zn(im)_2$] samples (b) activated with dry acetone and (c) degassed at 125 °C for 6 h.

Due to the failure of the acetone-activation step in fully liberating the ZIF pores and the consequent persistence of entrapped DPF and DBF molecules in the porosity, prior to N_2 adsorption-desorption analyses, the ZIF samples were further activated by degassing at 125 °C for 6 h under vacuum. It is worthy to note that these degassing conditions are different from the ones reported in the literature, where a degassing temperature of 50 °C (under vacuum) is employed.[1] This choice of the degassing temperature has been done as the reported temperature value appeared to be abnormally low compared to conventional degassing temperatures.

Figures 11a and 11b show the N_2 adsorption-desorption isotherms of the CAN-[$Zn(im)_2$] and AFI-[$Zn(im)_2$] materials after activation by soaking in dry acetone and degassing. Both ZIFs display Type I isotherms characteristic of microporous materials, with the presence of a hysteresis, which is more pronounced in the case of AFI-[$Zn(im)_2$], probably indicating an interparticular mesoporosity. However, the obtained BET surface areas (270 and 249 $m^2\ g^{-1}$ for the CAN-[$Zn(im)_2$] and AFI-[$Zn(im)_2$] materials, respectively) and microporous volumes (0.10 $cm^3\ g^{-1}$ for both materials) are much lower compared to the values reported in the literature (BET surface areas of 1178 and 1386 $m^2\ g^{-1}$ and microporous volumes of 0.54 and 0.64 $cm^3\ g^{-1}$ for CAN-[$Zn(im)_2$] and AFI-[$Zn(im)_2$], respectively).[1] In order to interpret these surprising results, the recovered materials were analyzed after N_2 sorption measurements with XRD. For both ZIF materials, the obtained XRD patterns reveal a further decrease in the crystallinity that could be clearly indicated by the growth of the humps between 14 and 18° 2θ and 12 and 20° 2θ for CAN-[$Zn(im)_2$] and AFI-[$Zn(im)_2$], respectively (Figures 8 and 9A). This is probably attributed to the distortion of the framework during degassing, while the DPF and DBF molecules are being removed from the ZIF pores and/or the harsh degassing conditions (heating at 125 °C for 6 h under vacuum) employed.

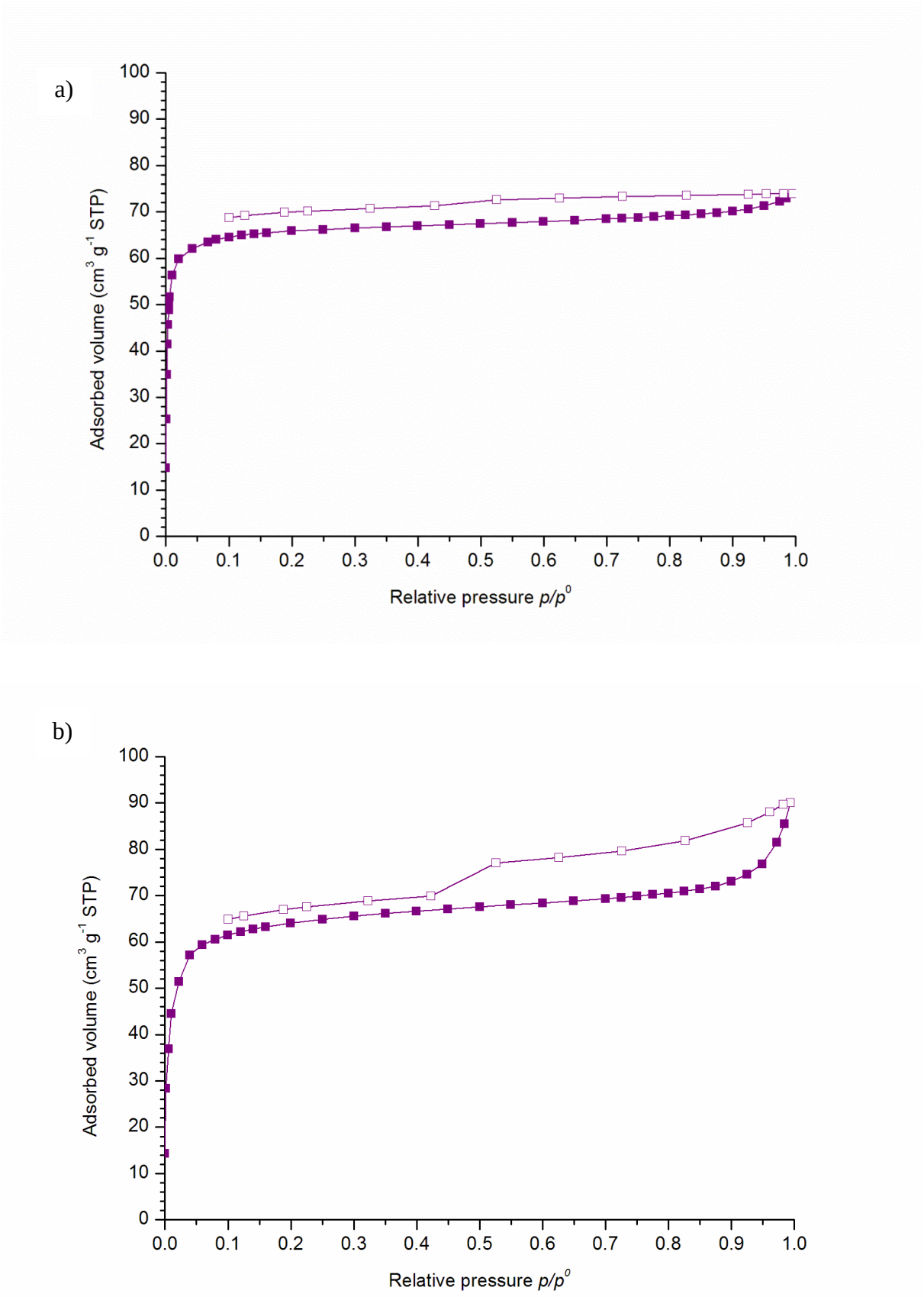

Figure 11. N_2 adsorption-desorption isotherms of the (a) CAN-[$Zn(im)_2$] and (b) AFI-[$Zn(im)_2$] materials. The filled and empty symbols refer to the adsorption and desorption branches, respectively.

Therefore, the activation process for both the CAN-[$Zn(im)_2$] and AFI-[$Zn(im)_2$] materials must be optimized so as to liberate the pores without compromising on the stability of the ZIFs' frameworks. However, before proceeding to optimize the activation step, we studied the stability of the CAN-[$Zn(im)_2$] and AFI-[$Zn(im)_2$] frameworks in water, which is an essential parameter for water intrusion−extrusion experiments. In this respect, the crude AFI-[$Zn(im)_2$] and dry acetone activated CAN-[$Zn(im)_2$] materials were suspended in water, for 48 h at room temperature, with a ZIF / H_2O mass ratio similar to the one employed during intrusion–extrusion experiments. The powder was then recovered by filtration and dried in air. Unfortunately, the results obtained from XRD analyses performed on both ZIFs after water stability tests reveal a large loss of crystallinity, accompanied with a phase transformation for CAN-[$Zn(im)_2$] and a change in the relative peak intensities in the case of AFI-[$Zn(im)_2$] (Figures 8 and 9A). These results could be assigned to a lower water stability of the CAN framework compared to AFI. Nonetheless, this attribution must be qualified as the natures (crude or activated) of the starting materials were not identical. Indeed, the CAN-[$Zn(im)_2$] framework had already lost some crystallinity during soaking in dry acetone and was further distorted during the water stability test, whereas an initially crystalline AFI-[$Zn(im)_2$] sample (crude sample) was used for the water stability test. Thus, the lack of water stability prevents the application of both materials to water intrusion–extrusion experiments. However, their energetic behavior can still be investigated using highly concentrated aqueous electrolyte solutions (such as LiCl 20 M aqueous solution). Nevertheless, the framework stability in the aqueous electrolyte medium should be first tested at ambient pressure.

In conclusion, XRD analyses reveal a partial amorphization of the CAN-[$Zn(im)_2$] and AFI-[$Zn(im)_2$] frameworks associated with the removal of the guest molecules (DPF and DBF) during the activation step using dry acetone. This amorphization seems to become more prominent during degassing at 125 °C, which is clearly shown by XRD and N_2 sorption analyses, even if TGA demonstrate a thermal stability of both ZIF materials up to 300 °C. Furthermore, based on XRD analyses, the ZIF frameworks are not stable in water. Indeed, this makes CAN-[$Zn(im)_2$] and AFI-[$Zn(im)_2$] unsuitable for water intrusion–extrusion experiments. However, their energetic performances may be investigated using a LiCl 20 M aqueous solution. To this end, future perspectives include the optimization of the activation processes for both ZIF materials so as to be studied in high-pressure intrusion–extrusion experiments of a LiCl 20 M aqueous solution.

II. Hydrophilic Mesoporous MOFs for Intrusion−Extrusion Experiments: Towards the Post-Synthetic Modification Route

As mentioned in the introduction of this chapter, the presence of water molecules coordinated to the metal center in some Secondary Building Units (SBU), renders, presumably, the material hydrophilic (as more water molecules may be added through hydrogen bonding), thus, limiting its application to water and, maybe, aqueous electrolyte solutions intrusion−extrusion experiments. Therefore, in order to make the materials hydrophobic, we aimed at post-synthetically modifying them at the metal sites, *via* the coordinate covalent route. The process involves dehydrating the MOF material i.e. removing the metal-coordinated water molecules, and substituting them by hydrophobic agents such as primary amines with perfluoroalkane. When coordinated to the metal center, these capping agents are also supposed to prevent or limit the rehydration of the modified MOF. This strategy is similar to the concept of post-synthetic modification (PSM) widely applied to the well-known MIL-101(Cr) and HKUST-1(Cu) MOF materials.[30] The latter is a highly porous MOF that consists of dimeric Cu(II) paddle-wheel SBUs linked through benzene-1,3,5-tricarboxylate (BTC) linkers, whereby labile aqua ligands on the Cu(II) paddle-wheel SBU can be removed by dehydration and then replaced by other molecules (pyridine for example).[30] Owing to structural analogies with HKUST-1(Cu), i. e. the presence of coordinated water molecules on copper atoms, MOF-919(Sc/Cu) was also selected, in addition to MIL-101(Cr), for studying the feasibility of their PSM in the aim of employing the post-synthetically modified hydrophobic MOF materials in water and aqueous electrolyte solutions intrusion−extrusion experiments. The next two sections present a description of the MIL-101(Cr) and MOF-919 materials, in addition to the work that has been performed on them.

A. MOF-919(Sc/Cu)

In the aim of increasing the amount of stored/absorbed energy by LHSs, mesoporous MOF-919(Sc/Cu) was considered as a good candidate for intrusion−extrusion experiments, mainly due to its high porous volume, estimated at 1,70 $cm^3\ g^{-1}$, and chemical stability.[6] Indeed, according to Liu *et al.*,[6] the activated MOF-919(Sc/Cu) material is thermally stable up to 280 °C and exhibits excellent chemical stability in air and humidity that was indicated by the unaltered XRD patterns, compared to the simulated pattern, after exposure to air for one week. In addition, the high water and chemical stabilities of MOF-919(Sc/Cu) were evidenced after suspending the powder in water and strong acidic and basic aqueous media (HCl and NaOH solutions, respectively) for 2 h. Indeed,

these characteristics of MOF-919(Sc/Cu) i.e. the high thermal, chemical, and water stabilities are highly desired for PSM and, later, for intrusion−extrusion experiments.

1. Description

MOF-919(Sc/Cu) is made up by the assembly of scandium and copper metal cations and 1-*H*-pyrazole-4-carboxylic acid (H_2Pyc). The structure (Scheme 4) consists of Sc- and Cu-SBUs. The former type of SBUs is formed by the coordination of trimeric scandium (III) units (Sc_3O) with the carboxylate groups from the pyrazolate (Pyc) linkers, where these linkers also form with copper cations a triangular SBU.

MOF-919(Sc/Cu) exhibits a moo topology, also displayed by MIL-100(Cr), which involves two types of mesoporous cages of permanent porosity; the *yys* and *liu* cages of 49 and 60 Å in diameter, respectively. The *yys* cage has twelve 10-membered ring pore apertures of 20 Å in diameter, whereas the *liu* cage, i. e the larger cage, in addition to twelve 10-membered ring pore apertures (similar to the ones exhibited by the *yys* cage) also has four 12-membered ring pore apertures of 25 Å in diameter (Scheme 4).[6]

a)

b)

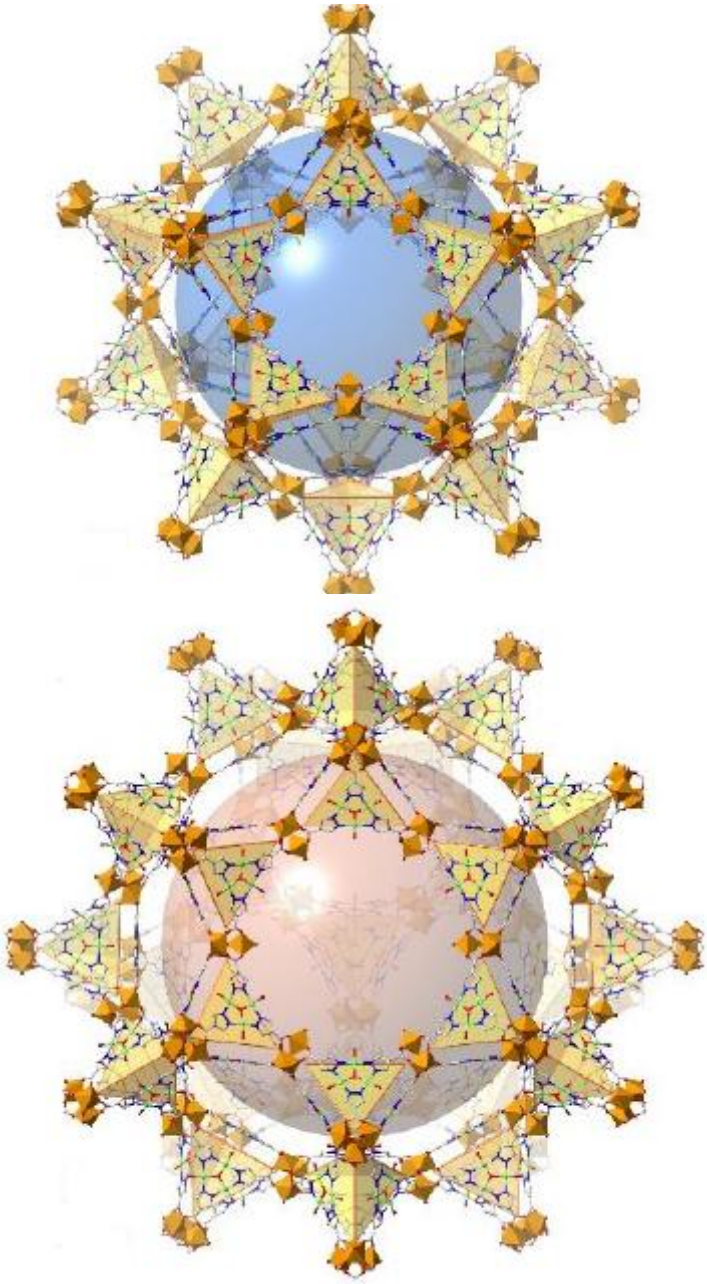

Scheme 4. Representations of the (a) *yys* and (b) *liu* cages in MOF-919(Sc/Cu). The trimeric ScO_3 units and Cu atoms are represented in brown and green, respectively.[6]

The formula of the guest-free (solvent-free) MOF-919(Sc/Cu) material suggested by Liu *et al*. is $[Sc_3(\mu_3\text{-}O)(OH)_3][Cu_3(\mu_3\text{-}O)(\mu\text{-}PyC)_3(H_2O)_6]_2$.[6] It was determined by taking into consideration the charge balance, XRD analysis results, and previous reports.[6, 31-33]

2. Synthesis

MOF-919(Sc/Cu) was prepared following the synthesis protocol published by Liu *et al.*[6] $ScCl_3 \cdot 6H_2O$ (76.2 mg, 0.2937 mmol) and $Cu(NO_3)_2 \cdot 3H_2O$ (135.6 mg, 0.5613 mmol) were dissolved in DMF by sonication in a 80 mL glass bottle. The organic precursor H_2Pyc (34.8 mg,

0.3105 mmol) was then added to the metal solution and the reaction mixture was sonicated. The reaction mixture, of molar composition; 1 $Sc(NO_3)_3$: 2 $Cu(NO_3)_3$: 1 H_2Pyc: 440 DMF: 12 H_2O, was heated in an oven at 100 °C for 15 h to yield green crystals after cooling down to room temperature. The crystals were recovered by filtration, washed with a few milliliters of DMF and left to dry in air during 48 h.

3. Characterizations

The obtained product was analyzed with XRD. Figure 12 shows the XRD pattern corresponding to the as-synthesized material compared to simulated pattern.

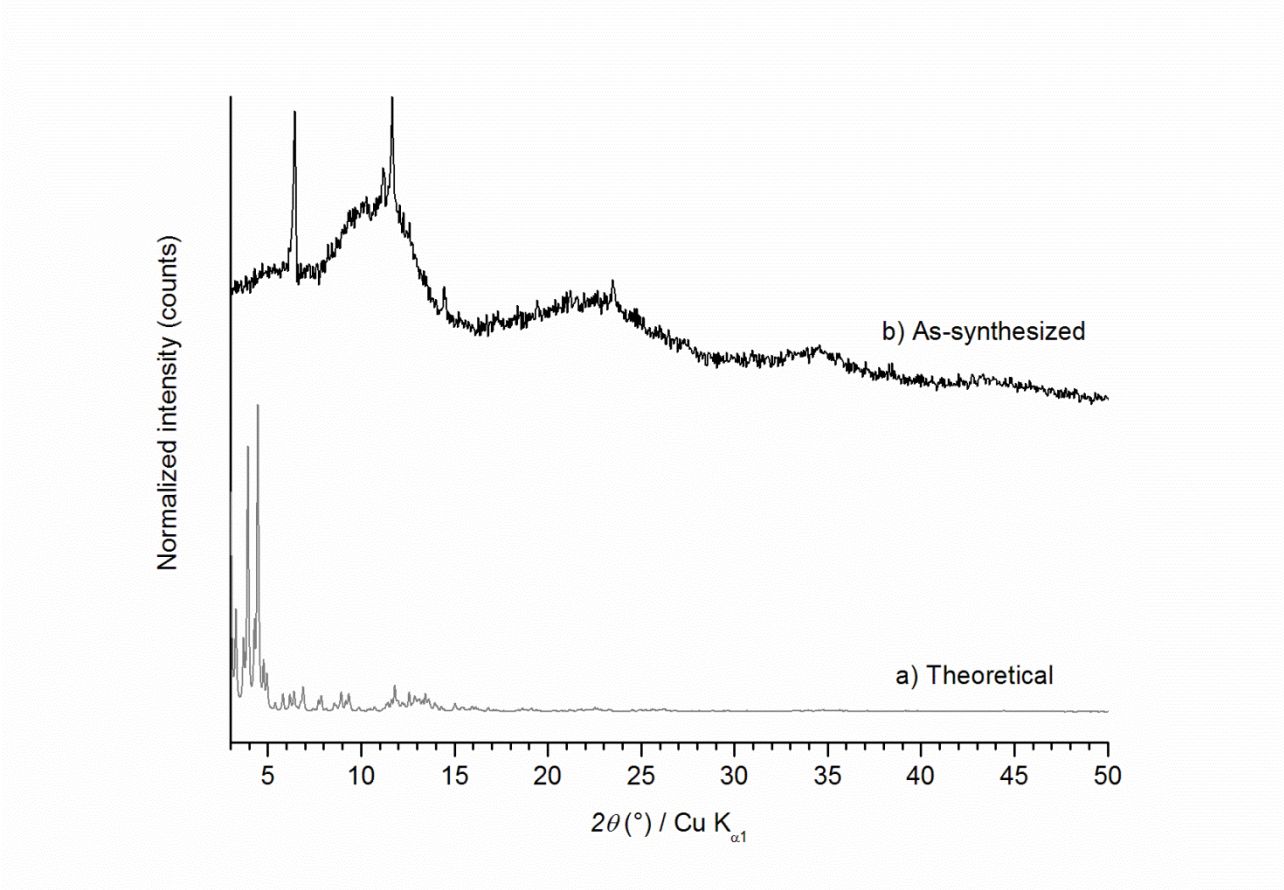

Figure 12. (a) Theoretical XRD pattern of MOF-919(Sc/Cu) and (b) XRD pattern of the as-synthesized MOF-919(Sc/Cu) sample.

Clearly, the product does not correspond to MOF-919(Sc/Cu) and is mostly amorphous, with five small peaks that do not belong to traces of the desired material. In this case, we decided not to go further with the optimization of the synthesis protocol of MOF-919(Sc/Cu), even though it remains an interesting candidate for the development of the PSM route and intrusion−extrusion experiments.

B. MIL-101(Cr)

1. Description

MIL-101(Cr) is one of the most representative mesoporous MOFs. Its structure is based on trimeric Cr(III) units, where three hexacoordinated chromium (III) atoms are sharing one oxygen atom (Scheme 5a).[34-35] These units are interconnected by benzene-1,4-dicarboxylate (BDC) linkers, thus, giving rise to a 3D structure, with a chemical formula of $Cr_3(O)F(H_2O)_2(BDC)_3 \cdot nH_2O$ (with $n \approx 25$). For two of the three chromium atoms of the trimeric unit, the coordination sphere is completed by four oxygen atoms from four BDC linkers and one oxygen atom from one water molecule. It should be noted that these chemisorbed water molecules are labile and that their de-coordination allows the formation of coordinatively unsaturated metal sites (CUS), also called open-metal sites. A post-activation grafting of nucleophilic agents on these sites is then possible, as it has been demonstrated by Férey and coworkers.[36] As for the third chromium atom, its environment is similar to that of the other two chromium atoms constituting the trimeric unit, except that the oxygen atom from water molecule is substituted by one hydroxo group or one fluorine atom, depending on the synthetic route.

The MIL-101(Cr) structure can be also depicted as the assembly of a super tetrahedron (Scheme 5b) and two types of mesoporous cages (Schemes 5c and 5d). Moreover, MIL-101(Cr) possesses a framework of MTN zeolite-type architecture (analogous to the framework of MTN-type zeolites, however, by increasing the size of the SiO_4 tetrahedron to a super tetrahedron). Concerning the mesoporous and quasi-spherical cages, the ratio is 2:1 (in favor to the smaller ones). The latter, of 27-29 Å in size, displays 3- and 5-membered ring pore windows (with the chromium trimeric units forming the vertexes), whereas the larger mesoporous cages, of 34 Å in size, are delimited by 3-, 5- and 6-membered ring pore windows. The dimensions of the pentagonal and hexagonal pore apertures, are evaluated around 12 and 14.5 Å x 16 Å, respectively.[5, 7, 34] Moreover, MIL-101(Cr) was reported to be stable under moisture and, more remarkably, after suspending in boiling water at 100 °C for a week.[7] Hence, these exceptionally large dimensions (resulting from the presence of mesoporous cages), in addition to a microporous volume surpassing 1 $cm^3\ g^{-1}$ and the remarkable chemical stability make MIL-101(Cr) an interesting candidate for intrusion−extrusion experiments.

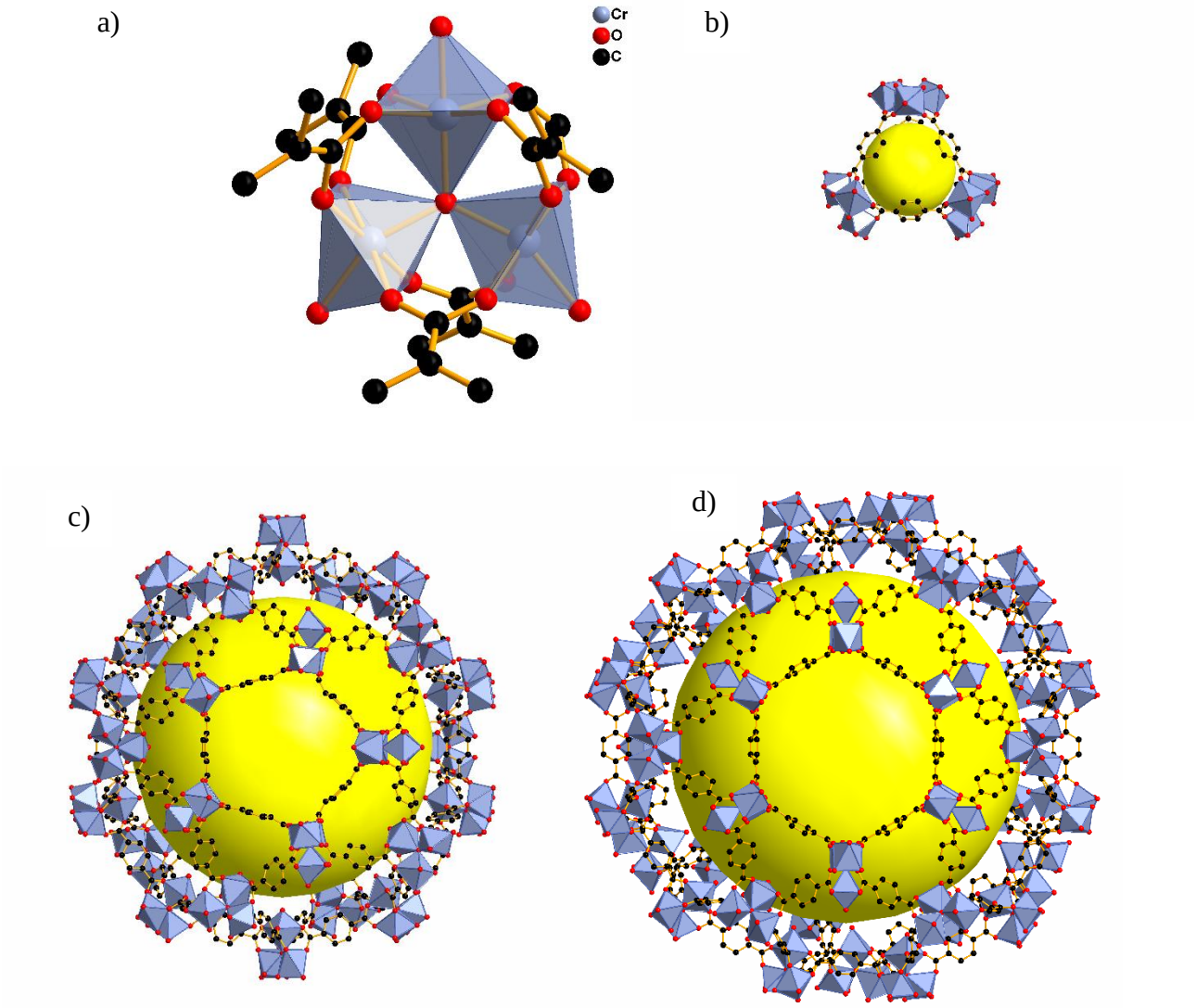

Scheme 5. Representations of the (a) trimeric Cr(III) unit, (b) super tetrahedron, (c) small cage, with 3- and 5-membered ring pore apertures and (d) large cage, with 3-, 5- and 6-membered ring pore apertures.

2. Synthesis and Activation

MIL-101(Cr) microcrystals were prepared following the synthesis protocol reported by Hong *et al.*[7] by dissolving the metal and organic precursors in a mixture of water and hydrofluoric acid (HF) and then heating the reaction mixture at 220 °C for 8 h. Thus, 5.02 g (12.5 mmol) of chromium nitrate nonahydrate ($Cr(NO_3)_3 \cdot 9H_2O$), were dissolved in 62.92 g (3492.6 mmol) of deionized water (by stirring over 10 min), then 0.63 g (12.5 mmol) of a 40 wt% aqueous solution of HF was added.

After mixing, 2.08 g (12.5 mmol) of terephthalic acid (H_2BDC) were added. The solution obtained with the following molar composition, 1.0 $Cr(NO_3)_3$:1.0 H_2BDC: 1.0 HF: 289.0 H_2O, was mixed during 1 min, under magnetic stirring, before being transferred into a 120 mL Teflon®-lined stainless steel autoclave. The reaction mixture was then heated at 220 °C for 8 h in a pre-heated oven. After cooling down to room temperature, a first filtration (using a grade 2 borosilicate filter) was performed in order to remove the unreacted and crystallized terephtalic acid present in the medium. Large amounts of deionized water were used to transfer the green MIL-101(Cr) microcrystals (containing terephtalic acid entrapped in the porosity) through the filter. The resulting green suspension was then filtered on a microfiltration setup (using a PTFE membrane, 1 µm) and the MOF microcrystals were recovered. In order to remove the residual terephthalic acid entrapped in the pores of the as-synthesized MOF sample (activation stage), three successive soaking/(micro)filtration steps were carried out, as suggested by Hong *et al.*[7]: The first step involved soaking the sample in deionized water at 70 °C under weak stirring (150-200 rpm) during 5 h. This was followed (after recovering the powder from water by filtration) by soaking in absolute ethanol at 60 °C also under weak stirring over 5 h. Finally, in the last activation step, the MOF microcrystals were suspended in an aqueous NH_4F solution (3.10^{-2} M) at 60 °C during 15 h, in order to transform the remaining entrapped H_2BDC molecules into an ammonium salt, which is more soluble in water.

3. Characterizations

The theoretical XRD pattern of the activated MIL-101(Cr) was generated based on the published structure, which reveals a cubic symmetry (space group F*d-3m*).[35] According to Figure 13, the XRD pattern of the activated MIL-101(Cr) material and the theoretical MIL-101(Cr) pattern are similar in terms of the peak positions, which indicates the high crystallinity and phase purity of the sample. Nonetheless, compared to the theoretical XRD pattern, the XRD pattern of the activated MIL-101(Cr) material reveals a difference in the relative peak intensities.

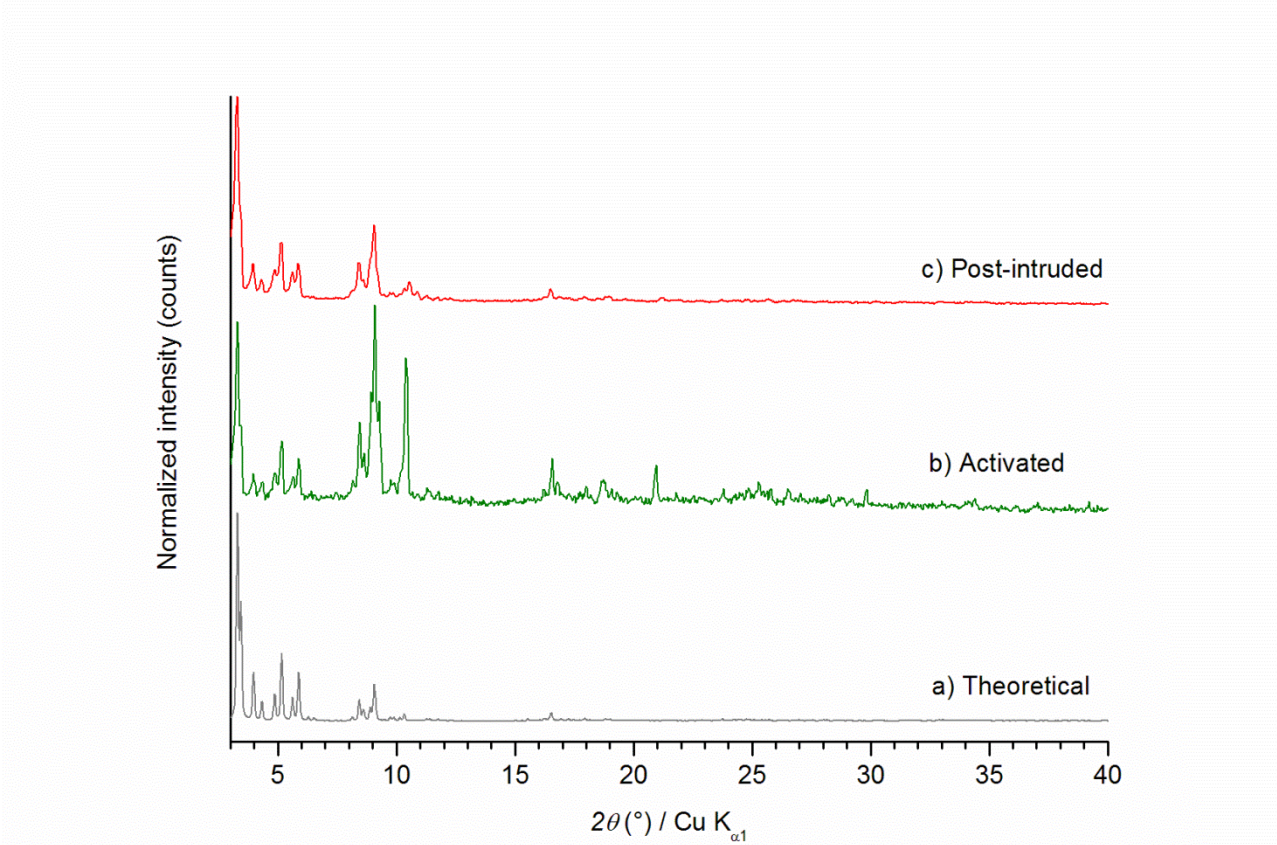

Figure 13. (a) Theoretical XRD pattern of MIL-101(Cr) and XRD patterns of the (b) activated and (c) post-intruded MIL-101(Cr) samples.

The activated sample was also investigated with N_2 sorption measurements (Figure 14). Even if in our case the low pressure domain was not explored (so as to save time), the N_2 sorption isotherm displays the general profile already reported.[7, 34, 37] Before achieving the complete filling of the porosity, slightly below a relative pressure of 0.30, two nitrogen uptake steps are observable at relative pressure values of 0.15 and 0.25 and are correlated with the filling of the two types of cages. The values for the porous volume and BET surface area are determined as 1.10 $cm^3\ g^{-1}$ and 2103 $m^2\ g^{-1}$, respectively. Even though these values (especially in terms of the porous volume) are slightly lower compared to the literature, however, they still demonstrate the high porosity of MIL-101(Cr).[38-39]

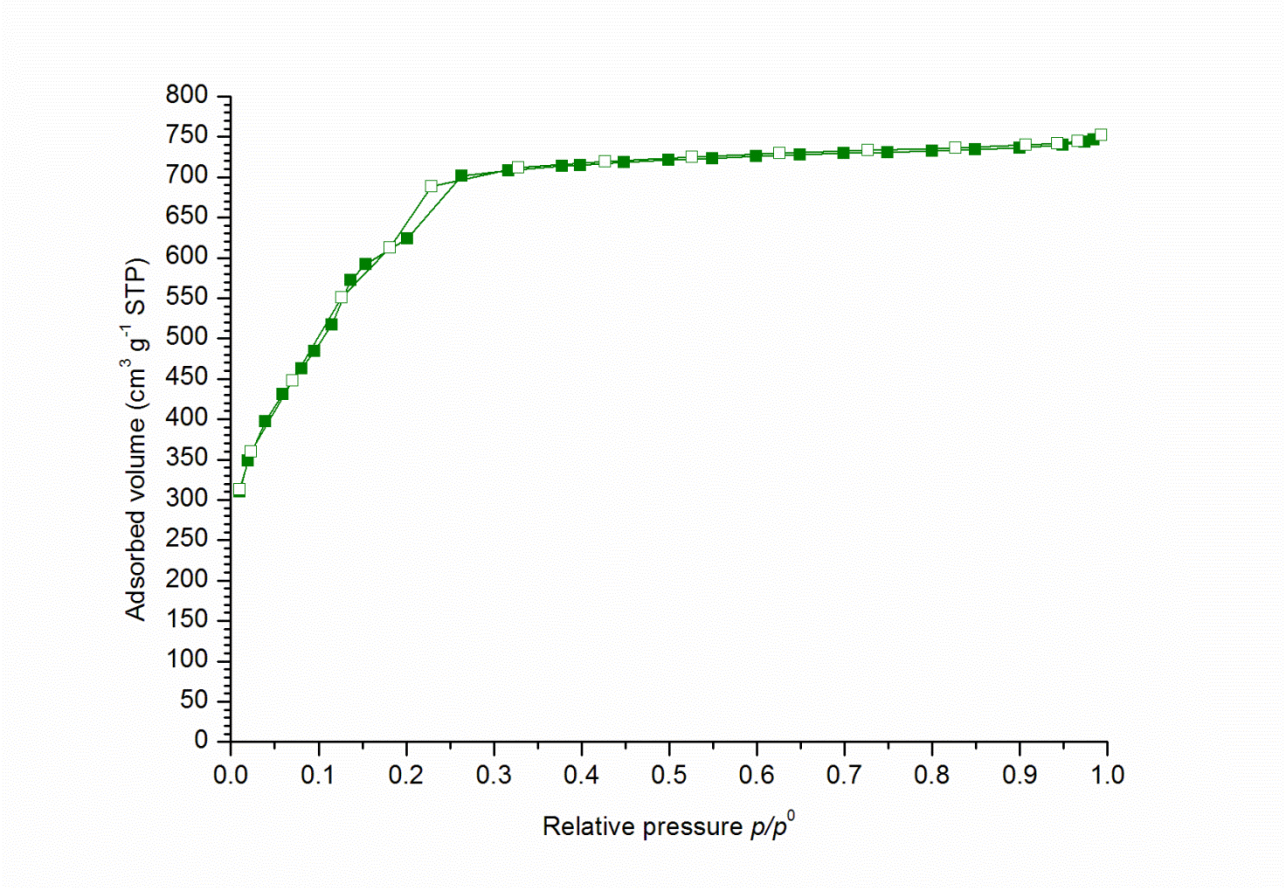

Figure 14. N_2 adsorption-desorption isotherms of the activated MIL-101(Cr) sample. The filled and empty symbols refer to the adsorption and desorption branches, respectively.

4. Intrusion−Extrusion Experiments

By virtue of its high porosity, and knowing that this material has never been explored in intrusion−extrusion experiments before, a first attempt to determine its energetic behavior using a LiCl 20 M aqueous solution as a non-wetting liquid was undertaken on the degassed sample. The obtained intrusion−extrusion curve (Figure 15) reveals no volume variation step characteristic of the intrusion of the non-wetting liquid molecules into the MIL-101(Cr) pores. The volume variations observed during the three cycles are only attributed to the compression-decompression of the non-wetting liquid molecules in the intrusion−extrusion cell.

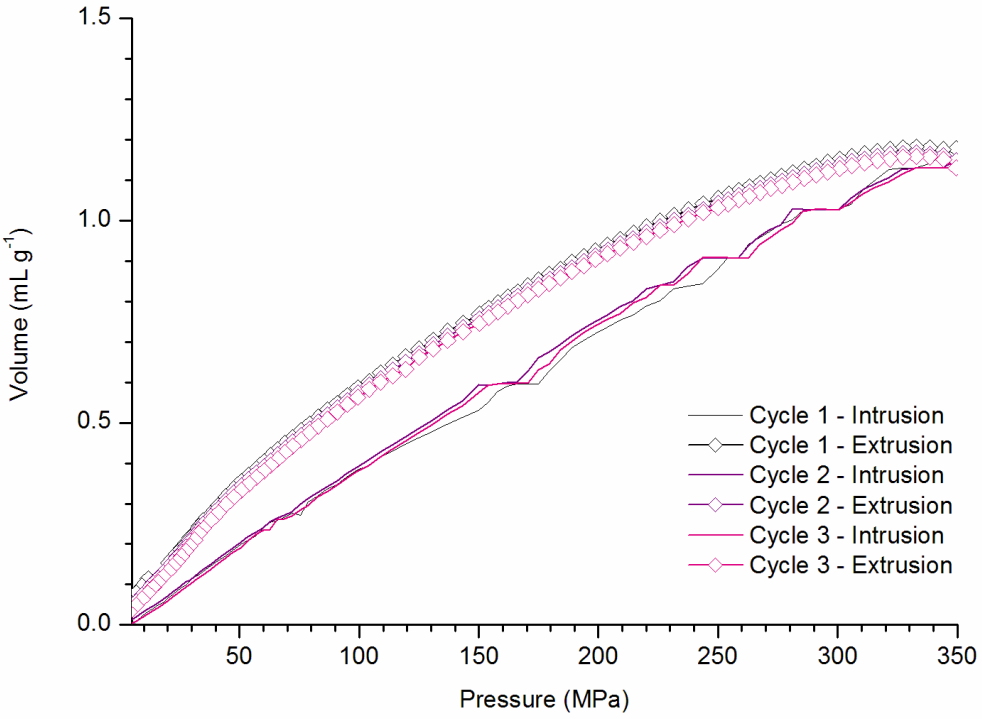

Figure 15. Pressure-volume diagrams of the "MIL-101(Cr)−LiCl 20 M aqueous solution" system.

Figure 13 shows the XRD pattern of the post-intruded MIL-101(Cr) sample. Clearly, the MOF structure is retained after three intrusion−extrusion cycles realized up to 350 MPa, which indicates the high stability of the MIL-101(Cr) framework under the combined effect of both the high pressure and the aqueous medium. Moreover, the absence of an intrusion step may be attributed to the hydrophilic character of MIL-101(Cr), which might have led to the adsorption of some water molecules at low pressures, thereby preventing the further intrusion of any non-wetting liquid molecules at elevated pressures. Nevertheless, post-intrusion N_2 sorption analysis is also necessary in order to confirm the stability of the MOF framework.

III. **Conclusions**

By virtue of their high porosity and novelty, several reported MOFs/ZIFs i. e. NOF-1, ZIF-76, AFI-$Zn(im)_2$, CAN-$Zn(im)_2$, MOF-919(Sc/Cu), and MIL-101(Cr), were considered promising candidates for intrusion−extrusion experiments. Thus, we intended to synthesize these materials, fully characterize them, and explore their energetic behaviors in intrusion−extrusion experiments using water and/or LiCl 20 M aqueous solution as non-wetting liquids. Unfortunately, for MOF-919(Sc/Cu), the synthesis was not reproducible. As for NOF-1, problems were encountered during activation by soaking in MeOH, where the ZIF structure loses crystallinity. The activation step was also complicated in the case of the AFI- and CAN-type ZIF materials, as it was associated with a partial amorphization of the structure and did not lead to fully activated pores, which were indicated from XRD and N_2 adsorption-desorption measurements, respectively. Moreover, based on our experimental results, the AFI- and CAN-type ZIF materials are unstable in water (with the AFI-type material being slightly more stable in water compared to CAN). Consequently, due to the lack of reproducibility, problems encountered during activation, and the low water stability, in addition to the lack of the time required to further optimize the synthesis and activation processes, NOF-1, MOF-919(Sc/Cu), and the AFI- and CAN-type ZIF materials were not investigated in water or aqueous electrolyte solutions intrusion−extrusion experiments.

In contrast, ZIF-76 and MIL-101(Cr) were successfully reproduced (synthesized several times and fully activated). Nonetheless, due to the hydrophilic character of MIL-101(Cr), in addition to the low water stability of ZIF-76, water intrusion−extrusion experiments were not realized on these two materials. But, it was worth studying their energetic behavior using a LiCl 20 M aqueous solution. Based on the experimentally obtained results, the $P-V$ diagrams of MIL-101(Cr) shows no intrusion step, which can be attributed to its hydrophylic character and probably explained by the adsorption of some water molecules at low pressure values, thus, preventing the intrusion of the non-wetting liquid at elevated pressures. However, our results indicate that this material is stable under pressures as high as 350 MPa and in contact with a LiCl 20 M aqueous solution. Thus, it remains a good candidate for the strategy involving PSM followed by intrusion−extrusion experiments. As for ZIF-76, the "ZIF-76–LiCl 20 M aqueous solution" system exhibits a volume variation step upon intrusion. Further investigation, in particular, complementary intrusion−extrusion experiments (realized under lower pressures, i.e 80 MPa) in addition to post-intrusion−extrusion characterizations, are required in order to gain better insight into the energetic performances of this system.

Finally, this chapter highlights the difficulty of MOF synthesis. Indeed, published syntheses are not always easily reproducible. The activation step can also be delicate. In addition, the stability of

MOF materials in water or in aqueous media, which is crucial for intrusion−extrusion experiments, is difficult to predict.

References

1. Shi, Q.; Xu, W.-J.; Huang, R.-K.; Zhang, W.-X.; Li, Y.; Wang, P.; Shi, F.-N.; Li, L.; Li, J.; Dong, J., Zeolite CAN and AFI-Type Zeolitic Imidazolate Frameworks with Large 12-Membered Ring Pore Openings Synthesized Using Bulky Amides as Structure-Directing Agents. *J. Am. Chem. Soc.* **2016,** *138*, 16232-16235.

2. Mortada, B.; Chaplais, G.; Veremeienko, V.; Nouali, H.; Marichal, C.; Patarin, J., Energetic Performances of ZIF-8 Derivatives: Impact of the Substitution (Me, Cl, or Br) on Imidazolate Linker. *J. Phys. Chem. C* **2018,** *122*, 3846-3855.

3. Mortada, B.; Chaplais, G.; Nouali, H.; Marichal, C.; Patarin, J., Phase Transformations of Metal-Organic Frameworks MAF-6 and ZIF-71 during Intrusion-Extrusion Experiments. *J. Phys. Chem. C* **2019,** *123*, 4319-4328.

4. Diring, S.; Wang, D. O.; Kim, C.; Kondo, M.; Chen, Y.; Kitagawa, S.; Kamei, K.-i.; Furukawa, S., Localized Cell Stimulation by Nitric Oxide using a Photoactive Porous Coordination Polymer Platform. *Nat Commun.* **2013,** *4*, 2684-2692.

5. Bullot, L.; Vieira-Sellai, L.; Chaplais, G.; Simon-Masseron, A.; Daou, T. J.; Patarin, J.; Fiani, E., Adsorption of 1,2-Dichlorobenzene and 1,2,4-Trichlorobenzene in Nano- and Microsized Crystals of MIL-101(Cr): Static and Dynamic Gravimetric Studies. *Environ. Sci. Pollut. Res.* **2017,** *24*, 26562-26573.

6. Liu, Q.; Song, Y.; Ma, Y.; Zhou, Y.; Cong, H.; Wang, C.; Wu, J.; Hu, G.; O'Keeffe, M.; Deng, H., Mesoporous Cages in Chemically Robust MOFs Created by a Large Number of Vertices with Reduced Connectivity. *J. Am. Chem. Soc.* **2019,** *141*, 488-496.

7. Hong, D.-Y.; Hwang, Y. K.; Serre, C.; Ferey, G.; Chang, J.-S., Porous Chromium Terephthalate MIL-101 with Coordinatively Unsaturated Sites: Surface Functionalization, Encapsulation, Sorption and Catalysis. *Adv. Funct. Mater.* **2009,** *19*, 1537-1552.

8. Ban, Y.; Li, Y.; Peng, Y.; Jin, H.; Jiao, W.; Liu, X.; Yang, W., Metal-Substituted Zeolitic Imidazolate Framework ZIF-108: Gas-Sorption and Membrane-Separation Properties. *Chem. - Eur. J.* **2014,** *20*, 11402-11409.

9. Tian, Y.-Q.; Zhao, Y.-M.; Chen, Z.-X.; Zhang, G.-N.; Weng, L.-H.; Zhao, D.-Y., Design and Generation of Extended Zeolitic Metal-Organic Frameworks (ZMOFs): Synthesis and Crystal

Structure of zinc(II) Imidazolate Polymers with Zeolitic Frameworks. *Chem. - Eur. J.* **2007,** *13*, 4146-4154.

10. Peralta, D.; Chaplais, G.; Simon-Masseron, A.; Barthelet, K.; Pirngruber, G. D., Synthesis and adsorption properties of ZIF-76 isomorphs. *Microporous Mesoporous Mater.* **2012,** *153*, 1-7.

11. Banerjee, R.; Phan, A.; Wang, B.; Knobler, C.; Furukawa, H.; O'Keeffe, M.; Yaghi, O. M., High-Throughput Synthesis of Zeolitic Imidazolate Frameworks and Application to CO2 Capture. *Science (Washington, DC, U. S.)* **2008,** *319*, 939-943.

12. Pham, T.; Forrest, K. A.; Furukawa, H.; Eckert, J.; Space, B., Hydrogen Adsorption in a Zeolitic Imidazolate Framework with lta Topology. *J. Phys. Chem. C* **2018,** *122*, 15435-15445.

13. Grosu, Y.; Li, M.; Peng, Y.-L.; Luo, D.; Li, D.; Faik, A.; Nedelec, J.-M.; Grolier, J.-P., A Highly Stable Nonhysteretic {Cu2(tebpz) MOF+water} Molecular Spring. *ChemPhysChem* **2016,** *17*, 3359-3364.

14. Huang, L.; Wang, H.; Chen, J.; Wang, Z.; Sun, J.; Zhao, D.; Yan, Y., Synthesis, Morphology Control, and Properties of Porous Metal-Organic Coordination Polymers. *Microporous Mesoporous Mater.* **2003,** *58*, 105-114.

15. Ortiz, G.; Nouali, H.; Marichal, C.; Chaplais, G.; Patarin, J., Energetic Performances of the Metal–Organic Framework ZIF-8 Obtained Using High Pressure Water Intrusion–Extrusion Experiments. *Phys. Chem. Chem. Phys.* **2013,** *15*, 4888-4891.

16. Ferey, G.; Mellot-Draznieks, C.; Serre, C.; Millange, F., Crystallized Frameworks with Giant Pores: Are There Limits to the Possible? *Acc. Chem. Res.* **2005,** *38*, 217-225.

17. Wu, T.; Bu, X.; Zhang, J.; Feng, P., New Zeolitic Imidazolate Frameworks: From Unprecedented Assembly of Cubic Clusters to Ordered Cooperative Organization of Complementary Ligands. *Chem. Mater.* **2008,** *20*, 7377-7382.

18. Yang, J.; Zhang, Y.-B.; Liu, Q.; Trickett, C. A.; Gutierrez-Puebla, E.; Monge, M. A.; Cong, H.; Aldossary, A.; Deng, H.; Yaghi, O. M., Principles of Designing Extra-Large Pore Openings and Cages in Zeolitic Imidazolate Frameworks. *J. Am. Chem. Soc.* **2017,** *139*, 6448-6455.

19. Tian, Y.-Q.; Yao, S.-Y.; Gu, D.; Cui, K.-H.; Guo, D.-W.; Zhang, G.; Chen, Z.-X.; Zhao, D.-Y., Cadmium Imidazolate Frameworks with Polymorphism, High Thermal Stability, and a Large Surface Area. *Chem. - Eur. J.* **2010,** *16*, 1137-1141.

20. Zhu, A.-X.; Lin, R.-B.; Qi, X.-L.; Liu, Y.; Lin, Y.-Y.; Zhang, J.-P.; Chen, X.-M., Zeolitic Metal Azolate Frameworks (MAFs) from ZnO/Zn(OH)2 and Monoalkyl-Substituted Imidazoles and 1,2,4-Triazoles: Efficient Syntheses and Properties. *Microporous Mesoporous Mater.* **2012,** *157*, 42-49.

21. Nguyen, N. T. T.; Furukawa, H.; Gandara, F.; Nguyen, H. T.; Cordova, K. E.; Yaghi, O. M., Selective Capture of Carbon Dioxide under Humid Conditions by Hydrophobic Chabazite-Type Zeolitic Imidazolate Frameworks. *Angew. Chem., Int. Ed.* **2014,** *53*, 10645-10648.

22. Park, K. S.; Ni, Z.; Cote, A. P.; Choi, J. Y.; Huang, R.; Uribe-Romo, F. J.; Chae, H. K.; O'Keeffe, M.; Yaghi, O. M., Exceptional Chemical and Thermal Stability of Zeolitic Imidazolate Frameworks. *Proc. Natl. Acad. Sci. U. S. A.* **2006,** *103*, 10186-10191.

23. Hayashi, H.; Cote, A. P.; Furukawa, H.; O'Keeffe, M.; Yaghi, O. M., Zeolite A Imidazolate Frameworks. *Nat. Mater.* **2007,** *6*, 501-506.

24. Karagiaridi, O.; Bury, W.; Sarjeant, A. A.; Stern, C. L.; Farha, O. K.; Hupp, J. T., Synthesis and Characterization of Isostructural Cadmium Zeolitic Imidazolate Frameworks via Solvent-Assisted Linker Exchange. *Chem. Sci.* **2012,** *3*, 3256-3260.

25. Biswal, B. P.; Panda, T.; Banerjee, R., Solution Mediated Phase Transformation (RHO to SOD) in Porous Co-Imidazolate Based Zeolitic Frameworks with High Water Stability. *Chem. Commun. (Cambridge, U. K.)* **2012,** *48*, 11868-11870.

26. Yao, S.-Y.; Tian, Y.-Q., An Exceptional Self-Penetrating 4-Connected Network Derived from a (3,4)-Connected Net of tfa-c Topology. *CrystEngComm* **2010,** *12*, 697-699.

27. Wang, B.; Cote, A. P.; Furukawa, H.; O'Keeffe, M.; Yaghi, O. M., Colossal Cages in Zeolitic Imidazolate Frameworks as Selective Carbon Dioxide Reservoirs. *Nature (London, U. K.)* **2008,** *453*, 207-211.

28. Wu, T.; Bu, X.; Liu, R.; Lin, Z.; Zhang, J.; Feng, P., A New Zeolitic Topology with Sixteen-Membered Ring and Multidimensional Large Pore Channels. *Chem. - Eur. J.* **2008,** *14*, 7771-7773.

29. Banerjee, R.; Furukawa, H.; Britt, D.; Knobler, C.; O'Keeffe, M.; Yaghi, O. M., Control of Pore Size and Functionality in Isoreticular Zeolitic Imidazolate Frameworks and their Carbon Dioxide Selective Capture Properties. *J. Am. Chem. Soc.* **2009,** *131*, 3875-3877.

30. Wang, Z.; Cohen, S. M., Postsynthetic Modification of Metal-Organic Frameworks. *Chem. Soc. Rev.* **2009,** *38*, 1315-1329.

31. Feng, D.; Wang, K.; Su, J.; Liu, T.-F.; Park, J.; Wei, Z.; Bosch, M.; Yakovenko, A.; Zou, X.; Zhou, H.-C., A Highly Stable Zeotype Mesoporous Zirconium Metal-Organic Framework with Ultralarge Pores. *Angew. Chem., Int. Ed.* **2015,** *54*, 149-154.

32. Ferey, G.; Serre, C.; Mellot-Draznieks, C.; Millange, F.; Surble, S.; Dutour, J.; Margiolaki, I., A Hybrid Solid with Giant Pores Prepared by a Combination of Targeted Chemistry, Simulation, and Powder Diffraction. *Angew Chem Int Ed Engl* **2004,** *43*, 6296-301.

33. Furukawa, H.; Gandara, F.; Zhang, Y.-B.; Jiang, J.; Queen, W. L.; Hudson, M. R.; Yaghi, O. M., Water Adsorption in Porous Metal-Organic Frameworks and Related Materials. *J. Am. Chem. Soc.* **2014,** *136*, 4369-4381.

34. Anon, A Chromium Terephthalate-Based Solid With Unusually Large Pore Volumes and Surface Area. *Science* **2005,** *310*, 1119.

35. Lebedev, O. I.; Millange, F.; Serre, C.; Van Tendeloo, G.; Ferey, G., First Direct Imaging of Giant Pores of the Metal-Organic Framework MIL-101. *Chem. Mater.* **2005,** *17*, 6525-6527.

36. Hwang, Y. K.; Hong, D.-Y.; Chang, J.-S.; Jhung, S. H.; Seo, Y.-K.; Kim, J.; Vimont, A.; Daturi, M.; Serre, C.; Ferey, G., Amine Grafting on Coordinatively Unsaturated Metal Centers of MOFs: Consequences for Catalysis and Metal Encapsulation. *Angew. Chem., Int. Ed.* **2008,** *47*, 4144-4148.

37. Jiang, D.; Burrows, A. D.; Edler, K. J., Size-Controlled synthesis of MIL-101(Cr) nanoparticles with Enhanced selectivity for CO2 over N2. *CrystEngComm* **2011,** *13*, 6916-6919.

38. Sun, J.; Yu, G.; Huo, Q.; Kan, Q.; Guan, J., Epoxidation of Styrene over Fe(Cr)-MIL-101 Metal-Organic Frameworks. *RSC Adv.* **2014,** *4*, 38048-38054.

39. Chowdhury, P.; Bikkina, C.; Gumma, S., Gas Adsorption Properties of the Chromium-Based Metal Organic Framework MIL-101. *J. Phys. Chem. C* **2009,** *113*, 6616-6621.

Conclusions and Perspectives

Heterogeneous systems formed of solid porous matrices such as ZIF materials and non-wetting liquids, also known as lyophobic heterogeneous systems (LHS), which can be used for mechanical energy storage and dissipation, have been explored in high-pressure intrusion−extrusion experiments. Tables 1 and 2 summarize the results obtained from all the intrusion−extrusion experiments conducted during this PhD work and from a few experiments previously reported in the literature. The tables tackle cage-type MOFs and the energetic characteristics of their related systems when water (Table 1) and aqueous electrolyte solutions (Table 2), restricted to KCl 4 M and LiCl 20 M, are used as non-wetting liquids.

Different parameters have been proven to influence the energetic behaviors and/or performances of ZIF-based LHSs during intrusion–extrusion experiments. The impacts of these parameters, that are the topology of the ZIF-type material, the functionalization of the linker, and the nature of the non-wetting liquid, are discussed in the next paragraphs.

The **topology** of ZIF-type materials appears to be probably one of the most impacting parameters on both energetic behaviors and performances of ZIF-based LHSs. As examples, the water-based systems involving, on one hand, ZIF-8 and ZIF-8_Cl of SOD topology and, on the other hand, ZIF-25 and ZIF-71 of RHO topology, can be cited. It is recalled that these materials are functionalized either by methyl groups (ZIF-8 and ZIF-25) or chlorine atoms (ZIF-8_Cl and ZIF-71). Whereas the LHSs based on SOD-type ZIFs display spring behavior with stored energies of around 11 J g^{-1} and intrusion pressures of 22-27 MPa, those elaborated from RHO-type ZIFs give rise to perfect shock-absorber behavior with stored energies of around 26-30 J g^{-1} and intrusion pressures of 57-71 MPa. These results are somewhat surprising as highest stored energies and, more especially, intrusion pressures were expected for LHSs involving SOD-type ZIFs, according to a model governed by the dimensions of cage apertures. Even though the structural flexibility of ZIF-8 and ZIF-8_Cl materials has been demonstrated, thereby implying an increase in the size of cage windows, this trend based on the ZIFs topology remains to be deepened.

The effect of the **linker's functionalization** can be, indeed, demonstrated through differences encountered in the physicochemical properties of ZIF material (such as their chemical stability), in addition to the energetic performances and behaviors of the ZIF-based LHSs. First, in order to illus-

Table 1. Composition, structural and textural properties of MOFs and the energetic characteristics of the corresponding "MOF–water" systems.

MOF sample	Composition	Topology	Largest cage aperture	$V_{micropore}$ ($cm^3\ g^{-1}$)	P_{int} (MPa)	P_{ext} (MPa)	V_{int} ($mL\ g^{-1}$)	E_s ($J\ g^{-1}$)	E_r ($J\ g^{-1}$)	Energy yield (%)	Energetic behavior new definition
ZIF-8	$Zn(mim)_2$	SOD	6 MR	0.66	27	24	0.40	10.8	9.8	91	S
ZIF-8_Cl	$Zn(cim)_2$			0.57	22	20	0.48	11	10	91	S
ZIF-8_Br	$Zn(bim)_2$			0.35	*a*	*a*	*a*	-	-	-	-
ZIF-67	$Co(mim)_2$			0.68	24	19	0.53	12.7	10.3	81	S
CdIF-1	$Cd(mim)_2$			0.86	Phase transformation into CdIF-3 in contact with water						
Zn(dcim)$_2$-SALE	$Zn(dcim)_2$			0.23	No observed intrusion-extrusion phenomenon in the range 0-350 MPa						
ZIF-7	$Zn(bim)_2$			0.21	No observed intrusion-extrusion phenomenon in the range 0-350 MPa						
ZIF-71	$Zn(dcim)_2$	RHO	8 MR	0.39	71	30	0.36	25.5	10.8	42	SA
MAF-6	$Zn(eim)_2$			0.61	Phase transformation into phase X						
ZIF-25	$Zn(dmim)_2$			0.55	57	25	0.52	30	13	42	SA
ZIF-11	$Zn(bim)_2$			0.46 0.58	No observed intrusion-extrusion phenomenon in the 0-300 MPa pressure range						

The diameters of the pore openings are estimated based on structure analyses. Intrusion (P_{int}) and extrusion (P_{ext}) pressures, intrusion volume (V_{int}), stored (E_s) and restored (E_r) energies of MOF materials studied. S, SA, and B correspond to spring, shock-absorber, and bumper behaviors, respectively. Cells corresponding to results from previous works are grayed out. *a* indicates that the value could not be determined from the intrusion−extrusion curves.

trate the impact of functionalization on the **chemical stability** of porous materials, the "ZIF-25–" and "MAF-6–water" systems can be considered (Table 1). Those two materials possess the RHO topology and alkyl groups as substituents (with two methyl groups placed in positions 4 and 5 for ZIF-25 and one ethyl group borne in position 2 for MAF-6). Whereas "ZIF-25–water" system adopts, as mentioned above, perfect shock-absorber behavior, MAF-6 undergoes a phase transformation under the combine effect of the pressure and water, thus, leading to the formation of a new pseudo-polymorph named phase X. The series of LHSs, based on water and SOD-type ZIFs such as ZIF-8, ZIF-8_Cl, ZIF-8_Br, $Zn(dcim)_2$-SALE, and ZIF-7 (Table 1), provide another example of the impact of the functionalization on the energetic performances and behaviors of LHSs. The systems incorporating ZIF-8 and ZIF-8_Cl, as described previously, behave as a spring. In contrast, no volume variation on the pressure–volume diagrams is evidenced for the LHSs incorporating ZIF-8_Br, $Zn(dcim)_2$-SALE, and ZIF-7. This difference highlights the importance of the imidazolate's functionalization and, interestingly also, that of the **steric hindrance** related to the nature of the substituents. Indeed, the bromine atom in position 2 (ZIF-8_Br), the two chlorine atoms in positions 4 and 5 ($Zn(dcim)_2$-SALE), and the benzyl group adjoining the imidazolate moiety at positions 4 and 5 (ZIF-7) are believed to block the diffusion of water molecules through the materials' porosity. Another consequence induced by the functionalization is the remarkable **flexibility/stiffness** of the linker in ZIFs. The influence of this structural parameter, which can be also correlated to steric hindrance, is particularly emphasized by the series of the LHSs based on ZIF-8 and its halogenated derivatives, with water as the non-wetting liquid (Table 1). Based on experimental and simulated nitrogen sorption measurements, ZIF-8 and ZIF-8_Cl are flexible, whereas ZIF-8_Br is stiff, which affects distinctly the energetic behaviors of the related systems during intrusion−extrusion experiments. Therefore, the functionalization can regulate the **dimensions of cage apertures** directly *via* the steric hindrance, or indirectly through the linker's flexibility, thereby, impacting the energetic performances of LHSs.

The **nature of the non-wetting liquid** constitutes also a significant component directing the energetic performances and behaviors of LHSs. Indeed, depending on the used non-wetting liquid, the chemical stability of the porous material, the intrusion pressure, and the behavior may be affected significantly. The "ZIF-71–water" and "ZIF-71–LiCl 20 M aqueous solution" systems provide examples illustrating the effect of the nature of the non-wetting liquid on the **chemical stability** of ZIFs (Tables 1 and 2). In fact, upon pressure and in the presence of LiCl 20 M aqueous solution, ZIF-71 is transformed into one of its known polymorphs; ZIF-72 of lcs topology. Even if ZIF-71 and ZIF-72 display the same chemical composition, the transformation from ZIF-71 to ZIF-72 implies an alteration of chemical stability. In contrast, with water, ZIF-71 leads to a system displaying perfect shock-absorber behavior.

Table 2. Composition, structural and textural properties of MOFs and the energetic characteristics of the corresponding "MOF−non-wetting liquid" systems.

MOF sample	Composition	Topology	Largest cage aperture	$V_{micropore}$ ($cm^3\ g^{-1}$)	Non-wetting liquid	P_{int} (MPa)	P_{ext} (MPa)	V_{int} ($mL\ g^{-1}$)	E_s/E_a ($J\ g^{-1}$)	E_r ($J\ g^{-1}$)	Energy yield (%)	Energetic behavior new definition
ZIF-8	$Zn(mim)_2$	SOD	6 MR	0.66	KCl 4 M	39	34.7	0.50	19.5	17.4	89	S
					LiCl 20 M	186	-	0.56	**104**	-	0	**B**
ZIF-8_Cl	$Zn(cim)_2$			0.57	KCl 4 M	44	34	0.40	18	14	78	SA
					LiCl 20 M	202	180	0.38	**77**	68	88	**S**
ZIF-8_Br	$Zn(bim)_2$			0.35	KCl 4 M	11	-	0.16	2	-	0	B
					LiCl 20 M	167	150	0.25	42	38	90	S
ZIF-71	$Zn(dcim)_2$	RHO	8 MR	0.39	KCl 4 M	96^a 62^b	36	0.36^a 0.05^b	34.6^a 3.1^b	1.73^a 1.8^b	5^a 58^b	B
					LiCl 20 M	Phase transformation into ZIF-72						
MAF-6	$Zn(eim)_2$			0.61	LiCl 20 M	Phase transformation into phase X						
ZIF-76	$Zn(im)_{1.17}(cbim)_{0.83}$	LTA		0.56	LiCl 20 M	50	-	0.42	22	-	0	B
MIL-101(Cr)	$Cr_3(O)F(BDC)_3$	MTN	6 MR 14.5 Å x 16 Å	1.00	LiCl 20 M	No observed intrusion-extrusion phenomenon in the 0-350 MPa pressure range						

Intrusion (P_{int}) and extrusion (P_{ext}) pressures, intrusion volume (V_{int}), stored (E_s), absorbed (E_a) and restored (E_r) energies of MOF materials studied. S, SA, and B correspond to spring, shock-absorber, and bumper behaviors, respectively. The components, behaviors and absorbed/stored energies of the most relevant systems are written in bold and colored in **blue**. Cells corresponding to results from previous works are grayed out. ^{a} and ^{b} refer to the values obtained from the first and second intrusion/extrusion cycles, respectively.

Moreover, the ZIF-8-based systems, involving water as well as the KCl 4 M and LiCl 20 M aqueous solutions, reveal a strong variation of the **intrusion pressure** value as function of the nature of the non-wetting liquid (Tables 1 and 2). Taking into account the extreme cases, the intrusion pressure increases considerably from 27 MPa with water to 186 MPa with the LiCl 20 M aqueous solution. A similar trend is observed for the LHSs incorporating the halogenated derivatives of ZIF-8. Such results reflect the impact of the nature of the electrolyte and the concentration of the corresponding aqueous electrolyte solution on the strength of the inter-molecular water-water and water-electrolyte interactions. Keeping the same LHSs in mind, it can be noted that the non-wetting liquid may modify also the **energetic behavior**. Indeed, the "ZIF-8–water" system behaves as a spring, whereas the "ZIF-8–LiCl 20 M aqueous solution" system displays bumper behavior with a notable value of absorbed energy of 104 J g^{-1}. Moreover, for ZIF-8_Br, whereas no volume variation is observed for the LHS in the case where water is employed as the non-wetting liquid, with a LiCl 20 M aqueous solution, the LHS displays perfect spring behavior. As for the ZIF-8_Cl-based systems, the spring behavior is conserved whatever the nature of non-wetting liquid (water or the LiCl 20 M aqueous solution), with a remarkable stored energy value of 77 J g^{-1}. These variable energetic transformations not only emphasize the importance of the nature of the non-wetting liquid, but also suggest that the chemical composition of ZIFs and, therefore, the linker's functionalization play a non-negligible role. This states that the host-guest interactions between the building components of ZIFs, i.e. the linkers, and the constituent molecules from the non-wetting liquid, such as water and electrolytic species, influence the type of energetic behavior of the LHS. Thus, for the cases developed above, with the LiCl 20 M aqueous solution, it is argued that the presence of an electron-donating group, such as a methyl group, on the imidazolate linker increases its electron density and favors the interactions with the salt cations. In contrary, the presence of substituent with an electron withdrawing effect, such as a chlorine atom, decreases the electron density on the imidazolate linker and, hence, the electrostatic interaction with the salt cations. However, in the light of molecular dynamic simulation studies reported recently in the literature, the repulsive interactions of the hydrated chlorine anions with the imidazolate linker have to be also considered.

In addition to advances in understanding the key parameters governing the energetic performances and behaviors of MOF-based LHSs, this work also sheds light on the difficulty of MOF synthesis. Indeed, published syntheses are not always easily reproducible, which is clearly demonstrated in the case of ZIF-25 and MOF-919(Sc/Cu). The activation step can also be delicate. For instance, NOF-1, in addition to the AFI- and CAN-type ZIF materials reveal a loss of crystallinity during soaking in methanol and dry acetone, respectively. Furthermore, the stability of MOF materials in water or in aqueous media is difficult to predict, nonetheless, is an essential characteristic of MOFs applied to

intrusion−extrusion experiments. However, despite all the difficulties and after varying several compositional and process parameters, we achieved in optimizing the synthesis of ZIF-25 of RHO topology using acetic acid as a modulator. Based on X-ray diffraction and nitrogen sorption analyses, a pure RHO-phase material of high crystallinity and textural properties similar to those reported in the literature was obtained, with a yield of 36 %. Moreover, the ZIF-25 structure was successfully and fully refined in the *Pm*-3*m* space group, for the first time, through Rietveld refinement from a powder X-ray diffraction pattern.

In the aim of completing the study on the energetic performances of LHSs based on RHO-type ZIF materials, the "ZIF-25–LiCl 20 M aqueous solution" system is also intended to be investigated in intrusion–extrusion experiments. On the other hand, the activation processes for CAN-Zn(im)$_2$ and AFI-Zn(im)$_2$ should be enhanced, so as to completely liberate the pores, while maintaining a high crystallinity of both materials. Knowing that the CAN-Zn(im)$_2$ and AFI-Zn(im)$_2$ materials display both 1D channels accessed through large 12-memebered ring pore apertures (of 13.2 and 15.6 Å for the CAN- and AFI-type material, respectively), indeed, they are considered as attractive candidates for the investigation of the effects of the topology and, more importantly, the pore dimensionality and large pore aperture size on the energetic behaviors and performances of LHSs applied to high-pressure intrusion−extrusion experiments.

Other zeolitic topologies explored in this work are the LTA and MTN of ZIF-76 and MIL-101(Cr) materials, respectively. The "ZIF-76−LiCl 20 M aqueous solution" system reveals bumper behavior during intrusion–extrusion experiments realized up to 350 MPa (with an absorbed energy of 22 J g^{-1}), which, based on post-intrusion characterizations, leads to the amorphization of the ZIF-76 framework. However, it is important to note that the volume variation occurs in the 50-60 MPa pressure range for this system (with ZIF-76 displaying 4-, 6-, and 8-membered ring pore apertures), which is lower than the intrusion pressures obtained with the SOD topology (where the structure consists of 4- and 6-membered ring pore apertures only). Although the "ZIF-76−LiCl 20 M aqueous solution" system is still under investigation, these results seem to be in agreement with the hypothesis suggesting the decrease in intrusion pressure with the increase in the size of the window opening, even if the linker functionalization is different in each case. Complementary intrusion–extrusion experiments on ZIF-76 (LTA), under lower pressures (i. e. 80 MPa), in addition to post-intrusion−extrusion characterizations, are needed in order to gain better insight into the effect of the topology on the energetic behavior and performances of the "ZIF-76−LiCl 20 M aqueous solution" system. Concerning the "MIL-101(Cr)−LiCl 20 M aqueous solution" system, the intrusion−extrusion curves reveal no volume variation step characteristic of the intrusion of the non-wetting liquid molecules into the MIL-101(Cr) pores, which may be attributed to the hydrophilic

character of MIL-101(Cr) that might have led to the adsorption of some water molecules at low pressure (rehydration of the activated sample), thereby preventing the further intrusion of any non-wetting liquid molecules at elevated pressures. Therefore the post-synthetic modification route seems to be the only perspective for employing hydrophilic materials of such a high pore volume in intrusion−extrusion experiments. Mainly, the mesoporous MIL-101(Cr) and MOF-919(Sc/Cu) materials are among the considered candidates for this strategy, which can be achieved through the grafting of a fluorinated primary amine, for example, on the metal center. This is intended to be followed by water- and aqueous electrolyte solution-intrusion–extrusion experiments, in the aim of obtaining high amounts of stored/absorbed energies, indeed, by virtue of the high porosity of these materials. Nevertheless, the synthesis of MOF-919(Sc/Cu) needs to be optimized first.

Finally, it is also important to note that even though the basic hypothesis suggests that increasing the porosity leads to higher stored/absorbed energy values, however, the experimentally obtained results clearly demonstrate that this is not the only parameter that controls the LHS's energetic performances during intrusion−extrusion experiments. For instance, for certain systems, a relatively high stored/absorbed energy value is the result of both a relatively high intruded volume and intrusion pressure, which is, indeed, the case for the "ZIF-8_Cl−LiCl 20 M aqueous solution" system that, as previously mentioned, registers until now the largest amount of stored energy (77 J g^{-1}) for a spring behavior obtained during intrusion−extrusion experiments.